

# Ultrafast Reaction Dynamics of Polyatomic Molecules Probed by Ionization



Astrid M. Müller

*Cover: image of a white-light plasma on a black screen.* The white-light plasma is generated by strongly focusing a short-pulse Ti:sapphire laser beam (70 fs, 1.8 mJ, 800 nm) in air. Nonlinear processes take place at very high intensities. Due to the highest intensity in the center, the blue area arises from the third-harmonic generation of the fundamental wavelength in the isotropic medium air. Other visible colors are generated by self-phase modulation of the original 800-nm pulse. The laser table below the bright area is illuminated by light scattered from the screen. (Photo: Astrid M. Müller, 1999.)

Dissertation zur Erlangung des Doktorgrades  
der Fakultät für Chemie und Pharmazie  
der Ludwig-Maximilians-Universität München

Ultrafast Reaction Dynamics  
of Polyatomic Molecules  
Probed by Ionization

Astrid M. Müller

aus

Weingarten

2000

## Erklärung

Diese Dissertation wurde im Sinne von § 13 Abs. 3 bzw. 4 der Promotionsordnung vom 29. Januar 1998 von Prof. Dr. Dr. h.c. K.-L. Kompa betreut.

## Ehrenwörtliche Versicherung

Diese Dissertation wurde selbständig, ohne unerlaubte Hilfe erarbeitet.

München, am 12. Dezember 2000

  
.....  
(Unterschrift des Autors)

Dissertation eingereicht am 8. November 2000

1. Gutachter Prof. Dr. Dr. h.c. K.-L. Kompa

2. Gutachter Prof. Dr. W. Zinth

Mündliche Prüfung am 11. Dezember 2000

*To my parents*



# Contents

<b>1</b>	<b>Introduction</b>	<b>1</b>
<b>2</b>	<b>Fundamental aspects of ultrafast photodynamics</b>	<b>4</b>
2.1	Ultrafast unimolecular reactions in photochemistry and photobiology . . . . .	4
2.1.1	Potential energy surfaces in reaction dynamics . . . . .	4
2.1.1.1	Born-Oppenheimer approximation . . . . .	6
2.1.1.2	Woodward-Hoffmann model . . . . .	8
2.1.1.3	Fermi's Golden Rule and Landau-Zener model . . . . .	11
2.1.2	Conical intersections . . . . .	13
2.1.2.1	Evidence of conical intersections in photochemistry and photobiology . . . . .	19
2.2	Photochemistry of 1,3,5-cyclooctatriene and 7-dehydrocholesterol . . . . .	22
2.3	Photoionization . . . . .	26
2.3.1	Keldysh adiabaticity parameter . . . . .	27
2.3.2	Molecules in strong laser fields . . . . .	29
<b>3</b>	<b>Experimental</b>	<b>30</b>
3.1	Principles of amplified short-pulse lasers . . . . .	30
3.2	Fundamentals of frequency conversion . . . . .	35
3.3	Setups used . . . . .	38
3.4	Laser system and optical setup for initial experiments . . . . .	38
3.4.1	Laser system . . . . .	38
3.4.2	Optical setup for pump-probe measurements . . . . .	40
3.5	Laser system and optical setup for final experiments . . . . .	43
3.5.1	Laser system . . . . .	43
3.5.2	Diagnostics for pulse characterization . . . . .	47
3.5.3	Optical setup for pump-probe measurements . . . . .	50
3.5.4	Optical setup for photoionization and photofragmentation measurements . . . . .	54
3.5.4.1	Experiments without nonlinear distortions of the laser beam . . . . .	54
3.5.4.2	Setup for the investigation of effects induced by continuum generation . . . . .	56
3.6	Time-of-flight mass spectrometer for initial experiments . . . . .	57
3.7	Time-of-flight mass spectrometer for final experiments . . . . .	61
3.8	Data acquisition . . . . .	65
3.8.1	Acquisition of mass spectra by a fast multiscaler . . . . .	66
3.8.2	Acquisition of time-dependent signals from pump-probe measurements . . . . .	67
3.9	Sample preparation . . . . .	68
<b>4</b>	<b>Results and discussion</b>	<b>69</b>
4.1	Data evaluation procedures . . . . .	69
4.1.1	Intensity-dependent measurements . . . . .	69
4.1.2	Time-dependent measurements . . . . .	71
4.2	Photoionization and photofragmentation of toluene . . . . .	74
4.2.1	Mechanism of the photoionization of toluene . . . . .	75
4.2.2	Influence of continuum generation on the fragmentation of toluene . . . . .	91

---

4.3	Pump-probe measurements of 1,3,5-cyclooctatriene . . . . .	96
4.3.1	Intensity-dependent measurements . . . . .	99
4.3.2	Time-dependent measurements . . . . .	99
4.3.3	Reaction dynamics of the photoinduced electrocyclic ring opening of 1,3,5-cyclooctatriene . . . . .	106
4.4	Pump-probe measurements of 7-dehydrocholesterol . . . . .	110
4.4.1	Time-dependent measurements . . . . .	110
4.4.2	Reaction dynamics of the photoinduced electrocyclic ring opening of 7-dehydrocholesterol . . . . .	113
<b>5</b>	<b>Summary</b>	<b>116</b>
<b>A</b>	<b>Derivation of the fit function of Eq. 4.1</b>	<b>119</b>
	<b>Abbreviations</b>	<b>123</b>
	<b>References</b>	<b>128</b>
	<b>Acknowledgements</b>	<b>137</b>
	<b>Curriculum vitae</b>	<b>141</b>



# 1 Introduction

Ultrafast photochemical reactions are characterized by an excited state lifetime that is in the order of only a few vibrational periods. Since this is the shortest possible timescale for a chemical reaction, studies of ultrafast reactions give a direct view on elementary reaction steps. As such studies of ultrafast chemical dynamics touch upon the old question of the course of a chemical reaction and, therefore, are of fundamental importance. In particular, microscopic comprehension of processes occurring at ultrashort timescales might play an important role in the future for predicting the course of chemical reactions. Moreover, ultrafast reactions play a central role in many processes not only in photochemistry, but also in photobiology such as in the vision process, in photosynthesis systems, in light protecting pigments and in the vitamin D synthesis. From a theoretical point of view, it is increasingly recognized that ultrafast reactions of polyatomic molecules involve easily accessible conical intersections as a characteristic feature [1–7]. Such potential energy surface transitions provide the basis for extremely fast interstate relaxation. As stated by Y. Haas, M. Klessinger, and S. Zilberg in a special issue of *Chemical Physics*, “conical intersections are now considered to be one of the central keys that may open the way to a better understanding of photochemistry [8].”

Since the development of short-pulse lasers in the early 1980s, the real-time investigation of ultrafast photochemical reactions has become a topic of rapidly growing activity. After having been pioneered since the mid 1980s by A.H. Zewail [9–13], to whom the 1999 Nobel Prize in Chemistry was awarded, “femtochemistry” as the field is commonly called has now become one of the most intensively pursued issues of research in chemistry. Of course, it is impossible to obtain a direct image of an evolving molecule by taking, for instance, a photograph, but the change of optical properties during a reaction opens up ways to visualize the evolution of a reacting molecule. This is done, for instance, by invoking special optical techniques in combination with theoretical approaches that are indispensable for a reliable interpretation of the often complicated data sets obtained from experiments. The technique used in the present work is the wide-spread pump-probe method which is based on the use of two subsequent light pulses, of which the first starts the process, while the second interacts with the system and produces a signal that depends on the momentary state of the system. Monitoring this signal as a function of the relative delay between the two pulses leads to a data curve related to the dynamical development of the system observed, in response to the action of the first pulse.

In the present work, the time-resolved dynamics of the photoinduced unimolecular reactions of the two cyclic polyenes 1,3,5-cyclooctatriene and 7-dehydrocholesterol is investigated. From a fundamental point of view, the 1,3,5-cyclooctatriene system is believed to give great impetus to a deeper insight in the elementary reaction steps of photoinduced electrocyclic ring openings of cyclic polyenes. The photoinitiated ring opening of 7-dehydrocholesterol, which is a substituted polyene and, furthermore, as vitamin D<sub>3</sub> precursor, has a special biological significance, may provide information on the influence of steric hindrance on the speed of such reactions.

The investigation of electrocyclic ring-opening reactions has been of ongoing scientific interest in the last few years. Intensive theoretical studies on the 1,3-cyclohexadiene system, which is the photochemically active part of 7-dehydrocholesterol, revealed the fundamental characteristics of the potential energy surfaces involved in driving this reaction and of molecular geometries at conical intersections [14–18]. Its photochemical reaction, which is induced by the absorption of one UV photon, proceeds from the excited state ( $1B_2$ ) via the spectro-

scopically dark  $2A_1$  state to the ground state ( $1A_1$ ), forming the ring-like 1,3,5-hexatriene product or again the reactant. These facts should also be applicable to the 1,3,5-cyclooctatriene system. However, in this case, there are strong arguments towards the participation of two different reaction channels leading to three primary products. The present work aims to prove the existence of these two channels corresponding to two different conical intersections to the ground state. In the literature, descriptions of experimental investigations of the photoreactions of 1,3,5-cyclooctatriene and 7-dehydrocholesterol exist. P.J. Reid *et al.* deduced from a ps time-resolved resonance Raman experiment a ground-state appearance time of  $(12 \pm 2)$  ps for the 1,3,5-cyclooctatriene ring-opening reaction [19,20]. However, the relaxation time of this molecule is expected to be much shorter, due to its structural resemblance to 1,3-cyclohexadiene. Recently, R.J. Sension *et al.* studied the photoactivated ring opening of 7-dehydrocholesterol to previtamin  $D_3$  in methanol *solution* with fs transient absorption spectroscopy [21], and established an  $S_1$  lifetime of  $(0.95 \pm 0.1)$  ps and an  $S_2$  decay time of  $\leq 0.1$  ps. In contrast to that, the present work aims to determine the temporal behavior of this reaction in the *gas phase*. The difference between the relaxations of the 7-dehydrocholesterol system and of an unsubstituted cyclic polyene is believed to provide information about the influence of bulky substituents on the reaction speed. Measurements of the two different molecules under similar conditions are required to establish the role of a steric factor.

In order to elucidate reaction dynamics of molecules without the potentially disturbing influence of a solvent, matrix or surface, all molecules in the present work are investigated in the gas phase. This ensures the comparability of experimental with theoretical results. Since in this case the particle density is too small for transient absorption experiments, the probe step in pump-probe experiments is performed using the photoionization technique. The cations produced are detected by time-of-flight mass spectrometry. To shed more light on this probe method, the photoionization and photofragmentation of the medium-sized organic molecule toluene is investigated in detail. This compound was chosen because its ionization mechanism may be characteristic for similar-sized molecules. Moreover, there is a controversy in the literature on its ionization mechanism and fragmentation behavior. Especially in fs experiments, careful analysis of the measuring conditions is a *conditio sine qua non* for a proper understanding of experimental work. Combined with quantum-chemical calculations, the investigations of the present work give new insight into ultrafast molecular dynamics.

This thesis is organized as follows: the next chapter gives a background survey of fundamental aspects of ultrafast unimolecular reactions in photochemistry and photobiology including the concept of conical intersections. Then, the specific photochemical properties of 1,3,5-cyclooctatriene and 7-dehydrocholesterol are described and an overview of photoionization is given. In the subsequent chapter, the fundamentals of short-pulse lasers and frequency conversion are introduced. Then, the experimental setups and methods used are described. The ensuing chapter is devoted to experimental results of the photoexcitation of toluene and the pump-probe measurements of 1,3,5-cyclooctatriene and 7-dehydrocholesterol, and includes a description of the data evaluation procedures used. The photoionization mechanism of toluene using intense, short pulses in the near-infrared (NIR) and its photofragmentation behavior under the influence of continuum generation are presented. In addition, the potential of the latter method for the coherent control of fragmentation is demonstrated. Moreover, time-resolved measurements of the electrocyclic ring-opening reaction of 1,3,5-cyclooctatriene are presented with particular emphasis on the probe process, the details of which were thoroughly investigated. The total transient pump-probe signal is simulated taking into account the time-dependent behavior of the probe step, and the measured decay times are assigned to molecular dynamics. The last section of this chapter deals with the

---

results of pump-probe measurements of the ring opening of 7-dehydrocholesterol elucidating the role of steric hindrance in ultrafast reactions. In chapter 5, finally, the main results of this thesis are summarized.

## 2 Fundamental aspects of ultrafast photodynamics

### 2.1 Ultrafast unimolecular reactions in photochemistry and photobiology

Modern quantum-chemistry aims, among other topics, to elucidate ultrafast chemical reactions involving more than one electronic state. The development of powerful computers over the past two decades gives a great impetus to theoretical research. The (numerical) calculation of complex problems resulting in huge data amounts, in particular, can only be performed by devices exhibiting sufficient large storage capacities and computing power. The use of parallel processing, in particular, makes the quantum-chemical calculation of such problems possible. Besides the progress concerning computers, the quantum-chemical methods have been improved significantly, too. The most prominent researchers involved in the theoretical and computational development are W. Kohn and J. Pople who were awarded the Nobel Prize in Chemistry 1998 [22]. W. Kohn developed the density-functional theory, which has become the basis for simplifying the mathematics in describing the bonding of atoms. J. Pople developed a complete quantum-chemical methodology and designed the GAUSSIAN computer program [23], which implements the fundamental laws of quantum mechanics. Thereby, the theoretical study of molecules, their properties, and the way they act together in chemical reactions are now accessible.

#### 2.1.1 Potential energy surfaces in reaction dynamics

The idea to describe the evolution of a reacting molecule by means of a path on potential energy surfaces has the purpose of making the changing arrangement of the atoms and bonds in a molecule and the corresponding change of potential energy conceivable.

From a basic point of view, a molecule is a collection of nuclei and electrons. In quantum mechanics, such a system can be described by its total wavefunction  $\Psi$  and the Schrödinger equation, given by (neglecting the spin coordinates):

$$\left[ -\hbar^2 \sum_i \frac{1}{2m_i} \nabla_i^2 + V(\mathbf{r}, \mathbf{R}, t) \right] \Psi(\mathbf{r}, \mathbf{R}, t) = i\hbar \frac{\partial \Psi(\mathbf{r}, \mathbf{R}, t)}{\partial t}. \quad (2.1)$$

In this equation  $V$  is the potential,  $\mathbf{R}$  and  $\mathbf{r}$  are the relative positions of the nuclei and of the electrons inside the molecule, respectively, and a summation is made over all particles  $i$  (nuclei and electrons), with  $m_i$  being the mass of the particle  $i$ . The differential operator on the left side is known as Laplacian and is a generalization of the partial differentiation  $\partial^2/\partial x^2$  to more dimensions

$$\nabla^2 = \frac{\partial^2}{\partial x^2} + \frac{\partial^2}{\partial y^2} + \frac{\partial^2}{\partial z^2}. \quad (2.2)$$

The energy of the system can be obtained by solving the Schrödinger equation for  $\Psi$ . In general, the solution is given by many different wavefunctions. If the potential  $V$  is not a function of time, the Schrödinger equation can be simplified by a mathematical technique called separation of variables. This way two equations are obtained, one depending only on the position of the particles (i. e. the conformation of the molecule), the other being a

function of time alone. The time-independent Schrödinger equation is then given by

$$\hat{H} \Psi(\mathbf{r}, \mathbf{R}) = E \Psi(\mathbf{r}, \mathbf{R}). \quad (2.3)$$

In this equation  $E$  denotes the energy of the molecule in a certain conformation, and the operator  $\hat{H}$  is the Hamiltonian which corresponds to the expression in brackets in Eq. 2.1. The various solutions to this equation correspond to different energy eigen-values, or in other words, to different stationary states of the molecule. Solving the Schrödinger equation for the electrons in the potential of the atomic nuclei then gives the electronic states of the system. The stationary state belonging to the lowest energy eigen-value is called the electronic ground state, whereas states with higher energies are called excited states. The Schrödinger equation is generally solved for a certain arrangement of the particles in the molecule. Since the wavefunction as well as the potential are dependent on the relative position of these particles, the variation of the molecular conformation leads to different sets of energy eigen-values. In principle, whole potential energy surfaces can be calculated this way, their dimensionality depending on the number of particles. In general,  $3N$  spatial coordinates are required to describe an  $N$ -atomic molecule. This number contains three translational and three (or in case of linear molecules two) rotational degrees of freedom. If no external forces are present, the total momentum and the total angular momentum are conserved. Then, a coordinate system with  $3N - 6$  (or, for linear molecules,  $3N - 5$ ) independent variables representing the internal coordinates of the molecule can be applied, thus focusing on the intrinsic properties of the molecule. The choice of a suitable coordinate system depends of course on the particular problem.

The concept of motion of reacting systems on potential energy surfaces is the most stringent approach in the theoretical treatment of reaction dynamics. Stable molecular structures always correspond to local minima on potential energy surfaces. These can be calculated by a procedure called geometry optimization, usually via gradient methods. In addition to these stationary problems, the determination of other properties of a potential energy surface can also be of great interest, if molecular dynamics is to be investigated. If a molecule receives a sufficient amount of energy, e. g. by absorption of one or more photons, it is able to reach areas on the potential energy surface exhibiting a topology leading to larger changes of the molecular geometry. Namely the curvature of a potential energy surface presets the direction in which the evolving molecule is accelerated, or, in other words, this quantity determines which products form with which internal state distribution in which yield and in which reaction time.

The Hamiltonian  $\hat{H}$  in Eq. 2.3 is the sum of kinetic and potential energy operators

$$\hat{H} = \hat{T} + \hat{V}. \quad (2.4)$$

The kinetic energy operator  $\hat{T}$  is a summation of the Laplacian over all particles  $i$  (nuclei and electrons) in the molecule

$$\hat{T} = -\hbar^2 \sum_i \frac{1}{2m_i} \nabla_i^2, \quad (2.5)$$

whereas the potential energy operator  $\hat{V}$  represents the Coulomb interaction between each pair of charged particles, treating each nucleus as a single charged mass,

$$\hat{V} = \frac{1}{4\pi\epsilon_0} \sum_j \sum_{k < j} \frac{q_j q_k}{r_{jk}}. \quad (2.6)$$

In this equation,  $r_{jk}$  is the distance between two distinct particles  $j$  and  $k$  exhibiting the charges  $q_j$  and  $q_k$ . For an electron the charge amounts to  $-e$ , and for an atomic nucleus it is  $Ze$ , with  $Z$  being the ordinal number of the particular atom.

The Schrödinger equation is a non-relativistic description of a system which is not valid if the velocities of the particles approach the speed of light. Thus it does not give an accurate picture of core electrons in heavy nuclei (such as transition metals or rare earths). But for the molecules treated in this work (hydrocarbons), relativistic effects are negligible.

### 2.1.1.1 Born-Oppenheimer approximation

The Born-Oppenheimer approximation is used to simplify the solution of the Schrödinger equation. In what follows, I want to point out the general importance of this approximation for calculating potential energy surfaces. Its applicability to ultrafast surface transitions, however, is restricted, as will be described below. The Born-Oppenheimer approximation simplifies the general (multi-dimensional) molecular problem by the assumption that the motions of atomic nuclei and electrons can be separated. This is possible, since electrons move fast compared to nuclei due to the great mass difference between these two types of particles. As a consequence, the electrons react essentially instantaneously to changes in nuclear positions, thus forming a quasi-stationary electron state at every configuration of nuclei. This leads to the reasonable approximation that the electron distribution is only a function of the instantaneous positions of the nuclei and not of their velocities. Therefore, the quantum-mechanical problem of electron motion can be solved first in the field of fixed nuclei, resulting in an effective electronic energy  $E(\mathbf{R})$  which is then included as part of the potential energy for the subsequent calculation of the nuclear motion. The effective energy is a function of all nuclear coordinates  $\mathbf{R}$ . The electronic Schrödinger equation cannot be solved analytically (for complicated molecules). Consequently, it is solved “point by point” for many nuclear arrangements  $\mathbf{R}$ . Then the function  $E(\mathbf{R})$  is available point by point, too, and can be modeled by suitable approximation functions (e. g. quadratic functions for the harmonic approximation or Morse functions). The functions  $E(\mathbf{R})$  obtained by using the Born-Oppenheimer approximation are called adiabatic potential energy surfaces of the system. Solving the equation for the nuclear motion quantum-mechanically for complex systems is very tedious. Instead of this, classical approximations are used, by considering the atomic nuclei as classical particles for which Newton’s equations of motion can be solved. This results in classical path lines for the nuclear motion, called trajectories. Another possibility to simplify the solution of the Schrödinger equation for nuclear motion is to reduce its dimensionality, so that the nuclear motion can nowadays be calculated quantum-mechanically using numerical methods.

Due to the assumption that the separation of electron and nuclear motion is possible, the Hamiltonian can be decomposed into the sum

$$\hat{H} = \hat{H}_{(nuc)} + \hat{H}_{(el)}, \quad (2.7)$$

with

$$\hat{H}_{nuc} = \hat{T}_{(nuc)} + \hat{V}_{(nuc,nuc)}, \quad (2.8)$$

containing only nuclear coordinates. However, besides pure electronic parts, the electron Hamiltonian also contains the electron-nucleus interaction

$$\hat{H}_{(el)} = \hat{T}_{(el)} + \hat{V}_{(el,el)} + \hat{V}_{(el,nuc)}. \quad (2.9)$$

Due to the assumption of the separability of electron and nuclear motion, a product ansatz can be made for the wavefunction

$$\Psi(\mathbf{r}, \mathbf{R}) = \psi_{(el)}(\mathbf{r}; \mathbf{R}) \phi_{(nuc)}(\mathbf{R}). \quad (2.10)$$

In this approximation the nuclear wavefunctions  $\phi_{(nuc)}$  depend only on nuclear coordinates. The electron wavefunctions  $\psi_{(el)}(\mathbf{r}; \mathbf{R})$ , however, contain electron coordinates as variables, but additionally nuclear coordinates as parameters. First, the electron motion is treated for a fixed arrangement of nuclei. This means that the kinetic energy of the nuclei is  $\hat{T}_{(nuc)} = 0$ , and the operator of the nuclear repulsion  $\hat{V}_{(nuc,nuc)}$  is constant. Insertion of Eq. 2.10 into the Schrödinger equation (Eq. 2.3) gives thus

$$(\hat{H}_{(el)} + \hat{V}_{(nuc,nuc)}) \psi_{(el)} \phi_{(nuc)} = E \psi_{(el)} \phi_{(nuc)}. \quad (2.11)$$

Since the term  $\hat{V}_{(el,nuc)}$  in Eq. 2.9 is an operator used multiplicatively, Eq. 2.11 can be written as

$$\phi_{(nuc)} \hat{H}_{(el)} \psi_{(el)} + \hat{V}_{(nuc,nuc)} \psi_{(el)} \phi_{(nuc)} = E \psi_{(el)} \phi_{(nuc)}. \quad (2.12)$$

Division of this equation through  $\phi_{(nuc)}$  results in the so-called electronic Schrödinger equation

$$\hat{H}_{(el)} \psi_{(el)}(\mathbf{r}; \mathbf{R}) = E_{(el)}(\mathbf{R}) \psi_{(el)}(\mathbf{r}; \mathbf{R}) \quad (2.13)$$

whose energy eigen-values  $E_{(el)}$  are parametrically dependent on each nuclear arrangement  $\mathbf{R}$ . The total energy is then given by the sum of the electronic energy  $E_{(el)}(\mathbf{R})$  and the nuclear repulsion energy  $V_{(nuc,nuc)}$  (see Eq. 2.6), the latter being constant for each particular nuclear conformation.

$$E(\mathbf{R}) = E_{(el)}(\mathbf{R}) + V_{(nuc,nuc)} \quad (2.14)$$

The electronic Schrödinger equation having been solved, the nuclear motion can be calculated subsequently. For this purpose, the following equation derived from insertion of Eq. 2.7 and Eq. 2.10 into Eq. 2.3 is used.

$$(\hat{H}_{(nuc)} + \hat{H}_{(el)}) \psi_{(el)}(\mathbf{r}; \mathbf{R}) \phi_{(nuc)}(\mathbf{R}) = E \psi_{(el)}(\mathbf{r}; \mathbf{R}) \phi_{(nuc)}(\mathbf{R}) \quad (2.15)$$

This equation can be simplified using Eq. 2.13 for the effect of the electronic Hamiltonian on  $\phi_{(nuc)} \psi_{(el)}$ . Unfortunately, the effect of  $\hat{H}_{(nuc)}$  on  $\phi_{(nuc)} \psi_{(el)}$  leads to derivations of electronic wavefunctions with respect to nuclear coordinates. If these mixed terms are small, as is in the framework of the Born-Oppenheimer approximation, i. e. the separation of electron and nuclear motion, they can be neglected. Therefore, simplification of Eq. 2.15 is only approximately possible, leading to

$$\psi_{(el)} \hat{H}_{(nuc)} \phi_{(nuc)} + \phi_{(nuc)} E_{(el)} \psi_{(el)} = E \psi_{(el)} \phi_{(nuc)} \quad (2.16)$$

Division by  $\psi_{(el)}$  results in the approximated Schrödinger equation for the nuclear motion

$$(\hat{H}_{(nuc)} + E_{(el)}(\mathbf{R})) \phi_{(nuc)}(\mathbf{R}) = E \phi_{(nuc)}(\mathbf{R}). \quad (2.17)$$

Due to Eq. 2.8 and 2.14 this equation can be converted into

$$(T_{(nuc)} + E(\mathbf{R})) \phi_{(nuc)}(\mathbf{R}) = E \phi_{(nuc)}(\mathbf{R}). \quad (2.18)$$

This means that the nuclei exhibiting the kinetic energy  $T_{(nuc)}$  move under the influence of an effective field formed by all other nuclei and additionally by the electrons at each nuclear arrangement  $\mathbf{R}$ .

The Born-Oppenheimer approximation is a very good approach for potential energy surfaces separated by a significant energy gap. However, if such potential energy surfaces become closer or even intersect for certain nuclear arrangements, the separation of electron and nuclear motion is no longer possible. This is a result of a dramatic increase of the so-called non-adiabatic couplings (which correspond to the mixed terms mentioned above), so that the Born-Oppenheimer approximation becomes invalid. A rule for this limit is that the energy gap between electronic potential energy surfaces must be essentially larger than the gap between the eigen-states of the nuclear motion corresponding to the vibrational levels [24].

### 2.1.1.2 Woodward-Hoffmann model

As already mentioned above, potential energy surfaces play a crucial role in theoretical descriptions of molecular reactions. The Woodward-Hoffmann model [25] aims to predict molecular structures of the product(s), interpret chemical reactions, and obtain approximate information on potential energy surfaces. The fundamental idea of this concept is that the orbital symmetry is conserved in synchronously proceeding reactions, e. g. pericyclic reactions. The explicit definition of a pericyclic reaction is that the binding relations change synchronously on a closed curve. In this section, the basic assumptions and methods of this powerful concept are to be portrayed and discussed with the help of the reaction of 1,3-cyclohexadiene to form 1,3,5-hexatriene, which is the photochemically active part of 7-dehydrocholesterol (see Sec. 2.2).

According to R.B. Woodward and R. Hoffmann, the stereochemical course of a pericyclic reaction is essentially determined by conservation of symmetry properties of electronic orbitals of reactants and products. It is sufficient to consider qualitatively  $\pi$ - and semi-localized  $\sigma$ -molecular orbitals, which can be characterized by the signs of their wavefunctions and the number of nodal surfaces. Molecular orbitals must be either symmetric or antisymmetric with respect to any specific symmetry element of the molecular system. Therefore, at first an inspection of the symmetry of the reactant and the product is required. To a good approximation, the carbon backbone of the two molecules can be taken to be planar [26], as depicted in Fig. 2.1. Accordingly, both molecules exhibit the following symmetry elements, the iden-

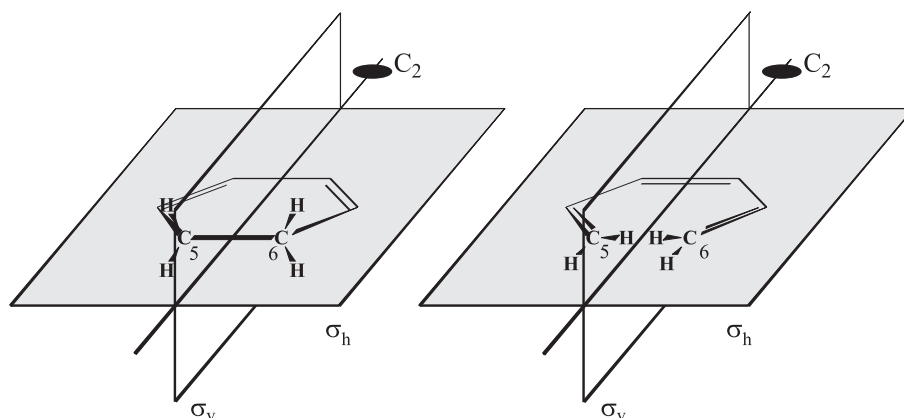


**Figure 2.1:** Idealized geometry of 1,3-cyclohexadiene and *s-cis,Z,s-cis*-1,3,5-hexatriene with the two mirror planes  $\sigma_h$  and  $\sigma_v$ , as well as the principle axis  $C_2$ , which is the intersection of  $\sigma_h$  (identical to the molecular plane) and  $\sigma_v$  (perpendicular to this plane).

tity  $E$ , the two-fold rotary axis  $C_2$ , as well as two mirror planes  $\sigma_h$  and  $\sigma_v$ , the first one equal to the molecular plane, and the latter one perpendicular to this plane. Consequently, both molecules belong to the point group  $C_{2v}$ .



During the ring-opening reaction the bond between the carbon atoms marked with the numbers 5 and 6 in Fig. 2.1 is broken in favor of forming a third double bond. Due to the change in hybridization connected with this, the hydrogen atoms at these carbon atoms rotate into the molecular plane. If the motion of these two hydrogen pairs exhibits the same handedness, the twofold principle axis is conserved, and the reaction is called conrotatory. On the other hand, a reaction containing a rotation of the two hydrogen pairs in opposite directions is named a disrotatory reaction. In this case the vertical mirror plane  $\sigma_v$  would be preserved.

If the qualitative orbital energy patterns are known for the initial and the final state of the reaction of interest, an orbital correlation diagram can be derived. For this purpose, all molecular orbitals involved in the photoinduced ring-opening reaction of 1,3-cyclohexadiene to form *s-cis,Z,s-cis*-1,3,5-hexatriene are arranged according to increasing energy. The required molecular orbitals are derived by means of a universal method known as linear combination of atomic orbitals (LCAO approximation). A linear variation ansatz can be used to approximate the total wavefunction (i. e.  $N$  molecular orbitals) as a superposition of  $N$  one-electron functions centered at the particular atoms,

$$\psi_i = \sum_{k=1}^N c_{ik} \chi_k \quad (i = 1, \dots, N) \quad (2.19)$$

with the coefficients  $c_{ik}$  and the atomic orbitals  $\chi_k$ , also called basis functions. Insertion into the Schrödinger equation gives a secular equation system. Its solution delivers a set of coefficients for each energy  $E_1 \leq E_2 \leq \dots \leq E_N$ . The accuracy of the molecular orbital approximated by atomic orbitals depends on the size of the basis set, i. e. the number of basis functions used. The molecular orbitals thus obtained are one-electron states exhibiting nodal surfaces, the number of which being in accordance with the order of the energetic levels. This is in agreement with quantum-chemical calculations of energetic levels. In order to treat multi-electron systems by this method, these molecular orbitals are occupied sequentially by all available electrons according to the aufbauprinzip, i. e. under consideration of the Pauli exclusion principle and Hund's rules [27]. This results in molecular electron configurations. In the case just described, the molecule would be in the ground state. According to the frontier orbital method, the highest occupied molecular orbital is called HOMO, and the lowest unoccupied orbital is named LUMO [28,29]. In the context of the LCAO approximation, excited states are described by energetically lower molecular orbitals which are unoccupied in favor of an occupation of higher-lying states.

This way, an orbital correlation diagram, as illustrated in Fig. 2.2, can be constructed for the reaction of 1,3-cyclohexadiene to form *s-cis,Z,s-cis*-1,3,5-hexatriene.

If the two-fold rotary axis  $C_2$  is the symmetry element to be conserved, the molecular orbitals can be denoted as *symmetric* (s) or *antisymmetric* (a) with respect to rotation around this  $C_2$ -axis, as is shown in Fig. 2.2. According to the Woodward-Hoffmann rules, orbitals exhibiting the same symmetry and similar energies correlate. Based on this, it can be directly derived that the ring opening of 1,3-cyclohexadiene to form *s-cis,Z,s-cis*-1,3,5-hexatriene is a photoinduced reaction, because the correlation between the HOMO of the reactant and the LUMO of the product (and vice versa) results in being passed the Fermi level (dotted line in Fig. 2.2). Therefore, an electronic excitation is required for this process. Since the HOMO of 1,3-cyclohexadiene and *s-cis,Z,s-cis*-1,3,5-hexatriene, respectively, do not correlate to a ground state, this reaction is thermally forbidden. Besides, it becomes clear that the photochemical ring opening and ring closure proceed in a conrotatory way, to allow the transformation of the HOMO of the reactant into the LUMO of the product (and vice versa).

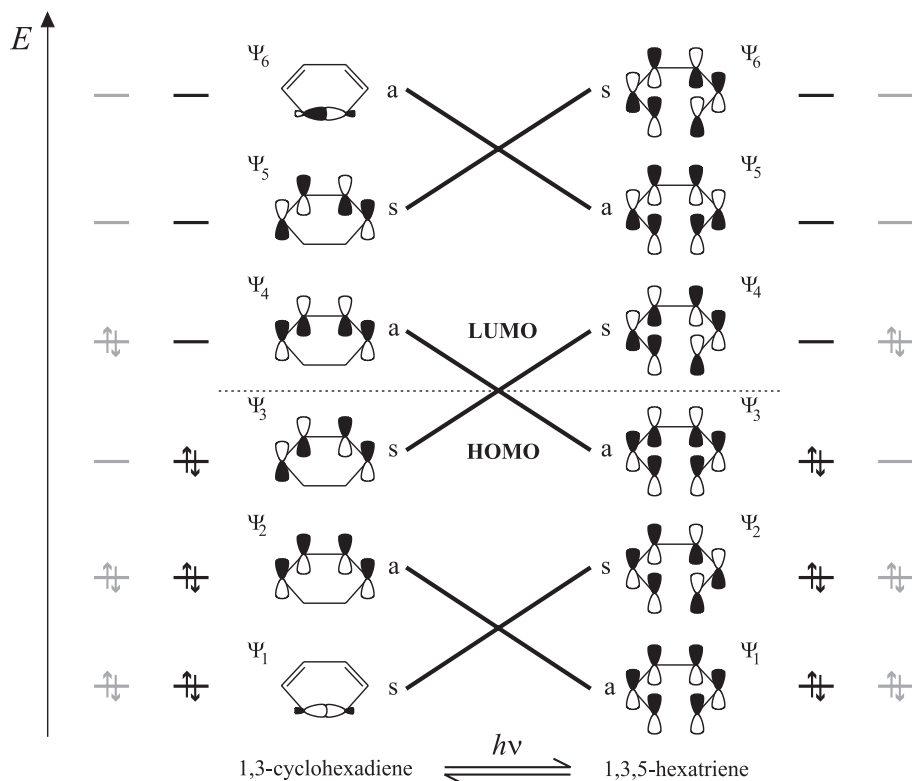


**Figure 2.2:** Orbital correlation diagram for the reaction of 1,3-cyclohexadiene to form *s-cis,Z,s-cis*-1,3,5-hexatriene according to R.B. Woodward and R. Hoffmann. The lobes represent atomic orbitals; opposite signs of the wavefunction are coded by black and white. Further details concerning the interpretation of this diagram are given in the text.

This can be used to predict the stereochemistry of the product. The populations of the ground state (black) and the two-electron excited state (gray) involved in this photoreaction are marked in Fig. 2.2.

According to W.T.A.M. van der Lugt and L.J. Oosterhoff [30], a configuration and state correlation diagram (see Fig. 2.3) can be derived from the orbital correlation diagram based on the Woodward-Hoffmann rules for a given pericyclic reaction.

With the help of the van der Lugt-Oosterhoff model, valuable information about the excited state potential energy curve as well as energy minima and barriers can be obtained. Filling up the orbitals of the molecules involved by the available electrons according to the excitation leads to different electron assignments corresponding to different electron configurations. For this purpose, only the frontier orbitals are of interest, because all other orbitals are either completely populated or empty at the configurations to be considered here. Inspection of the configuration correlation diagram gives the answer to the question, which reactant and product configurations correlate, by connecting configurations exhibiting the same symmetry by lines (broken lines in Fig. 2.3) [25]. Taking into account all configuration interactions, the state correlation diagram is obtained from the configuration correlation diagram. Due to this interaction, the non-crossing rule is valid for correlation lines corresponding to the same symmetry, leading to an avoided crossing. A thus constructed state correlation diagram can be considered as a section through the potential energy surface of the system and delivers an at least qualitative description of the position of energy minima and barriers along the symmetry preserving reaction coordinate [31]. For the 1,3-cyclohexadi-

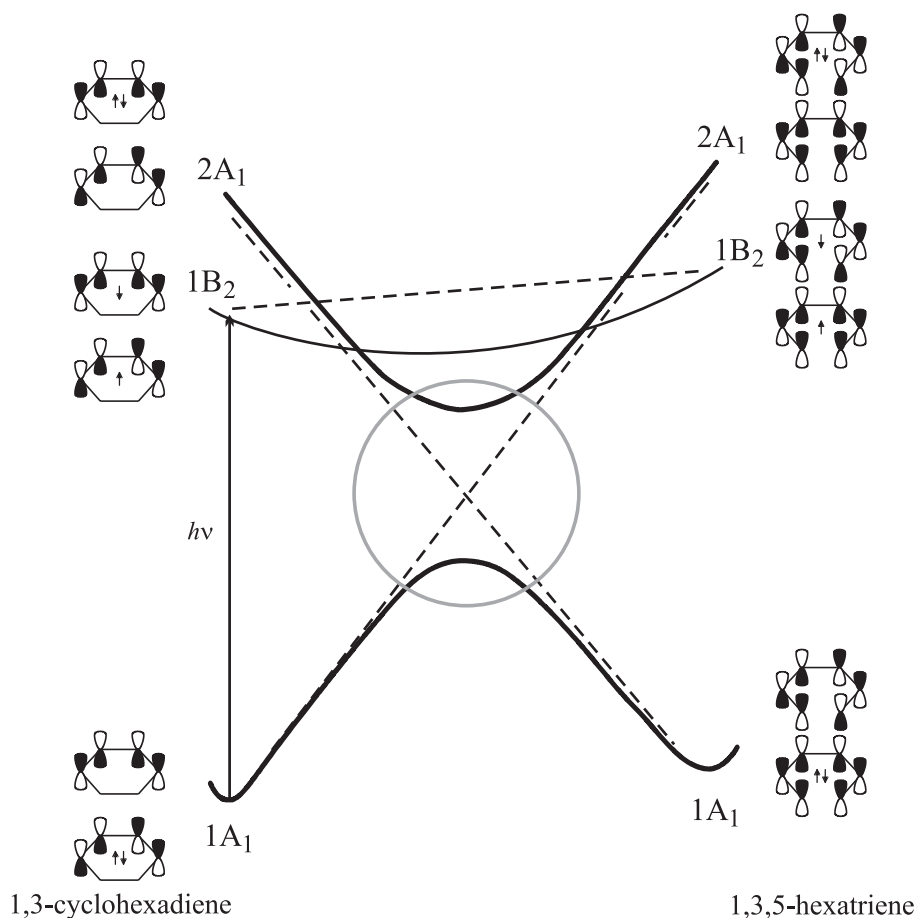


**Figure 2.3:** Configuration correlation diagram (dotted lines) and state correlation diagram (solid lines) for the 1,3-cyclohexadiene/*s-cis,Z,s-cis*-1,3,5-hexatriene system according to W.T.A.M. van der Lugt and L.J. Oosterhoff [30]. In the state correlation diagram an avoided crossing exists between the  $2A_1$  and the  $1A_1$  state for symmetry reasons.

ene/*s-cis,Z,s-cis*-1,3,5-hexatriene system the crossing between the doubly excited state ( $2A_1$ ) and the ground state ( $1A_1$ ) is avoided, because the two electron configurations involved in this crossing exhibit the same symmetry. Consequently, the reaction has a very high thermal barrier and is forbidden in the electronic ground state. However, if the reactant is excited into the singly excited electronic state ( $1B_2$ ) by absorption of light, it can evolve there without a large barrier along the reaction coordinate. Because the  $1B_2$  states of the two molecules correlate, the electrocyclic ring opening of 1,3-cyclohexadiene under conservation of the  $C_2$  symmetry is allowed in a conrotatory way.

### 2.1.1.3 Fermi's Golden Rule and Landau-Zener model

From the Woodward-Hoffmann model and van der Lugt-Oosterhoff concept the question arises, how a transition between two potential energy surfaces covering such a large energy gap can take place at the ultra-short timescales treated in this thesis. In principle, the rate for a radiationless relaxation from one electronic state into another is determined by the transition probability. There are several approaches to describe this quantity. In this section, Fermi's Golden Rule and the Landau-Zener model are treated in more detail. Because radiationless transitions from one electronic potential energy surface to another are impossible

in the framework of the Born-Oppenheimer approximation, it is necessary to go beyond this and to include the interaction between different electronic states, called coupling.

The Fermi's Golden Rule is used to determine the transition rate from an initial state ( $i$ ) to a quasi-continuous band considered as the final state ( $f$ ) (see Fig. 2.4). This assumption

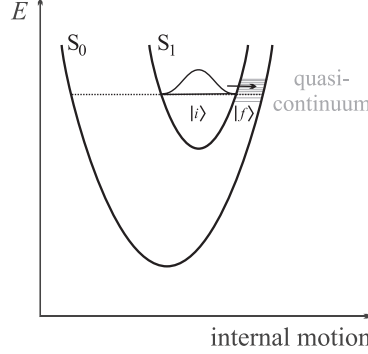


**Figure 2.4:** Illustration of a transition between two potential energy curves according to Fermi's Golden Rule. The excited state  $S_1$  couples only weakly to the quasi-continuous band of the ground state  $S_0$ .

is justified, if numerous states of similar energy exist. Then the transition probability is the sum of all the transition probabilities over this band of energies. With  $\rho_N(E_f) dE$  being the number of states in the energy range  $E_f$  to  $E_f + dE$ , where  $\rho_N(E_f)$  is called the density of states and approximated by its value at the centre of the band  $\rho_N(\bar{E}_f)$ , the total transition rate is given by

$$k_{i \rightarrow f} = 2\pi |V_{fi}|^2 |FCF|^2 \rho_N(\bar{E}_f). \quad (2.20)$$

In this equation, the matrix element  $V_{fi}$  denotes the adiabatic coupling between initial and final state; it can be expressed as  $\langle i | \frac{\hat{H}}{\Delta E} | f \rangle$  with  $\Delta E$  being the energy gap between the two states, and  $FCF$  is the Franck-Condon factor. This equation is well-known as Fermi's Golden Rule for the dynamics of transitions between states. It is based on the time-dependent perturbation theory and therefore only valid for *weak* coupling between a pair of states corresponding to a rather large energy gap. As a consequence, the relaxation rates are slow ( $\sim 10^{-8}$  s).

Another approach to treat radiationless transitions in the two-state case is the Landau-Zener model [32,33]. Based on the Schrödinger equation and various simplifications concerning the coupling and the potential energy curves, i. e. the potentials are approximated by a simple linear expression, the off-diagonal coupling term is taken to be constant, and the nuclear motion is treated classically, the Landau-Zener formula for the probability of a transition between the adiabatic surfaces  $S_1$  and  $S_0$  can be derived,

$$P_{LZ} = \exp \left[ -\frac{\pi^2 \Delta E^2}{h v \Delta s} \right]. \quad (2.21)$$

In this equation  $\Delta E$  denotes the energy gap caused by the avoided crossing between the two potential energy curves in the adiabatic picture. According to the Landau-Zener expression, a classical trajectory will have the largest probability for jumping to the other surface at the avoided crossing. In Eq. 2.21  $v$  is the maximum conceivable speed of the wavepacket, and  $\Delta s$  represents the slope difference of the two curves. Insertion of typical values for these quantities, i. e.  $\Delta E = 1$  eV,  $v = 10^{13}$  Å/sec, and  $\Delta s = 5$  eV/Å, gives a probability of penetrating from  $S_1$  to  $S_0$  of  $P_{LZ} \approx 10^{-21}$ . To explain ultrafast radiationless transitions between two potential energy surfaces which are the topic of the present work, however, a

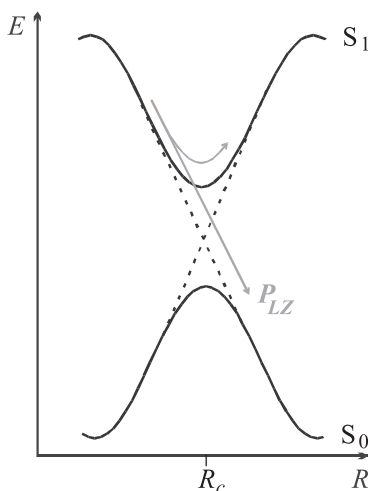


**Figure 2.5:** Adiabatic picture of two potential energy curves  $S_0$  and  $S_1$  exhibiting an avoided crossing at the critical internuclear distance  $R_c$ .

probability near unity is required. As a consequence, the energy gap between the two states should vanish or at least shrink to a value below 0.1 eV at an easily accessible location. In a one-dimensional model, however, the potential energy surfaces are not allowed to approach closely to each other or even to cross.

### 2.1.2 Conical intersections

All concepts presented above are valuable theoretical approaches to determine the general features of potential energy surfaces involved in (unimolecular) photochemical reactions, but they cannot explain the existence of *ultrafast* photochemical reactions which are characterized by surface transitions taking place at the shortest timescales. For reaction times in the order of hundreds of fs, reaction paths leading in a straight, unimpeded way to the product(s) are prerequisite. This view implies the existence of potential energy surface intersections that are easily accessible for the wavepacket traveling from one electronic state to another.

The non-crossing rule for potential energy curves exhibiting the same symmetry is strictly valid only for diatomics. For polyatomic molecules the potential energy surfaces depend on many coordinates  $\mathbf{q}$  (see Sec. 2.1.1). Two such surfaces intersect if the energy eigen-values  $E_1(\mathbf{q})$  and  $E_2(\mathbf{q})$  of the two electronic wavefunctions  $\psi_1$  and  $\psi_2$  corresponding to the two electronic states  $|1\rangle$  and  $|2\rangle$  relevant for the considered reaction are degenerate. The eigen-values  $E_1$  and  $E_2$  are not independent of each other, but *two* solutions of the same eigen-value problem of one electronic Hamiltonian  $\hat{H}(\mathbf{q})$  [34,35] depending on the particular geometry of the molecule. If all other electronic wavefunctions  $\psi_i$  ( $i \neq 1, 2$ ) are eigen-functions of the same Hamiltonian, the conditions for an intersection of both potential energy surfaces can be derived (see also Ref. [36]),

$$\det \begin{pmatrix} \hat{H}_{11}(\mathbf{q}) - E(\mathbf{q}) & \hat{H}_{12}(\mathbf{q}) \\ \hat{H}_{21}(\mathbf{q}) & \hat{H}_{22}(\mathbf{q}) - E(\mathbf{q}) \end{pmatrix} = 0, \quad (2.22)$$

with

$$\hat{H}_{ij}(\mathbf{q}) = \int \psi_i^*(\mathbf{r}, \mathbf{q}) \hat{H}(\mathbf{q}) \psi_j(\mathbf{r}, \mathbf{q}) d\mathbf{r}. \quad (2.23)$$

In this equation  $i$  and  $j$  are the indices of the electronic states,  $\mathbf{r}$  are the spatial coordinates of the electrons, and  $\mathbf{q}$  are the internal coordinates (i. e. the nuclear configuration). The energy

eigen-values determined by solving the secular equations following from Eq. 2.22 are given by

$$E_{1,2} = \frac{\hat{H}_{11} + \hat{H}_{22}}{2} \pm \sqrt{\left(\frac{\hat{H}_{11} - \hat{H}_{22}}{2}\right)^2 + \hat{H}_{21}\hat{H}_{12}}. \quad (2.24)$$

Consequently, the intersection point of both potential energy surfaces is determined by two conditions for the Hamiltonian,

$$\hat{H}_{11}(\mathbf{q}) = \hat{H}_{22}(\mathbf{q}), \quad (2.25)$$

and

$$|\hat{H}_{12}(\mathbf{q})| = 0. \quad (2.26)$$

From Eq. 2.25 and Eq. 2.26 it becomes evident that (for a molecule with  $s$  internal coordinates) an  $(s - 2)$ -dimensional subspace exists in the whole configuration space in which these two conditions are satisfied. Accordingly, only the other two coordinates determine the energy gap between the two states. In the vicinity of a conical intersection, a coordinate system can be chosen in which the variation of two special coordinates, named branching coordinates, cancels the degeneration. In the projection to these branching coordinates, the two potential energy surfaces have consequently the shape of a double cone. Accordingly, the intersection space is represented in this branching space by a single point. A suitable variation of one or more of the  $s - 2$  coordinates, not branching coordinates, does not alter the energy degeneration, but has the consequence that the conical intersection at that location in the whole configuration space belonging to minimum energy becomes accessible. Generally, molecules undergoing pericyclic reactions change potential energy surfaces with a geometry exhibiting a lower symmetry than expected at the pericyclic minimum [37]. The pericyclic minimum is the minimum of the excited state in the state correlation diagram according to R.B. Woodward and R. Hoffmann or W.T.A.M. van der Lugt and L.J. Oosterhoff (see Sec. 2.1.1.2).

If the considerations on conical intersections are compared with the Woodward-Hoffmann model, it becomes obvious that the potential energy curves derived from the van der Lugt-Oosterhoff model are always a cut (corresponding to symmetry conservation) through the real potential energy surfaces (see Fig. 2.6). Consequently, two states exhibiting the same symmetry are allowed to cross only outside this cut plane. Therefore, photochemical pericyclic reactions require inevitably a symmetry breaking, at least if they proceed ultrafast.

To shed light on the processes a molecule undergoes at a conical intersection, the  $\text{H}_3$  molecule is treated here as the simplest possible example. The molecular structure of  $\text{H}_3$  in the highest possible symmetry is an equilateral triangle (point group  $\text{D}_{3h}$ ). In this configuration the three  $1s$ -electrons form three molecular orbitals, one of them lying energetically below the two others which have identical energies. Filling up these orbitals with the three electrons available, taking into account the Pauli exclusion principle and Hund's rules [27], results in two degenerate states. According to H.E. Jahn and E. Teller [38,39] any nonlinear molecular system in a degenerate electronic state will be unstable and will undergo some kind of distortion that will lower its symmetry and split the degenerate state (Jahn-Teller effect). If this distortion of the symmetry happens in the  $\text{H}_3$  molecule, the two degenerate states diverge from each other and form two potential energy surfaces having the shape of a double cone (see Fig. 2.7) [40]. In other words, the potential energy surfaces of  $\text{H}_3$  cross at a Jahn-Teller induced conical intersection. The model potential energy surfaces exhibit three-fold symmetry, because each of the three H atoms can vibrate and thus destroy the highly symmetric configuration ( $\text{D}_{3h}$ ). The branching space is described by two degenerate normal

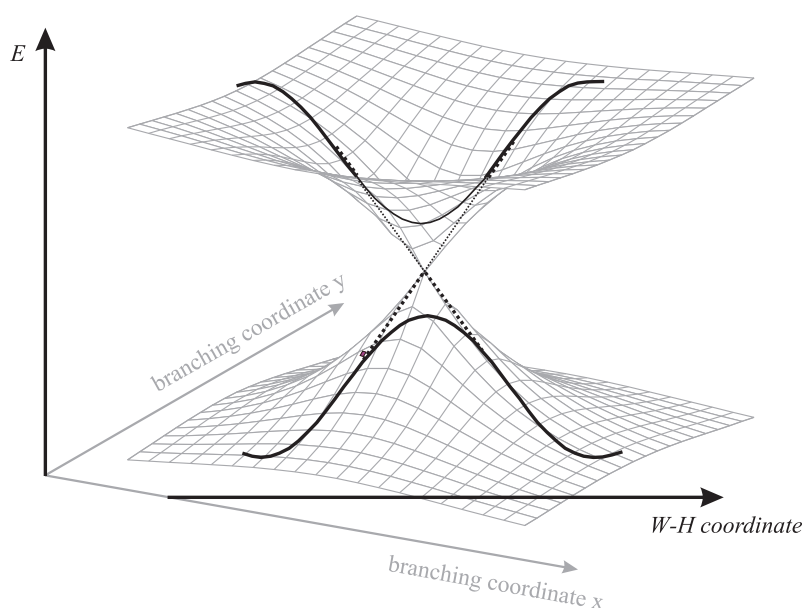


**Figure 2.6:** Schematic illustration of the shape of a conical intersection in the branching space (gray). For comparison, the corresponding potential energy curve belonging to the symmetry conserving Woodward-Hoffmann (W-H) coordinate exhibiting an avoided crossing is drawn in (black).

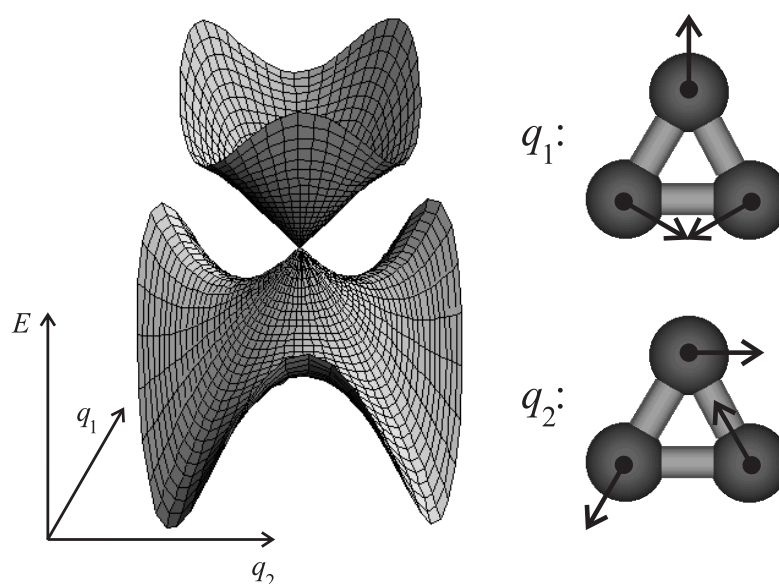


**Figure 2.7:** Dynamical Jahn-Teller effect in  $\text{H}_3$  leading to a splitting of the two potential energy surfaces which are a function of the asymmetric vibrational coordinates  $q_1$  and  $q_2$ . The point where the two potentials are degenerate corresponds to the highly symmetric configuration of  $\text{H}_3$  ( $D_{3h}$ ) [40], or in other words, to a Jahn-Teller induced conical intersection. The three-fold symmetry of the  $\text{H}_3$  molecule is also found in the shape of the model potential energy surfaces involved [41,42].

modes ( $q_1$  and  $q_2$  in Fig. 2.7) [41–43]. Therefore,  $\text{H}_3$  has a dynamic molecular structure, the single structures being allowed to convert into each other at the ground state surface without

passing the (energetically higher) conical intersection. Between these three single structures, barriers exist which are energetically low compared to the energy of the conical intersection.

If unimolecular photochemical reactions of molecules larger than  $H_3$  are to be treated, the calculation of topological properties of (excited) potential energy surfaces including surface transitions as well as the corresponding molecular structures is much more complicated (and the computational costs rapidly grow with increasing number of degrees of freedom). By the development of special quantum-chemical algorithms, the theoretical groups of F. Bernardi, M. Olivucci, and M.A. Robb succeeded for the first time in calculating positions in the configuration space where conical intersections are located and in the prediction of molecular structures at these positions [44–46]. They found in their calculations for many different molecules that a biradicaloid intermediate consisting of three or four centers is predestined for ultrafast potential energy surface transitions (cf. Refs. [47,46]). The possible achievable substructures which are found in the intersection space are depicted in Fig. 2.8. Independent of the number

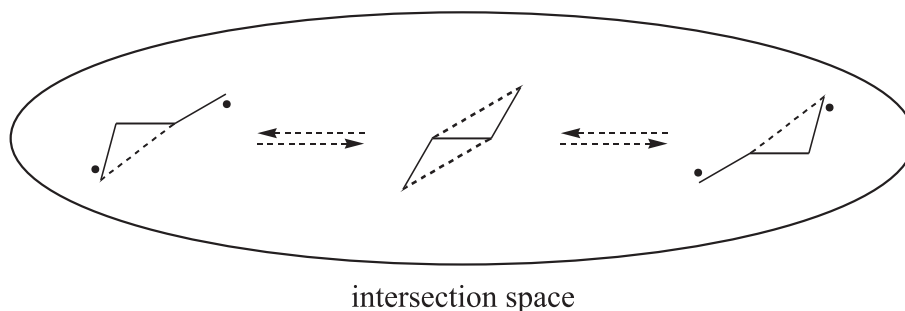


**Figure 2.8:** Typical geometrical properties of molecular substructures conical intersections playing an essential role in polyene photochemistry [48–50].

of participating atoms (three or four), all structures have in common that the fundamental element is a triangle. Depending on the molecular structure, inside the intersection space for the  $S_1 \rightarrow S_0$  potential energy surface transition, the intermediate structures may be converted into each other [49,50] affecting the stereochemistry of the product(s). These results suggest that, in general, the molecular structure at a conical intersection consists of a triangle. This substructure provides, in fact, the possibility to achieve the energy degeneration required for a conical intersection. As will be shown in Sec. 2.2, also the molecules treated in the present work follow this rule. If the molecule is composed of more than three atoms (such as  $H_3$ ), a 3-electron-3-center system may be formed inside the molecule by three atoms of particular relevance to the reaction. This is depicted schematically in Fig. 2.9 for the electrocyclic ring opening of 1,3-cyclohexadiene. The existence of this triangular substructure was also proved experimentally by investigating the *cis-trans* isomerization of previtamin  $D_3$  to form *s-cis,E,s-trans*-tachysterol in a cold matrix. From the inspection of the stereochemistry of the reactant and the product, the isomerization mechanism could be established to proceed via the so-called Hula-Twist isomerization which allows only a triangular 3-center-3-electron bonding as the intermediate structure [51–53].

For the prediction of molecular structures at conical intersections, it is not the gap between potential energy surfaces, but rather the exchange interactions  $k$  between the orbitals involved in the particular photoreaction that are to be considered (see Fig. 2.10). The orbital energies of the excited state (exs) and the ground state (gs) become degenerate, if the following equation is satisfied,

$$E_{\text{exs, gs}} = Q \pm \sqrt{k_{12}^2 + k_{23}^2 + k_{13}^2 - k_{12}k_{23} - k_{12}k_{13} - k_{23}k_{13}} \stackrel{!}{=} 0, \quad (2.27)$$



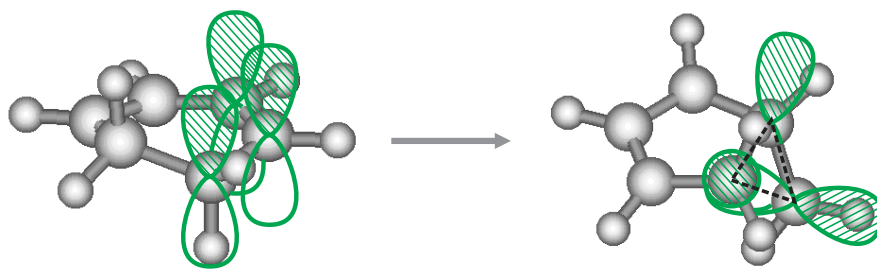


**Figure 2.9:** Typical molecular structures appearing at the ring opening reaction of 1,3-cyclohexadiene (left, equilibrium ground state geometry; right, geometry at the conical intersection between  $2A_1$  and  $1A_1$  state). The structure parameters for the latter geometry are taken from Ref. [26]. Additionally, the  $\pi$ -orbitals involved in this reaction are depicted schematically. The triangular structure of the part of the molecule playing the key role during the ring opening is marked by broken lines.

where  $Q$  is the absolute energy of the conical intersection. This results in the condition for the exchange interaction terms,

$$k_{12} = k_{23} = k_{13}. \quad (2.28)$$

From this equation it becomes clear that the three orbitals have not necessarily to be orthogonal to each other, which could be expressed as  $k_{12} = k_{23} = k_{13} = 0$ . This situation represents only a rare special case [48].

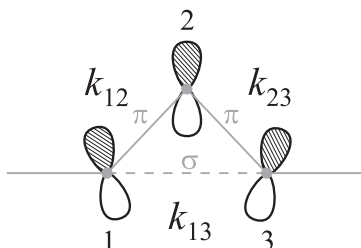


**Figure 2.10:** Schematic illustration of the orbitals and the exchange interactions between these orbitals in a polyene.

In what follows, the problem of the accessibility of such a conical intersection will be discussed. From the considerations above, it becomes obvious that this problem is closely associated to the ability of a molecule to form the triangular substructure and thus to the flexibility of this molecule. The opposite is the case when rigidly bridged molecules are used as fluorescent or laser dyes. The stiffness of such molecules is associated with potential energy surfaces without easily accessible conical intersections, but, according to the photochemically active part, quite large energy gaps between the excited and the ground state. Therefore, radiating relaxation is the preferred process. Sufficiently flexible molecules, however, can reach the substructure needed easily enough to provide the condition for a radiationless potential energy surface transition at a conical intersection lying on an unimpeded path to the ground state and consequently for an ultrafast photochemical reaction. In Fig. 2.11, such reaction paths through conical intersections are schematically depicted. The principal characteristic of this view is to approach the evolution of a molecule during its reaction by a pathway on the involved potential energy surfaces paying attention to local details, such as slopes, barriers, saddle points, and collecting funnels. Within the framework of this “pathway approach” picture, the potential energy surface transition takes place at an easily accessible conical intersection having the effect of a collection funnel, where a very efficient non-radiative

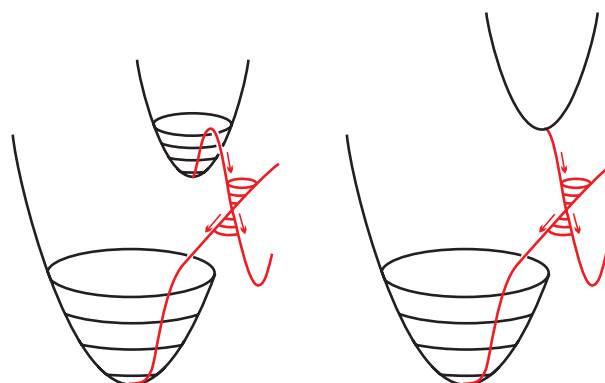


**Figure 2.11:** Schematic potential energy surfaces in the branching space representation. Left, conical intersection accessible via a barrier, tunneling (not indicated) through the barrier is possible; right, easily accessible conical intersection. The arrows indicate the continuous pathways along the surfaces [54].

decay may occur. The evolving molecule moves along these surfaces, guided by the steepest descent path influenced by local properties of the surfaces, such as minima, slopes, curvatures, and transition states. The branching into the final ground state photoproducts or back to the reactant takes place at the location corresponding to the collection funnel [54]. However, it should be noted that the term reaction path on potential energy surfaces denotes a static path which neglects all kinetic energy terms. In contrast to trajectories which form solutions of the equations of motion, reaction paths cannot have a direct physical meaning. Therefore, such paths should not be interpreted as indicating the detailed stereochemical course of a reaction. Nevertheless, the reaction pathway, also often called reaction coordinate, has a great chemical importance, because “it represents a leading line around which the trajectories of the reaction should be mainly oriented” [55].

After the detailed description of the structural properties playing a role at conical intersections and the evolution of molecules on reaction pathways, now a closer look will be taken at the question, how fast and how completely wavepackets can travel from one electronic state to another through such potential energy surface transitions. Since the coupling between two adiabatic states is inversely proportional to the energy gap between these states, the adiabatic couplings diverge in the vicinity of a conical intersection. Accordingly, the Born-Oppenheimer approximation (see Sec. 2.1.1.1) becomes invalid and the picture of energy surfaces with well-defined energies breaks down. From this the difficulty arises of how to establish the temporal course of such transitions between different adiabatic electronic potential energy surfaces. However, W. Domcke *et al.* succeeded in explaining theoretically ultrafast potential energy surface transitions of vibrational wavepackets [56], showing that transitions between different adiabatic electronic energy surfaces induced by non-Born-Oppenheimer couplings are very common in the photoinduced dynamics of polyatomic systems. The divergence of the adiabatic couplings in the vicinity of an intersection and the strong anharmonicity of the adiabatic potential energy surfaces give rise to very strong couplings between the electronic states involved as well as the mode-mode couplings dominating the processes at fs timescales [57]. Their theoretical approach to modeling the dynamics of polyatomic molecules quantum-mechanically is based on the fundamental assumption that a “separation of timescales” is possible. Accordingly, “only a few active modes, which are strongly coupled to the optical transition, are assumed to dominate the dynamics at the shortest timescales; the coupling of the active modes with the large number of inactive modes is believed to be weaker and

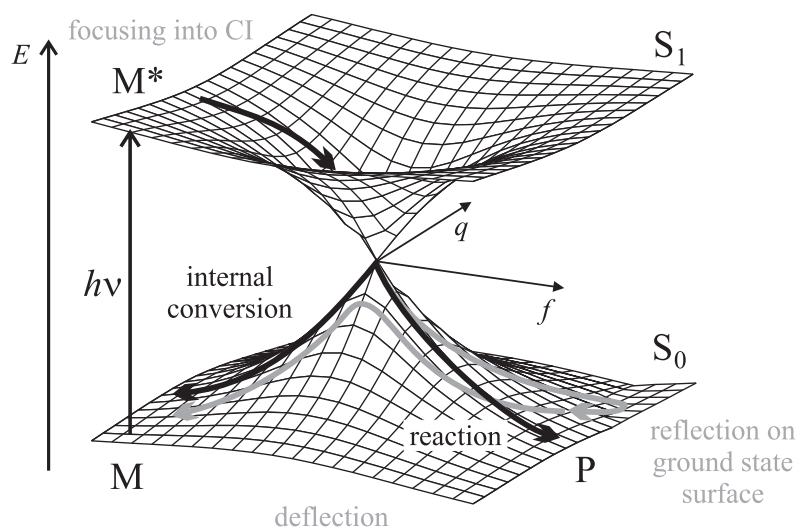


**Figure 2.12:** Fundamental processes occurring at a conical intersection. The two promoting modes correspond to the coordinates  $f$  and  $q$  extending the branching space. During the unimolecular photochemical reaction, the molecule  $\mathbf{M}$  reaches the excited state  $S_1$  from the ground state  $S_0$  by absorption of light and forms the excited molecule  $\mathbf{M}^*$ . In the vicinity of a conical intersection, the wavepacket is focused into the funnel of the conical intersection. After passing it, the wavepacket contains a lot of vibrational energy from the upper state, causing a reflection on a rising area of the ground state surface sooner or later. This can be prevented by including a third mode for energy dissipation. This way, the molecule can form the product(s)  $\mathbf{P}$  (reaction), or relax to the ground state as  $\mathbf{M}$  once more (internal conversion).

to become relevant only at longer timescales. It can therefore be neglected in a first approximation when considering photoinduced dynamics at the shortest timescales.” [56]. These theoreticians could prove that at a conical intersection the basic processes of an irreversible population and phase relaxation of a wavepacket are already sufficiently expressed by taking into account *three* strongly coupled modes: the so-called tuning and coupling modes, which are also named promoting modes, and a third one, called the accepting mode, required for the dissipation of vibrational energy in the ground state [58–61]. Without this third mode, the wavepacket would return to the excited state by a reflection on a rising area of the ground state surface (see Fig. 2.12). Therefore, systems treated with less than three vibrational modes show a population oscillation between the electronic states [56,62].

### 2.1.2.1 Evidence of conical intersections in photochemistry and photobiology

As described in the previous section, radiationless potential energy surface transitions are of great importance in photochemical reactions. They mainly take place when potential energy surfaces closely approach or even intersect each other. Although the existence of conical intersections between different electronic potential energy surfaces of molecules have been known since the 1920s [34,35,63], it is only recently been increasingly realized that they are a most common phenomenon in photoinduced reactions of polyatomic systems [1–7]. The reason for this is that in the past conical intersections were assumed to occur only at potential energy surface locations that are difficult to reach. In this section, the fundamentals of photochemistry including the role of conical intersections as well as photoinduced biological processes important for life are discussed.

After a detailed description of the nature of conical intersections, photochemical reactions as a whole will now be considered. Generally, such reactions proceed according to the scheme shown in Fig. 2.13. A reactant in the ground state reaches an excited state by absorption of one or more photons. After leaving the Franck-Condon region, two possibilities exist in principle. Either a reaction and a *concomitant* relaxation into the ground state via a radiationless decay occur which corresponds to the involvement of a conical intersection. Or an adiabatic reaction to an excited state product and a *subsequent* relaxation to the ground state via several possible processes (see Fig. 2.14) take place.

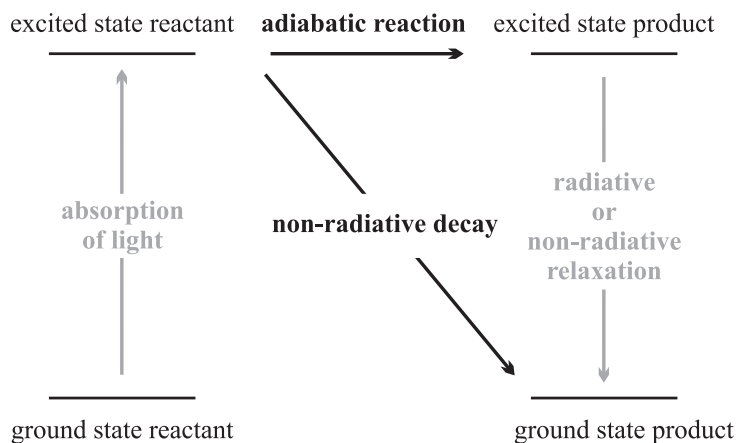


**Figure 2.13:** Basic scheme of photochemical reactions.

In Fig. 2.14, the fundamental non-radiative and radiative processes of interstate relaxation (except via conical intersections) after a vertical excitation are summarized using a schematic Jablonski diagram. Basically, there are three radiationless processes. The isoenergetic transition from an electronically excited state into an excited vibrational level of a lower electronic state is called internal conversion (IC), if both electronic states exhibit the same multiplicity (here singlet  $\rightarrow$  singlet). In contrast, the process named intersystem crossing (ISC) occurs with electronic states having a different multiplicity (here singlet  $\rightarrow$  triplet) and is mostly much slower because of the required spin inversion based on spin-orbit couplings. In addition, non-radiative vibrational cooling (IVR) can take place within any given electronic state. An excited molecule can also undergo a radiative relaxation from the lowest vibrational level of an electronically excited state to the lowest vibrational level of the electronic ground state. Such an emission of photons is called phosphorescence if the transition occurs between electronic states with a different multiplicity, whereas it is named fluorescence if the involved states have identical multiplicity. Phosphorescence takes place subsequently to ISC. Because the transition from the triplet excited into the singlet ground state is spin-forbidden, the light emission is delayed, usually not very strong, and persistent. In contrast, the latter phenomenon is not noticeable for (the spin-allowed) fluorescence, but in this case the quantum yield can approach unity for rigid aromatic compounds [64]. According to Kasha's rule [65], fluorescence usually appears from the first excited state of a given multiplicity to the ground state, but exceptions are known (e. g. azulene [66]).

The evidence of conical intersections in singlet photochemistry is based on the fact that they are considered to funnel electronically excited molecules very quickly to the ground state. At the same time, the experimental proof of the existence of ultrafast reactions actually excludes other relaxation mechanisms. Obviously, the explanation of ultrashort relaxation times of molecules, also of those investigated in the present work, by means of easily accessible conical intersections seems to be inevitable.

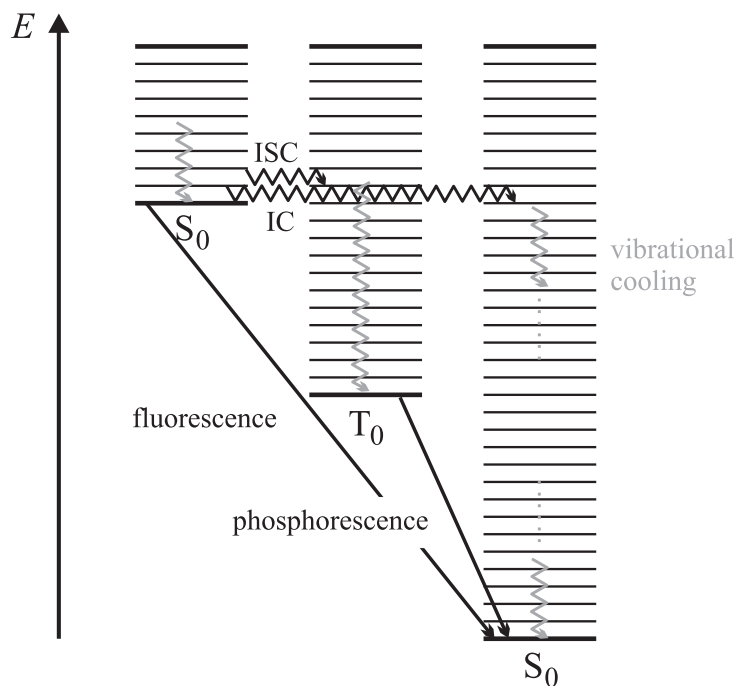


**Figure 2.14:** Fundamental processes of interstate relaxation. The abbreviation ISC stands for intersystem crossing, and IC for internal conversion. The wavy lines correspond conventionally to non-radiative processes.

A number of ultrafast photoinduced reactions is of particular biological relevance. One example is the vision process. Light transduction is mediated by rhodopsin, the photoreceptor of almost all known biological visual systems [67]. The chromophore of rhodopsin is actually 11-*cis*-retinal protonated Schiff base. In the primary event of visual excitation, visible light isomerizes the 11-*cis*-retinal to all-*trans*-retinal. Since the all-*trans*-retinal does not fit the binding site of the surrounding protein opsin for 11-*cis*-retinal, the rhodopsin molecule becomes unstable and undergoes a series of conformational changes leading to the separation between all-*trans*-retinal and the opsin matrix. This reaction cascade is required for signal amplification. When the signal strength is sufficiently high, the signal passes on to stimulate the optic nerve, which conducts it to the brain. The particular reaction speed and quantum yields of the photoisomerization of retinal in rhodopsins (i. e. rhodopsin, bacteriorhodopsin, and halorhodopsin) crucially depend on the specific surrounding of the chromophore in the protein. In rhodopsin, the human retina visual pigment, the 11-*cis*-retinal isomerizes with a high quantum yield of 67% [68] and the electronic transition from the excited state to the ground state occurs extremely fast (200 fs) [69]. Also bacteriorhodopsin, which serves as a light-driven proton pump exploited by *Haloarchaea* as an alternative form of photosynthesis, photoreacts with a high quantum yield of 65% [70] and the electronic relaxation is also very fast (500 fs) [71,72]. In general, photosynthesis is a photoreaction being essential for all known life. The overall process yields in the splitting of water by sunlight into oxygen and metabolically bound hydrogen. This forms the basis for the existence of higher organized living systems on Earth [73–75]. Photosynthesis can be formally described as charge separation induced by electron transfer with the positive charge used for oxidation of  $H_2O$  and the negative charge for reduction of  $CO_2$ . The photon energy is absorbed by pigment-protein complexes in the light-gathering antennae, which also contain carotenoids for energy transfer and protection against high-energy photons. The primary photoinduced electron-transfer

event proceeds very fast (within 2.8 ps) [76–78]. A further class of ultrafast biological reactions are the photoinduced processes in human skin. Carotenoids as light protection pigments and 7-dehydrocholesterol as vitamin D<sub>3</sub> precursor play a particular role. Vitamin D<sub>3</sub> is important in calcium metabolism. It is required for calcium absorption and the mineralization of bone. The primary step of the vitamin D<sub>3</sub> formation, i. e. the electrocyclic ring opening of 7-dehydrocholesterol to form previtamin D<sub>3</sub> which is investigated in the present work, also proceeds ultrafast. This reaction is also known to be very efficient (quantum yield 34% [79]).

From the rapidity observed for these primary events of biologically relevant photoreactions, the question arises, why these processes are so fast. In fact, the biosynthesis of such ultrafast reacting molecules which have been developed in the evolutionary process is mostly quite difficult and expensive in terms of energy. Additionally, each of these ultrafast primary steps is followed by much slower subsequent reactions. With the vision process as a well-investigated example [80–83], this question is discussed. The reaction rate on the order of  $\sim 100$  fs for the *cis-trans* photoisomerization of rhodopsin is followed by the much slower reactions of the reaction cascade which reduce the speed by a factor of  $\sim 10000$ . The nerve impulse propagation proceeds within a few  $\mu\text{s}$  leading to an additional reduction of the speed by a factor of  $\sim 1000$ . Consequently, the overall speed reduction from the primary step to the brain amounts to approximately seven orders of magnitude. Based on this, the actual reason for the rapidity of the primary step of the human vision process is still to be discovered. Obviously, the short reaction time itself cannot be the reason for the high speed of the primary step of the human vision process, because the reaction cascade and the nerve conduction slow down the signal processing. But *selectivity* and *efficiency* seem to play an important role, because unambiguity and optimization of the signal/noise ratio can be gained by reducing the reaction time. Side reactions and other unwanted reaction channels as well as the possibility of a molecule absorbing light energy and relaxing consequently without a reaction (i. e. radiative or by internal conversion) are suppressed when the desired reaction is faster than all these processes. This way, only the wanted reaction is selected and leads efficiently to an unambiguous signal, which is then processed in the brain. Furthermore, a molecule reacting ultrafast via a conical intersection reaches the ground state in an initially hot state. This large content of vibrational energy may be exploited for subsequent reactions.

## 2.2 Photochemistry of 1,3,5-cyclooctatriene and 7-dehydrocholesterol

In this section, the photoinduced unimolecular reactions of the two molecules, 1,3,5-cyclooctatriene and 7-dehydrocholesterol, investigated in the present work will be discussed in detail. Both molecules undergo ultrafast pericyclic reactions, when they are irradiated by UV light. This fundamental reaction class is exceedingly important in polyene photochemistry and photobiology and can be subdivided into cycloadditions/cycloreversions, electrocyclic ring openings/closures, and sigmatropic/cheletropic reactions. All pericyclic reactions share the applicability of the Woodward-Hoffmann rules (see Sec. 2.1.1.2). In particular, the photoreactions of 1,3,5-cyclooctatriene and 7-dehydrocholesterol are electrocyclic ring openings defined as single-bond breaking between the ends of a polyene system under simultaneous formation of a new  $\pi$ -bond [84].

In principle, for the photoinduced unimolecular reaction of 1,3,5-cyclooctatriene ( $M = 106.17 \text{ g mol}^{-1}$ ), the formation of three primary products (cf. Fig. 2.15: all-*cis*-1,3,5,7-octatetraene (**I**), bicyclo[5.1.0]octa-2,4-diene (**II**) and tricyclo[4.1.0.0<sup>6,8</sup>]octa-2-ene (**III**)) is

expected. Their structures can be derived from inspection of the intermediate structures possible at the  $S_1-S_0$  conical intersections. In contrast to the electrocyclic ring opening of 1,3-cyclohexadiene, in this case the formation of the bicyclus containing a three-membered ring (**II**) cannot be neglected. The molecular structures of some of the secondary products occurring are shown gray in Fig. 2.15 and are taken from the literature (*s-trans*,*Z*,*s-cis*,*Z*,*s-trans*-1,3,5,7-octatetraene (**IV**) cf. [85], bicyclo[4.2.0]octa-2,7-diene (**V**) cf. [86]). Inspection

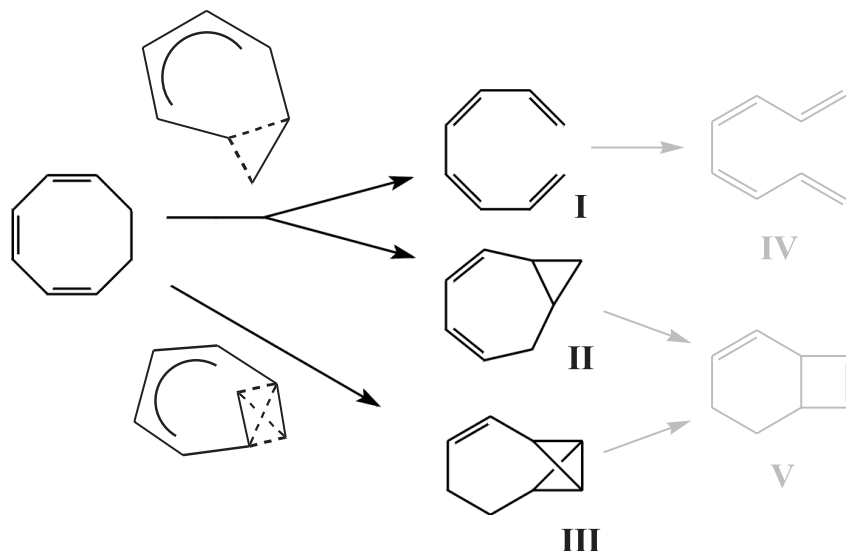


**Figure 2.15:** Photoinduced electrocyclic ring opening of 1,3,5-cyclooctatriene proceeding via conical intersections.

of the stereochemical course of the formation of the primary products from the reactant suggests that the reaction proceeds via two different paths involving two different intermediate molecular structures consisting of three or four centers corresponding to two different conical intersections (see Fig. 2.15). Because the dynamics of the formation of the three primary products is expected to proceed ultrafast, only measurements with a sufficiently high time resolution have a chance of proving the existence of these two reaction paths. Since the products **II** and **III** formed independently in the primary step are both precursors for the subsequent reaction to compound **V**, the information about the two paths disappears at long time-scales. In contrast to the example described in Sec. 2.1.1.2 (1,3-cyclohexadiene  $\rightarrow$  1,3,5-hexatriene), the photoinduced ring opening of 1,3,5-cyclooctatriene is known to proceed with a *disrotatory* motion of the methylene portion of the ring [85,87].

By means of 7-dehydrocholesterol ( $M = 384.65 \text{ g mol}^{-1}$ ) the influence of bulky substituents on the reaction rate can be investigated. The photochemically active part of 7-dehydrocholesterol is the 1,3-cyclohexadiene system (see Fig. 2.16) which undergoes a *conrotatory* motion of the methylene portion of the ring, as described in Sec. 2.1.1.2. This reaction

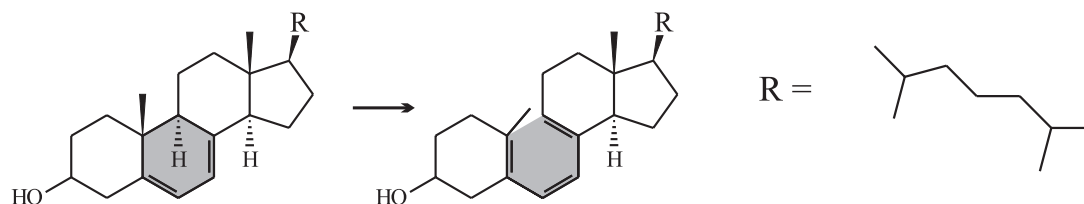


**Figure 2.16:** Photoinduced electrocyclic ring opening of 7-dehydrocholesterol. The six-membered ring marked gray corresponds to the unsubstituted 1,3-cyclohexadiene system.

proceeds via a symmetry-forbidden conical intersection between the  $2A_1$  and the  $1A_1$  state corresponding to a molecular geometry exhibiting a triangular substructure to the primary product *s-cis,Z,s-cis*-1,3,5-hexatriene [26] (see Fig. 2.17).

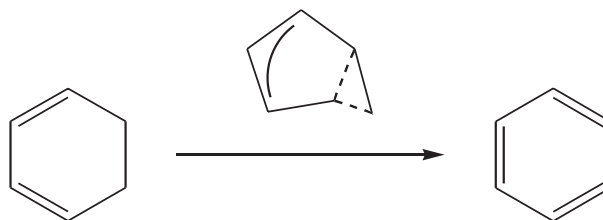


**Figure 2.17:** Photoinduced electrocyclic ring opening of 1,3-cyclohexadiene. The molecular structure at the  $2A_1$ – $1A_1$  conical intersection exhibits a triangular substructure (marked by a dashed line) according to M. Olivucci *et al.* [26].

In contrast to the unsubstituted 1,3-cyclohexadiene, 7-dehydrocholesterol reacts to stereochemically distinguishable products. Additionally, in the latter case, the electrocyclic ring opening can proceed only in a photoinduced fashion, because the steric hindrance inside the molecule is too strong for the disrotatory course to take place in a thermally induced reaction. Despite these advantages of 7-dehydrocholesterol for experimentalists, up to now only the reaction rate of the unsubstituted 1,3-cyclohexadiene has been investigated in the gas phase [88–90]. The reason for this is the poor volatility of 7-dehydrocholesterol (vapor pressure  $\sim 5.5 \times 10^{-5}$  mbar at 298 K [91]). However, measuring the lifetime of gaseous 7-dehydrocholesterol is expected to elucidate the possible role of substituent effects (or steric factor) in electrocyclic ring opening reactions. Moreover, 7-dehydrocholesterol has a particular biological relevance, as explained in Sec. 2.1.2.1.

In general, the electrocyclic ring opening reactions of 1,3,5-cyclooctatriene and 7-dehydrocholesterol are singlet processes, believed to proceed from the initially prepared excited  $1B_2$  state via the spectroscopically dark  $2A_1$  state to the ground state ( $1A_1$ ) [20]. A schematic one-dimensional potential energy curve diagram valid for both reactions is depicted in Fig. 2.18. The crossing between  $1B_2$  and  $2A_1$  surfaces is symmetry-allowed. In contrast, the  $2A_1$  and

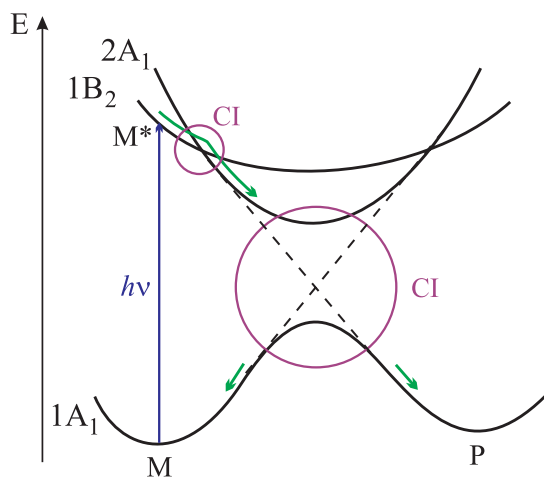


**Figure 2.18:** Schematic one-dimensional potential energy diagram valid for the electrocyclic ring opening reactions of 1,3,5-cyclooctatriene and 7-dehydrocholesterol.

$1A_1$  surfaces exhibit the same symmetry leading to a symmetry-forbidden conical intersection for a transition to the ground state.



In order to prepare 1,3,5-cyclooctatriene and 7-dehydrocholesterol in the  $1B_2$  state, the ground state molecules have to be irradiated by photons of the right wavelength. Both 1,3,5-cyclooctatriene and 7-dehydrocholesterol exhibit a strong absorption in the UV range from  $\sim 310$  nm to  $\sim 250$  nm, as illustrated in Fig. 2.19.

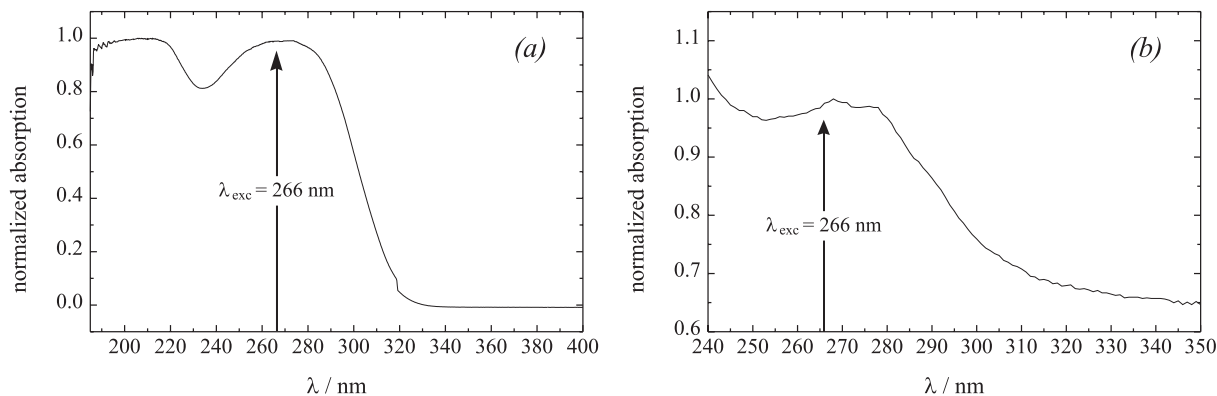


**Figure 2.19:** Normalized absorption spectra of the molecules investigated in the present work. (a), 1,3,5-cyclooctatriene recorded as pure substance between two 1-mm-thick quartz optical flats ( $d < 100$   $\mu\text{m}$ ); (b), gaseous 7-dehydrocholesterol recorded at  $T \approx 417$  K and a roughly estimated sample pressure of  $\sim 3 \times 10^{-2}$  mbar in a heatable gas cell ( $d = 10$  cm) [91]. The arrows mark the central excitation wavelength of the short pulses used in the present work.

Obviously, a central excitation wavelength of 266 nm corresponding to 4.65 eV, which is the third harmonic of the fundamental laser wavelength (see Sec. 3.4.2 and Sec. 3.5.3), leads to a very efficient absorption of light. Of course, the ultrashort pump pulses ( $\tau \approx 90$  fs) contain a range of wavelengths according to their spectral widths (see Fig. 2.20). According

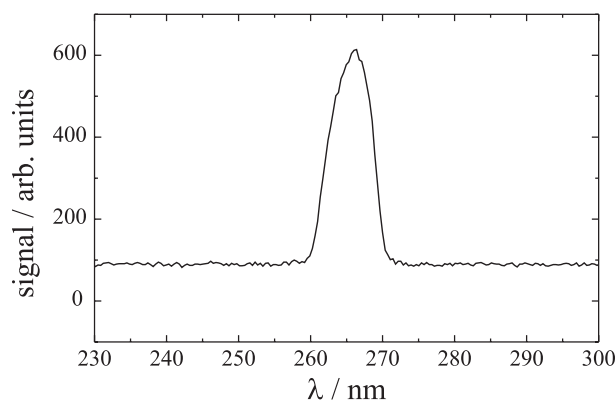


**Figure 2.20:** Typical wavelength spectrum of a pump pulse ( $\tau \approx 90$  fs).

to quantum-chemical calculations (using second-order-perturbation-theory) of M. Olivucci *et al.* for 1,3-cyclohexadiene, the spectroscopically bright  $1B_2$  state lies 4.75 eV above the ground state in the Franck-Condon region [14]. Additionally, except the spectroscopically dark  $2A_1$  state, no other electronically excited state with a similar energy exists. Consequently, the absorption of a single 266-nm photon results in the preparation of a wavepacket in the Franck-Condon region of the  $1B_2$  state from which the molecule evolves. Since 7-dehydrocholesterol differs only in the substituents from 1,3-cyclohexadiene, the energetic level of the states in the Franck-Condon region of both molecules should be very similar. Unfortunately, 1,3,5-cyclooctatriene is not so well investigated. The homologous compounds 1,3-cyclohexadiene and 1,3,5-cyclooctatriene differ in the number of carbon atoms and double bonds. Since the

latter molecule is larger and exhibits one more double bond, the energetic level of the  $1B_2$  state in the Franck-Condon region should be lower than for 1,3-cyclohexadiene. Therefore, short pulses with a central wavelength of 266 nm are also suitable for excitation of 1,3,5-cyclooctatriene into this electronic state.

## 2.3 Photoionization

In order to elucidate reaction dynamics of molecules without the potentially disturbing influence of a solvent, matrix or surface, in the present work the molecules are investigated in the gas phase. Since in this case the particle density is too small for transient absorption experiments, the detection is performed by photoionization.

Photoionization is the photoinduced excitation of an electron into the ionization continuum and the escape of the electron thus freed from the atomic or molecular core. If photoionization occurs by absorbing a single photon, the photon energy of the applied (weak) intensity radiation must exceed the ionization energy  $IE$  of the system:

$$h\nu \geq IE. \quad (2.29)$$

The excess energy  $h\nu - IE$  is transferred to the electron as translational kinetic energy. At higher intensities, available using lasers (especially those delivering amplified ultrashort pulses), the simultaneous absorption of several photons becomes likely. This process is called multiphoton ionization. In experiments on molecules, photoionization can be followed by fragmentation. During the excitation into the ionization continuum, the nuclear arrangement initially remains unaltered. However, the loss of one or more electrons changes the binding relations. Thereby, the ionic molecule begins to vibrate, which can result in dissociation. With ultrashort pulses, a subsequent ionization of the generated fragments is unlikely, because the separation process lasts much longer than the pulse duration.

With increasing laser intensities, the effect of the external electric field on the bound electrons becomes more and more apparent, inducing a shift of the molecular states based on the ac Stark effect. When a free electron is placed in an alternating electromagnetic field, it is forced to perform an oscillatory motion. In other words, it acquires (in addition to any directed translational kinetic energy) a quiver energy the time-averaged value of which is called ponderomotive energy and is given by

$$U_p = \frac{e^2 E^2}{4 m_e \omega^2} \quad (2.30)$$

where  $e$  is the charge of the electron,  $E$  the local electric field amplitude of the laser,  $m_e$  the mass of the electron and  $\omega$  the angular frequency of the laser field. The time-averaged laser intensity  $\bar{I}$  is related to the corresponding electric field by

$$\bar{I} = \frac{1}{2} c \varepsilon_0 E^2, \quad (2.31)$$

in SI units. A very intense laser field will have a noticeable effect on bound electrons, too. Electrons in Rydberg levels behave similar to free electrons, because they are only weakly bound. Therefore, their induced shifts are very close to the ponderomotive energy. Inner-shell electrons in states with a smaller polarizability, however, exhibit a weaker interaction with the light. Consequently, these lower states undergo a smaller shift which is negligible

compared to the shift of Rydberg series and ionization continua. Therefore, the ionization energy of an atom or molecule in an intense laser field increases by approximately  $U_p$  [92].

An inherently present phenomenon occurring in high intensity laser mass spectrometry where the ions are generated in the focus of a laser beam with a nonuniform temporal and spatial profile is the volume effect. It describes the dependence of the detectable ion yield on the interaction volume in which a multiphoton ionization can take place. The size of this interaction volume itself is related to the applied laser intensity. Accordingly, the measured ion yield is a weighted integral of the ionization probability  $P(I)$ ,

$$\text{signal} \propto \int \frac{dV}{dI} P(I) dI. \quad (2.32)$$

Across the focus, there is a spatial variation of intensity, pulse length and phase (see Fig. 2.21). Performing experiments with short-pulse lasers and collecting signals from all over the focal

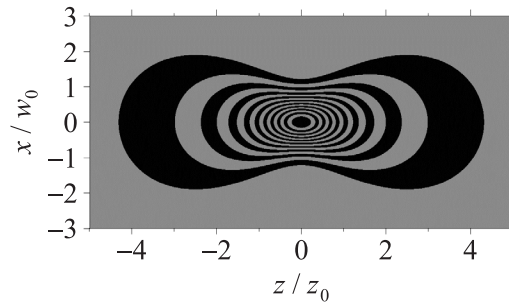


**Figure 2.21:** Calculated spatial intensity distribution of a perfect Gaussian focus in a plane through the propagation direction of the laser beam ( $z$ -axis);  $w_0$  is the  $1/e^2$  width at focus and  $z_0$  the Rayleigh length (see Eq. 3.22). Twenty different areas are shown, each corresponding to a 5%-interval of the maximum intensity in the center [93].

volume consequently results in focal averaging. Therefore, ion yield curves show usually only two intensity-dependent features. At low intensities, there is an  $I^N$  dependence which can be accurately modeled by lowest-order perturbation theory, with  $N$  being the minimum number of photons required to reach a specific ionization level of the system. This dependence is normally expected as the result of energy conservation. Beyond saturation, i. e. that intensity above which no more ionization can occur since all neutral sample atoms/molecules available at focus have been ionized, there is the  $I^{3/2}$  dependence which is characteristic for a spherically focused Gaussian beam [94].

### 2.3.1 Keldysh adiabaticity parameter

A useful theoretical approach to classify photoionization processes, at least for *atoms*, is the Keldysh adiabaticity parameter  $\gamma$  [95]. It is defined as

$$\gamma = \frac{\omega_{\text{laser}}}{\omega_{\text{tunnel}}} = \sqrt{\frac{IE}{2U_p}}, \quad (2.33)$$

where  $\omega_{\text{laser}}$  is the laser frequency,  $\omega_{\text{tunnel}}$  the tunnel frequency of the electron,  $IE$  the ionization energy of the atom, and  $U_p$  the ponderomotive energy (see above). If this parameter exceeds unity, which is typically the case for low intensities, high light frequency, and high ionization energy, the laser field oscillates too fast for a tunneling of the electron through

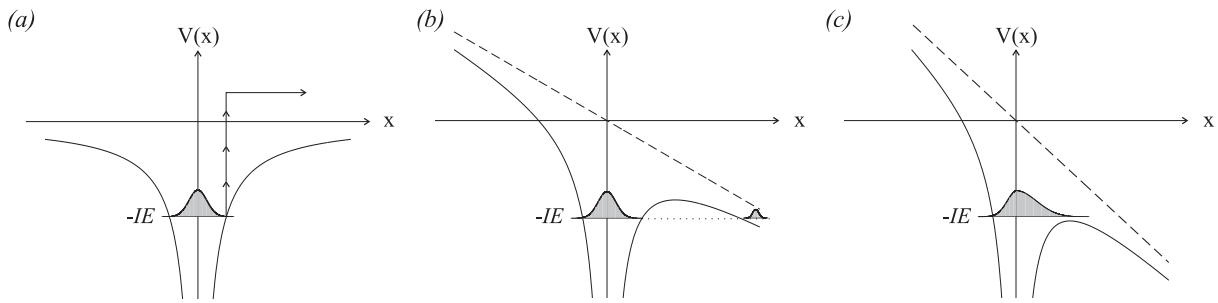


**Figure 2.22:** Illustration of the influence of a static electric field on the atomic potential in which the electron is bound. At low intensities ( $\gamma \gg 1$ ) the distortion of the potential is negligible. Therefore, in (a) multiphoton ionization dominates. Panel (b) shows the situation for tunneling ionization which becomes possible at increased intensities ( $\gamma < 1$ ). (c) In very intense fields with high laser frequency, the potential barrier is suppressed to such an extent that the electron can leave the atom without tunneling.

the potential barrier. Therefore, multiphoton ionization (MPI) takes place. Depending on the energetic level of the atomic states and the energy of the applied photons, such an MPI process can be resonance-enhanced if at least one real state is involved. In the case of non-resonant MPI, the atom is ionized via virtual intermediate states that are energetically far from the energy levels of the atom. Applying a stronger laser field with a lower light frequency to atoms with a quite low ionization energy ( $\gamma \ll 1$ ) results in a significant distortion of the atomic potential leading to the onset of other ionization mechanisms. Then the ionization processes are expected to be well described by the tunneling of an electron through the potential barrier that results from the combined action of the electric fields of the laser and the ionic core. For a sufficiently strong laser field, this barrier can be lowered to such an extent that the electron can simply cross it without tunneling. This process is called over-the-barrier-ionization (OTBI). It should be noted that in a certain laser frequency range, the OTBI regime can be directly reached from the MPI regime without interim tunneling ionization, as is illustrated in Fig. 2.23 (cf. [96,97]). In case of  $\gamma \approx 1$ , it is often difficult to determine the specific ionization mechanism.

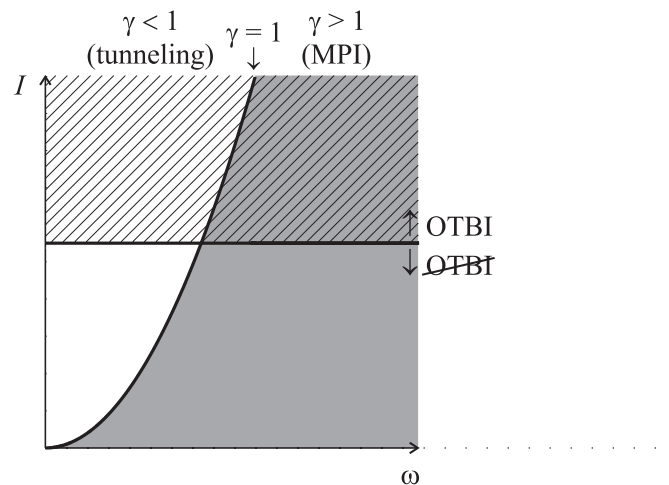


**Figure 2.23:** Different ionization regimes as a function of laser intensity and laser frequency. The Keldysh adiabaticity parameter divides the plot into MPI and tunneling ionization regimes. The onset of OTBI depends only on laser intensity, independent of frequency (cf. [96,97]).

### 2.3.2 Molecules in strong laser fields

The photodynamics of *molecular* systems in high intense fs laser fields is currently a research topic attracting great attention. For instance, Ref. [98] notes that “the understanding of the intense laser-induced processes in polyatomic molecules is in a nascent state.” Analogous to the classification of ionization regimes for structureless atoms by means of the Keldysh adiabaticity parameter, the ionization of polyatomic molecules can also be described by using a modified Keldysh parameter [99–102]. The model has been developed for the ionization of large polyatomic molecules exposed to intense laser radiation of fs duration with peak intensities beyond  $10^{13} \text{ W cm}^{-2}$  corresponding to a field strength  $> 1 \text{ V \AA}^{-1}$  that is responsible for the stability of these systems. In contrast to atoms, the vibrational and rotational degrees of freedom as well as the possibility for dissociation additionally play a role for molecules. The modified Keldysh adiabaticity parameter takes into account molecular structure and the model should, therefore, be able to predict the intensity range in which the transition from MPI to tunnel ionization occurs. In addition, it predicts the influence of molecular structure on the photoionization probability. However, the claimed applicability of this model to all polyatomic molecules has not yet been proved experimentally. Probably, the complexity of molecular systems and their photodynamics are so comprehensive that a “general” description must involve more than just a single classification parameter.

## 3 Experimental

In the present work, ultrafast photochemical reactions with a time resolution in the fs region are investigated. In order to achieve such a high temporal resolution, the well-established fs pump-probe technique is used [103]. Since the time resolution that is achieved depends mainly on the duration of the light pulses applied, it is necessary to use a laser system delivering sub-100-fs pulses and to generate short pulses in the UV by frequency conversion of the fundamental wavelength of this laser via nonlinear processes (second-harmonic generation and subsequent sum-frequency mixing), because the molecules investigated here can only be excited by radiation in the ultraviolet region, as their absorption spectra indicate (see Sec. 2.2). All experiments are carried out in the gas phase, because the systems are undisturbed compared to absorption experiments in solution. In the latter case, the dynamics of the solvent, e.g. cooling of the molecule by the solvent, always overlaps with the reaction dynamics of the molecule of interest, even on the sub-100-fs time scale [103]. On the other hand, the small absorption coefficients of the molecules under investigation in the gas phase at low pressures rules out probing by absorption which is the “standard” probe method. Instead, the ionization of the excited molecules has been chosen as the probe process. However, for multiphoton ionization processes the radiation field must be sufficiently intense. Besides the good time resolution, this is the second advantage of using amplified ultrashort pulses for this purpose. The cations produced are detected in a time-of-flight mass spectrometer based on the Wiley-McLaren principle [104].

The following sections describe in general the generation of intense short laser pulses and their frequency conversion as well as the laser systems used, the pump-probe setup, the detection of ions in a time-of-flight mass spectrometer, the data sampling, and the purification of chemicals and sample preparation.

### 3.1 Principles of amplified short-pulse lasers

In contrast to a narrow bandwidth laser where only a single longitudinal mode is filtered out in the frequency domain, in case of a short-pulse laser, the modes starting to oscillate in the laser cavity with a random phase and amplitude (quasi-cw operation) must be temporally restricted by a suitable filter, in order to obtain the desired pulsed operation. The *Kerr lens mode-locking* (KLM) principle has proved its power for this purpose [105,106]. A light beam with a sufficiently high intensity traveling through a nonlinear material induces a change of the refractive index  $n$  of the medium proportional to the optical intensity  $I$  of the incident laser beam according to

$$n(I) = n + n_2 I. \quad (3.1)$$

This phenomenon is known as the *optical Kerr effect*. This self-induced effect is generally based on a change in polarizability of the medium under the influence of strong electric fields. For Kerr-like media, this effect is often found to be very rapid, the response time being on the order of a rotational period of the outermost electrons of the atom [107].

The optical Kerr effect takes place when a pulse with a spatially and temporally non-uniform intensity (e.g. a Gaussian shape) travels through a Kerr-like medium as often used in solid-state lasers. It leads to an intensity-dependent lens in the material and thus to a self-amplification of the shortest possible pulse, if the cavity is optimized for the presence of that lens (see Fig. 3.1). The underlying physical effect is called *self-focusing*. If an intense

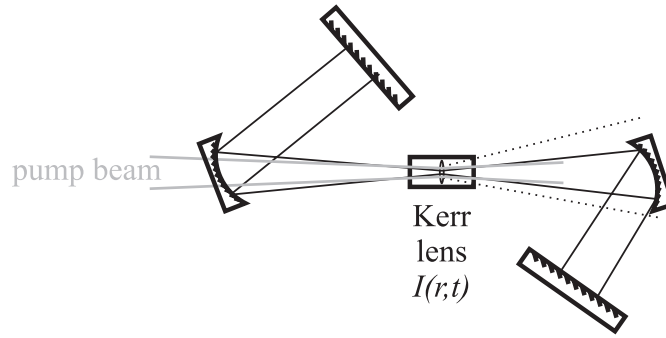


**Figure 3.1:** Generation of ultrashort pulses in a solid-state laser medium. The optical Kerr effect leads to an intensity-dependent lens in the Ti:sapphire crystal, where only the shortest, i. e. most intense, pulses are allowed to travel inside the cavity (solid lines). Only high intense pulses generate the Kerr lens providing minimized losses, which is the condition for mode-locking to take place.

laser beam is transmitted through a nonlinear material exhibiting the optical Kerr effect, the change of the refractive index is dependent on the spatial intensity profile of the laser beam. If its highest intensity is at the center, for example, the maximum change of the refractive index is also at the center, as illustrated in Fig. 3.2. Accordingly, the nonlinear material acts

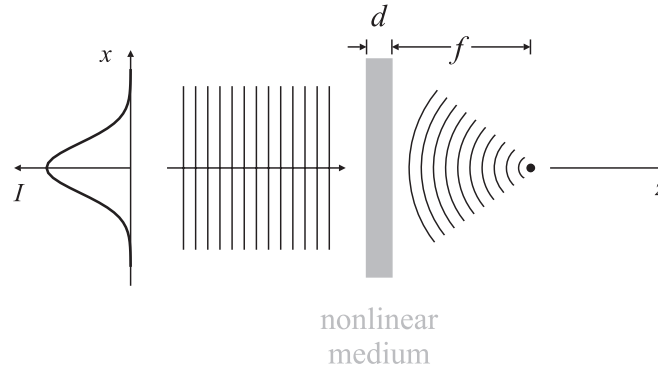


**Figure 3.2:** Principle of self-focusing. A nonlinear medium exhibiting the Kerr effect of the thickness  $d$  behaves as a lens (for paraxial rays) whose focal length  $f$  depends on the intensity  $I$  of the incident laser beam.

as a graded-index medium which causes a wavefront curvature, because the wave undergoes a nonuniform phase shift. The more the laser beam contracts spatially, the higher the intensity and the more pronounced the optical Kerr effect becomes. This leads to a self-amplification of the shortest possible pulse which can be explained by the fact that the longer pulses are suppressed, since the shorter ones have fewer cavity losses than the longer ones. This mechanism can be seen as a “survival-of-the-fittest” and is also calculated this way [108]. Self-focusing is always accompanied by a process called *self-phase modulation* (SPM). Thus a laser beam with power  $P$ , cross-sectional area  $A$  and fundamental wavelength  $\lambda_0$  traveling the optical path  $L$  in a medium with an index of refraction  $n$  generates, in addition to the overall phase shift  $\Delta\varphi_0 = -\frac{2\pi n_0}{\lambda_0} L$  the following phase shift,

$$\Delta\varphi_2 = -\frac{2\pi n_2 L}{\lambda_0 A} \cdot P = -\frac{2\pi n_2 L}{\lambda_0} \cdot I. \quad (3.2)$$

One of the criteria limiting the formation of short pulses is the emission spectrum of the laser material. It has been established that crystalline sapphire doped with Ti, which is an

ultrabroadband gain medium (bandwidth  $\sim 100$  THz) and also possesses a large nonlinear refractive index, is a very attractive material for generating ultrashort pulses with wavelengths in the near-infrared (NIR) region [109].

In what follows, the *mode-locking* process is described. Since solid-state lasers have spectrally broad gain regions, many equally spaced resonant cavity axial modes lie inside the gain bandwidth when the cavity length is about 1 m. If the electric fields of a number of resonant cavity axial modes are locked in phase (mode-locked) by modulating a parameter such as the quality factor of the resonator, the axial mode fields interfere coherently and constructively for short times of the order of the reciprocal of the bandwidth of the lasing medium. The result is a train of high intense, short light pulses with spacing in time determined by the length of the cavity. The cavity round-trip time is approximately given by the product of the pulse length times the number of locked modes  $N$ . The pulse power is then  $N$  times the power of the corresponding continuous wave.

For the most efficient utilization of the optical Kerr effect, the intensity in the spatially homogeneously pumped Ti:sapphire crystal should be optimized. Therefore, the geometry of a short-pulse oscillator is such that the oscillating laser wave is focused into this crystal. To minimize the losses inside the cavity, the Ti:sapphire crystal is cut in the Brewster angle for the linearly polarized laser beam. In order to attain the most homogeneous and most efficient pumping of the Ti:sapphire crystal, it is pumped in the longitudinal direction by a focused laser beam, so that the population inversion appears only in a small cross section along the beam axis. Additionally, the pump beam is focused slightly behind the crystal to compensate for the absorption of the pump light in the Ti:sapphire bulk. The alignment, however, is very critical with respect to the position of the focus of the pump beam, because it generates a thermal lens in the laser crystal leading to gradients of the refractive index. The cross section of the pump beam should be a little larger than that of the NIR beam in order to avoid temperature gradients causing distortions of the beam profile. Since resonator modes with lower intensities have larger cross sections, they interact only weakly with the pumped volume. If several modes get locked in phase accidentally, intensity surmounts occur. The higher intensity inside the crystal leads to a contraction of the beam due to self-focusing and therefore to a much better interaction with the volume of population inversion. Hence intensity fluctuations amplify themselves until the strongest intensity surmount is large enough to deplete the whole population inversion leading to one single pulse. This pulse shortens at every passage through the crystal due to the intensity-dependence of the amplification, because restoring the population inversion takes more time than one round-trip of the pulse. Simultaneously, only the transverse electromagnetic mode TEM<sub>00</sub> develops, because other transverse modes have larger cross sections and are therefore suppressed. The effect that different wavelengths (a short pulse exhibits a broad frequency spectrum, the least width of which is generally limited by the Fourier theorem [110]) have different group velocities in a dispersive medium (medium with a wavelength-dependent refractive index) is called group velocity dispersion (GVD). Due to the GVD, to which all optical components contribute, the generated ultrashort pulse broadens temporally. Therefore, it must be recompressed (see below), e. g. by a prism compressor.

Since the pulse energy of the oscillator output (about 10 nJ) is in many cases not sufficiently high, the seed pulses need to be amplified. One way to do this is to use a *chirped pulse amplifier* (CPA) [111], which consists of a pulse stretcher, a regenerative amplifier and a pulse compressor. The regenerative amplifier is actually a laser resonator with a pumped active medium (Ti:sapphire), in which the oscillator pulses are suitably fed in. Then they are amplified during several round-trips inside the cavity. When the population inversion



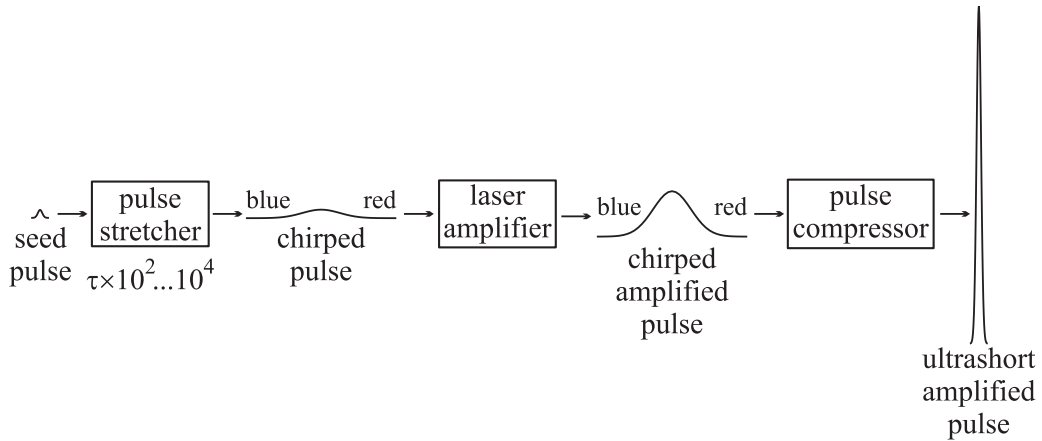


**Figure 3.3:** Principle of chirped pulse amplification.

in the Ti:sapphire crystal is depleted, they are switched out again. In order to attain an optimized pumping to generate the population inversion in the Ti:sapphire amplifier crystal, it is necessary to focus the pump laser beam to a diameter of around  $200 \mu\text{m}$ . This leads to pump intensities of approximately  $10^7 \text{ W cm}^{-2}$  depending on the pump laser used. Again, the diameter of the beam to be amplified must be slightly smaller than the cross section of the pump focus inside the crystal. Even stretching of these seed pulses via GVD owing to the repeated passage through optical components, e. g. the amplifier crystal, typically by a factor of  $\sim 500$  results in peak intensities up to  $3 \times 10^{11} \text{ W cm}^{-2}$ . Such high intensities are above the damage threshold of crystalline Ti:sapphire ( $\sim 10^{10} \text{ W cm}^{-2}$  [112]). Other optical components inside the laser, which are exposed to slightly lower intensities due to the fact that the beam is not so strongly focused there, would be destroyed, too. To avoid such damage, a pulse stretcher, which chirps the seed pulses before amplification, is used. In this process, the amplitude of each of the spectral components of the pulse remain unchanged, but they are temporally shifted in a well-defined way with respect to their relative phases. This, in fact, means that each frequency contribution is converted according to  $A(\omega) \rightarrow \tilde{A}(\omega) = A(\omega)e^{it_0\omega}$ , because this gives a shift  $t_0$  in time. This leads to a lengthening of the pulse. After amplification of the stretched pulse, the spectral components can be fit together again in a compressor as a result of the defined change of their relative phase position to one another. By this means, the pulses can be recompressed almost to their original lengths. This CPA principle is illustrated in Fig. 3.3.

A typical stretcher setup is shown in Fig. 3.4. Its operation is based on the use of two gratings, two lenses and a retroreflector, that are arranged so that the whole setup has a positive GVD. The spectral components with shorter wavelengths travel a longer optical path than those with longer wavelengths. Therefore, the “red” spectral components precede the “blue” ones. A stretcher in a CPA-laser lengthens the pulses typically by a factor of  $10^2 \dots 10^4$ . In contrast to a stretcher, a pulse compressor exhibits a negative GVD, i. e. those spectral parts of the pulse with shorter wavelengths travel shorter optical paths. The positive GVD of the stretcher and the optical components of the amplifier can thus be compensated by the compressor. The value of the GVD can be adjusted by changing the distance between both gratings (see Fig. 3.5). The length of the amplified pulse can be minimized in this way. However, the compressed amplified pulse is always longer than the seed pulse, because during amplification the spectral width of the original pulse is reduced and higher order phase modulations take place.

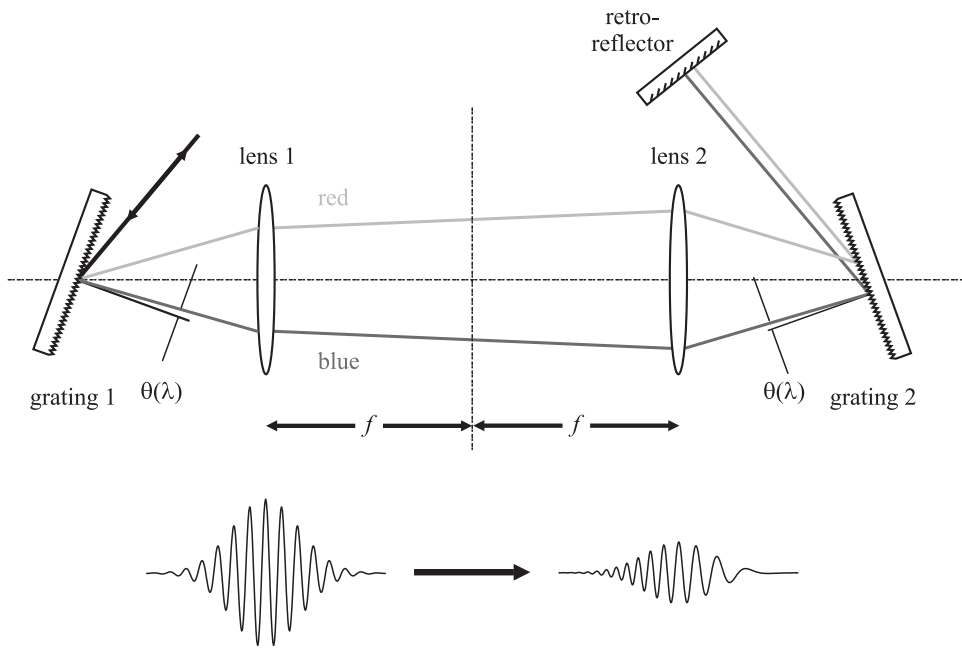


**Figure 3.4:** Principle of a grating stretcher.

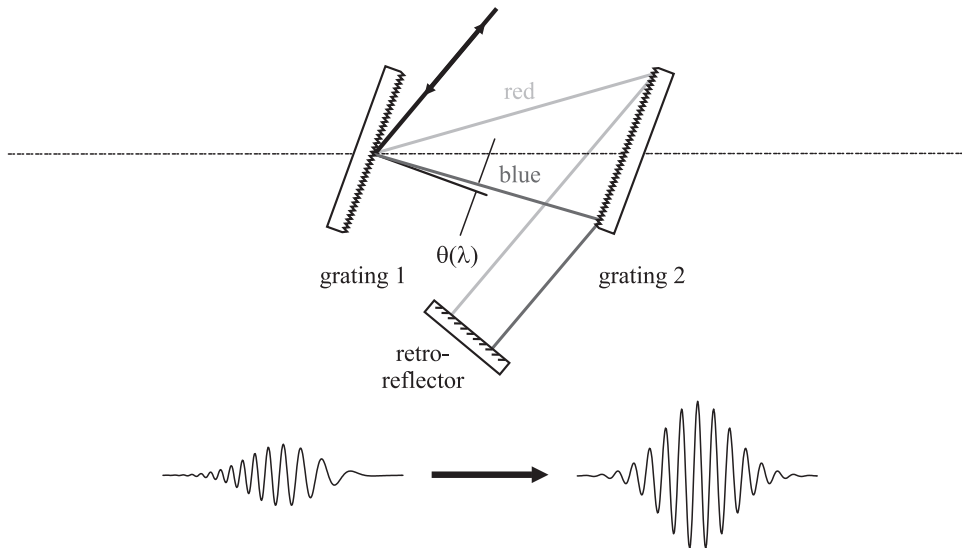


**Figure 3.5:** Principle of a grating compressor.

The technical realization of an amplified short-pulse laser requires the *synchronization* of the seed pulses from the oscillator with pulse repetition rates of the order of tens of MHz and the pump pulses containing much more energy per pulse but therefore having pulse repetition rates only in the kHz region. This means that only a small fraction of the many seed pulses must be selected, and when exactly one of these seed pulses is fed into the amplifier resonator, a pump pulse generating the population inversion must just have passed the amplifier crystal. Typical cavity round-trip times of around 10 ns demand devices with response times in the same temporal range. For linearly polarized light pulses, such fast switching operations can be realized in a so-called *Pockels cell*. This works in combination with a polarization analyzer (e.g. a thin film polarizer). The switching in or out of pulses occurs by suitably rotating

the polarization direction of the light which is consequently transmitted or reflected into a different direction by the analyzer, respectively. The *Pockels effect* (also known as the electrooptic effect) describes the modification of the refractive index of a material induced by an electric field and is closely related to the electro-optical Kerr effect. In general, the field  $E$  applied to a special crystal induces birefringence, i. e. a different index of refraction for a different polarization direction, which leads to a rotation of the polarization direction of linearly polarized light.

## 3.2 Fundamentals of frequency conversion

For the pump-probe experiments described in Sec. 3.4.2 and Sec. 3.5.3, short pulses of wavelengths different from the fundamental radiation delivered by the laser system are required. In particular, 800-nm pulses are frequency-doubled resulting in 400-nm light and a frequency tripler is designed and constructed to generate short pulses of 266 nm. Additionally, difference-frequency mixing techniques are used to determine pulse lengths. In what follows, the principles of nonlinear optical mixing techniques (see also for example [113–116]) are discussed.

Nonlinear optical effects become observable at light intensities so high that the optical electric field is significant in comparison with the Coulomb field ( $\sim 10^8$  V/cm) in atoms, molecules, or condensed matter. The most important nonlinear effects can be described by a nonlinear optical polarization of the form,

$$\frac{\vec{P}}{\varepsilon_0} = \chi^{(1)} \cdot \vec{E} + \chi^{(2)} : \vec{E}\vec{E} + \chi^{(3)} : \vec{E}\vec{E}\vec{E} + \dots, \quad (3.3)$$

with the dielectric polarization  $P$  and the electric field  $E$ . For isotropic media, the linear susceptibility  $\chi^{(1)}$  is related to the dielectric constant  $\varepsilon$  through  $\varepsilon = \varepsilon_0(1 + \chi^{(1)})$  in the SI-system. The material susceptibilities  $\chi^{(1)}$ ,  $\chi^{(2)}$  and  $\chi^{(3)}$  are tensors with coefficients dependent on the frequencies of the electric field. In materials exhibiting inversion symmetry, the susceptibility  $\chi^{(2)}$  vanishes. Therefore, nonlinear optical phenomena described by the  $\chi^{(2)}E^2$  polarization term such as optical second-harmonic generation (SHG,  $\omega + \omega \rightarrow 2\omega$ ), sum-frequency generation (SFG,  $\omega_1 + \omega_2 \rightarrow \omega_+$ ) and difference-frequency generation (DFG,  $\omega_1 - \omega_2 \rightarrow \omega_-$ ) require the absence of an inversion center. Typical phenomena related to nonlinear optics, not found in linear optics, are the strong dependence on the intensity of light and the coherent generation of light at combination frequencies. The conversion of photon energies with frequencies  $\omega_1$  and  $\omega_2$  to sum and difference frequencies through the  $\chi^{(2)}E^2$  polarization term corresponds to the appearance of combination frequencies  $\omega_+$  and  $\omega_-$  in the resulting polarization. For low intensities, the power radiated at the combination frequencies is proportional to the product of the incident powers at  $\omega_1$  and  $\omega_2$ . For amplified fs laser pulses, however, saturation effects normally limit this yield to lower values. Second-harmonic generation allows the efficient conversion of visible or infrared laser light to higher frequencies where suitable laser sources are not available. Pulsed or continuous light with a power  $> 1$  W can be frequency-doubled with a high conversion efficiency in optical systems with highly nonlinear crystals.

For the optimization of frequency conversion of fs pulses (i. e. nonlinear gain vs. pulse lengthening), several effects must be taken into account:

- phase-matching
  - spectral acceptance
  - angular acceptance
- spatial and temporal walk-off
  - crystal double-refraction
  - group velocity mismatch
- material damage threshold

To attain a maximum frequency conversion efficiency, the phases of the coupled fields should match across the whole interaction length  $l$ . For spectrally broad fs pulses, however, this cannot be accomplished. Therefore, the phase difference  $\Delta k l$  can only approach zero where  $\Delta k$  denotes the difference between the propagation constants of incident and generated wave. The condition  $\Delta k l \rightarrow 0$  implies that  $\Delta k$  has to approach zero, because the interaction length must be finite. However, material dispersion inhibits the phase-matching, leading to an increase in  $\Delta k$ , with the result that the interacting fields gradually lose their relative optimum phase with propagation through the nonlinear medium. If the phase mismatch at the end of the crystal amounts to  $\pi$ , destructive interference of the fields generated in the crystal occurs. Consequently, no frequency-converted light can be produced. Due to material dispersion, there is an upper limit to the maximum interaction length useful in the frequency conversion processes mentioned above. This value amounts to approximately a few  $\mu\text{m}$  depending on the involved wavelengths. Therefore, if dispersion is present, the nonlinear efficiency will be insignificant. In practice, the phase-match condition,  $\Delta k \rightarrow 0$ , is met by exploiting the birefringence of optically anisotropic media to compensate exactly for the normally large dispersive difference between the interacting fields. With appropriate polarization states and crystal orientation, it is consequently possible to achieve phase-matching at every point along the direction of propagation for the particular combination of frequencies. Then the maximum useful interaction length becomes limited only by the available crystal length. Generally, two different types of phase-matching exist. For SFG for instance, the polarization vectors of  $\omega_1$  and  $\omega_2$  are required to be parallel in type I phase-matching, whereas they must be orthogonal in type II phase-matching. The choice of polarization directions for phase-matching depends on the optical properties of the crystal and the sign of its birefringence. If phase-matching can be achieved in a material, in either the type I or type II scheme, depends on the values of its refractive indices, the strength of its birefringence, and the particular frequencies involved. Additionally, the finite frequency spectrum and the spatial divergence of the light beams involved restrict the quality of the phase-matching. Consequently, all the frequency and angular components of the interacting waves cannot be brought into phase-matching simultaneously and  $\Delta k$  increases. Under these real conditions, the maximum useful interaction length is no longer infinite, but amounts to some finite value depending on the degree of phase mismatch. The increase of  $\Delta k$  arising from the finite bandwidth of the coupled waves can be calculated from the refractive index data of the material in terms of the quantity  $\partial(\Delta k)/\partial\omega$ . This is then used to determine the spectral acceptance bandwidth of the crystal. The sensitivity of the phase-matching to the angular deviations can also be calculated in a similar way by evaluating the quantity  $\partial(\Delta k)/\partial\theta$  defining, together with the condition for optimum phase-matching,  $\Delta k l \rightarrow 0$ , the angular acceptance bandwidth of the crystal in the  $\theta$ -direction. The acceptance bandwidths of a crystal can be used to ascertain the maximum useful interaction length, given by the spectral linewidth and divergence of the beams involved in the frequency conversion process. Using ultrashort pulses, maximum useful interaction lengths are limited to only a few mm, because of the large bandwidths associated with fs pulses. In practice, (uniaxial) crystals used for frequency conversion exhibit a special

section angle  $\theta$  between the normal of the incident surface and the principal axis of the crystal to allow them to be positioned perpendicular to the incident laser beam.

In addition to phase mismatch, spatial and temporal walk-off play an important role in frequency conversion processes in nonlinear crystals. Walk-off effects can severely restrict the maximum useful interaction length, even in the presence of perfect phase-matching, thus causing serious degradation in the nonlinear gain. Such effects occur as a consequence to the reduction of the spatial and temporal overlap of the interacting beams traveling through the nonlinear medium. Spatial walk-off arises from crystal double-refraction. In birefringent anisotropic materials the direction of the energy flow is generally different from the wave propagation direction perpendicular to the wavefront. This means that the corresponding rays walk off from one another in a collinearly phase-matched interaction with propagation through the medium resulting in a decreased energy transfer between the fields. Therefore, the nonlinear interaction can become ineffective after a certain distance which sets an upper limit to the maximum useful crystal length. Since double-refraction is a consequence of birefringence, the use of crystals exhibiting small double-refraction is not attractive, because this can constrain phase-matching. However, spatial walk-off effects can be eliminated by employing geometries where the beams propagate along one of the principal index axes of the crystal, not exhibiting double-refraction in these directions. Temporal walk-off effects can also strongly influence frequency conversion processes and can deteriorate nonlinear gain by limiting the useful interaction length. Such effects are especially relevant in the ultrashort pulse regime, leading to a reduced nonlinear coupling and energy transfer between the interacting pulses of the fundamental wavelength and the frequency-doubled light. Therefore, despite matching of phase velocities, the efficiency of nonlinear interaction can be severely reduced by group velocity mismatch. Temporal walk-off effects can be minimized by using suitable materials (like LBO or BBO). Depending on the material dispersion, input pulse characteristics, and the wavelengths involved in the interaction, group velocity walk-off can affect the temporal and spectral pulse characteristics in frequency conversion processes by pulse broadening and compression or by modifying the chirp of the pulses.

One of the most important considerations in the choice of a suitable nonlinear crystal is its damage threshold. Since the nonlinear efficiency is dependent on the input intensity, attainment of the operation threshold in nonlinear devices requires high pumping intensities of typically  $10^7$  W cm<sup>-2</sup> or more. This means that for efficient conversion the nonlinear crystal must have the ability to withstand very high power densities. If the material damage threshold is too low, the maximum possible yield of nonlinear generation will be suppressed by the onset of damage, regardless of all other criteria being satisfied. Exact determination of the optical damage threshold for a given material is often difficult, because it depends on the wavelength of the radiation, the quality of the beam profile, pulse duration, crystal quality and length, as well as the exact experimental conditions. Nonlinear crystals such as LBO and BBO exhibit damage thresholds as high as 10-20 GW cm<sup>-2</sup> under pulse pumping [117], whereas for instance in LiNbO<sub>3</sub> the corresponding damage threshold is as much as two orders of magnitude lower under the same pumping conditions. In addition to a high optical damage threshold, a large effective nonlinear coefficient (i. e. the efficiency of the nonlinear coupling in a given direction), and reasonable phase-matching conditions are necessary. Other material requirements include a wide transmission range as well as favorable mechanical and chemical properties. In particular, the material has to be hard, non-hygroscopic and chemically stable as well as available in bulk form and large size and be able to be polished.

These remarks form the basis for the choice of crystals used in nonlinear devices for short-pulse experiments. The lengths of such crystals are always a compromise between

conversion efficiency, on the one hand, and pulse lengthening, on the other hand, depending on the characteristics of the input beam. In particular, SHG, SFG and DFG are used in the measurements described in the present work. In order to decide which nonlinear material at which section angle  $\theta$  and especially which crystal length should be chosen to set up a frequency tripler (see Sec. 3.5.3), the calculated curves of efficiency in terms of effective nonlinear coefficient  $d_{\text{eff}}$ , phase-matching angle, spectral acceptance, angular acceptance, (temporal) walk-off angle, group velocity mismatch, and figure-of-merit (defined as  $d_{\text{eff}}^2/n^3$ ) dependent on the wavelength [118,119] are compared, with the aim of a minimized pulse lengthening [120,121].

### 3.3 Setups used

In the framework of the present investigations, measurements have been carried out using two different setups. In what follows, these setups will be labeled “initial” and “final” with respect to the temporal order of their usage. Although the initial setup is not optimally suited for pump-probe measurements in all aspects (for example degree of nonlinear deformation of the pulses, uncertainties about reactant pressures and detection efficiency), it is still discussed here, in order to illustrate the influence of these parameters on the 1,3,5-cyclooctatriene system. The results of these measurements instigated further measurements. These are carried out using the final setup in which particular care is taken to control the degree of nonlinearity present in the beam, and a different time-of-flight philosophy is implemented to avoid the uncertainty regarding target pressure, since this hampered the interpretation of measurements with the initial setup.

## 3.4 Laser system and optical setup for initial experiments

### 3.4.1 Laser system

A commercial laser system consisting of a Ti:sapphire oscillator for the generation of short pulses and a Ti:sapphire amplifier is used for the initial experiments (see Fig. 3.6).

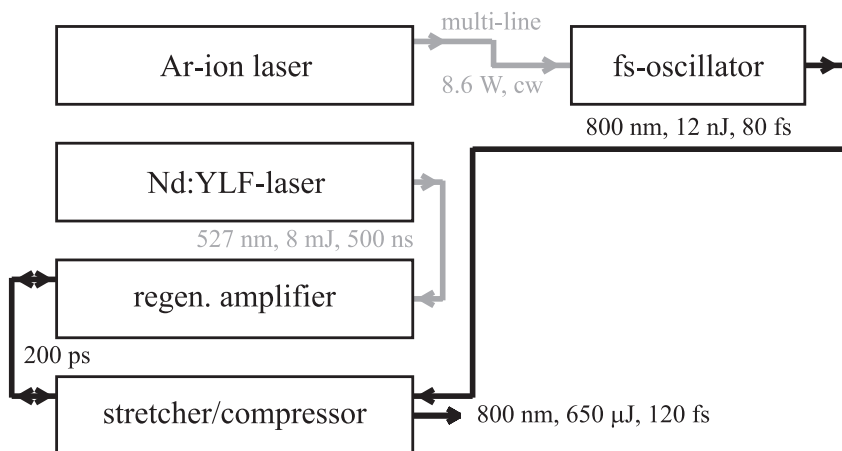


**Figure 3.6:** Block scheme of the laser system for initial experiments.

The oscillator (Spectra-Physics Tsunami) pumped by an Ar-ion laser (Spectra-Physics BeamLok 2080A-12, typically 8.6 W cw output power) is tunable in the region from 720 nm to 850 nm, determined by the emission spectrum of the Ti:sapphire medium and the bandwidth of the high-reflective dielectric mirrors. At a wavelength of 800 nm, the emitted pulses have a duration of around 80 fs limited by the large GVD of the four BK7 prisms integrated in the laser for pulse compression. Between the two central prisms the optical paths of the spectral components lie parallel to each other, making it possible to adjust the central wavelength of the laser pulses using a movable slit at this position, because only a narrow part of the spectrum can pass the slit. The pulse repetition rate of the oscillator is given by its resonator length and is 82 MHz corresponding to a cavity round-trip time of 12.5 ns. It delivers an averaged power of around 1 W, with a pulse energy of merely 12 nJ. The pulse length is determined by measuring the autocorrelation function by means of an autocorrelator (Spectra-Physics Mod. 409), assuming a temporal  $\text{sech}^2$ -profile. The frequency spectrum is monitored by a grating spectrometer (Oriel Multispec 77400) connected with a photodiode-array (EG&G, 1024 pixels) read out by a computer interface (Cronin). It is established to be 13 nm (FWHM). Consequently, the resulting pulse length bandwidth product [122] is 0.488, 55% above the theoretical limit (0.315) [110] which is acceptable.

Although this laser system is critical to align, it is possible to achieve an acceptable compromise regarding the pulse parameters by taking much care. This will be described in detail in the following. The short seed pulses travel  $\sim 2.5$  m through air, before they are fed into the pulse stretcher. The amplification of the seed pulses is carried out in a commercially available regenerative amplifier (Quantronix Model 4811), which is constructed as a folded three-mirror resonator, for space-saving reasons (see Fig. 3.7). In contrast to

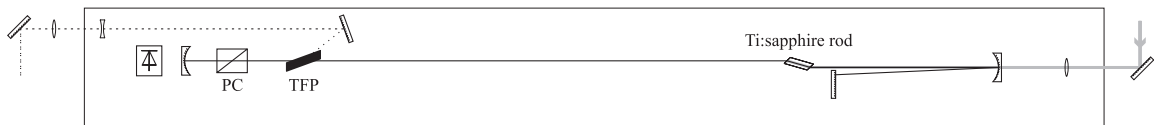


**Figure 3.7:** Schematic illustration of the regenerative amplifier for initial experiments. The pump light (solid gray line) from the Nd:YLF-laser is focused slightly behind the Ti:sapphire rod. The seed pulses (dotted line) coming from the stretcher are switched in by a Pockels cell (PC) working in combination with a thin film polarizer (TFP). The solid black line shows the beam path of the wave oscillating inside the amplifier cavity. The light leaking through the high-reflective mirrors of the resonator generates an electric signal in a photodiode (PD) positioned behind one of these mirrors. This way, the pulse train oscillating in the cavity is monitored by an oscilloscope (Tektronix TDS2465A, 350 MHz).

a two-mirror resonator, it has two more degrees of freedom for the position of the NIR beam inside the cavity, but no further criteria to reach a stable point of operation, which leads to problems in the alignment of this laser. Moreover, it contains only one Pockels cell for both feeding in seed pulses and switching out of amplified pulses controlled by a driver delivering the high voltage used for every switching operation. This construction has the drawback that during the switch-out operation, seed pulses can leak into the amplifier resonator. Although the three-mirror construction actually allows the positioning of the Pockels cell in a part where the beam is approximately collinear, it is placed in the divergent part. Additionally, the alignment of the Pockels cell for obtaining one single output pulse proves to be very critical, because an unambiguous criterion for the spatial orientation in the beam path does not exist. Further, the second voltage level (for the switch-out operation) delivered by the Pockels cell driver (Medox DR85-A) cannot be set to a sufficiently high value which results in afterpulses. The amplifier is pumped by an intra-cavity frequency-doubled,

Q-switched Nd:YLF-laser (Quantronix Model 527 DP-H) at a pulse repetition rate of 1 kHz, a wavelength of 527 nm, a pulse length of 500 ns, and a pulse energy up to 12 mJ (typical 8 mJ) dependent on the current applied to the high-pressure arc lamp which generates the population inversion in the laser crystal. Since the lenses of the telescope which are actually needed to collimate the divergent output of the Nd:YLF-laser cannot be individually moved or adjusted in the horizontal and vertical direction, it is not possible to align the telescope for an optimized beam profile of the pump light. Additionally, the pump beam profile in the amplifier crystal deteriorates by the fact that the pump beam remains divergent, because the laser box is too tight for setting up the telescope properly, before hitting the focusing lens and is therefore clipped at this lens. The poor quality of the pump beam profile causes that the amplifier does not generally oscillate in the TEM<sub>00</sub> mode. Another problem in the alignment results from the fact that the stretcher/compressor unit contains only one grating for both stretching and compressing of the NIR pulses. Generally, any change of the central wavelength, acquired by the transmission through the optical components of the amplifier, cannot be compensated in such a compressor, because another incidence angle  $\theta(\lambda)$  of the compressor grating compared with the stretcher grating is needed (see Fig. 3.4 and Fig. 3.5). This construction leads to the fundamental problem of an underdeterminate system. This means that there is a multitude of operational parameters, but no unambiguous recipe to select an optimized operation of the laser (energy, pulse length, frequency spectrum, beam profile, prepulses and afterpulses) exists, because the design of the laser does not allow these quantities to be changed independently. This problem can only be handled by taking significant care in alignment and by accepting compromises regarding the pulse parameters. Finally, the system delivers pulses at a central wavelength of 800 nm with an energy of 650  $\mu$ J measured with a power meter (Ophir) directly after the compressor and a length of 120 fs measured with a commercial autocorrelator (APE PulseCheck  $\tau$ 5050) also directly after the compressor at a pulse repetition rate of 1 kHz. The prepulses can be totally suppressed, whereas one afterpulse remains containing less than 5% of the energy of the main pulse, monitored by a high-speed photodiode (Valvo UVHC 20) connected with a large-bandwidth oscilloscope (LeCroy LC534M, 1 GHz).

### 3.4.2 Optical setup for pump-probe measurements

In the following, the setup for the preparation of the two pulses required for a pump-probe experiment and the adjustment of the relative delay between these pulses is described (see Fig. 3.8). First of all, the output beam of the laser system hits two bending mirrors in zig-zag configuration to define the main axis of the beam independent of the original direction of the laser output. Then the beam is divided into two parts in the ratio of one to one by means of a dielectric beam splitter in order to generate the two pulses with a fixed temporal correlation needed for a pump-probe experiment. To achieve the required wavelength of 267 nm, the pump pulse then travels through a commercial frequency tripler (CSK Super-Tripler) containing two different nonlinear crystals for the two frequency conversion steps (SHG@800nm, LBO, type I,  $8 \times 8 \times 0.5$  mm<sup>3</sup>,  $\theta = 32^\circ$ , anti-reflection coating; SFG@800nm+400nm, BBO, type I,  $8 \times 8 \times 0.2$  mm<sup>3</sup>,  $\theta = 44^\circ$ , protection coating). It delivers typically a conversion efficiency of 2.5% and pulse lengths of about 130...150 fs. The output of the tripler passes subsequently a variable delay-line consisting of translation stage driven by a stepper-motor (PI M-510.10) and an aluminum retro-reflector (Newport, beam deviation 1 arc s, wavefront distortion  $\leq \lambda/3$ ). Two iris diaphragms guarantee that the beam hits the retro-reflector exactly in the direction of the motion of the delay-line to avoid a ray offset during the mo-



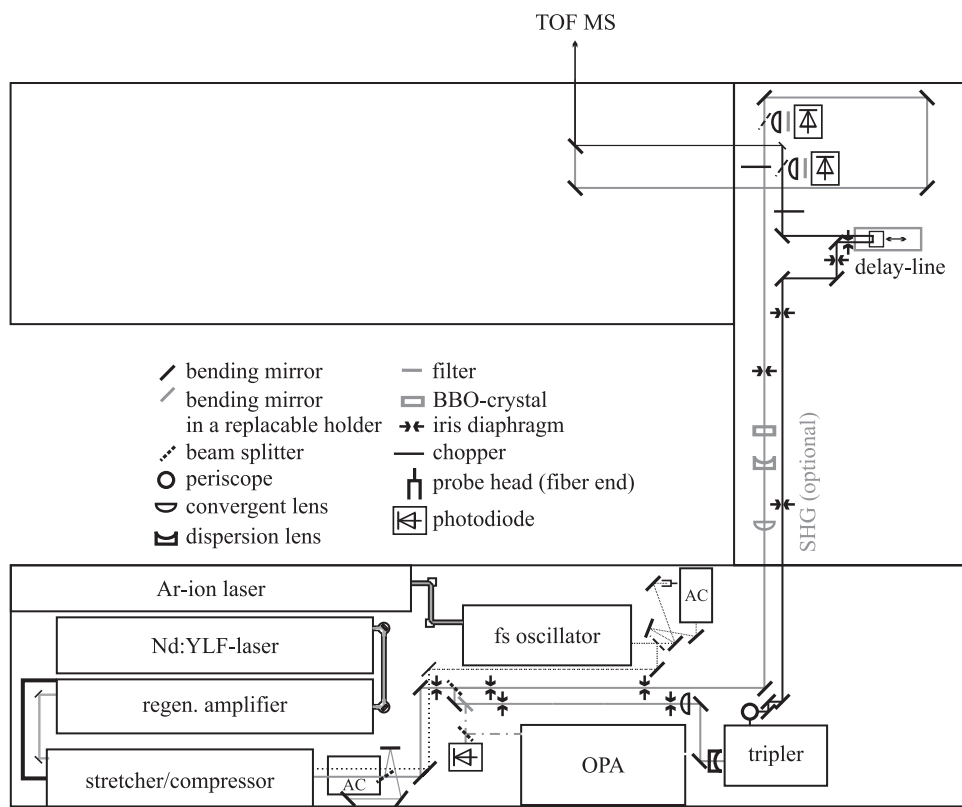


**Figure 3.8:** Optical setup for initial experiments. The dotted gray line represents the seed beam. The solid gray line shows the probe beam path and the solid black line the pump beam path after frequency tripling.

tion. If required, the wavelength of the probe beam can be changed from 800 nm to 400 nm by SHG in a BBO-crystal making it necessary to replace all subsequent dielectric mirrors high-reflective for 800 nm by ones for 400 nm. Two identical light choppers (head, EG& G; disk, Metafot) with specially produced disks exhibiting apertures which are twice as large as the bridges are placed in both beam paths. The chopper disks are synchronized with the laser clock rate divided by three, thus two of three laser pulses are transmitted and one is blocked. The phases of the chopper disks are adjusted in such way that each series of three pulses is transformed into the series pump-no probe, no pump-probe and pump-probe. Since the non-transient background signal is independent of the pump-probe, it can be determined in this way and then subtracted from the measured signal. In every beam path, a wedged quartz plate (30') used as a beam splitter is positioned after the chopper to supply a reflex after further attenuation by suitable filters to a high-speed photodiode (EG&G FND 100 Q). The signals of these photodiodes as well as the actual measurement signal are recorded by a computer, which allows pulses to be disregarded that are observed to deviate too much from the average energy. To ensure that the free rotation of molecules in the gas phase during the time between the pump and the probe pulse does not cause an additional time-dependent signal [123], the angle between the polarizations of pump and probe beams, which are both linearly polarized, is adjusted to the magic angle (i. e. that angle which fulfills the condition  $\cos^2 \vartheta = \frac{1}{3}$ ), using a  $\lambda/2$ -retarder-plate in the pump beam path. The angle  $\vartheta = 54.7^\circ$  is checked for correctness by means of a Glan polarizing prism. To achieve sufficiently high intensities in the vacuum system, the pump beam and the probe beam are focused by plano-

convex quartz lenses with different focal lengths ( $f_{\text{pump}} = 500$  mm and  $f_{\text{probe}} = 1000$  mm). Since the cross-sectional area of the pump beam is smaller than that of the probe beam, the demand for a homogeneous pumping is not met. This is required for minimization of the background signal produced by ionization of unexcited molecules. The pump pulse and the probe pulse, which originally evolved from one single pulse, but then are separated to be prepared in different beam paths in the way described above, are now reunited again by means of a dichroic mirror ( $d = 2$  mm) that is high-reflective for the pump wavelength, but high-transmitting for the probe wavelength. Two bending mirrors in zig-zag configuration are placed in each beam path to align both beams exactly through the centers of the entrance window and the exit window of the vacuum system. This way, the pump beam and the probe beam are brought roughly laterally into line, and then their directions are optimized with the help of the ion signal. To achieve synchronization, the probe beam path contains an additional distance to compensate for the longer beam path of the pump pulses due to frequency tripling. By means of a fast vacuum photodiode (Valvo UVHC 20) connected with a large-bandwidth oscilloscope (Tektronix TDS544A), the time-delay between the both pulses can be adjusted to zero with an accuracy of 200 ps. This value corresponds to a translation of 30 mm so that fine-tuning can be done using the delay-line which has a moving distance of 100 mm at maximum. The exact temporal coincidence between the two pulses is determined by irradiating a molecule exhibiting a long-lived excited state, e. g. toluene, by monitoring its transient signal as a function of pump-probe delay which exhibits a persistent step-like increase. This allows the pump-probe delay to be scanned using a reduced resolution. The position of the sharp increase corresponds to temporal coincidence between the two pulses which is then fine-tuned using the highest possible resolution of the delay-line which is 6.7 fs.

In short-pulse experiments, the degree of nonlinear deformation of the pulses has an important influence on the results. Therefore, a closer look will now be taken to the special features of this setup which are believed to cause nonlinear distortions of laser beams. The short distance of the  $\text{CaF}_2$  entrance window of the vacuum system to the center of the interaction volume of only  $\sim 130$  mm causes rather high intensities of the focused laser beams ( $f_{\text{pump}} = 500$  mm and  $f_{\text{probe}} = 1000$  mm) inside this window. The peak intensity to which the  $\text{CaF}_2$  window is exposed amounts to  $6.5 \times 10^{10}$  W cm $^{-2}$  for the pump light and to  $8.8 \times 10^{11}$  W cm $^{-2}$  for the probe beam (800 nm). Since  $\text{CaF}_2$  is a medium with a large bandgap, such high intensities (especially at 800 nm) are very likely to trigger coherent white-light continuum generation [124] and concomitant distortions of the temporal profile of the laser pulses. The beam path from the compressor grating to the interaction volume amounts to  $\sim 9.1$  m. Together with the optical components transmitted in the beam paths and the estimated peak intensities of  $I_0 = 3.3 \times 10^{10}$  W cm $^{-2}$  for the unfocused laser beam after the compressor,  $I_{\text{pu}} = 4.4 \times 10^9$  W cm $^{-2}$  for the pump beam after the frequency tripler and  $I_{\text{pr}} = 1.4 \times 10^{10}$  W cm $^{-2}$  for the probe beam after the beam splitter, the  $B$ -integral (see Sec. 3.5.2) is found to be about 1.4 for the pump light and 3.8 for the probe light. The latter value is somewhat on the high side with respect to the widely accepted upper limit of 3 to 5, so that nonlinear distortions of the beam by self-phase modulation or self-focusing cannot be excluded completely.

## 3.5 Laser system and optical setup for final experiments

### 3.5.1 Laser system

A commercial laser system consisting of a Ti:sapphire oscillator for the generation of short pulses and a Ti:sapphire amplifier is used for the final experiments (see Fig. 3.9), typically delivering pulses with an energy of 1.8 mJ, a duration of 70 fs, and a temporal as well as a spatial Gaussian profile at a central wavelength of 800 nm and a pulse repetition rate of 1 kHz.

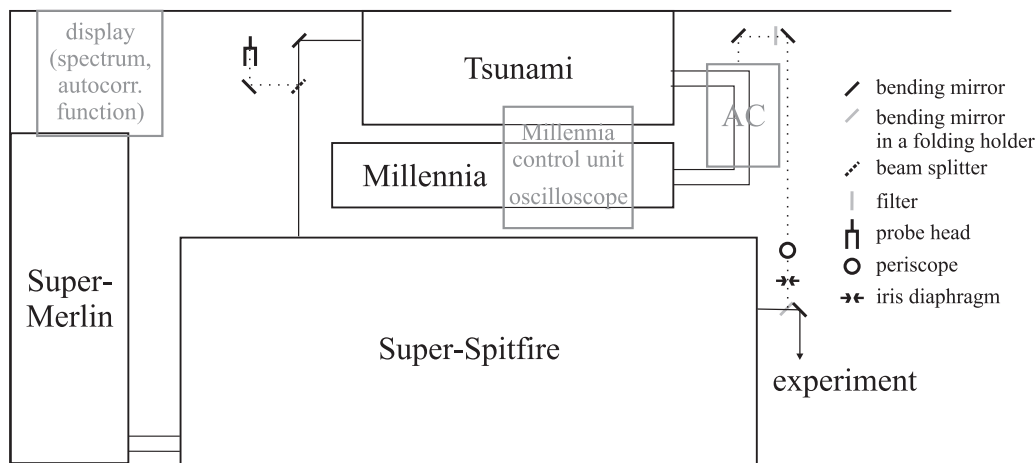


**Figure 3.9:** Scheme of the laser system for final experiments. To keep the beam paths as short as possible the devices for diagnostics and the control unit are placed above the laser boxes and the beam paths, respectively.

To achieve the population inversion in the Ti:sapphire crystal of the oscillator (Spectra-Physics Tsunami Lite), it is pumped by a diode-pumped Nd:YVO<sub>4</sub>-solid-state laser (Spectra-Physics Millennia-V) which delivers continuous wave light at a wavelength of 532 nm generated by intra-cavity frequency-doubling in an LBO-crystal. The maximum output power is 5.50 W, but typically only 4.90 W are used, because this provided an optimal pumping of the oscillator. The fs oscillator is optimized for short pulses and tunable in the region from 720 nm to 850 nm. At a central wavelength of 795 nm, it supplies an average power of around 0.9 W corresponding to a pulse energy of 11 nJ at a pulse repetition rate of 82 MHz and pulse lengths down to 50 fs. By means of the prism compressor integrated in the laser, the pulse length is typically set to 60 fs, because the broader spectrum of a shorter pulse would clip in the grating stretcher of the amplifier. The pulse length is measured one time by means of an autocorrelator (APE PulseScope) assuming a temporal  $\text{sech}^2$ -profile and compared with the frequency spectrum with a width of 13.9 nm (FWHM). Consequently, the resulting pulse-length-bandwidth-product [122] is 0.391, 24% above the theoretical limit (0.315) [110] which is satisfactory. Then, the frequency spectrum of the seed pulses is permanently monitored by a fiber spectrometer (APE PulseScope). The reflex of a wedged (30') quartz plate used as a beam splitter in the beam path to the amplifier is fed after further attenuation into an Ulbricht sphere where the fiber end is plugged in.

The CPA-amplifier (Spectra-Physics Super-Spitfire) consists basically of four components, a pulse stretcher, a regenerative amplifier, a double-pass amplifier, and a pulse compressor. This makes it possible to amplify up to 1000 seed pulses per second by a factor of  $7 \times 10^5$ ,

corresponding to an assumed seed pulse energy of 5.5 nJ after the stretcher (i. e. 50% energy loss) and an energy of the amplified pulse of 3.8 mJ before the compressor. For cost-saving reasons, the pulse stretcher contains only one grating which is exploited four times altogether via bending mirrors. It has a grating constant of 1200 lines/mm and a width of 11 cm limiting the spectral width of the seed pulses to approximately 15 nm. To avoid chromatic aberrations, the lenses in Fig. 3.4 are substituted by a concave mirror which is also used repeatedly. This way, the seed pulses are lengthened to about 1 ns. A second grating, which is adjustable in all directions independently of the stretcher, is employed in the pulse compressor (see Fig. 3.5) and analogously to the stretcher setup used twice by means of a retro-reflector. By adjusting the angle of the compressor grating compared to the stretcher grating and the distance between the grating and the retro-reflector, the amplified pulses can be recompressed to 70 fs having a temporal Gaussian shape proved by autocorrelation measurements.

Both the regenerative amplifier and the double-pass amplifier are pumped by an intra-cavity frequency-doubled Nd:YLF-laser (Spectra-Physics Super-Merlin) which is itself pumped by two high-pressure arc lamps delivering about 4 kW power for generating the population inversion in the Nd:YLF-rod. In order to achieve a high output power of the frequency-doubled light for an optimized pumping of the amplifier, this laser delivers pulses at a repetition rate of 1 kHz. For that purpose, the laser is Q-switched by an acousto-optical modulator inside the resonator. Frequency-doubling of the laser light leads to pulse energies up to 23 mJ (typically 20 mJ) at a wavelength of 527 nm and a pulse length of 300 ns. By means of a  $\lambda/4$ -retarder-plate and a polarization beam splitter, the pulse energy is split into two parts for pumping the regenerative amplifier (typically 8.8 mJ) and the double-pass amplifier (typically 10.9 mJ).

The stretched seed pulses are amplified in the regenerative amplifier (see Fig. 3.10) from a pulse energy of approximately 5.5 nJ to 1.8 mJ, i. e. by a factor of  $3 \times 10^5$ . Since a light pulse undergoes an amplification by a factor of approximately 3 per round-trip (which corresponds to passing the pumped Ti:sapphire crystal of the regenerative amplifier twice), the pulse must repeatedly travel through the crystal. Consequently, about 11 round-trips would be necessary to reach the preset amplification. Since the gain coefficient decreases at every transmission through the crystal due to the depletion of the population inversion, about 13 round-trips are needed. This value results from the time the pulse remains in the resonator given by the difference between the switch-in delay (typically 95 ns) and the switch-out delay (typically 212 ns) divided by the cavity round-trip time of 9.2 ns. For the optimization of the beam profile, the passages through the crystal should be collinear. The regenerative amplifier consists of two concave mirrors forming the cavity, two different Pockels cells working in combination with one  $\lambda/4$ -plate as well as with one thin film polarizer for coupling pulses in and out, respectively, and the Ti:sapphire rod cut in the Brewster angle to avoid reflection losses. Actually, this amplifier is tunable from 750 nm to 840 nm limited by the emission spectrum of the Ti:sapphire medium and the bandwidth of the high-reflective dielectric mirrors used, but a high output power can only be reached between 780 nm and 800 nm. The pump beam is collimated by a lens telescope and then focused by a third lens slightly behind the Ti:sapphire rod leading to a circular pump cross section inside the crystal. The vertically polarized stretched seed pulses are reflected into the resonator at the crystal surface of the Ti:sapphire rod. Then a seed pulse travels through the  $\lambda/4$ -plate to the concave mirror M1 and the same way back, the  $\lambda/4$ -plate rotating the polarization direction of the light after two passages by  $90^\circ$ . The now horizontally polarized pulse stay inside the resonator for one round-trip, until the pulse travels two further times through the  $\lambda/4$ -plate rotating the polarization direction once again, the pulse being consequently reflected out

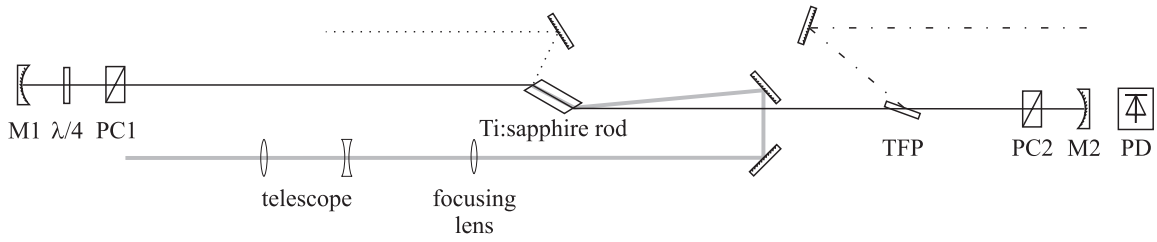


**Figure 3.10:** Setup of the regenerative amplifier (Spectra-Physics Super-Spitfire). The concave mirrors M1 and M2 form the resonator. The pump beam (solid gray line) collimated by a telescope is focused by a lens slightly behind the Ti:sapphire rod. The seed pulses (dotted line) are vertically polarized and therefore reflected into the cavity by the Ti:sapphire rod cut in the Brewster angle and switched in by the Pockels cell PC1 working in combination with a  $\lambda/4$ -plate. The amplified pulses are switched out by a second Pockels cell (PC2) working in combination with a thin film polarizer (TFP) and then travel to the double-pass amplifier (dash-dotted line). By means of the photodiode (PD) behind M2 connected with an oscilloscope (Tektronix TDS220), the pulse train oscillating in the cavity is visualized.

of the resonator at the crystal surface. If a pump pulse is present, the Pockels cell PC1 is switched in a way that it becomes also a  $\lambda/4$ -retarder compensating the effect of the  $\lambda/4$ -plate. Therefore, the horizontally polarized pulse remains inside the resonator for several round-trips being amplified. To reach a maximum pulse energy the pulse is switched out when the amplification is saturated by means of a second Pockels cell rotating the polarization direction of the pulse to the vertical direction so that the light is reflected at the thin film polarizer. In order to achieve a further amplification, the output of the regenerative amplifier is fed into a double-pass amplifier. There the pulses travel twice under slightly different angles through a second pumped Ti:sapphire crystal. The pulse energy increases to about 3.0 mJ after the first passage and to 3.8 mJ after the second transmission. Due to the reflection losses inside the grating compressor of about 40%, the pulse energy of the output beam is only 2.2 mJ at a wavelength of 800 nm. The beam profile is improved by clipping off a diffraction ring before the compressor using an iris diaphragm, and so this energy is further decreased to typically 1.8 mJ at a measured shot-to-shot stability of  $\pm 3.8\%$ . By means of a high-speed silicon photodiode (Melles-Griot, rise time 1 ns) and a digital oscilloscope the laser output is checked for prepulses and afterpulses (see Fig. 3.11). The overshooting signal 30 ns after the actual laser pulse arises from a reflection of the electric signal in the cable, as is easily proved by varying the length of this cable.

From measurements of the fractional power transfer through centered circular apertures of various diameters, the spatial profile and the diameter of a laser beam is determined (see Fig. 3.12) [125]. The beam profile is assumed to be Gaussian, the intensity at a certain point depending on the radial distance  $r$  of this point to the beam axis according to

$$I(r) = I_0 \exp \left[ - (r/r_0)^2 \right] , \quad (3.4)$$

with  $r_0$  the half width at  $1/e$  of the Gaussian-shaped intensity, which is identical to the half width of a uniform cylindrical beam (a “top hat” beam) with the same peak intensity as the cylindrical Gaussian beam. The energy  $E$  transmitted through a circular aperture with the diameter  $R$  is then

$$E(R) = \underbrace{\int_{-\infty}^{\infty} f(t) dt}_{t_{\text{eff}}} \int_0^R 2\pi r I(r) dr \quad (3.5)$$

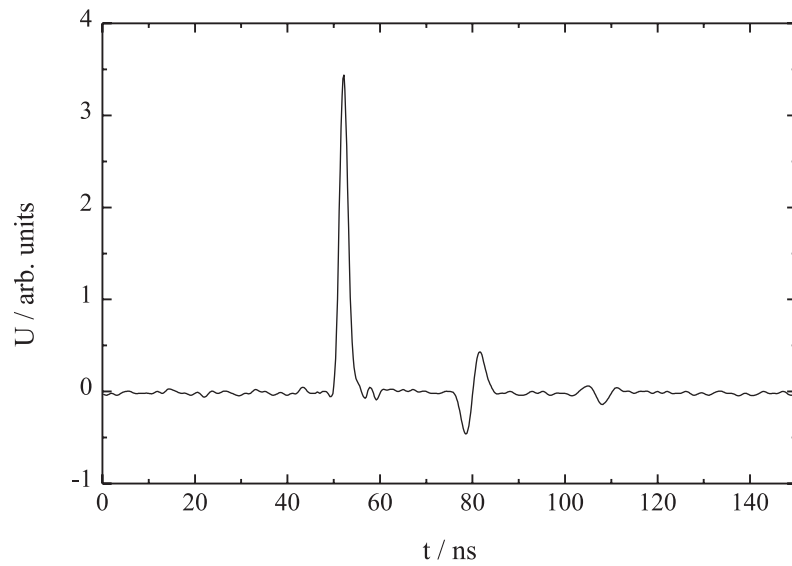


**Figure 3.11:** Laser output measured by a high-speed photodiode. The overshooting signal at 80 ns arises from a reflection of the electric signal in the cable, as is easily proved by varying the length of this cable.

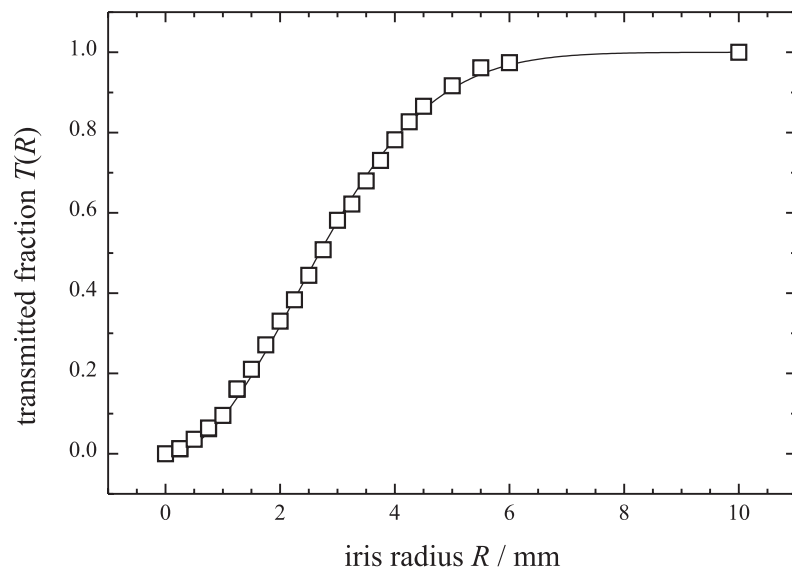


**Figure 3.12:** Determination of the spatial profile and the diameter of the unfocused collinear laser beam via measurement of the fractional power transfer through centered circular apertures of various diameters [125] (squares, measured data; solid line, fit (see Eq. 3.6)).

where  $f(t)$  represents the temporal profile of the pulse. With the limit of the transmitted energy  $E(R \rightarrow \infty) = t_{\text{eff}} I_0 \pi r_0^2$ , the fraction of energy  $T(R)$  transmitted through a circular aperture with the diameter  $R$  can be determined,

$$T(R) = \frac{E(R)}{E(R \rightarrow \infty)} = 1 - \exp[-(R/r_0)^2]. \quad (3.6)$$

From this measurement it is concluded that the spatial profile of the unfocused collinear laser beam has a FWHM diameter of  $d_{\text{FWHM}} = (5.37 \pm 0.02)$  mm. In fact, it is set on the large side to avoid disturbing temperature effects on the compressor grating due to high intensities.

### 3.5.2 Diagnostics for pulse characterization

Besides of the characterization of the laser output as a criterion for the optimization of the alignment, the laser beam parameters are additionally determined directly before the experiment.

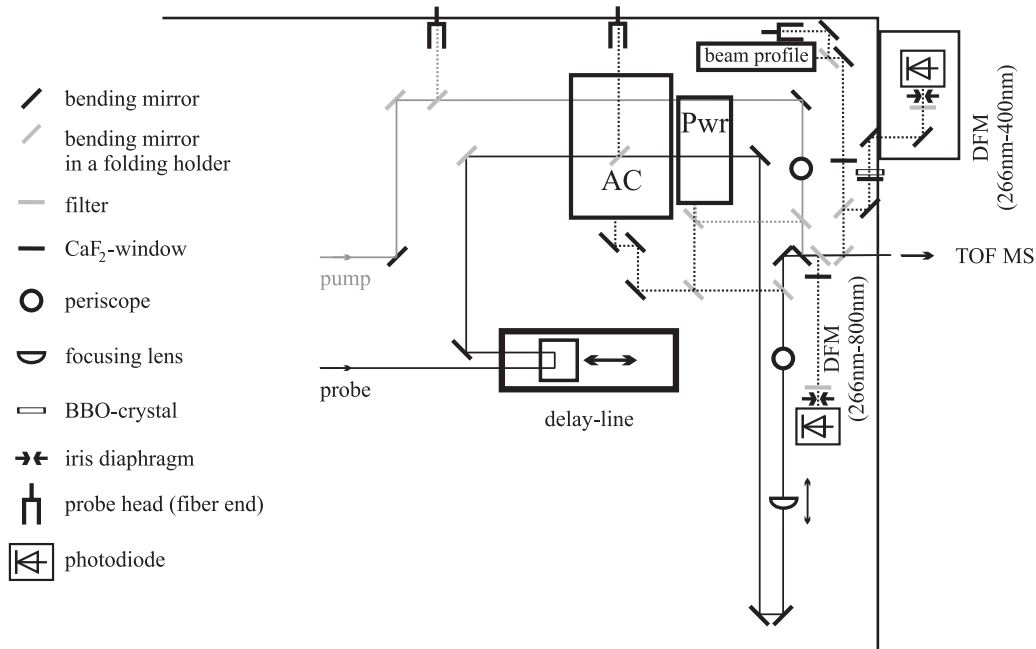


**Figure 3.13:** Diagnostics for pulse characterization directly before the experiment. The dotted lines represent the beam paths to the pulse diagnostics and the solid lines the paths to the experiment. The beam paths consist of two different heights separated by periscopes, 10.7 cm and 23.5 cm above the table. The devices for diagnostics, i. e. the autocorrelator (AC), the power meter (Pwr), the beam profile camera, sometimes the fiber ends of the spectrometer and the two setups for difference-frequency measurement (DFM), after the periscopes are therefore installed on the higher level. At the DFM between 266 nm and 400 nm two dielectric high-reflective mirrors for 800 nm are used in addition to the filter (OG570) for separating the signal from the input. At the DFM between 266 nm and 800 nm suitable filters (4×BG39 and 1×OD0.8) are sufficient. The use of bending mirrors in folding holders makes this setup very flexible.

In every beam path to each device used for diagnostics, the effect of the entrance window of the vacuum system is emulated by using a similar  $\text{CaF}_2$  window ( $d = 2$  mm, optical flat). The frequency spectra at all wavelengths used are measured by a fiber spectrometer (Ocean Optics SD2000), different fibers being employed for the UV (TOP Sensor Systems

FC-UV200-5) and the NIR (TOP Sensor Systems FC-IR200-5), respectively. The spatio-temporal intensity profile in the interaction volume (i. e. at focus) is determined as follows. Pulse energies of all wavelengths used (266 nm, 400 nm and 800 nm) are measured with a laser power meter (Laser Probe, Inc. Rm 6600 universal radiometer). The spatial beam profile at focus is measured by means of a windowless CCD camera (Spiricon Pulnix TM-6CN) which is sensitive in the spectral range from about 200 nm to 1000 nm and positioned in the same distance from the focusing lens as the interaction volume. The profile has an elliptical shape which is Gaussian in each transverse direction  $x$  and  $y$ . The software (Spiricon LBA-PC, version 2.60) allows the determination of the absolute value of the spot size at  $1/e^2$  by the so-called knife-edge technique [126]. An elliptical Gaussian shape can be expressed as

$$G(x, y) = \exp \left[ - \left( \frac{x}{\sigma_x} \right)^2 \right] \cdot \exp \left[ - \left( \frac{y}{\sigma_y} \right)^2 \right], \quad (3.7)$$

where  $\sigma$  denotes the half width at  $1/e$ . The beam cross section  $A_{\text{beam}}$  is then given by

$$A_{\text{beam}} = \int G(x, y) dx dy = \pi \sigma_x \sigma_y. \quad (3.8)$$

The quantity  $A_{\text{beam}}$  can be calculated starting from different full widths (FW) of the Gaussian profile at several clip levels (see Fig. 3.14),

$$\begin{aligned} A_{\text{beam}} &= \frac{\pi}{4} \cdot \text{FW}_{(1/e), x} \cdot \text{FW}_{(1/e), y} \\ &= \frac{\pi}{8} \cdot \text{FW}_{(1/e^2), x} \cdot \text{FW}_{(1/e^2), y} \\ &= \frac{\pi}{4 \ln 2} \cdot \text{FW}_{(1/2), x} \cdot \text{FW}_{(1/2), y} \end{aligned} \quad (3.9)$$

From the measured values  $D_x$  and  $D_y$  the value of  $A_{\text{beam}}$  can be determined by,

$$A_{\text{beam}} = \frac{\pi}{8} \cdot D_x \cdot D_y. \quad (3.10)$$

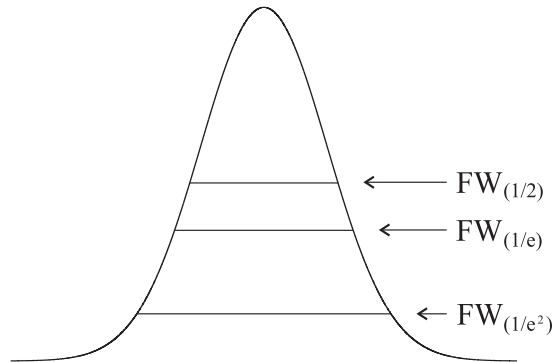


**Figure 3.14:** Illustration of the different clip levels in a Gaussian profile.



The pulse durations at the different wavelengths are ascertained as follows. To determine the temporal FWHM width of 800-nm pulses, autocorrelation measurements using a commercial autocorrelator (APE PulseCheck  $\tau$ 5050) are taken. The temporal profile of the pulses directly before the experiment (after several reflections from dielectric mirrors) is proved to be still Gaussian. The width of pulses in the UV cannot be determined by measuring the autocorrelation function of the frequency-doubled light, because suitable crystals meeting the phase-matching condition for SHG and exhibiting a sufficient transparency at these wavelengths do not exist for such a purpose. The crosscorrelation function is measured instead. For 266-nm pulses, the difference-frequency generation in a nonlinear crystal (BBO, type I,  $5 \times 5 \times 0.06 \text{ mm}^3$ ,  $\theta = 44.3^\circ$ , on 2 mm UVFS plate) between these pulses and the fundamental wavelength is used, resulting in 400-nm light. The temporal width of 400-nm pulses is measured by difference-frequency generation with 266-nm light in a nonlinear crystal (BBO, type I,  $5 \times 5 \times 0.06 \text{ mm}^3$ ,  $\theta = 44.3^\circ$ ,  $\varphi = 90^\circ$ ) leading to 800-nm light. In both cases the motorized, computer-controlled delay-line of the pump-probe setup is used to change the delay between the two colors. To separate the particular difference frequency from the input wavelengths, suitable filters are used before the difference frequency hits a photodiode (Thorlabs, DET210) producing an electric signal dependent on the delay between the two input pulses. This signal is visualized by an oscilloscope (Tektronics TDS220) and then recorded by means of a boxcar amplifier and a computer (for more details see Sec. 3.8.2).

The knowledge of the spatial and temporal profile as well as the energy  $E$  of a pulse allows its intensity to be calculated. The measured pulse energy is the integral over the spatial and temporal intensity distribution of the pulse. Because the spatial and temporal width of a pulse with a non-uniform intensity distribution is strongly dependent on the pulse shape and the point of reference of this shape, it is appropriate to assign the peak intensity  $I_0$ . Then the intensity inside a pulse goes always from 0 to  $I_0$ .

$$I(x, y, t) = I_0 \cdot G(x, y) \cdot F(t) \quad (3.11)$$

$$E = I_0 \cdot \int_{-\infty}^{+\infty} \int_{-\infty}^{+\infty} G(x, y) dx dy \int_{-\infty}^{+\infty} F(t) dt \quad (3.12)$$

If both the spatial and temporal shape are Gaussian, the integrals can be solved easily, giving

$$E = I_0 \cdot \pi^{3/2} \cdot x_{1/e} y_{1/e} t_{1/e}, \quad (3.13)$$

with the half widths at the  $1/e$ -point  $x_{1/e}$ ,  $y_{1/e}$ , and  $t_{1/e}$ . The conversion into half widths at the  $1/e^2$ -point of the intensity which equals to the  $1/e$ -point of the electric field ( $x_{1/e^2}$ ,  $y_{1/e^2}$ , and  $t_{1/e^2}$ ) or at FWHM ( $x_{\text{FWHM}}$ ,  $y_{\text{FWHM}}$ , and  $t_{\text{FWHM}}$ ) changes only the pre-factor,

$$E = I_0 \cdot \left(\frac{\pi}{2}\right)^{3/2} \cdot x_{1/e^2} y_{1/e^2} t_{1/e^2}, \quad (3.14)$$

$$E = I_0 \cdot \left(\frac{\pi}{\ln 2}\right)^{3/2} \cdot x_{\text{FWHM}} y_{\text{FWHM}} t_{\text{FWHM}}. \quad (3.15)$$

The peak intensity can also be seen as the intensity of a (uniform) “top hat” profile corresponding to a Gaussian profile, for example, with both shapes exhibiting the same peak intensity and area. Then the measured energy is related to the peak intensity through

$$E = I_0 \cdot \pi x_{\text{TH}} y_{\text{TH}} \sqrt{\pi} \cdot t_{1/e}, \quad (3.16)$$

with the cross-sectional area of a “top hat” profile  $A_{\text{TH}} = \pi x_{\text{TH}} y_{\text{TH}}$ .

Especially in high-intensity laser chemistry, a precise characterization of laser beams is a *conditio sine qua non* for a proper understanding of the experimental results. Therefore, the laser beams must be carefully and extensively checked for unwanted contributions from nonlinear effects (as expressed by, for instance, the  $B$ -integral [125]). For higher intensities the change of the index of refraction is proportional to the intensity,

$$n(I) = n_0 + \gamma I, \quad (3.17)$$

the proportionality factor thus has the unit  $\text{cm}^2 \text{W}^{-1}$ . In the literature, values for the nonlinear refractive index  $n_2$  are often given in electrostatic units (esu). The conversion into the nonlinear refractive index in units of  $\text{cm}^2 \text{W}^{-1}$  is given by [127,128]

$$\gamma = 4.19169 \cdot 10^{-3} \cdot \frac{n_2[\text{esu}]}{n_0}. \quad (3.18)$$

The linear and nonlinear refractive indices of some optical materials are given in Tab. 3.1, the values being only approximate, because they depend on the wavelength.

**Table 3.1:** Linear and nonlinear refractive indices of some optical materials [129,130].

material	$n_0$	$n_2 / \text{esu}$
air	1.000	$1.5 \times 10^{-16}$
quartz	1.456	$0.99 \times 10^{-13}$
BK7	1.517	$1.46 \times 10^{-13}$
CaF <sub>2</sub>	1.431	$0.65 \times 10^{-13}$

The  $B$ -integral is a measure of the distortions a laser beam with a specific intensity  $I$  undergoes in a nonlinear medium of the thickness  $L$  with a specific nonlinear refractive index  $\gamma$ . This integral is given by

$$B \equiv \frac{2\pi}{\lambda} \int_0^L \gamma I(z) dz. \quad (3.19)$$

In case of an experiment where the laser beam travels through different optical materials with different thicknesses, the total  $B$ -integral is additively composed of the single  $B$ -integrals, because the nonlinear contributions accumulate. According to Siegman [125] the cumulative  $B$ -integral should be kept below 3 to 5 “to avoid serious nonlinear damage and distortion effects due to either self-phase modulation or self-focusing.”

### 3.5.3 Optical setup for pump-probe measurements

In the following passage, the optical setup for the preparation of the pump and the probe pulses is described (see Fig. 3.15). Because the trigger signal from the Pockels cell driver of the laser system is affected by an electro-magnetic pickup from external devices leading to an unacceptably large jitter of the measured signal, a photodiode (Thorlabs DET210; filter, BG4) illuminated by scattered light is used as the trigger source. To achieve better mechanical stability, all optical parts that influence the direction or position of the beam are based on special pillars ( $\varnothing$  25.4 mm) made of stainless steel. Additionally, the beam height of the laser output is changed from originally 15.0 cm to 10.7 cm above the laser table. The periscope employed for that purpose is positioned between the two bending mirrors used to define the main axis of the beam independently of the original direction of the laser output. Then the beam is divided by means of a dielectric beam splitter into two parts in

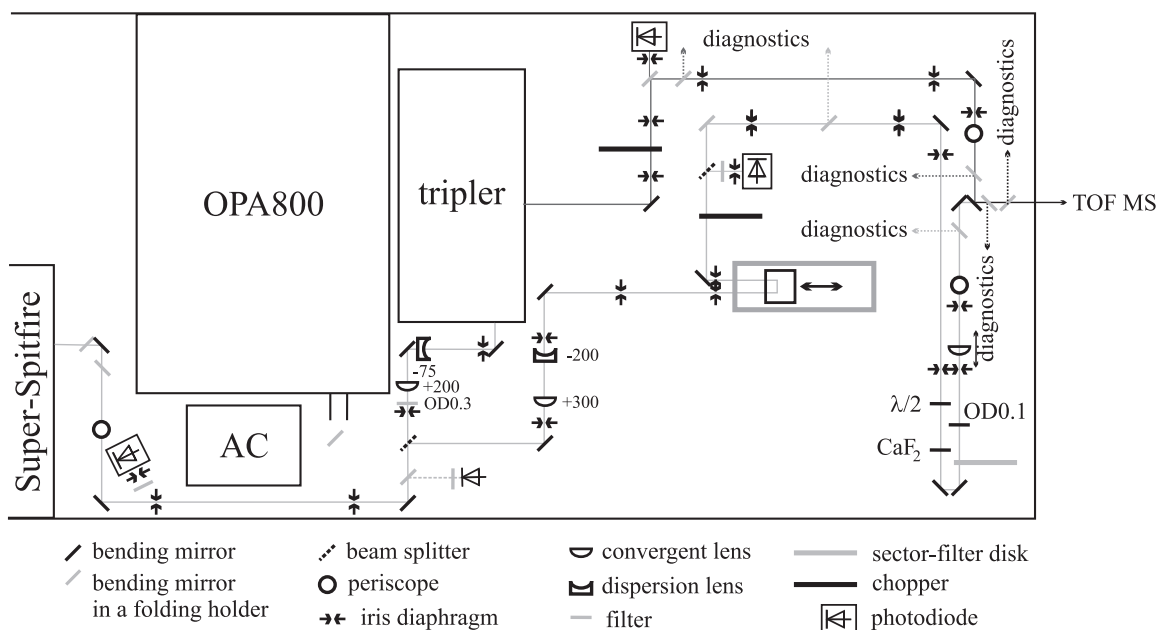


**Figure 3.15:** Optical setup for pump-probe measurements.

a 60:40 ratio for the pump and the probe pulse, respectively. On the one hand, this 60:40 ratio takes into account that energy losses occur during the frequency conversion processes to achieve the pump wavelength of 266 nm. On the other hand, several probe photons containing less energy than pump photons must be absorbed to ionize a molecule, even if it is already in the excited state. After the beam splitter, the diameter of the pump beam is decreased by a factor of 2.67 by means of a telescope consisting of a plano-convex and a plano-concave quartz lens ( $f = 200$  mm and  $f = -75$  mm) to optimize the efficiency of the frequency-tripling. The homebuilt tripler used here is designed as follows. The sufficiently intense input beam is first deflected by two dielectric mirrors in zig-zag configuration to allow alignment through two pinholes independent of the position or direction of the input beam. Then the second harmonic of the 800-nm pump light is generated and subsequently, in a second process via sum-frequency generation with the fundamental wavelength, converted to 266-nm light. The nonlinear crystals used for the two frequency conversion processes consist of BBO and are only 0.2 mm thick to avoid a pulse lengthening due to dispersion effects. For type I phase-matching they are cut to  $\theta = 29.2^\circ$  (for SHG@800nm) and to  $\theta = 44.2^\circ$  (for SFG@800nm+400nm), respectively, for a perpendicular incidence. After the SHG-crystal, the 400-nm light is separated from the unconverted 800-nm light by means of a 2-mm-thick dichroic mirror. Since the polarization direction of the fundamental beam is parallel to the laser table, the second harmonic is polarized vertically to the laser table. However, the same polarization direction of the two beams is required for the type I mixing process in the SFG-crystal (see Sec. 3.2). Because dispersion effects are smaller at longer wavelengths, the polarization direction of the unconverted 800-nm light is rotated by  $90^\circ$  by means of an anti-reflection-coated  $\lambda/2$ -plate (Halle, low order). Rotating it by an angle  $\alpha \neq 90^\circ$  is exploited to attenuate the 266-nm light suitably. With the translational stage in the 800-nm path, the temporal walk-off between the fundamental and the second harmonic can be compensated. The two beams with different wavelengths are merged by means of a second 2-mm-thick dichroic mirror, to achieve the spatial overlap inside the SFG-crystal. In order to separate the 266-nm light from the unconverted 800-nm and 400-nm light, two dichroic

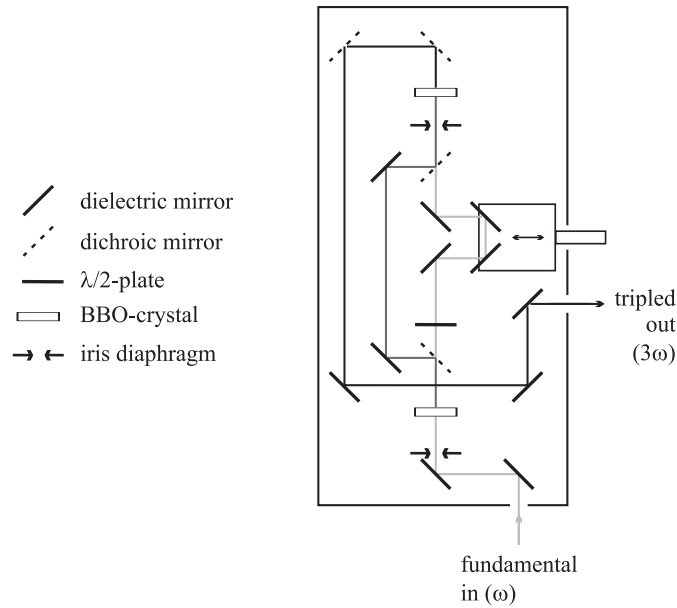


**Figure 3.16:** Setup of the homebuilt frequency tripler. For a detailed description of the beam path see text.

mirrors that are high-reflective for 266 nm and high-transmitting for 800 nm and 400 nm are used. At a pump energy of  $580 \mu\text{J}$  and a pulse length of 70 fs the SFG-efficiency amounts to  $\sim 12\%$  corresponding to  $70 \mu\text{J}$  pulse energy in the UV measured at the experiment (after nine reflections from dielectric mirrors). With these input parameters the SHG-efficiency amounts to 30%. Even higher values are achievable, but are connected with a spectral cutoff. The pulse length is determined as described in Sec. 3.5.2 and amounts typically to  $\sim 90$  fs (also after nine reflections from dielectric mirrors).

Because the cross section of the unfocused laser output beam is so large ( $d_{\text{FWHM}} = (5.37 \pm 0.02) \text{ mm}$ ) (see Sec. 3.5.1), the size of the probe beam has to be reduced, too, to avoid clipping of the beam by the chopper, which would cause distortions by diffraction. For this, a telescope consisting of a plano-convex and a plano-concave lens ( $f = 300 \text{ mm}$ , BK7, and  $f = -200 \text{ mm}$ , fused silica) is used. The collinear probe beam then travels through a variable delay-line consisting of a delay-line driven by a stepper-motor (PI M-510.10) and a hollow retro-reflector (Melles-Griot, beam deviation 1 arc s, wavefront distortion  $\lambda/6$ ). This retro-reflector is installed on two translational stages (Newport M-UMR8.25) to allow alignment in all directions. Due to the rather large weight of this flexible setup, the stepper relaxation time (time after stopping the movement and before starting the measurement) has to be carefully adjusted to avoid a disturbance of the signal by a laterally oscillating beam. Two iris diaphragms guarantee that the beam hits the retro-reflector exactly in the direction of the translation of the delay-line to avoid a ray-offset during the motion. The beam deviation is determined to be  $\sim 1 \text{ mm}$  at a distance of  $\sim 5 \text{ m}$  from the retro-reflector, moved over the whole shifting distance of the delay-line (100 mm), and is negligible compared to the beam diameters used in the interaction volume. The next devices in the two beam paths are the light choppers which are used in the same way as described in Sec. 3.4.2. In the probe path, a wedged ( $30^\circ$ ) quartz plate used as a beam splitter is positioned after the chopper to supply a reflex after further attenuation by suitable filters ( $2 \times \text{UG11}$ ) to a photodiode (Thorlabs DET110). To avoid an unnecessary distortion of the 266-nm pulses by the transmission through quartz glass due to the high dispersion at short wavelengths, in this case the light

transmitted through a dielectric mirror is used without further attenuation to illuminate a photodiode (Thorlabs DET110). The photodiode signals are treated analogously as portrayed in Sec. 3.4.2. Also in this final setup, the angle between the two linearly polarized beams is adjusted to the magic angle (see Sec. 3.4.2), but in contrast to the initial setup, the  $\lambda/2$ -plate is positioned in the probe beam, because the dispersion is smaller at longer wavelengths. A variable sector-filter disk is placed after the  $\lambda/2$ -plate to allow stepwise attenuation of the unfocused probe beam without changing other pulse parameters (see Sec. 3.5.4). To achieve a sufficiently high intensity in the vacuum system, the probe beam is focused by a plano-convex quartz lens with a focal length of  $f_{\text{probe}} = 1000$  mm. To align the focus to the axis of the TOF spectrometer, the yield of the parent ion of the substance to be investigated is maximized by moving the position of the focusing lens. Due to the high efficiency of the frequency tripler of 12% (see above), and because only a single-photon absorption is desired, the pump light is intense enough to be used without focusing. If required, the probe wavelength can be changed from 800 nm to 400 nm by means of a frequency-doubling crystal (BBO, type I,  $10 \times 10 \times 0.2$  mm<sup>3</sup>,  $\theta = 29^\circ$ ,  $\varphi = 90^\circ$ ) positioned  $\sim 240$  mm behind the focusing lens. To eliminate the unconverted 800-nm light, a filter (BG39) is placed in the beam path directly behind the crystal. Because the polarization direction of the beam is rotated by  $90^\circ$  during the SHG, the  $\lambda/2$ -plate has to be rotated by  $45^\circ$  to revert to the magic angle conditions for the relative polarization (see Sec. 3.4.2). The last two mirrors in each beam path are used to align both beams exactly through the center of both the entrance and the exit window of the vacuum system. In this way, position and direction of both the pump and the probe beam are roughly adjusted; in the experiment, these directions and positions are optimized using the ion signal. Then the pump pulse and the probe pulse, which originally evolved from one single pulse, but then are separated to be prepared in different beam paths in the way described above, are merged again by means of a dichroic mirror. To synchronize the beams, the probe beam path contain an additional distance to compensate for the longer beam path of the pump pulses required for frequency tripling. By means of a high-speed silicon photodiode (Melles-Griot, rise time 1 ns) connected to a large-bandwidth oscilloscope (LeCroy LC564A, 1 GHz), the time delay between the both pulses are pre-adjusted. Exact synchronization of the two pulses is achieved by evaluating a difference-frequency signal (see Sec. 3.5.2).

The length of the beam path from the compressor grating to the interaction volume is a compromise between flexibility regarding other experiments and shortness, the length amounting to  $\sim 6.9$  m. Much attention is paid to the possible role of nonlinear effects, such as self-focusing or self-phase modulation, that may be induced by nonlinear behavior of the optical materials the beam traverses due to the rather high intensities of the laser beams. Accordingly, the number of optical elements the beam passes through is kept as low as possible. The distance between the entrance window of the vacuum system and the interaction volume of  $\sim 280$  mm allows the probe beam to be focused by a lens with a rather long focal length ( $f_{\text{probe}} = 1000$  mm) and a sufficiently small pulse energy without considerable nonlinear effects inside this window. The CaF<sub>2</sub> window is exposed to peak intensities of  $5.7 \times 10^8$  W cm<sup>-2</sup> for the (unfocused) pump beam and  $1.9 \times 10^{11}$  W cm<sup>-2</sup> for the probe light. Although CaF<sub>2</sub> is a favorable medium for white-light continuum generation accompanied by self-focusing due to its large bandgap [124], it could be shown that the laser pulses remained essentially unaltered at these intensities. With typical peak intensities ( $4.2 \times 10^{10}$  W cm<sup>-2</sup> for the unfocused beam after the compressor,  $2.1 \times 10^{10}$  W cm<sup>-2</sup> for the fraction of the pump light between the beam splitter and the telescope,  $7.7 \times 10^{10}$  W cm<sup>-2</sup> for the pump light between the telescope and the SFG crystal,  $5.7 \times 10^8$  W cm<sup>-2</sup> for the

266-nm-light to the entrance window,  $1.4 \times 10^{10} \text{ W cm}^{-2}$  for the fraction of the probe light between the beam splitter and the telescope,  $2.4 \times 10^{10} \text{ W cm}^{-2}$  for the probe light between the telescope and the attenuator, and  $1.5 \times 10^{10} \text{ W cm}^{-2}$  for the probe light between the attenuator and the focusing lens), the cumulative  $B$ -integrals (see Sec. 3.4.2) of the pump and the probe light, respectively, are calculated to be 1.1 and 2.0, respectively, which is significantly below the widely accepted limit of 3 to 5 (see Ref. [125]). The absence of nonlinear distortions of the beams is verified by measurements of the temporal autocorrelation and of the cross-correlation function and the frequency spectra of the pulses after their passage through the entrance window of the vacuum system. As will be described in Sec. 4.2.1, indications are also found that the onset of continuum generation is accompanied by an increased fragmentation of gaseous toluene. This phenomenon is used to ascertain operation outside nonlinear conditions.

### 3.5.4 Optical setup for photoionization and photofragmentation measurements

#### 3.5.4.1 Experiments without nonlinear distortions of the laser beam

For ionization measurements carried out at the fundamental wavelength (800 nm), all available power is needed. In order to give the chance to use the experiment described in this section beside from the probe beam path (see Sec. 3.5.3) without big changes, as many optical elements of the probe beam path as possible are exploited. Therefore, the laser beam is deflected by a dielectric mirror in a folding holder directly before the beam splitter to another direction and is brought in line with the probe beam path again before the sector-filter disk. The different sectors of this 2-mm-thick quartz disk have metal coatings of various

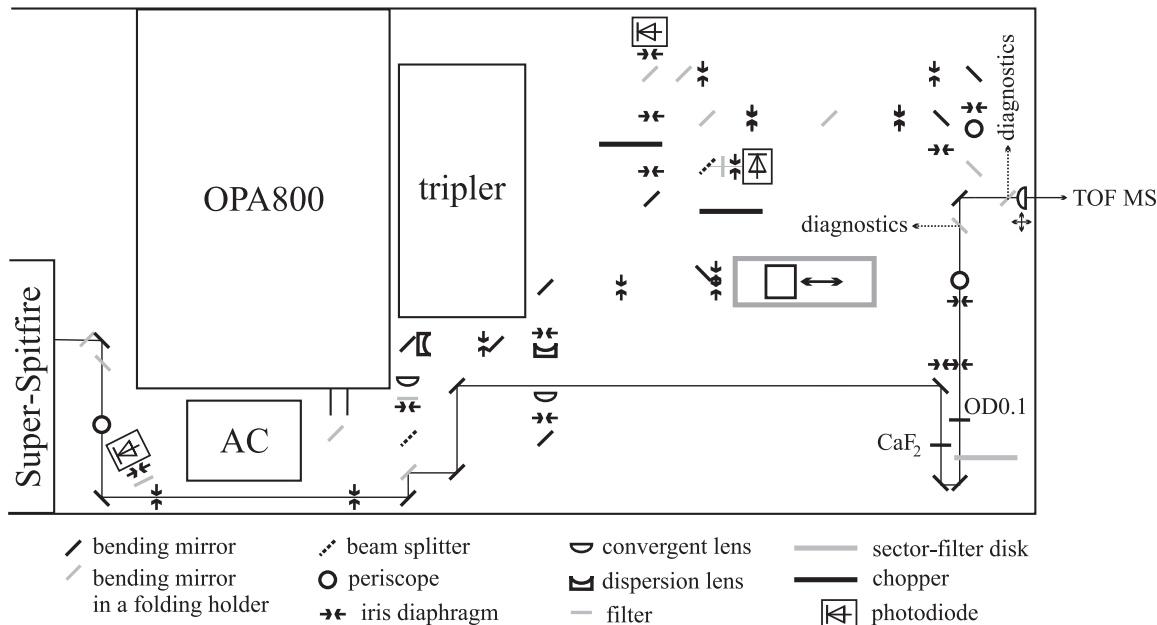


**Figure 3.17:** Illustration of the optical setup for photoionization and photofragmentation measurements. This beam path can be used on the side of the pump-probe experiment without big changes.

thicknesses, which allow the intensity to be reduced in steps of  $\sim 63\%$  (OD0.2). To bridge the gap between these steps, a 1.1-mm-thick Corning 7059 metal-coated neutral density filter

with a  $\sim 79\%$  transmission (New Focus, OD0.1) and a 2-mm-thick  $\text{CaF}_2$  optical flat with a  $\sim 92\%$  transmission are used in addition. The focusing lens of the probe beam path is removed. Instead of this, a plano-convex uncoated BK7-lens with a nominal focal length of  $f = 500$  mm is used to focus the laser beam. For cross-check experiments, two other plano-convex uncoated lenses are also used (nominal focal lengths,  $f = 300$  mm, BK7, and  $f = 1000$  mm, fused silica). With the beam diagnostics described in Sec. 3.5.2, the temporal and the spatial profile and the power of the pulses is measured. The autocorrelation measurements show that the temporal profile of the pulses directly before the focusing lens (after ten reflections from dielectric mirrors) have a Gaussian shape with a FWHM duration of  $t_{\text{FWHM}} = (81 \pm 1)$  fs. The spatial profile measured with a CCD camera is again Gaussian. With the diameter of the unfocused beam (see Sec. 3.5.1) the spatio-temporal variation of the intensity in the unfocused beam is given by

$$I(r, t) = I_0 \exp \left[ - \left( \frac{r}{r_0} \right)^2 \right] \exp \left[ - \left( \frac{t}{t_0} \right)^2 \right], \quad (3.20)$$

with  $r_0 = (3.23 \pm 0.01)$  mm and  $t_0 = (48.6 \pm 0.6)$  fs. For the highest pulse energy of 1.2 mJ used in these experiments, the peak intensity in the unfocused beam is then  $I_0 = 4.2 \times 10^{10}$  W cm $^{-2}$ . The focusing can be calculated using the *ABCD*-law for Gaussian beams [131], leading to the following expression

$$\frac{w_3}{w_1} = \frac{f/z_1}{\sqrt{1 + (f/z_1)^2}}, \quad (3.21)$$

with  $w_3$  being half the 1/e-width of the spatial intensity profile of the focused laser beam,  $w_1 = 3.23$  mm half the 1/e-width of the spatial intensity profile of the unfocused laser beam (see Sec. 3.5.1),  $f$  the focal length, and  $z_1$  the Rayleigh length of the unfocused beam. The Rayleigh length of a beam is given by

$$z_1 = \frac{\pi w_1^2 n}{\lambda}, \quad (3.22)$$

with the refractive index  $n$  and the wavelength  $\lambda$ . The Rayleigh length of the unfocused beam is correspondingly  $\sim 41$  m, proving it to be parallel. Typical measured and calculated FWHM diameters as well as Rayleigh lengths at focus for the three lenses used are given in Tab. 3.2. Under the assumption that the divergence of the beam at focus is  $< 1.5$ -times the diffraction

**Table 3.2:** Typical calculated and measured FWHM diameters as well as Rayleigh lengths at focus dependent on the focal lengths of the lenses used. The quantity  $d_{\text{FWHM,calc}}$  is the calculated FWHM diameter at TDL = 1 and the quantity  $d'_{\text{FWHM,calc}}$  is the one at TDL = 1.5. The number marked with an asterisk is less than the calculated diffraction limit. The reason for this unusual behavior is probably self-focusing in air and the entrance window of the vacuum system, leading to a decreased focal length and thus to a focal size smaller than expected.

$f/\text{mm}$	$w_3/\mu\text{m}$	$z_3/\text{mm}$	$d_{\text{FWHM,calc}}/\mu\text{m}$	$d'_{\text{FWHM,calc}}/\mu\text{m}$	$d_{\text{FWHM,measured}}/\mu\text{m}$
300	24	2.26	40	$< 60$	50.0
500	39	5.97	65	$< 98$	70.2
1000	79	24.5	131	$< 197$	101.9*

limit, the measured values are in agreement with the calculations, with the exception of the value measured with a 1000-mm lens, which is less than the calculated diffraction limit. This anomalous fact is probably caused by self-focusing in air and the entrance window of the

vacuum system, leading to a decreased focal length and thus to a focal size smaller than expected.

The entrance window of the vacuum system is a 2-mm-thick  $\text{CaF}_2$  optical flat positioned  $\sim 280$  mm from the focus. To align the focus to the axis of the TOF spectrometer, the yield of the parent ion of toluene is maximized by moving the position of the focusing lens. Ion yields are measured for both linear and circular polarization. To change the polarization of the beam, a zero-order air-spaced quarter-wave plate is used (Halle, RZQ4.15), with its fast axis either parallel to the linear polarization of the laser beam or at  $45^\circ$ . The correctness of the polarization direction is checked by means of a Glan polarizing prism. The linear polarization is perpendicular to the spectrometer axis. This direction is chosen because it allows the use of one and the same quarter-wave plate to change the polarization. Additional experiments with a half-wave plate to make the linear polarization parallel to the spectrometer axis are performed, to prove that choosing the linear polarization parallel or perpendicular to the spectrometer axis does not affect the results.

An important aspect of this setup is the possible influence of nonlinear effects on the results caused by exposing optical materials to too high intensities. However, even for the highest unfocused peak intensity  $I_0 = 4.2 \times 10^{10} \text{ W cm}^{-2}$  used here, the cumulative  $B$ -integral (see Sec. 3.4.2) in this setup for air plus optics amounts to 1.7 at most. Since this is much below the widely accepted critical limit of 3 to 5 (see Ref. [125]), nonlinear effects are not expected to have any influence. Then, large bandgap materials like  $\text{CaF}_2$  exposed to high intensities can cause self-focusing accompanied by coherent white-light continuum generation [124]. The peak intensity to which the  $\text{CaF}_2$  window is exposed amounts to at most  $\sim 7 \times 10^{10} \text{ W cm}^{-2}$  which is low enough to leave the used 800-nm pulses unchanged. Measurements of the temporal autocorrelation function and the frequency spectrum of the pulse after its passage through the entrance window of the vacuum system show that the laser pulse does remain essentially unaltered, which verifies the expectations.

### 3.5.4.2 Setup for the investigation of effects induced by continuum generation

In principle the same experimental setup (reported in detail in Sec. 3.5.4.1) as for ionization measurements without nonlinear distortions of the laser beam is used. Here, the special features required for the generation and investigation of white-light effects are described. The experimental arrangement is schematically depicted in Fig. 3.18. The peak intensities

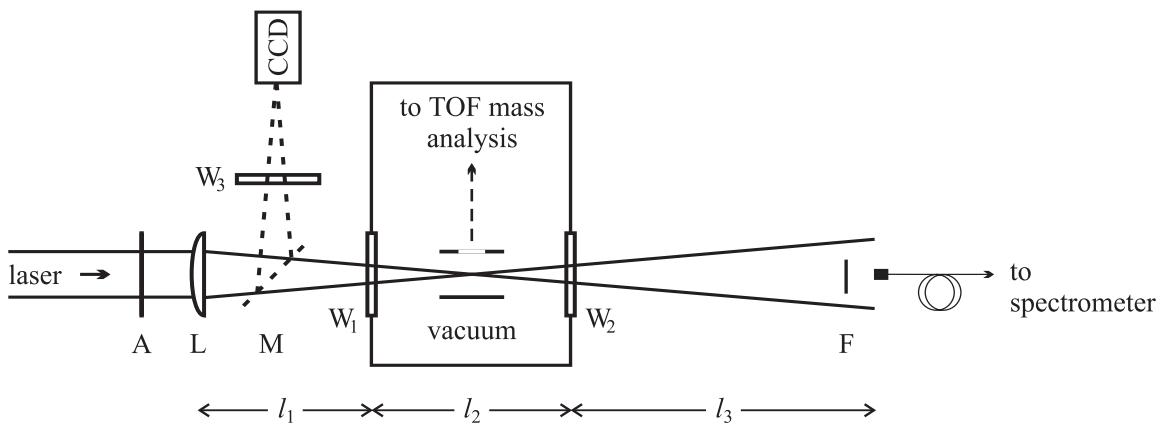


**Figure 3.18:** Setup for the investigation of effects induced by continuum generation. For a detailed description of the time-of-flight (TOF) mass spectrometer see Sec. 3.7.

are calculated from measurements of the autocorrelation function, the energy of the pulses



as well as of the spatial profile of the laser beam at focus, too. Stepwise attenuation is achieved by means of a 2-mm-thick sector-filter disk made of quartz with metal coatings of various thicknesses (A in Fig. 3.18) combined with a 1.1-mm-thick neutral density filter and a 2-mm-thick CaF<sub>2</sub> optical flat. A plano-convex uncoated quartz lens (L in Fig. 3.18) with a nominal focal length of  $f = 1000$  mm is used to focus the laser beam, which passes through the entrance window (W<sub>1</sub> in Fig. 3.18) consisting of a 2-mm-thick CaF<sub>2</sub> optical flat of the TOF mass spectrometer after a distance  $l_1 = 720$  mm. The focus is centered with respect to the entrance and exit window inside the evacuated mass spectrometer, at a distance of  $\sim 280$  mm from W<sub>1</sub>. The beam leaves the vacuum chamber through the exit window (W<sub>2</sub> in Fig. 3.18). Due to the divergence, only a fraction passes through selected filters (F, BG18 or BG39 or three neutral density filters (ND3.0+OD2.0+OD1.0)) positioned at the distance  $l_3 \sim 1100$  mm behind W<sub>2</sub>. This is necessary to avoid an additional continuum generation inside the filters or even damage that would occur placing them too close to the focus. The frequency spectrum is recorded by a fiber spectrometer (Ocean Optics SD2000) sampling over 1000 scans. With the focal length, the distances, and the intensities given above the actual intensities of the laser beam in the CaF<sub>2</sub> entrance window of the vacuum system, contributing most to nonlinearities in the beam, can be calculated.

### 3.6 Time-of-flight mass spectrometer for initial experiments

For the investigation of the photoreactions in the gas phase, a simple Wiley-McLaren time-of-flight (TOF) mass spectrometer [104,132] is used. The design, characterization, and electronic circuitry of the TOF mass spectrometer are described in this section.

The TOF mass spectrometer works as follows. The cations generated by the laser in the interaction zone are accelerated by an electric field before they drift in a straight line, i. e. linearly, through a field-free flight tube, being recorded by a special detector after a certain distance. The spectrometer axis is perpendicular to the propagation direction of the two collinear laser beams. The entrance window of the vacuum system is a 2-mm-thick CaF<sub>2</sub> optical flat positioned  $\sim 130$  mm from the interaction zone. A section of this spectrometer is given in Fig. 3.19. The system can also be used as a photoelectron spectrometer [132]. For this reason the  $\mu$ -metal magnetic shielding and an additional grid (G<sub>3</sub>, see below) are present. The time of flight from the interaction zone to the detector is proportional to  $\sqrt{M/q}$ , with the dimensionless mass of the ion  $M = m/u$  where  $u$  is the atomic mass unit, and the charge number  $q$ . Consequently, a mass spectrum can be derived from the distribution of the different arrival times of the ions at the detector,

$$t = t_0 + k\sqrt{M/q}. \quad (3.23)$$

where an offset time  $t_0$  has been introduced to take into account the time difference between the arrival of the light pulse in the interaction region and the detection of the trigger pulse at the oscilloscope or fast multiscaler (see Sec. 3.8). Compared to the distribution of the different arrival times, the thermal energy distribution ( $\sim 25$  meV at 300 K) is negligible. Equation 3.23 contains two variables that depend nonlinearly on each other. Therefore, in general, the Jacobian matrix would be required to transform functions of these variables into each other. In this special case, however, the recorded TOF spectra consist of discrete peaks, and the area under a given peak can be calculated by summation of all signal contributions

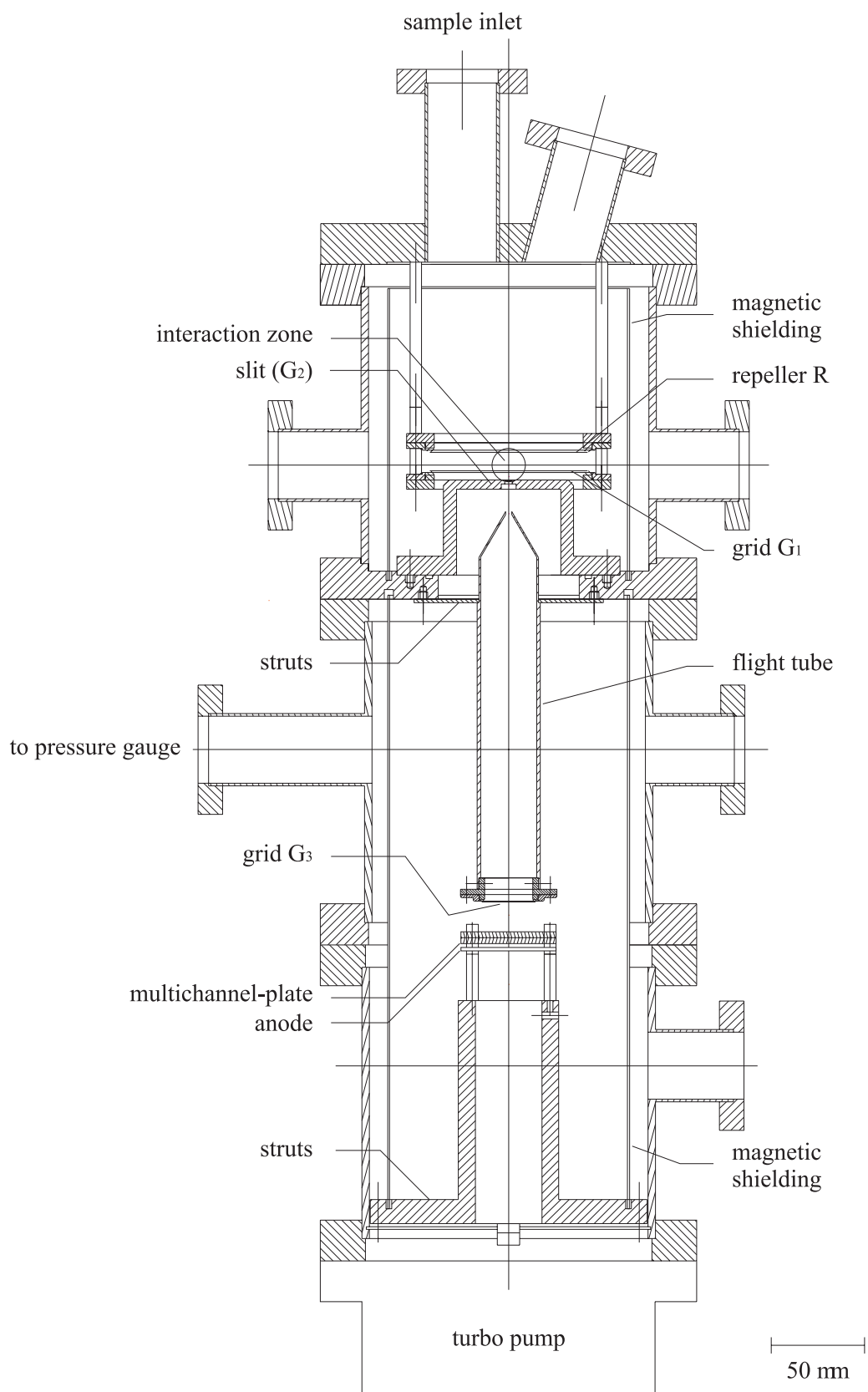


**Figure 3.19:** Design of the TOF mass spectrometer for initial experiments. The plane of drawing is a section perpendicular to the propagation direction of the laser beams.

in the time window of the peak, and doing so, the peak area is not affected by the conversion of the time of flight into the mass.

The TOF spectrometer consists of two vacuum chambers. The upper chamber is the interaction chamber: this is where the molecules under investigation are irradiated by the pump pulse, undergo subsequent reaction, and are then ionized by the probe pulse. A schematic drawing of this spectrometer is shown in Fig. 3.20. After being produced in the

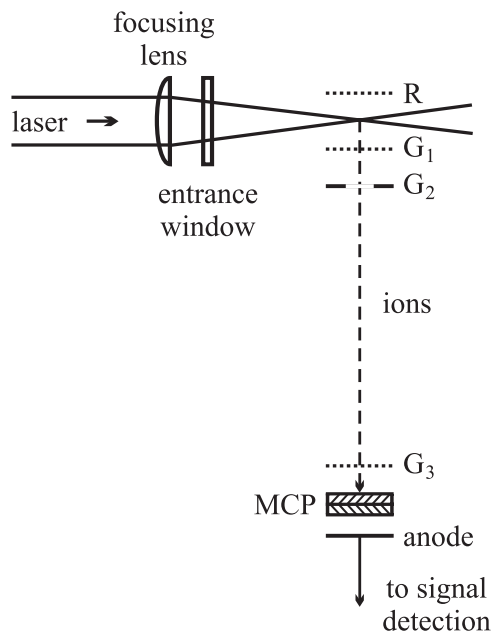


**Figure 3.20:** Schematic view of the time-of-flight spectrometer. Spatial focusing is achieved by means of the repeller R and the two grids G<sub>1</sub> and G<sub>2</sub>. The grid G<sub>3</sub> shields the field-free drift region from the electric field of the double-stage multichannel-plate (MCP).

focus of the probe laser beam, the ions pass through two acceleration sectors (distances between repeller R and first grid G<sub>1</sub>, 10 mm; between R and the center of the interaction zone, 7 mm; between G<sub>1</sub> and G<sub>2</sub>, 5 mm) to be spatially focused. The last electrode of the second acceleration stage consists of a solid plate in which a rectangular slit is present with dimensions  $31 \times 0.5 \text{ mm}^2$ , its longer dimension parallel to the propagation direction of the laser beams. Due to the small width of the slit, a fraction of the produced ions may be cut off making the spatial alignment of the two laser beams very critical. However, the dimension of the slit in the propagation direction of the laser is much larger than the Rayleigh lengths (see Eq. 3.22) of the pump and the probe beam which are  $\sim 8 \text{ mm}$  and  $\sim 11 \text{ mm}$ , respectively, with an estimated FWHM diameter of the unfocused beam of  $\sim 4 \text{ mm}$ , causing a volume effect in this direction. After passing through the slit, the ions enter a field-free drift region (distance between G<sub>2</sub> and G<sub>3</sub>,  $\sim 250 \text{ mm}$ ) located in the lower vacuum chamber (detection chamber). Typical operating voltages are 2800 V for R and 2185 V for G<sub>1</sub>. The electrodes G<sub>2</sub> and G<sub>3</sub> are always kept at ground potential. The grid G<sub>3</sub> shields the field-free drift region from the electric field of the double-stage multichannel-plate (MCP, Galileo, type chevron, detection quality). Finally, the ions impinge on the MCP operated at typically 2.1 kV for cation detection. The operational principle of an MCP corresponds approximately to that of a photomultiplier. Instead of single dynodes, here a multitude of fine channels through a substrate plate are used, each of them acting as a secondary emission multiplier. These channels have a length which is many times larger than their diameter and, in addition, they are tilted against the surface normal causing several collisions of an arriving charged

particle after its penetrating into one of the channels. This collision leads to the generation of secondary electrons. The entrance and the exit surfaces of the MCP are coated with a conducting material making it possible to apply a high voltage (typical 1.2 kV/plate). The achievable signal enhancement per plate amounts to  $\sim 10^4$ , which can be increased to  $\sim 10^6$  by the combination of two plates, leading to an electric charge detectable by the sensitive electronics. In the latter case, the entire amplification is not the product of the single amplifications due to saturation effects. For a detailed description of the operational mode of multichannel-plates see e. g. Ref. [133]. The distance between grid  $G_3$  and front face of the MCP amounts to  $\sim 16$  mm. The mass resolution achieved with this setup amounts to  $M/\Delta M \sim 100$  and is sufficient to separate the mass signals of the parent and the fragment ions even for medium-sized organic molecules.

The separation of the vacuum system into interaction and detection chamber by the slit makes it possible to maintain different pressures inside the two chambers using only one turbo pump (Balzers TPU450H, 450 l/s). The pressure in the detection chamber is limited to a maximum of  $10^{-6}$  mbar, given by the operation conditions of the MCP declared by the manufacturer. In the upper chamber a higher pressure is used simultaneously, to achieve a sufficiently large signal which, under collisionless conditions, is proportional to the partial pressure of the investigated substance in the interaction chamber. The gaseous substances are admitted to the upper vacuum chamber by means of a variable leak connected to a flask containing the liquid (or solid) substance and its saturated vapor at room temperature. For less volatile substances, the whole vacuum system can be heated up to  $\sim 393$  K. This feature also allows the system to be cleaned. The pressure is measured in the lower chamber only by means of a Bayard-Alpert gauge which leads to uncertainties regarding the pressure in the interaction chamber. Since the flight tube and the magnetic shielding are installed concentrically around the drift region, the pressure region under interest is almost "sealed" from this gauge. Consequently, the indicated value is probably lower than the actual target pressure. Additionally, the equilibrium between the pressure inside the flight tube and the pressure at the gauge only becomes established after several minutes. Only a rough pressure ratio of the upper to the lower chamber amounting to approximately 200 can be given [132]. For those reasons, the actual pressure in the interaction chamber can only be roughly estimated. With the pressures measured by the Bayard-Alpert gauge which are in the region of  $\sim 2 \times 10^{-8}$  mbar to  $\sim 9 \times 10^{-8}$  mbar and the pressure ratio given in Ref. [132], the pressures in the interaction chamber amount to between  $\sim 4 \times 10^{-6}$  mbar and  $\sim 2 \times 10^{-5}$  mbar.

Because both mass and photoelectrons can be measured in the spectrometer, the following features have to be realized which are actually not necessary for a pure mass spectrometer. The front face of the MCP is kept at  $\sim +200$  V required for the pre-acceleration of photoelectrons. This decreases the kinetic energy of cations only slightly. Consequently, the anode has to be at a more positive potential (typical  $\sim +2.8$  kV). Then the anode has to be connected to the signal output by means of a special coupling capacitor. Special diodes protect the connected measurement instruments against overvoltage spikes. However, for cations this is not necessary because the front face of the MCP can be attached to a negative potential making it possible to keep the anode at ground potential (see Sec. 3.7). This setup produces overshooting signals due to the impedance mismatch of the anode with the connection cables. The circuit containing the coupling capacitor increases this disturbance effect additionally. These overshooting signals hamper the evaluation of heavier isotopic variants of strong mass peaks, which would have been useful for the exclusion of saturation effects.

### 3.7 Time-of-flight mass spectrometer for final experiments

Also here a Wiley-McLaren time-of-flight (TOF) mass spectrometer [104] is used to investigate molecules in the gas phase. For this purpose, a TOF mass spectrometer under construction was adapted and modified to achieve an improved experimental performance. In this section, the design, dispersion relation, and electronic circuitry of this mass spectrometer are described.

The cations generated in the laser focus centered between the entrance and the exit window of the vacuum system are accelerated by an electric field to achieve spatial focusing. Then they pass a field-free drift region, and are recorded by an MCP after a certain distance. The measured time of flight  $t$  is then related to the mass of the ions  $M = m/u$  by  $t = t_0 + k\sqrt{M/q}$  (see Sec. 3.6). The spectrometer axis is perpendicular to the propagation direction of the laser. The entrance and the exit window of the vacuum system is a 2-mm-thick CaF<sub>2</sub> optical flat positioned  $\sim 280$  mm from the focus. The TOF spectrometer is depicted in Fig. 3.21. The system is designed as a molecular beam machine combined with a mass analysis. Therefore, the MCP is tilted by a small angle ( $(0.8 \pm 0.5)^\circ$ ) toward the direction of the molecular beam against the spectrometer axis to compensate for the transverse velocity of the molecules. In the present work, however, the TOF mass spectrometer is used with a static gas pressure. Therefore, a gas inlet system is designed and installed which allows the evacuation of the sample separate from the upper vacuum chamber to remove unwanted gas such as air from the non-evacuated sample flask by means of a auxiliary turbo pump (Pfeiffer TMU022, 22 l/s).

In the following, the mode of operation of this TOF mass spectrometer is described in detail. The abbreviations used apply to Fig. 3.20. After their creation in the focus of the probe laser beam, the ions pass through a two-stage acceleration sector (distance between R and G<sub>1</sub>, 10.0 mm; between G<sub>1</sub> and G<sub>2</sub>, 20.0 mm) and then enter the field-free drift region (distance between G<sub>2</sub> and G<sub>3</sub>, 760 mm). Typical operating voltages are  $U_1 = 2233$  V applied to R and  $U_2 = 1992$  V applied to G<sub>1</sub>. These values are determined by calculating the dispersion relation [134], the total time of flight  $\text{TOF}_{\text{total}}$  being additively composed of three single times of flight ( $\text{TOF}_1$ ,  $\text{TOF}_2$ , and  $\text{TOF}_3$ ) related to the three different acceleration sections of the spectrometer,

$$\frac{d(\text{TOF}_{\text{total}}(a, x))}{dx} = \frac{d}{dx} \left[ \underbrace{l_1 \cdot \frac{\sqrt{2} \sqrt{\frac{(a-1)x}{l_1}}}{a-1}}_{\text{TOF}_1} + l_2 \cdot \underbrace{\left[ \sqrt{2 \cdot \frac{(a-1)x}{l_1} + 2} - \sqrt{2} \cdot \sqrt{\frac{(a-1)x}{l_1}} \right]}_{\text{TOF}_2} + l_3 \cdot \underbrace{\frac{1}{\sqrt{2 \cdot \frac{(a-1)x}{l_1} + 2}}}_{\text{TOF}_3} \right] \cdot \frac{\sqrt{M}}{\sqrt{U_2}} \stackrel{!}{=} 0, \quad (3.24)$$

with the following variables,  $a = U_1/U_2$  the voltage ratio to be optimized ( $U_2$  is varied),  $l_1$  the distance between R and G<sub>1</sub>,  $l_2$  the distance between G<sub>1</sub> and G<sub>2</sub>,  $l_3$  the distance between G<sub>2</sub> and MCP (the pre-acceleration in front of the MCP is neglected),  $x$  the location of the interaction zone above G<sub>1</sub>, and  $M$  the dimensionless mass of a singly charged ion. Of course,

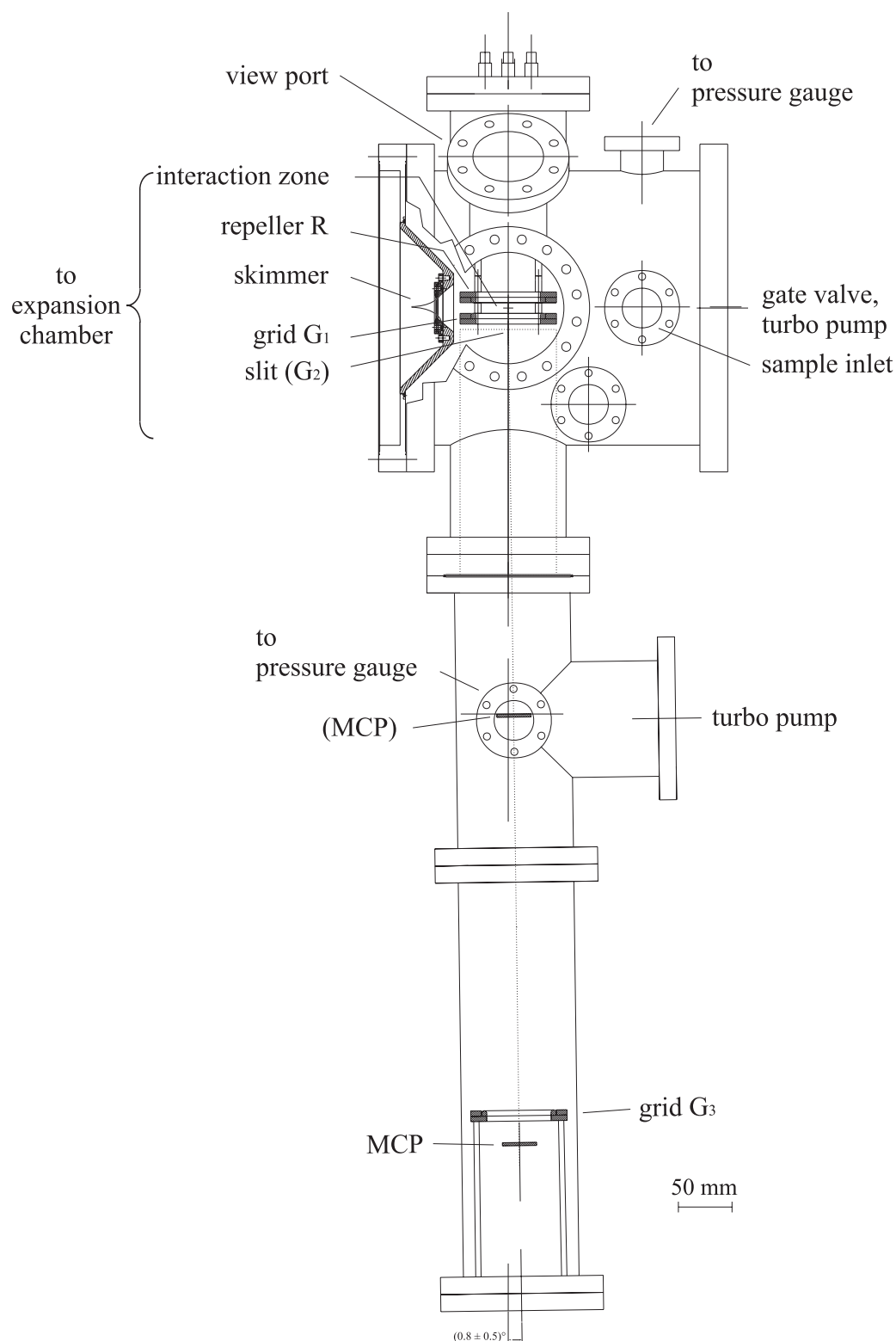


**Figure 3.21:** Design of the TOF mass spectrometer for final experiments. The plane of drawing is a section perpendicular to the propagation direction of the laser beams. The system is designed as a molecular beam machine combined with a mass analysis. The distance from the interaction zone to the MCP can be varied.

in principle, an infinite number of pairs  $\{a, x\}$  can be found that would solve Eq. 3.24. In practice, Eq. 3.24 needs to be solved for  $x$  equals the distance of the laser above  $G_1$  and this uniquely fixes  $a$ . The result of this calculation as well as the measured toluene ion yield ( $M = 92$ ) dependent on the acceleration field are shown in Fig. 3.22. Obviously, calculation

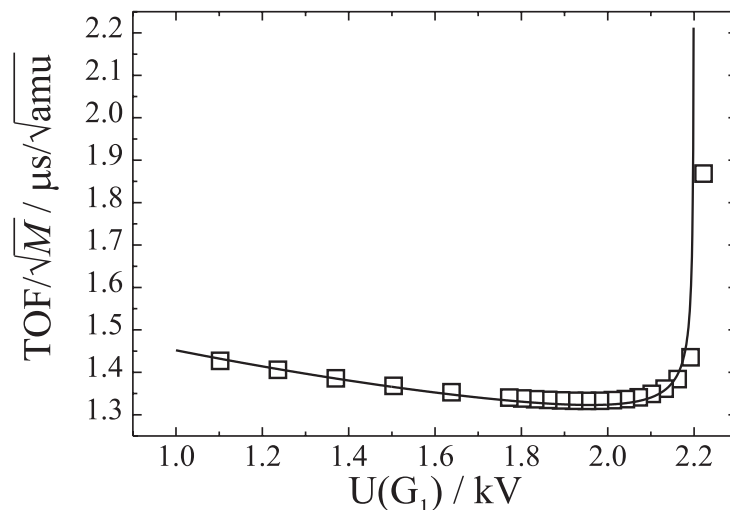


**Figure 3.22:** Optimization of the operating voltages for the spatial focusing of cations. The black squares represent the measured times of flight normalized to the square root of mass of the toluene parent ion dependent on the voltage applied to  $G_1$ . The black line corresponds to the calculation according to Eq. 3.24.

and measurement are in good agreement which proves that the TOF mass spectrometer is correctly operated. The repeller and the grid  $G_1$  consist of electroformed mesh made of copper with 70 wires/inch and a transmission of 90% (Buckbee-Mears MC-17). To avoid the disturbing influence of surface charges potentially accumulating on the non-conducting Vespel elements (DuPont Vespel SP-1) of the setup, these elements are shielded using copper rings (see Fig. 3.23) [135].

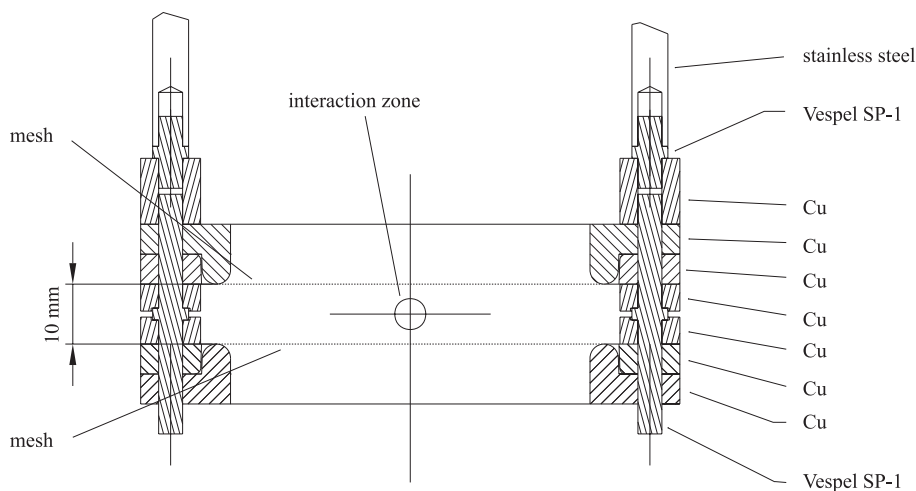


**Figure 3.23:** Section through the first acceleration stage of the TOF mass spectrometer. The insulator (Vespel SP-1) between the two mesh electrodes is shielded by copper rings to avoid the disturbing influence of surface charges.

The electrodes  $G_2$  and  $G_3$  are always kept at ground potential. In the solid electrode  $G_2$ , there is a rectangular entrance slit with dimensions  $10.0 \times 1.2 \text{ mm}^2$ , its longer dimension

parallel to the propagation direction of the laser beam. These dimensions are chosen to avoid a restriction of the interaction volume in the transverse direction and to maintain a suitable pressure ratio that fulfilled the different pressure demands in the two vacuum chambers (see below). With this arrangement the appearance of a volume effect in the transverse direction cannot be prevented anyway. Therefore, the width of the slit is much larger than typical beam diameters at focus even for the lens with the largest focal length ( $f = 1000$  mm) (see Tab. 3.2). The length of the slit is a compromise between the avoidance of a volume effect in the propagation direction of the laser determined by the Rayleigh lengths (see Tab. 3.2) and the provision of a sufficiently large signal. After traveling through this slit, the ions enter a field-free drift region (distance between  $G_2$  and  $G_3$ ,  $\sim 760$  mm). After crossing the final grid  $G_3$ , the ions are accelerated to a kinetic energy of 4.4 keV and then impinge on the front face of a double-stage multichannel-plate (MCP, Galileo, type chevron, image quality) assembly operated at typically 2 kV for ion detection. The operational principle of an MCP is described in Sec. 3.6. The distance between grid  $G_3$  and front face of the MCP is  $\sim 20$  mm. The mass resolution achieved with this arrangement amounts to  $M/\Delta M \sim 200$  which is sufficient to separate the mass signals of parent and fragment ions even for larger organic molecules.

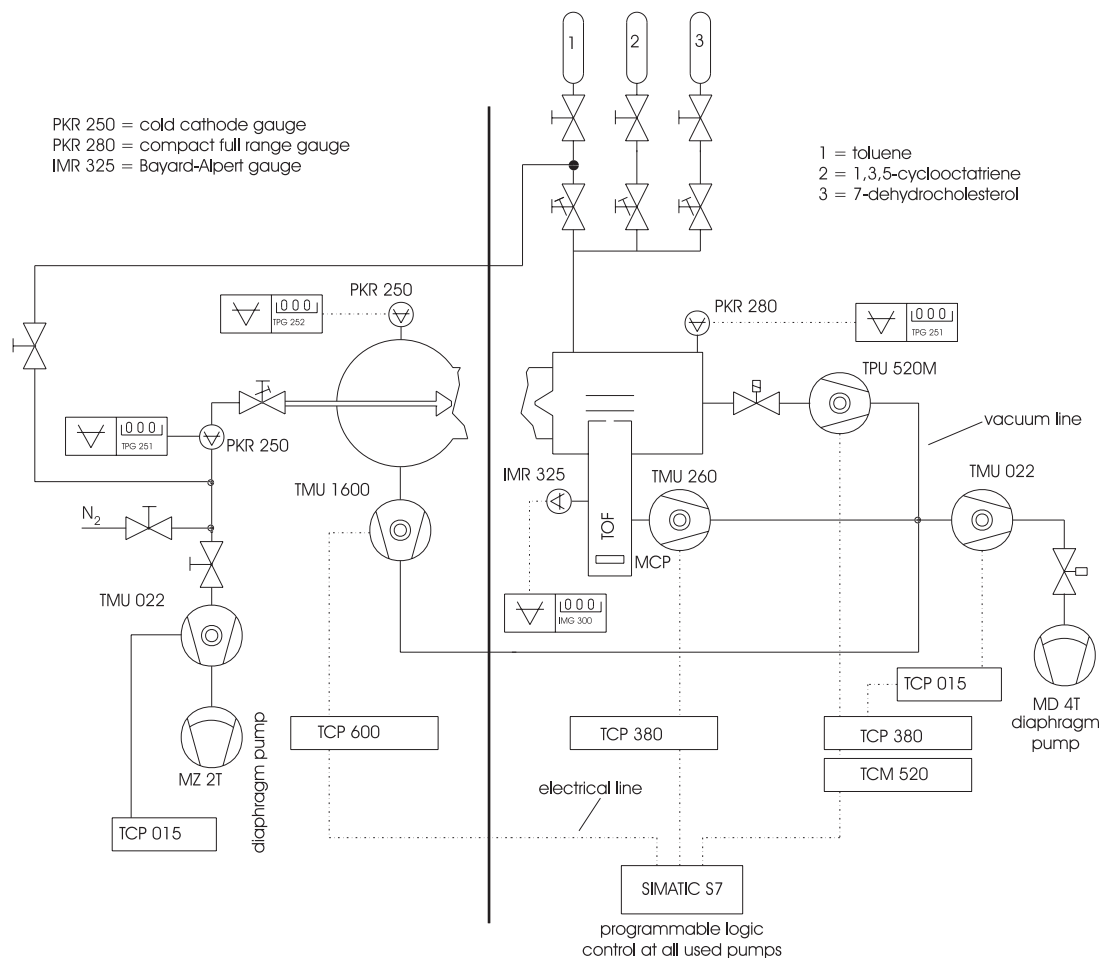


**Figure 3.24:** Overview of the vacuum system. The vertical solid line marks the separation of the expansion chamber (left) and the interaction and detection chamber (right).

The division of the vacuum system into two chambers by the slit makes it possible to have different pressures in the interaction and in the detection chamber without losing more substance than necessary. Because the system is designed as a molecular beam machine, two



additional pumps exist (see Fig. 3.24) which caused only marginal substance losses, because the turbo pump of the expansion chamber (Pfeiffer TMU1600, 1600 l/s) is positioned behind the nozzle with a diameter of 100  $\mu\text{m}$  and the turbo pump evacuating the molecular beam chamber (Pfeiffer TPU520M, 520 l/s) can be separated by means of a gate valve.

Although a higher pressure is used simultaneously in the upper chamber, care is taken to keep the pressure in the lower chamber at  $10^{-6}$  mbar at maximum, in agreement with the operation conditions of the MCP declared by the manufacturer. Similar to the initial setup, the gaseous substances are admitted to the vacuum chamber by means of a variable leak connected to flasks containing the liquid or solid substances and their saturated vapors at room temperature. The whole vacuum system can be heated up to  $\sim 423$  K to also allow the system to be cleaned. The pressures are measured in both chambers by means of ionization gauges. The fact that the calibration of an ionization gauge depends on the nature of the gas under investigation must be taken into account to ascertain the correct pressure in the vessel. For a rough estimation, the pressure reported by an ionization gauge system calibrated to  $\text{N}_2$  must be multiplied by a factor of 0.33 for Xe and 0.1 to 0.4 for higher hydrocarbons [136]. For the upper chamber a compact full-range gauge and for the lower chamber a Bayard-Alpert gauge are used which allowed the actual target pressure to be measured in addition to the pressure in the lower chamber needed to prevent MCP damage. Dependent on the laser intensity, the sample pressures in the upper chamber are chosen to exclude space charge effects.

The detection unit of this TOF mass spectrometer is connected as follows. The anode is kept at ground potential making it necessary to apply a negative potential ( $-2268$  V) to the front face of the MCP. The two stages of the MCP are connected to the same power supply (Electron Tubes Limited PM28B), the output of which is divided by a homebuilt voltage divider. The anode and its shielding have a conical shape to improve the impedance matching between the MCP and the connecting coaxial cable to provide a signal without overshoots [137]. The anode is connected to the next measuring instrument via an overvoltage protector (Huber & Suhner AG, 3401.01.G) to eliminate high-voltage spikes.

### 3.8 Data acquisition

For correct synchronization of the different data acquisition devices, a trigger signal is required. For the initial measurements, a signal delivered from the Pockels cell driver of the laser system is used. However, for the final experiments, a photodiode illuminated by scattered light is used as the trigger source, because the trigger signal delivered from the Pockels cell driver of the laser system is influenced by an electro-magnetic pickup from external devices leading to an unacceptably large jitter of the measured signal. Using a photodiode has the additional advantage that the trigger signal is not shifted in time relative to the light pulse, even if the internal timing of the laser is changed. The electric signal coming from the photodiode is fed into a pulse generator (Stanford Research DG535) to convert it into well-defined digital signals (see Fig. 3.25). Moreover, this device allows the production of a number of different types of electronic signals (TTL, fast NIM) in parallel.

Counting and analog data acquisition techniques (described in Sec. 3.8.1 and 3.8.2) are used for all experimental setups (see above). For the investigation of toluene, acquisition of mass spectra is performed using a large-bandwidth oscilloscope (LeCroy LC564A, 1 GHz). Recording mass spectra in this way has the advantageous possibility to perform online mathematical operations with these data (e.g. the integration of peaks or the determination of the ratio of a specific ion and its heavier isotopic variant). This facilitates the elimination

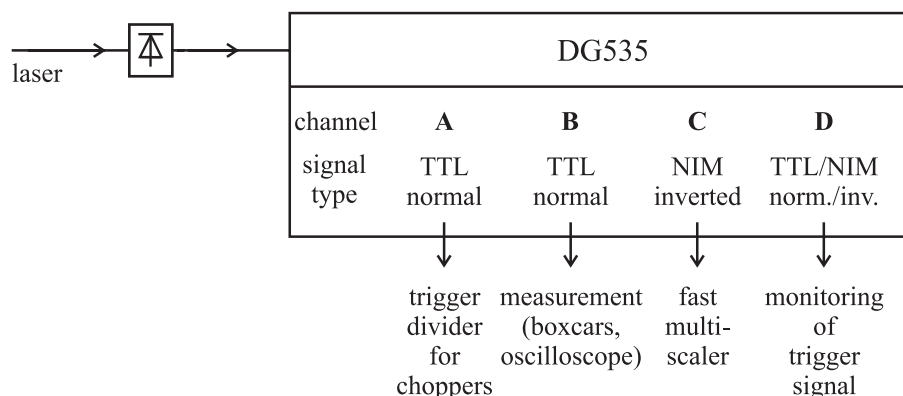


**Figure 3.25:** Usage of the various trigger signals generated by a photodiode combined with a pulse generator.

of distortions of the measured signal caused by saturation effects, for example. In addition, this technique allows data to be acquired at a higher counting rate thus reducing the measurement time. The resolution of the time of flight is decreased by a factor of 2 compared with measurements recorded in the counting mode but provides nevertheless adequate mass resolution for the toluene molecule.

### 3.8.1 Acquisition of mass spectra by a fast multiscaler

The fast multiscaler method is required in cases in which a higher mass resolution is needed, compared to the resolution achievable with the large-bandwidth oscilloscope, or when only a very low count rate is available. The fast multiscaler works in principle as follows. The trigger signal (fast NIM) connected to the start input starts a counter which is incremented every  $\sim 0.5$  ns. Then a signal from the MCP (stemming from a single ion) reaches the stop input causing the present counter position (i. e. time delay between start and stop pulses) to be registered. From these raw data, a histogram is generated by a special software giving the number of events in every 0.5-ns-time slot. Each of these channels corresponds to a specific time of flight. This way, a complete mass spectrum can be recorded from the addition of many sweeps. The count rate must be carefully observed to exclude distortions of the measured spectrum by lost events.

In case of the acquisition of mass spectra by a fast multiscaler (FAST Comtec, model 7886E, 2 GHz) for the initial experiments, a separate pre-amplifier and a discriminator are used to distinguish between significant pulses and electronic noise by adjusting a lower threshold for the signal to be recorded.

However, in case of the acquisition of mass spectra for the final experiments, a newer version of this fast multiscaler (FAST Comtec, model 7886P, 2 GHz) is used. Its improved features allow to adjust the threshold level of the input circuit by software making the use of an external discriminator unnecessary. Because the ions are pre-accelerated in front of the MCP to  $\sim 4.4$  keV, the signal strength is sufficient to be fed into the multiscaler using a pre-amplification factor of approximately 5. Usually, the mass calibration is experimentally ascertained by means of a calibration substance with a known mass spectrum (for instance Xe) and Eq. 3.23 as the fit function.

All mass spectra of the substances 1,3,5-cyclooctatriene and 7-dehydrocholesterol are recorded averaging over 150000 sweeps with this method. These spectra give additional information for the evaluation of time-dependent measurements, especially for the deter-

mination of the order of the ionization process via intensity-dependent measurements (of 1,3,5-cyclooctatriene).

### 3.8.2 Acquisition of time-dependent signals from pump-probe measurements

Pump-probe measurements require two subsequent light pulses. The first one starts a chemical reaction and the second one interacts with the molecule in a specific way to produce ions. The detection of the ions yields an electronic signal that depends on the momentary state of the reacting molecule. Monitoring this signal as a function of the relative delay between the two pulses leads to a curve that contains information on the dynamical development of the observed system after applying the pump pulse. The detection circuitry is as follows (see

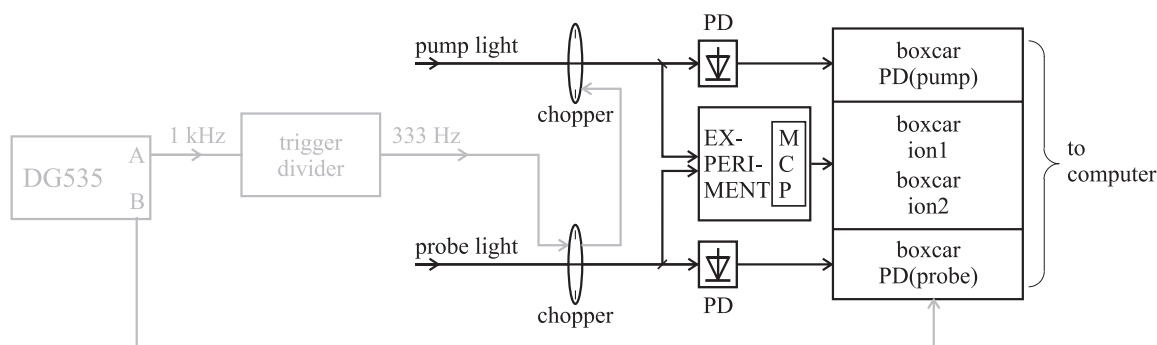


**Figure 3.26:** Schematic illustration of the data acquisition of pump-probe experiments. The desired time windows are selected from the signals of the MCP and the photodiodes (PD), respectively, by means of boxcar integrators. The solid gray lines represent the path of the trigger signal, the solid black lines the paths of the laser light and the light-induced signals.

Fig. 3.26). The ion signal from the MCP is fed into a boxcar amplifier (Stanford Research SR250). The boxcar amplifier is used as a gated integrator to select a particular peak from the whole mass spectrum, i. e. to integrate all signal contributions of the TOF spectrum of the produced ions within a rather small time window (typically 40 ns). The connection of two of these boxcar integrators to the MCP signal allows two mass peaks to be recorded simultaneously. Two further boxcar integrators are used to record the pump and the probe pulse energy by means of photodiodes in each beam path (see Sec. 3.4.2 and 3.5.3). The output signals of the four boxcar integrators are fed into an analog-to-digital converter inside the measurement computer and stored after averaging over typically 1000 laser pulses. For every measurement, three different ion signals are recorded produced by irradiating the gaseous sample firstly by one pump pulse only, secondly by one probe pulse only, and finally by both pump and probe pulses together, achieved by the choppers described in Sec. 3.4.2 and 3.5.3. This cycle of three events means that averaging actually occurs over 3000 laser pulses. With a pulse repetition rate of 1 kHz delivered by the laser, the period for the storage and evaluation of the data is smaller than 1 ms to record the four signals without losing laser shots. This way, the total time needed for a measurement is reduced to a minimum. Variation of the delay between the pump and the probe pulse is achieved by a well-defined change of the optical path length of one of these two pulses against the optical path length of the other pulse. For this purpose, a stepper-motor-driven delay-line controlled by the measurement computer is used. This together with the procedure for data storage described above allows for recording two ion signals simultaneously with their background signals produced by the pump and the probe light alone. The subtraction of these two latter signals from

that recorded with both pulses present yields transient time-dependent signals containing the desired dynamical information. It should be noted that this subtraction only works if no saturation effects occur.

### 3.9 Sample preparation

All substances used are commercially available. They are used in the gas phase after different purification procedures described in the following.

Toluene with purity > 99.9% (Merck Uvasol®) is used at 296 K after having been subjected to several pump-freeze-thaw cycles using liquid nitrogen. The absorption spectrum (spectrometer, Perkin Elmer Lambda9 UV/VIS) of the sample used for elucidating the ionization mechanism is measured in a 1-mm-thick optical cell, the substance dissolved in cyclohexane (Merck Uvasol®) with a volume dilution of 1:600 and 1:3000, respectively. The comparison with literature data [138] shows that the substance contains essentially no contaminants. A semi-quantitative GC-MS analysis [139] of the sample used for the investigation of effects induced by continuum generation verifies substantially the declared degree of purity. Compared to the amount of toluene, only traces of ethylbenzene, *m*-xylol, *p*-xylol, benzaldehyde, and a cyclic C<sub>8</sub>-alkene, together amounting to 0.08 mass% can be detected.

1,3,5-Cyclooctatriene (Organometallics, Inc., declared purity 97-99%) is further purified by cryodistillation. Purification of the substance by complex formation from AgNO<sub>3</sub> dissolved in water, recrystallization of the crystalline complex, and subsequent decomposition of the complex by NH<sub>4</sub>OH as described in literature [140] is not carried out due to the danger of the possible formation of highly explosive azides. In accordance with the material safety data sheet given by the manufacturer, 1,3,5-cyclooctatriene is stable, but can self-isomerize during storage at room temperature for prolonged periods (months). Under these conditions, polymerization can occur as well, but the thus formed molecules do not affect the measurement due to their smaller volatility and the possibility to identify them by their higher masses. For these reasons, the substance has been ordered shortly before its usage and is subsequently stored in cold, dark conditions. Furthermore, the formation of the isomer bicyclo[4.2.0]octa-(2,4)-diene (barrier height  $(107 \pm 2)$  kJ mol<sup>-1</sup> [141]) would easily be recognized in a mass spectrum taken at long pump-probe delay times, because this compound is known to undergo cycloreversion resulting in benzene and ethylene (mass 28) [86]. The 1,3,5-cyclooctatriene sample is used at 296 K after having been subjected to a few pump-freeze-thaw cycles using liquid nitrogen. Its absorption spectrum (spectrometer, Perkin Elmer Lambda9 UV/VIS) is measured as pure substance between two 1-mm-thick quartz optical flats ( $d < 100$  μm).

7-Dehydrocholesterol (Sigma-Chemie) has a declared purity of only ~ 96% determined by HPLC, associated with the production process. Because the substance is sensitive to oxidation and photoreactions, the purity is further decreased during storage in air and exposed to sunlight for prolonged periods. Therefore, the substance is recrystallized from methanol (Merck LiChrosolv®, gradient grade, purity > 99.8%) under argon and dried by evacuation [142]. The purified substance has been in cold, dark conditions under argon. It is admitted to the vacuum chamber by means of a variable leak connected with a flask containing the 7-dehydrocholesterol and its saturated vapor at ~ 373 K, while keeping the whole vacuum system at this temperature.

Xe (AGA, xenon 4.5, CF<sub>4</sub>-free) is directly admitted to the vacuum chamber using a variable leak connected with the bottle containing the gas.

## 4 Results and discussion

### 4.1 Data evaluation procedures

In the data evaluation process, the measured raw data must be analyzed carefully, taking into account the limitations and assumptions that underlie the theory to be applied, and the errors in the data. This is the prerequisite for extracting reliable results. Molecular reaction dynamics can be monitored by evaluation of time-dependent signals obtained in pump-probe measurements. The strength of such transient signals depends on the delay between pump pulse and probe pulse. The resulting temporal behavior is a reflection of the actual reaction dynamics of the investigated molecule but is also influenced by the temporal shape of the laser pulses used and by details of the probe process.

If the relaxation time of intramolecular processes is significantly longer than the pulse durations, the laser pulses can be considered as  $\delta$ -pulses. In that case, the time-dependent signals can be explained as follows: all molecules excited by the pump pulse begin to react simultaneously. Subsequently, the state of the ensemble of excited molecules at a precisely defined moment is analyzed by the probe pulse. Then the data evaluation procedure can be simplified by separating the temporal decay from the overlapping laser pulses. This separation is only possible in the case of rather long decay times, because only then the signal is still strong enough to fit reliable time constants in a delay region where those signal components originating only from the pump pulse and the probe pulse have already dropped to zero.

If intramolecular processes take place on the same timescale as the laser pulses applied, however, the data evaluation procedure is more tedious. Restricting the fit of such short time constants to time delays where the pump and probe pulses no longer overlap would produce huge errors or would even fail, because the amplitude of the decay function is too small. Therefore, it is not possible, in this case, to separate the time behavior of the evolving molecules from that of the laser pulses. Hence another method is needed to extract information about the molecular dynamics from the measured transient signals. The solution is the use of a convolution of the response function produced by pump pulse and probe pulse on the one hand, and the time-dependence of the probe signal generated by the reacting molecule, on the other hand, to describe the measured data. This procedure requires detailed knowledge about the temporal behavior of the laser pulses in order to extract reliable short time constants. In addition, it must be proven that the excitation of molecules occurs by exactly one pump photon which is required to reach the  $1B_2$  state desired to be populated in the molecules investigated in the present work. Moreover, the probe process itself is closely related to the monitored signal which also contains information about molecular dynamics. Consequently, the probe step must be investigated carefully. In order to extract reliable information about molecular dynamics, the ionization mechanism must be elucidated, which is done in this work by intensity-dependent measurements. Besides the use of short, well-defined laser pulses, it is also worth the effort to undertake an almost noise-free measurement, by the use of a stable setup, because the time-resolution is improved significantly.

In the rest of this section, the procedures for evaluation of intensity-dependent as well as time-dependent data are described in detail.

#### 4.1.1 Intensity-dependent measurements

To record intensity-dependent data, the peak intensity of the laser light is varied by changing the pulse energy, leaving other parameters like pulse length and concomitant to this rise time

and frequency spectrum as well as beam diameter unchanged. Ledingham *et al.* point out that “there exists clearly a controversy between multiphoton versus tunneling ionization in the intense laser regime, which requires careful analysis of existing and future data, particularly with respect to the length, rise time, and shape of the laser pulses” [143].

In an intensity-dependent measurement, each data point corresponds to the ion yield of a single mass peak of a mass spectrum, taken at a certain peak intensity. The peak intensity of the laser beam used can be calculated if the pulse energy, the temporal profile, and the cross-sectional area of the beam are known. Note that in contrast to a numerical determination of the cross-sectional area of the beam, which is generally possible, an analytical description of the spatial profile (see Sec. 3.5.2) simplifies the transformation of a beam diameter obtained from a non-constant spatial shape into the diameter of the equivalent “top hat” profile (required for the calculation of the peak intensity). Also the temporal profile should exhibit a shape which can be described analytically, but for time-dependent measurements a Gaussian shape is preferable, as will be shown in Sec. 4.1.2. The laser beams with different wavelengths used in the present work are found to exhibit spatial Gaussian shapes. Typical beam profiles are depicted in Fig. 4.1.

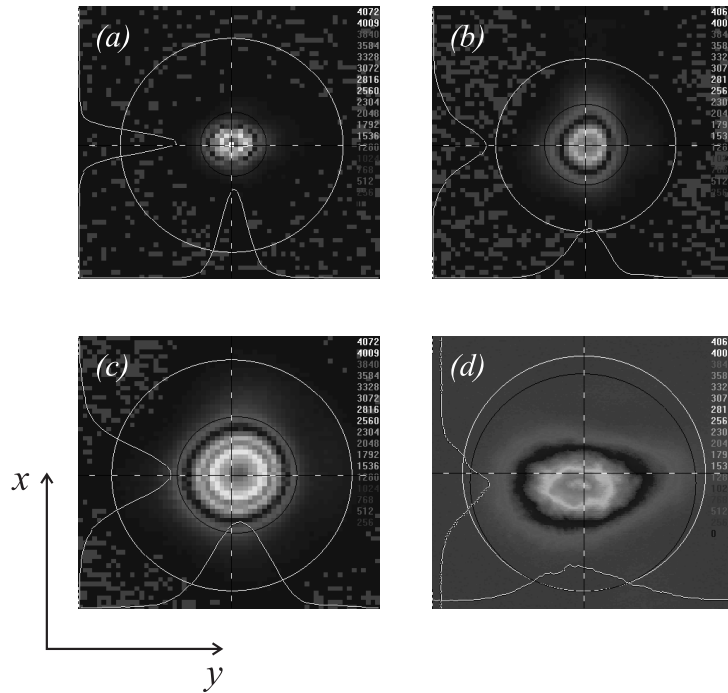


**Figure 4.1:** Typical measured beam profiles in false color representation. The particular intensity distributions in the  $x$ - and  $y$ -directions are drawn in as white lines. The spatial shapes using different wavelengths are approximately Gaussian. (a) Profile of the focused beam used for the investigation of the ionization of toluene; (b) and (c) spatial shapes of the probe beams ( $\lambda = 400$  nm and  $\lambda = 800$  nm) at focus; (d) profile of the unfocused pump beam. The profile of the pump beam (which is two orders of magnitude larger than the probe beam sizes) deviates slightly from the perfect Gaussian shape, but this does not influence the experiment, because no intensity-dependent measurements are taken with the pump light.

Varying the peak intensity over a wide range has the consequence that the measured ion yields cover several orders of magnitude. Then a measurement at different sample pressures is required to keep the signal within the dynamic range of the apparatus. To keep the data sets taken at different sample pressures comparable to each other, at least one mass spectrum is recorded at two different pressures, but otherwise unchanged conditions. Thus

it is possible to normalize the ion yields to one sample pressure. For the interpretation of the measurements in this work it is not necessary to gauge the ion yield. Therefore, this quantity is given in arbitrary units. It may be more useful to measure all mass spectra at the same sample pressure (which is possible in a small intensity range), but strong signals may suffer from detector saturation. Then it is legitimate to evaluate the signals of the heavier isotopic variants instead of the corresponding main peaks.

### 4.1.2 Time-dependent measurements

To record time-dependent data, the delay between pump pulse and probe pulse is varied in steps, the size of which is a compromise between resolution (at minimum  $2 \mu\text{m} \hat{=} 6.7 \text{ fs}$ ) and measuring time (for details see Sec. 3.4.2). For each value of this delay, signals are obtained by averaging over at least 4000 laser pulses. The transient signal results from the total signal by subtracting those parts of the total signal generated by pump light alone (which is always only noise) and by the probe light alone. This method is allowed if no saturation effects occur, which is proved by recording a mass spectrum of Xe at an even higher pressure than typical pressures used for all other experiments and checking the isotopes abundances (see Fig. 4.2). Xe as structureless compound is expected to be ionized instantaneously and not to show any

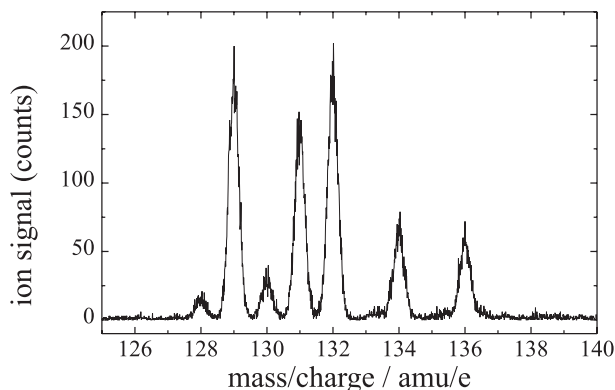


**Figure 4.2:** Mass spectrum of Xe taken at a pump wavelength  $\lambda_{\text{pu}} = 266 \text{ nm}$ , a probe wavelength  $\lambda_{\text{pr}} = 800 \text{ nm}$ , and  $I_{\text{pu}} = 8.5 \times 10^8 \text{ W cm}^{-2}$ ,  $I_{\text{pr}} = 4.3 \times 10^{12} \text{ W cm}^{-2}$ , for a sample pressure of  $p = 2 \times 10^{-7} \text{ mbar}$ .

dependence on the pump-probe delay. Xe is chosen of all atomic gases, because rare gases are easy to handle and Xe has the lowest ionization energy of all rare gases. Integration of the measured Xe isotope peaks results in the isotopic ratios listed in Tab. 4.1. Clearly, the measured isotopic ratios are in good agreement with literature values which proves saturation effects to be essentially absent.

The change in the ionization probability resulting from variation of the pump-probe delay is a consequence of the evolution of the reacting molecule. Unfortunately, in the case of a multiphoton ionization process as the probe step, the actual molecular dynamics is superimposed by the ionization dynamics, i. e. the time-dependence of the ionization probability. To ascertain the latter time-dependent quantity, the different ionization cross sections as well as the corresponding orders of the ionization process of the transient signal must be determined at many distinct time delays. With some effort, the order of the probe process can be measured. For the determination of the ionization cross sections, however, the saturation intensities of the transient signal at each pump-probe delay are needed. A transient signal can be recorded only in a small intensity region. The purpose of the pump light is to

**Table 4.1:** Xe isotope abundances as determined from an experimental mass spectrum (see Fig. 4.2) compared with natural abundances taken from literature [144].

Xe isotope mass / $u$	measured abundance / %	natural abundance / % from Ref. [144]
128	$1.8 \pm 0.1$	1.91
129	$26.6 \pm 0.3$	26.4
130	$4.4 \pm 0.1$	4.11
131	$20.9 \pm 0.3$	21.2
132	$26.8 \pm 0.3$	26.9
134	$10.2 \pm 0.2$	10.4
136	$9.1 \pm 0.2$	8.91

excite as many molecules as possible, but not to ionize any molecule. Therefore, a number of molecules is always left in the ground state. The lower limit for the probe intensity is determined by the ionization threshold of the excited molecules. The determination of the saturation intensity of the transient signal, however, is impossible, because an increase of the probe intensity is always connected with an increase of the signal coming from ionization of unexcited molecules. In general, this non-transient part can be subtracted from the total signal, but if it grows too large, the transient component becomes too noisy for a reliable evaluation. Therefore, it is impossible to include this ionization dynamics into the fit function. As will be described below, it can be shown on the basis of a model simulation (see Sec. 4.3.2) that the extracted time constants are not strongly influenced by the ionization dynamics. The molecular dynamics part seems to be well described by an exponential decay. If required, one or more additional exponential functions can be added as further summands to the formula given in Eq. 4.1 (which is derived in App. A).

$$F(\Delta t) = y_{\text{offs}} + \underbrace{\int_0^\infty \frac{1}{\sqrt{\pi}w} \cdot \exp \left[ - \left( \frac{t' - (\Delta t - S)}{w} \right)^2 \right]}_{\text{response function}} \cdot \underbrace{\left[ A_D \cdot \exp \left[ - \frac{t'}{\tau} \right] + y_0 \right]}_{\text{exponential decay of the evolving molecule}} dt' \quad (4.1)$$

In this equation,  $A_D$  is the amplitude of the exponential function reflecting the molecular dynamics,  $S$  is the temporal shift of the measured signal versus a simultaneously measured reference ion signal (e.g. the parent ion or Xe), and  $w$  is the half 1/e-width of the response function between the pump pulse and the probe pulse including the actual orders of the processes. The parameters  $y_{\text{offs}}$  and  $S$  are needed to adjust the unknown origin of the measured curve. The offset  $y_0$  is related to molecular properties and is nonzero if the ionization efficiency of the product generated by the photoreaction is different from that of the reactant. The components of the fit function (Eq. 4.1) are illustrated in Fig. 4.3.

The claim that the decay of the time-dependent signal stemming from molecular dynamics is exponential deserves some discussion. First, an exponential decay fits in a satisfactory way to the measured data, as will be shown below. Moreover, inspection of the process behind shows that this seems to be physically meaningful. As described in Sec. 2.1.1, molecules evolve on potential energy surfaces. By means of the pump pulse exciting the molecule, a wavepacket is generated in an excited state. Its width depends on the shape of the ground state potential energy surface and the pump pulse duration. After the excitation, this wavepacket starts its



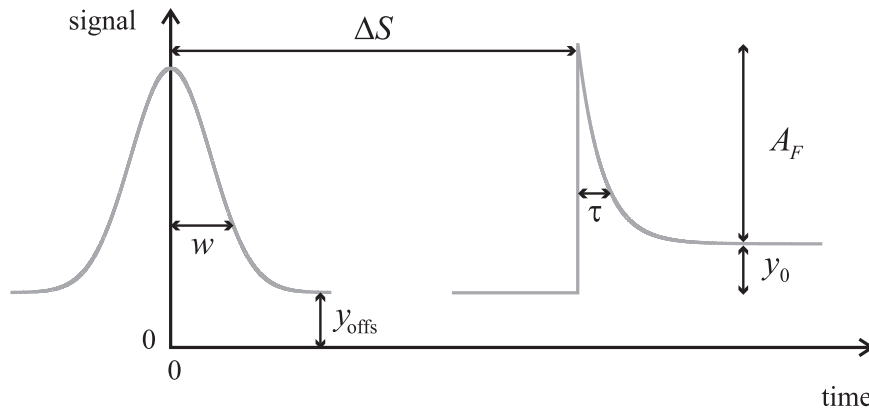


**Figure 4.3:** Illustration of the components of the fit function (Eq. 4.1) used for the evaluation of time-dependent data (left curve, response function; right curve, exponential decay).

downhill motion on the upper potential energy surface changing its width with respect to the shape of the potential, but preserving its total energy. This wavepacket can travel into a region, where the couplings to another potential energy surface become strong enough for a potential energy surface transition (as is the case at a conical intersection). Depending on the shape of the potential energy surface, the wavepacket oscillates and reaches this conical intersection repeatedly. If the conical intersection is located at a high potential energy (i. e. it is only accessible by a wavepacket with a rather high vibrational energy), or if the spatial extension of the region of strong couplings is much smaller than that of the wavepacket, only a fraction of the wavepacket can change the potential surface each time the wavepacket passes the intersection region. If the fraction dropping down always corresponds to the same percentage, the volume of the wavepacket on the upper potential energy surface decreases exponentially, leading to the postulated exponential decay of the measured signal, since the detection occurs from the upper surface. These oscillations do not appear in the signals measured in the present work indicating that the oscillation periods are much less than the pulse lengths used.

The response function itself is a convolution of pump and probe pulses with excitation probability  $P_{\text{pu}}$  and ionization probability  $P_{\text{pr}}$  including the order of the pump process, which equals unity, and the order of the probe process  $N$ :

$$R(\Delta t) = \int_{-\infty}^{\infty} P_{\text{pu}}^1(t - \Delta t) \cdot P_{\text{pr}}^N(t) dt \quad (4.2)$$

If the particular pulses exhibit temporal Gaussian shapes, the response function is again a Gaussian curve with the half 1/e-width  $w$  (see Fig. 4.3).

Knowledge of the response function is of paramount importance to obtain reliable time constants by fitting the time-dependent signal by the convolution given in Eq. 4.1. Therefore, in the final experiment, the temporal shapes and widths of all pulses used are measured in this work by means of frequency mixing processes in suitable crystals (see Sec. 3.5.2). For Gaussian pump and probe pulses, the resulting response function is also Gaussian and has a 1/e-width given by

$$w = \sqrt{\tau_{\text{pu}}^2 + \frac{1}{N} \tau_{\text{pr}}^2} \quad (4.3)$$

with the order of the probe process  $N$  and the pump pulse and the probe pulse lengths  $\tau_{\text{pu}}$  and  $\tau_{\text{pr}}$ , respectively. Note that in contrast to Eq. 4.1, all numbers given for pulse widths

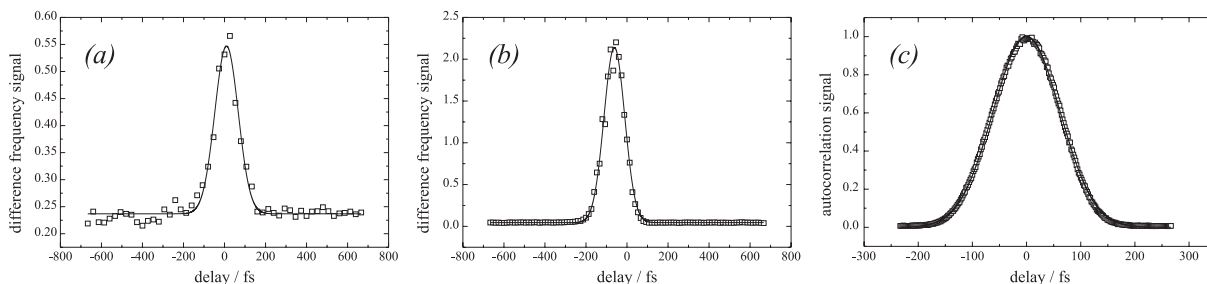


**Figure 4.4:** Typical temporal pulse shapes using the final setup. The solid lines are Gauss fits to the measured data points (squares). (a) difference-frequency mixing between 266 nm and 800 nm ( $\tau_{266} = 88$  fs); (b) difference-frequency mixing between 266 nm and 400 nm ( $\tau_{400} = 80$  fs); (c) autocorrelation measurement of 800-nm light ( $\tau_{800} = 104$  fs).

are full width at half maximum (FWHM) values. In order to determine the quantity  $w$ , not only the pulse lengths but also the orders of the pump and the probe step must be measured. If the ionization energy of the investigated molecule is less than the energy of two pump photons, and the pump intensity is kept low enough so that no signal occurs from irradiating the sample with pump light alone, it can be easily checked that only one pump photon is absorbed to excite the molecule. Knowledge of the order of the probe process is obtained by measuring the intensity dependence of the transient ion signal at several different pump-probe delays (for details see Sec. 4.1.1).

## 4.2 Photoionization and photofragmentation of toluene

In the present work, several aspects of the photoexcitation of gaseous toluene are investigated. Toluene as a medium-sized organic molecule is chosen for two reasons. First, its ionization mechanism may be characteristic for similar-sized molecules, and it is regarded as a model system for elucidating the probe step in pump-probe experiments. Second, there exists a controversy in the literature on its ionization mechanism as well as its fragmentation behavior.

The photodynamics of molecules under the influence of short ( $< 100$  fs), strong laser pulses is now becoming a topic of wide interest. For intensities beyond  $1.3 \times 10^{13}$  W cm $^{-2}$ , the electric field produced by a laser exceeds the value  $1$  V Å $^{-1}$ . The behavior of molecules exposed to such strong fields, which are comparable in strength to the electrostatic fields that are responsible for the stability of molecules, is more complex than one might expect. For instance, it was shown very recently [143,145,146] that stable, multiply charged parent ions of medium-size aromatic molecules are created by intense 800-nm, sub-90-fs laser pulses, and that photofragmentation plays a very minor role under these conditions. This “atomic-like” behavior, which favors “soft ionization” leading predominantly to parent ions and is therefore sometimes called femtosecond laser mass spectrometry (FLMS), is surprising, because at the energies required to create higher charge states, several fragmentation channels are known to be easily accessible. Results of similar photoionization and photofragmentation experiments on medium-size aromatic and non-aromatic molecules with various degrees of bond saturation were also published recently [147,148,98,99]. Experiments of this kind strongly contribute to the data-gathering phase, which must be the first step taken whenever a new field of research is being explored, as is the case with intense, ultrashort laser field molecular photoionization and photofragmentation. A logical next step would be a careful inspection of the data collected to identify and resolve possible controversies. This is the approach adopted here to

study the photoionization and photofragmentation of the toluene molecule. Recently, the photodynamics of this molecule was investigated by several groups [143,145–147,98], who do not agree, however, on a common ionization/fragmentation scenario. These discrepancies are most probably largely due to undesired contributions from nonlinear effects in the laser beam (as expressed by, for example, the so-called  $B$ -integral [125], see also Sec. 3.5.2). Therefore, in the present “case study” of toluene, the experimental conditions, under which the ionization/fragmentation data were obtained, are carefully and extensively defined and discussed. Especially in high-intensity laser physics, a precise characterization of laser beams is a *conditio sine qua non* for a proper understanding of experimental work. A further unresolved question seems to be the exact nature of the ionization process of molecules in FLMS. For the case of an atom with an ionization energy ( $IE$ ), the often-cited and well-known Keldysh adiabaticity parameter  $\gamma$  [95] (see Sec. 2.3) makes a rough subdivision of ionization processes into MPI (multiphoton ionization) processes (for which  $\gamma \gg 1$ ) and tunneling processes (for which  $\gamma \ll 1$ ). Useful as this is as a starting point, this subdivision is not so sharp as one might wish it to be, and ionization processes will often be a mixture of these two extremes. Moreover, the Keldysh parameter was derived for structureless particles (atoms), and although often mentioned in relation to molecular studies it does not take into account typical features of molecules such as their extended size in relation to atomic systems. At least one group has introduced some kind of molecular Keldysh parameter [148] and successfully applied it to a specific class of molecule (see Sec. 2.3.2). Aiming to identify the ionization process of toluene, its ion yields are followed over several orders of magnitude as a function of laser peak intensity in the range between  $1.9 \times 10^{13} \text{ W cm}^{-2}$  ( $\gamma \approx 2$ ) and  $2.8 \times 10^{14} \text{ W cm}^{-2}$  ( $\gamma \approx 0.5$ ).

### 4.2.1 Mechanism of the photoionization of toluene

A typical TOF spectrum recorded with linearly polarized radiation at a peak intensity of  $2.0 \times 10^{14} \text{ W cm}^{-2}$  is shown in Fig. 4.5. The spectrum is dominated by the parent ion  $\text{C}_7\text{H}_8^+$  ( $M = 92$ ). The only fragment produced in observable quantities is  $\text{C}_7\text{H}_7^+$  ( $M = 91$ ). The peak at  $M = 93$  is due to  $^{12}\text{C}_6^{13}\text{CH}_8^+$ . For the whole intensity range studied here (between  $1.9 \times 10^{13}$  and  $2.8 \times 10^{14} \text{ W cm}^{-2}$ ), and for both linear and circular polarization, these are the only peaks observed.

In an initial phase of the experiment, one TOF spectrum has been recorded with an  $f = 1000 \text{ mm}$  plano-convex lens for a peak intensity of  $6.4 \times 10^{13} \text{ W cm}^{-2}$ . With this lens some fragmentation products that are absent with the  $f = 500 \text{ mm}$  lens appear, such as  $\text{C}_3\text{H}_i^+$  ( $i = 0, \dots, 5$ ),  $\text{C}_4\text{H}_i^+$  ( $i = 0, \dots, 5$ ),  $\text{C}_5\text{H}_i^+$  ( $i = 3, 5, 6$ ),  $\text{C}_6\text{H}_5^+$ , and  $\text{C}_7\text{H}_i^+$  ( $i = 5, 6$ ), but, more surprisingly, at the same time doubly charged ions such as  $\text{C}_7\text{H}_i^{2+}$  ( $i = 6, 7, 8$ ) appear that are also definitely absent in all other TOF spectra, some of which are even recorded for higher intensities! On the other hand, the use of a lens with a *shorter* focal length of  $300 \text{ mm}$  leads to the same mass spectra as obtained with the  $500\text{-mm}$  lens. To understand this result, it must be noted that the use of the  $f = 1000 \text{ mm}$  lens exposes the air between the lens and the  $\text{CaF}_2$  entrance window of the vacuum system plus the entrance window itself to intensities of up to  $5.5 \times 10^{11} \text{ W cm}^{-2}$ , and as a result the  $B$ -integral grows to 2.9. This suggests that the laser beam is strongly distorted by nonlinear effects, and all of the striking new features that are observed in the TOF spectrum must be ascribed to this. It is known [124] that self-focusing effects trigger continuum generation. Most probably, therefore, the high value of the  $B$ -integral indicates that conditions are created under which the effects of continuum generation become noticeable. Indeed, measurements of the frequency spectrum show that

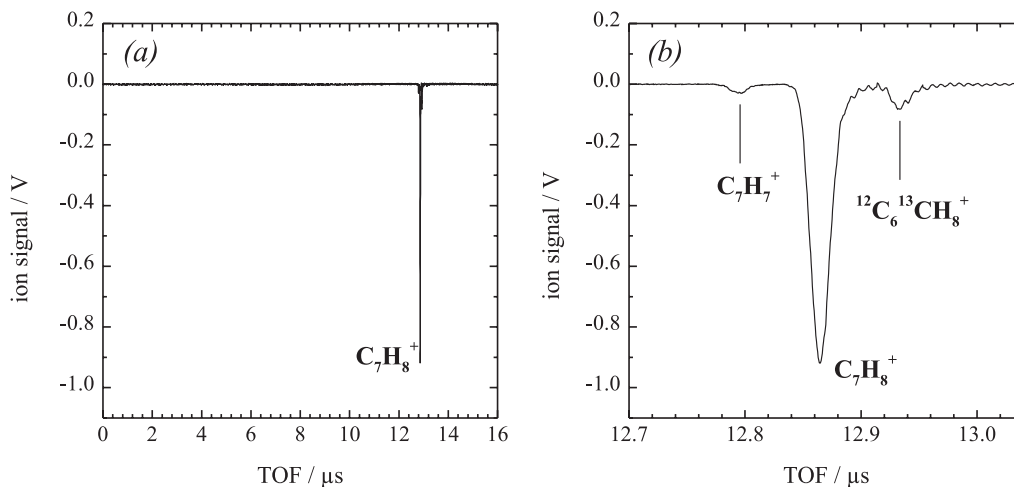


**Figure 4.5:** Time-of-flight spectrum of toluene recorded with 800-nm, 80-fs, linearly polarized laser pulses for a peak intensity of  $2.0 \times 10^{14} \text{ W cm}^{-2}$ . (a) complete spectrum; (b) expanded view of the same spectrum. The spectrum is dominated by the parent ion,  $\text{C}_7\text{H}_8^+$  ( $M = 92$ ), accompanied by its heavier isotopic variant,  $^{12}\text{C}_6^{13}\text{CH}_8^+$  ( $M = 93$ ). Only one other mass peak is found, corresponding to the fragment ion,  $\text{C}_7\text{H}_7^+$  ( $M = 91$ ), which is created in limited quantities.

it changes considerably; a marked broadening around 800 nm is observed. Therefore, a comparison of the TOF spectrum obtained with the  $f = 1000$  mm lens with the TOF spectra obtained with the  $f = 500$  mm lens can only be done with utmost reservation.

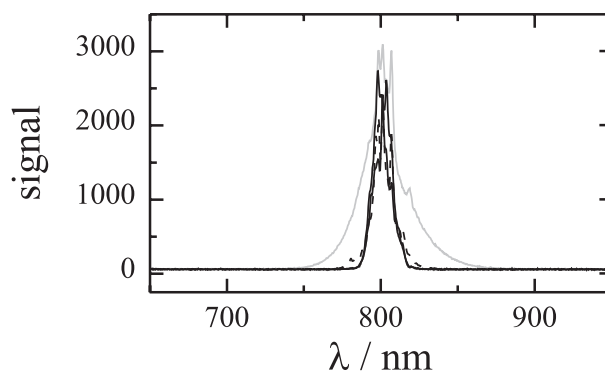


**Figure 4.6:** Measured frequency spectra of the laser light after penetrating a focusing lens and a 2-mm  $\text{CaF}_2$  optical flat positioned in the same distance from the lens as the entrance window of the TOF spectrometer in the experiment. Black curves, spectra obtained with lenses with nominal focal lengths of  $f = 300$  mm and  $f = 500$  mm corresponding to distances to the  $\text{CaF}_2$  window of  $\sim 20$  mm and  $\sim 220$  mm, respectively, and for comparison without lens (dashed line); gray curve, spectrum obtained with a lens with nominal focal length of  $f = 1000$  mm corresponding to a distance to the  $\text{CaF}_2$  window of  $\sim 720$  mm.

In a very recent publication [147], Castillejo *et al.* present TOF spectra resulting from ionization and fragmentation of toluene and a small number of other aromatic and sigma-

bonded hydrocarbons obtained under similar conditions (800 nm, 50 fs) for intensities up to  $2.5 \times 10^{14} \text{ W cm}^{-2}$ . Surprisingly, they observe fragmentation products such as  $\text{C}_2\text{H}_n^+$  and  $\text{C}_3\text{H}_n^+$  already at  $3.1 \times 10^{13} \text{ W cm}^{-2}$ , and find the doubly charged parent ion for intensities above  $\sim 10^{14} \text{ W cm}^{-2}$ . Neither observation is in agreement with the results obtained in the present work, which show no doubly charged ions, and where the only fragmentation product is  $\text{C}_7\text{H}_7^+$  in limited amounts. The latter photodynamics of the toluene molecule is in qualitative agreement with the results of Refs. [143,145,146]. It must be noted, however, that the TOF spectra of Castillejo *et al.* are, in fact, qualitatively very similar to the spectrum measured here when nonlinear effects distort the beam properties as just described. Therefore, there should be a considerable degree of nonlinear distortion in the laser beam of Castillejo *et al.* One reason for this could be that their attenuation method makes use of Glan polarizing prisms. This has the obvious disadvantage that the laser beam has to travel through several centimeters of optical material, probably making their *B*-integral too large.

In the TOF spectra recorded with the  $f = 500 \text{ mm}$  lens, where the beam is not subjected to distortions caused by nonlinear effects, the only species found in measurable quantities are  $\text{C}_7\text{H}_8^+$  and  $\text{C}_7\text{H}_7^+$ . The yields of these two species as a function of the peak intensity in the pulse are shown in Fig. 4.7 (for linear polarization) in double-logarithmic representation.

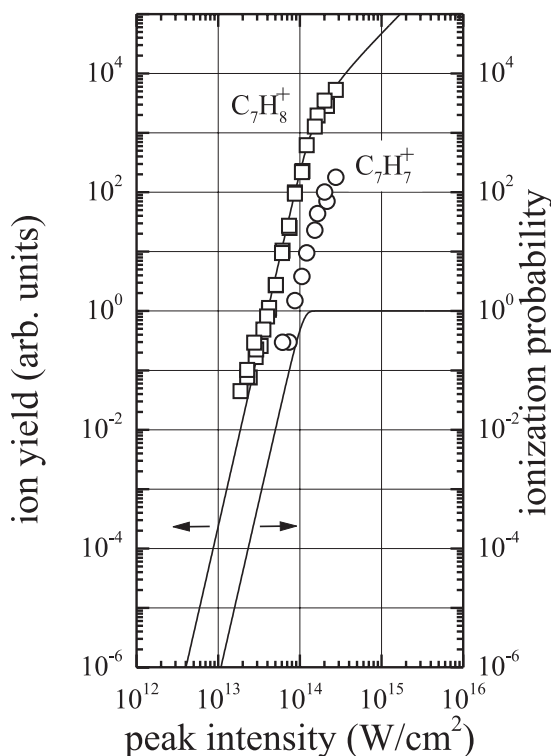


**Figure 4.7:** Ion yields as a function of peak intensity for 800-nm, 80-fs, linearly polarized laser pulses irradiating gaseous toluene. Squares, parent ion,  $\text{C}_7\text{H}_8^+$ ; circles, fragment ion,  $\text{C}_7\text{H}_7^+$ . The solid line passing through the parent ion data (left ordinate axis) is obtained by volume-integrating the ionization probability for a 6-photon process (lower solid curve, right ordinate axis).

The peak intensities are calculated from measured values of the pulse energy, pulse duration, and spatial width of the focus (see Sec. 3.5.2). The ion yields are determined as integrals of the corresponding mass peaks. Because the yield of  $\text{C}_7\text{H}_7^+$  is only a few percent of the parent ion yield, there is no need to correct the ion yields for the presence of the heavy carbon isotope  $^{13}\text{C}$  (natural abundance 1.1%) in the toluene molecule, the ratio be-

tween  $^{12}\text{C}_6^{13}\text{CH}_n^+ / ^{12}\text{C}_7\text{H}_n^+$  being equal to 7.8%. Even for the highest intensities, where the parent ion yield starts deviating from a straight line, this ratio is found for the parent ion and its heavier satellite, indicating that the bending is due to saturation of the ionization process, and that no saturation of the experimental detection setup takes place which could conceivably cause a similar kind of bending.

As Fig. 4.7 shows, the non-saturated  $\text{C}_7\text{H}_8^+$  data points are all on a straight line; a linear fit gives  $5.94 \pm 0.10$  for the slope of this line. Evidently, the parent ion yield increases proportionally to the sixth power of the intensity. This would be in agreement with lowest-order perturbation theory behavior for minimal field intensity; for the 1.55 eV photon energy corresponding to 800-nm radiation, six photons would be the minimum number required to ionize the toluene molecule, which has an ionization energy of  $IE = (8.828 \pm 0.001)$  eV [149]. As already mentioned, the deviation from the straight line of the data points obtained for the highest intensities is due to saturation of the ionization process, i. e., to depletion of the ensemble of neutral toluene molecules. For an intensity-independent generalized six-photon cross section  $\sigma_{(6)}$  (in  $\text{cm}^{12} \text{s}^5$ ), the ionization probability depends on the peak intensity  $I_0$  according to

$$P(I_0) = 1 - \exp \left[ -\sigma_{(6)} \left( \frac{I_0}{\hbar\omega} \right)^6 t_{\text{eff}} \right], \quad (4.4)$$

where the effective pulse duration has been introduced, which for the Gaussian pulse shape can be written as  $t_{\text{eff}} = \int_{-\infty}^{\infty} \exp(-6(t/t_0)^2) dt$  and equals  $\sqrt{(\pi/6)}t_0$  or 35.2 fs. With the saturation intensity  $I_{\text{sat}}$  defined as the intensity for which the ionization probability has a value of  $1 - e^{-1} \approx 0.632$ , the effective six-photon cross section can be written as

$$\sigma_{(6)} = \left( \frac{\hbar\omega}{I_{\text{sat}}} \right)^6 t_{\text{eff}}^{-1}, \quad (4.5)$$

The solid line in Fig. 4.7 represents a best fit to the experimental data points based on Eq. 4.4. In this fit, the volume effect (see Eq. (4.10) below) has been taken into account, assuming the focus to have a Gaussian spatial profile, which is experimentally verified by imaging techniques (see Sec. 3.5.2 and Sec. 4.1.1). From the fit, a saturation intensity of  $I_{\text{sat}} = 1.0 \times 10^{14} \text{ W cm}^{-2}$  and a corresponding generalized six-photon cross section of  $\sigma_{(6)} = 5.9 \times 10^{-183} \text{ cm}^{12} \text{ s}^5$  are found. This value can be assessed by comparing it with a scaling law value [150]. Taking the cubic root of the polarizability ( $12.3 \text{ \AA}^3$ ) as a rough measure of the size of the toluene molecule, a scaling law value of  $\sigma_{(6)} \approx 2.0 \times 10^{-177} \text{ cm}^{12} \text{ s}^5$  is found. The experimental value is more than five orders of magnitude smaller than this scaling law value, but it must be kept in mind that the scaling law was derived for structureless atoms and not for molecules. Furthermore, it must be noted that a six-photon generalized cross section is the square of an effective six-photon dipole matrix element; a difference of five orders of magnitude is thus equivalent to a difference of only  $(10^5)^{1/12}$ , or less than a factor of three, in a dipole matrix element of a single photon transition.

Smith *et al.* [145] have recorded ion mass spectra for benzene, toluene, and naphthalene using both 375-nm, 90-fs and 750-nm, 50-fs pulses (both linearly polarized). Remarkably, the toluene parent ion yield that these authors recorded for 750 nm between  $\sim 2.4 \times 10^{13} \text{ W cm}^{-2}$  and  $\sim 3.5 \times 10^{14} \text{ W cm}^{-2}$  can again be fitted to a curve based on Eq. 4.4 assuming a Gaussian focus; this procedure then gives a saturation intensity of  $3.2 \times 10^{13} \text{ W cm}^{-2}$ . Smith *et al.* note that their 375-nm curves are less steep than their 750-nm curves, and interpret this as indicating an MPI process, although they speculate on the possibility of tunneling ionization. Unfortunately, Smith *et al.* recorded their ionization curves largely in the saturation regime,

where the ion yield has the well-known volume-determined  $I^{3/2}$  dependence on the peak intensity, and only a few points recorded at their lowest intensities are available that could give information on the ionization process. As a result, not much can be said about the order of the ionization process; although their data are not at variance with an order of six, a somewhat different order (e. g. five) could just as well be fitted to their data. In the present work, the increase of the ion yield is followed over almost four orders of magnitude before saturation set in. For a wavelength of 750 nm, Smith *et al.* also observe multiply charged parent ions for intensities above  $\sim 5 \times 10^{13} \text{ W cm}^{-2}$ , whereas the 800-nm spectra observed in the present work do not show multiple ionization up to the highest peak intensity of  $2.8 \times 10^{14} \text{ W cm}^{-2}$ .

In another publication of the Glasgow group [146], it is reported that the molecules 1,3-butadiene, carbon disulphide, deuterated benzene, toluene, and naphthalene are multiply ionized when irradiated with laser pulses with a duration below 90 fs, a wavelength between 750 and 790 nm, and an intensity of up to  $10^{15} \text{ W cm}^{-2}$ ; fragmentation does not occur to any great degree. Doubly and triply charged parent ions are observed for all these molecules (for toluene, the doubly charged parent ion is the highest charge state observed). This behavior is the result of a sequential ionization process, and the authors refer to the sequential mechanism proposed by Lambropoulos [151] for multiple ionization of atoms under similar circumstances. The 1+ level is believed to be due to MPI processes, whereas the higher charge states are ascribed to tunneling and/or over-the-barrier mechanisms. The very modest amount of fragmentation, which essentially consists of hydrogen loss processes, and the notion of an MPI mechanism that creates the 1+ species are in agreement with the present work. The data presented in Ref. [146] show that the tendency towards multiple ionization is least for toluene: even for  $2.9 \times 10^{15} \text{ W cm}^{-2}$ , the height of the 2+ peak is less than 20% of the 1+ peak and the 3+ peak is absent, whereas for all other molecules studied by these authors a larger relative 2+ signal and a clear 3+ peak are already found for lower intensities. In agreement with this finding, in the present work no 2+ signal is observed for toluene for the highest peak intensity of  $2.8 \times 10^{14} \text{ W cm}^{-2}$ .

DeWitt *et al.* [99] have investigated the photoionization and photodissociation of benzene, toluene, ethylbenzene, and *n*-propylbenzene using 780-nm, 170-fs radiation in the intensity range between  $1.0 \times 10^{13}$  and  $3.8 \times 10^{13} \text{ W cm}^{-2}$ , finding limited dissociation (7%) for the highest intensity, but this dissociation is rapidly reduced to noise level for laser intensities that are only a few percent lower. Within a rather limited intensity interval (between  $2.4 \times 10^{13}$  and  $3.8 \times 10^{13} \text{ W cm}^{-2}$ ) they observe an increase of the toluene parent ion yield proportional to  $I^{8.6}$ , whereas for 780 nm one would again expect an ionization order of 6.

Although the  $\text{C}_7\text{H}_8^+$  data points recorded here evidently follow a straight line with an effective slope of six, a description based on only a six-photon MPI process must be incomplete. For the wavelength and intensities used here, a considerable amount of ponderomotive (quiver) energy may be acquired by the electron after it has been freed from the molecular ionic core (see also Sec. 2.3). In practical units, this ponderomotive energy  $U_p$  is given (for  $\lambda = 800 \text{ nm}$ ) by

$$U_p(\text{eV}) = 5.976 \times 10^{-14} I (\text{W cm}^{-2}), \quad (4.6)$$

which, for the range of peak intensities used here, lies between 1.1 and 16.7 eV. The relative ac Stark shift between the ground state and the ionization energy can be considered to be equal to the ponderomotive energy. As a result, channel closing will occur (see Refs. [152] and [153] for similar effects in atoms), and a seven-photon process (not six) would be required (at least during part of the temporal evolution of the pulse) even for the lowest peak intensity, since  $IE + U_p = 8.828 \text{ eV} + 1.1 \text{ eV} = 6.4 \hbar\omega$ . Only for peak intensities below

$7.9 \times 10^{12} \text{ W cm}^{-2}$  could a six-photon process be active during the whole temporal evolution of the pulse. Channel closing would drastically change the order of the MPI process during the temporal evolution of the pulse: for the highest peak intensity applied here, 17 photons would have to be absorbed to reach the ac Stark shifted ionization continuum! As will be demonstrated below, the slope of six observed in the present work is in fact an effective slope brought about by the combined operation of several different MPI processes with orders between 6 and 11 inclusive. In any case the slope of 8.6 observed in the measurements of DeWitt *et al.* within a rather narrow intensity range seems to contradict the present measurements. DeWitt *et al.* noted the unexpected character of their results and speculate on the possibility of above-threshold ionization (ATI), i. e., absorption of more photons than the minimum number required for ionization. They immediately rule out this possibility, however, for three reasons: (1) their slope has a constant value (albeit over a narrow intensity range!), whereas they expect the absorption of additional photons for increasing intensities to increase the slope; (2) dissociation is “essentially absent” for benzene and toluene in their measurements, which indicates that no excess energy is absorbed by the molecule; and (3) no trend in the ionization order is observed for increasing molecular complexity (benzene  $\rightarrow$  toluene  $\rightarrow$  ethylbenzene  $\rightarrow$  *n*-propylbenzene), although they expect the density of states to increase for this series, which would favor ATI.

Because only one molecule is investigated here, not much can be said about argument (3) of DeWitt *et al.* (the influence of molecular complexity on the order of the ionization process). However, inspection of the present results in view of arguments (1) and (2) is most instructive. The results obtained in the present work do seem to deviate slightly from a straight line in a concave way, i. e., before saturation sets in, the slope of the ionization yield can be seen to increase somewhat for increasing intensities, although the average slope is six. Furthermore, a small but significant  $\text{C}_7\text{H}_7^+$  fragmentation signal for intensities beyond  $\sim 6 \times 10^{13} \text{ W cm}^{-2}$  appears. To demonstrate how these observations can be explained as a result of the combined action of several MPI processes with different orders, it will be useful to write the spatio-temporal intensity distribution as  $I(\mathbf{r}, t) = I_0 G(\mathbf{r}) \exp(-(t/t_0)^2)$ , where  $\mathbf{r} = 0$  coincides with the center of the focus and  $G(\mathbf{r} = 0) = 1$ . For a given peak intensity  $I_0(\mathbf{r}) = I_0 G(\mathbf{r})$ , the  $N$ -photon process will be closed and the  $(N + 1)$ -photon channel opened as soon as the intensity has reached the value  $I(t_N)$  given by

$$IE + U_p = IE + 5.976 \times 10^{-14} I(t_N) = N\hbar\omega, \quad (4.7)$$

where the unit of energy is the eV and the intensity is measured in  $\text{W cm}^{-2}$ . (For clarity, sometimes the explicit notation of the spatial dependence of the intensity is omitted.) In other words, the ionization probability per unit of time for a neutral molecule changes order during the temporal evolution of the pulse and is given on the rising edge of the pulse by

$$\begin{aligned} \sigma_{(6)} (I(t) / \hbar\omega)^6 & \quad \text{for } t \leq t_6, \\ \sigma_{(7)} (I(t) / \hbar\omega)^7 & \quad \text{for } t_6 < t \leq t_7, \\ \sigma_{(8)} (I(t) / \hbar\omega)^8 & \quad \text{for } t_7 < t \leq t_8, \\ \dots & \quad \text{etc.,} \end{aligned} \quad (4.8)$$

where the highest order appearing depends on the peak intensity  $I_0$ , and by a similarly decreasing series of orders on the falling edge of the pulse. The quantities  $\sigma_{(N)}$  are the generalized cross section for an  $N$ -photon MPI process, measured in units of  $\text{cm}^{2N} \text{ s}^{N-1}$ .



The ionization probability after the pulse is over is then given by

$$P(I_0) = 1 - \exp \left[ - \left( \int_{-\infty}^{t_6} \sigma_{(6)} \left( \frac{I(t)}{\hbar\omega} \right)^6 dt + \int_{t_6}^{t_7} \sigma_{(7)} \left( \frac{I(t)}{\hbar\omega} \right)^7 dt + \int_{t_7}^{t_8} \sigma_{(8)} \left( \frac{I(t)}{\hbar\omega} \right)^8 dt + \dots \right) \right], \quad (4.9)$$

with the actual number of different orders to be evaluated depending on the peak intensity  $I_0$ ; in Fig. 4.8 this maximum order is plotted as a function of  $I_0$  (cf. Eq. 4.7). In what follows, the generalized cross sections will be considered to have fixed values, i. e., they are taken to be intensity-independent. A calculation of these quantities for a molecule as complex as the

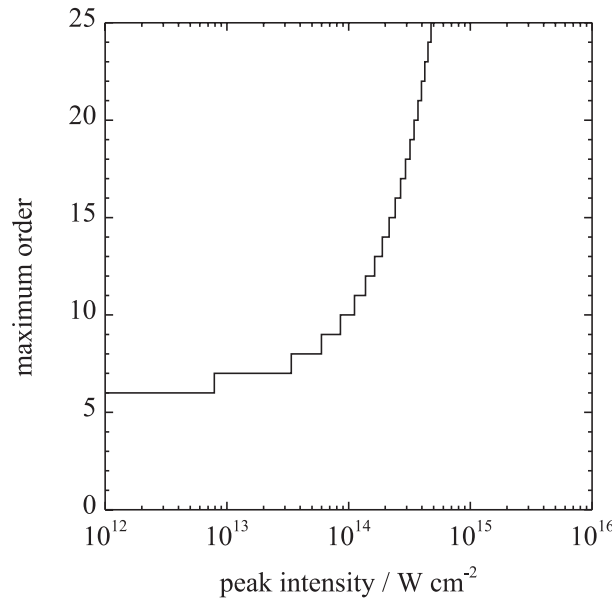


**Figure 4.8:** Channel closing: highest order expected for an MPI process as a function of peak intensity for gaseous toluene and 800-nm radiation.

15-atom toluene molecule is prohibitively complicated; in any case it is far beyond the scope of the present work. But it should be possible to find values for them by comparing those calculations with the experimental data. To do so, the calculation of the spatial integral of  $P(I_0(\mathbf{r}))$  over the whole focal region is required (see also Sec. 2.3); more specifically, the ion yield  $Y(I_0)$  for a given value of the absolute peak intensity  $I_0$  (i. e., the peak intensity in the center of the focus) is given by

$$Y(I_0) \propto \iiint_{\text{all space}} P(I_0(\mathbf{r})) d\mathbf{r} \quad (4.10)$$

As an illustration to the derived multi-order model, Fig. 4.9 shows how the ionization probability per unit of time (as given in Eq. 4.8) changes during the temporal evolution of the pulse for a number of different peak intensities. For peak intensities below  $7.9 \times 10^{12} \text{ W cm}^{-2}$  (where the 6-photon channel would close) the 6-photon process is active during the whole pulse (panels (a) and (b)). For a peak intensity of  $1.0 \times 10^{13} \text{ W cm}^{-2}$  (panel (c)), the 6-photon channel is closed in the center of the pulse, where now a 7-photon process is active; the 6-photon process is active in the wings only. The size of the discontinuous jump depends

on the ratio between  $\sigma_{(6)}$  and  $\sigma_{(7)}$ . For higher peak intensities (panels (d) and (e)), the activity of the 6-photon process is pushed more and more into the wings of the pulse, and the 7-photon process gradually starts dominating the ionization process. This process is closed in turn at an intensity of  $3.4 \times 10^{13} \text{ W cm}^{-2}$ . For a peak intensity beyond this value (see panel (f)), the ionization process is composed of three different orders; a 6-photon process in the far wings of the pulse, a 7-photon process in the intermediate intensity regimes, and an 8-photon process in the center of the pulse, where the intensity is highest. In Fig. 4.10

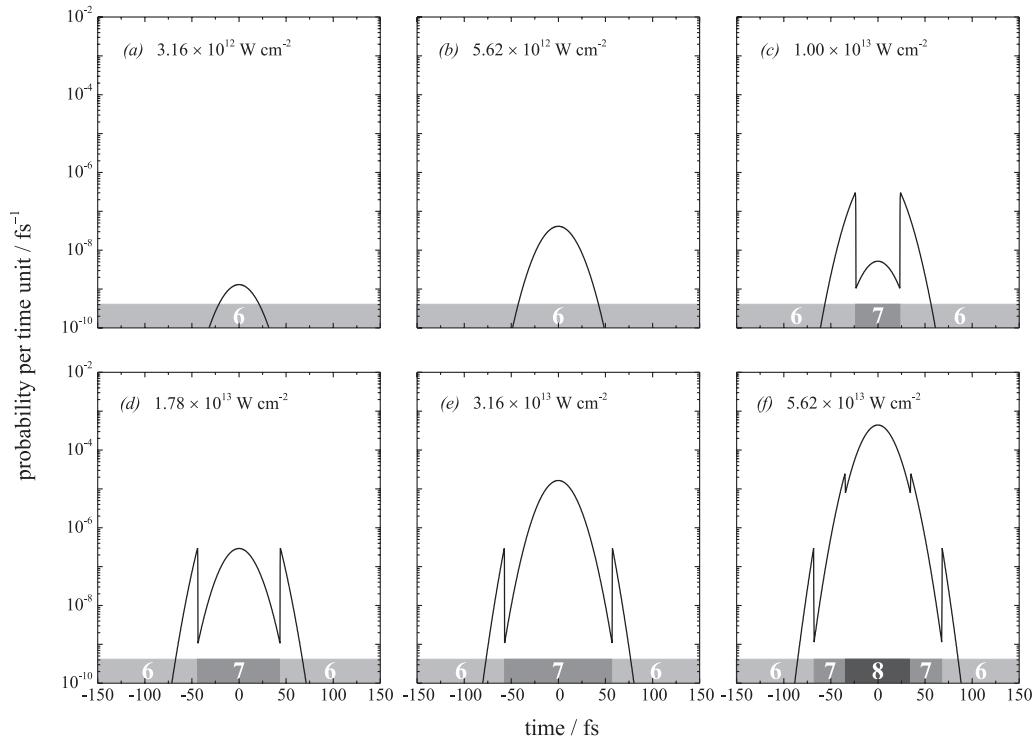


**Figure 4.9:** Ionization probability per unit of time of a neutral gaseous toluene molecule for various peak intensities of 800-nm, 80-fs, linearly polarized laser pulses. The discontinuities are due to channel closing. The order of the process is indicated in the strip at the bottom of each graph.

the time-integrated ionization probability (Eq. 4.9) is shown as a function of peak intensity (lower solid line, right ordinate axis). As a result of the discontinuities shown in Fig. 4.9, this probability has jumps at the channel-closing intensities as given by Eq. 4.7, although these jumps are somewhat smoothed due to the time integration. The volume integral according to Eq. 4.10 is given by the solid line passing through the parent ion data in Fig. 4.10. The agreement with the experimental data is almost perfect. Values for the generalized cross sections attained by fitting to these data are given in Tab. 4.2. Remarkably, it must be concluded that the inclusion of higher-order MPI processes still leads to an effective slope of 6. In the calculations introduced here, orders up to 11 are included. Still, the curve through the data points in Fig. 4.10 never has a slope steeper than 7.9; this slope is found for a peak intensity of  $9.4 \times 10^{13} \text{ W cm}^{-2}$ . Perhaps the observation by DeWitt *et al.* [98] of a slope of 8.6 in a rather narrow intensity range corresponds to such a sector in the parent ion yield curve. The considerations that led to the decision to choose the eleventh order as the highest order deserve some discussion. Note that on a logarithmic scale the intensity intervals between two successive channel-closing intensities become smaller and smaller for increasing intensities (see Fig. 4.8). For the highest peak intensities employed, orders up to 17 could be expected in principle. Then values for a set of 12 different generalized cross sections have

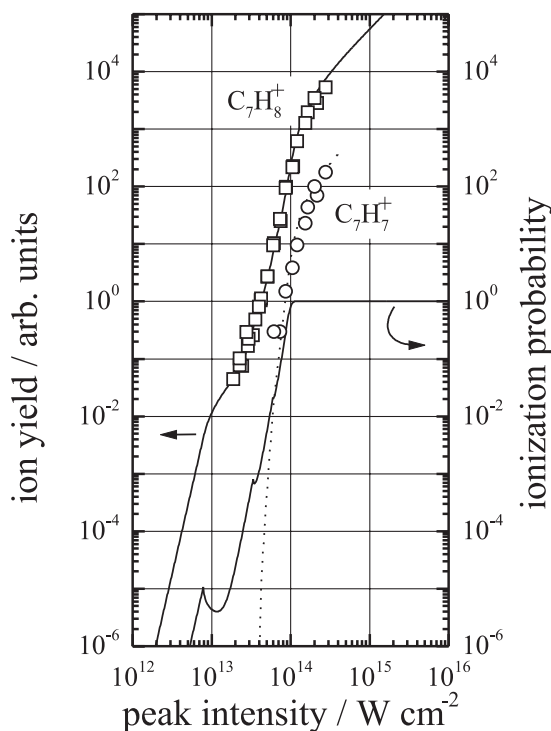


**Figure 4.10:** Ion yields as a function of peak intensity for 800-nm, 80-fs, linearly polarized laser pulses irradiating gaseous toluene. Squares, parent ion,  $C_7H_8^+$ ; circles, fragment ion,  $C_7H_7^+$ . The solid line passing through the parent ion data (left ordinate axis) is obtained by volume-integrating the ionization probability that results from the combined action of 6-, 7-, 8-, 9-, 10-, and 11-photon processes (lower solid curve, right ordinate axis). The jumps in the ionization probability curve are the result of channel closing (cf. Fig. 4.9). The dotted line shows the expected effective  $C_7H_7^+$  fragment ion yield on the assumption that the internal energy of the toluene cation equals the ponderomotive energy of the electron.

**Table 4.2:** Generalized MPI cross sections  $\sigma_{(N)}$  with orders  $N$  between 6 and 11 of gaseous toluene under the influence of 800-nm, 80-fs, linearly polarized laser pulses. The quantities  $\Lambda_N$  defined as  $\Lambda_N = -(1/N) \log_{10} \sigma_{(N)}$  reach a constant value for the highest orders  $N$ , which suggests that tunneling ionization sets in (cf. Ref. [151]) for intensities close to the saturation intensity (see text).

order $N$	generalized MPI cross section $\sigma_{(N)}$	$\Lambda_N = -\frac{1}{N} \log_{10} \sigma_{(N)}$
6	$3.1 \times 10^{-181} \text{ cm}^{12} \text{ s}^5$	30.0
7	$3.0 \times 10^{-215} \text{ cm}^{14} \text{ s}^6$	30.6
8	$6.4 \times 10^{-248} \text{ cm}^{16} \text{ s}^7$	30.9
9	$1.4 \times 10^{-280} \text{ cm}^{18} \text{ s}^8$	31.1
10	$5.4 \times 10^{-313} \text{ cm}^{20} \text{ s}^9$	31.2
11	$2.0 \times 10^{-344} \text{ cm}^{22} \text{ s}^{10}$	31.2

to be fitted. However, some arguments against including orders even higher than 11 can be given. First, the eleventh-order channel-closing intensity is at  $1.4 \times 10^{14} \text{ W cm}^{-2}$ , less than a factor of two away from the highest intensity available in this work, and the experimental data show that saturation already sets in for intensities around  $\sim 10^{14} \text{ W cm}^{-2}$ . The more one penetrates into the saturation regime, the more the shape of the fitting curve is determined by volume effects, and, as a result, the shape of the fitting curve becomes increasingly immune to the value of very high-order ( $N > 10$ ) generalized cross sections. In a self-consistent way, if the highest order included is  $N_{\text{max}}$ , the values for  $\sigma_{(6)}, \sigma_{(7)}, \dots, \sigma_{(N_{\text{max}})}$  have to be chosen so that they describe an ionization process that saturates for a peak intensity that is lower than the ( $N_{\text{max}}$ )-photon channel-closing intensity. The values given in Tab. 4.2 satisfy this condition. Second, the picture of an ever increasing MPI order for increasing intensities must break down at some point. After all, the Keldysh adiabaticity parameter starts to become smaller than unity at least during the central part of the pulse for peak intensities beyond the value  $7.4 \times 10^{13} \text{ W cm}^{-2}$  (the 9-photon channel closes at a slightly higher intensity,  $8.6 \times 10^{13} \text{ W cm}^{-2}$ ). Tunneling ionization and/or over-the-barrier processes could then, at some point, be expected to take over in the center of the pulses for the highest intensities, with pure MPI processes still being active in the wings of the pulse. However, the value of unity for the Keldysh parameter should not be taken as “a strict demarcation line” but rather as a “characteristic region”, as was stressed by Lambropoulos [151], who also showed that a constant value (independent of  $N$ ) of the quantity  $\Lambda_N$ , defined as  $\Lambda_N = -(1/N) \log_{10} \sigma_{(N)}$ , must be related to tunneling. Inspection of these quantities in the case treated here (see Tab. 4.2) show that they do have a tendency to approach some limit for increasing  $N$ , although they depend more strongly on  $N$  than in the hydrogen case that is described in Ref. [151]. In the model calculations presented in this work, tunneling and/or over-the-barrier processes are not included; instead, for all peak intensities, the order of the process is taken as being equal to the lowest possible order, taking into account channel closing. Tunneling could be thought of as the simultaneous action of several processes with different orders, not just the lowest possible order as is the case in this model. Once within the tunneling regime, the contributions of all these different processes become comparable. It could be demonstrated that the inclusion of MPI processes with (lowest possible) orders higher than 6 can still produce an effective slope of six, and that results of this procedure are in agreement with the experimental data obtained in this work. This justifies replacing the whole set of conceivable orders by merely the lowest-order-perturbation theory (LOPT) order, which in turn implies that tunneling is not a very dominant mechanism here. It must be noted that tunneling and/or over-the-barrier processes cannot be completely excluded as long as these field processes take place for intensities close to the saturation intensity, where the experimental ion yield is mainly determined by volume effects. If tunneling and/or over-the-barrier processes contribute to the ionization process at all, their significance to the ionization process is confined to a narrow intensity regime, somewhere between  $\sim 7.4 \times 10^{13} \text{ W cm}^{-2}$  (where the adiabaticity parameter starts falling below unity) and  $\sim 1 \times 10^{14} \text{ W cm}^{-2}$  (the experimental saturation intensity).

As mentioned above, DeWitt *et al.* measured a negligible amount of fragmentation in their toluene experiments and used this observation as an argument *against* absorption of excess photons. In the experiments presented here, a clear signal from the fragmentation product  $\text{C}_7\text{H}_7^+$  (see Figs. 4.5 and 4.7) *is* observed, which becomes detectable for intensities above  $\sim 6 \times 10^{13} \text{ W cm}^{-2}$ . It will be demonstrated, how the fragmentation data obtained in the present work support the multiple-order MPI model with orders up to 11 inclusive derived here. Fragmentation of the excited toluene cation is known [154] to produce two isomers of

$C_7H_7^+$ , tropylium and benzylium. Since the TOF method merely detects mass/charge ratios, this fragmentation can be symbolically written as



The lowest energy secondary fragmentation process is the breakdown of the  $C_7H_7^+$  formed into  $C_5H_5^+$  and  $C_2H_2$  [154]. The appearance energy of the  $C_5H_5^+$  fragment starting from the neutral toluene molecule is 14.55 eV, but for detection times of the order of 10  $\mu\text{s}$ , it appears only beyond  $\sim 16$  eV [154]. In the experiments presented here, the  $C_5H_5^+$  fragment is not observed; this fact is consistent with the multiple-order MPI model, as will be shown below. Rate-energy functions  $k(E_{\text{int}})$  for the unimolecular decay reaction (4.11) are given in Refs. [154] and [155], where the internal energy dependence of the fragmentation was investigated by photoelectron-photoion coincidence spectroscopy (PEPICO) starting from neutral toluene. In Ref. [154], an RRKM expression for  $k(E_{\text{int}})$  was fitted to the breakdown curve of  $C_7H_8^+$  close to the onset of reaction (4.11) in the energy range between  $11.2 \text{ eV} \leq IE + E_{\text{int}} \leq 12.1 \text{ eV}$ . The authors of Ref. [154] conclude that their results can only be explained by two competitive unimolecular decay processes, and identify these processes as the formation of tropylium and benzylium. For  $IE + E_{\text{int}} \leq 12.1 \text{ eV}$ , the formation of tropylium dominates. For higher internal energies, the fitted RRKM curves predict that the faster but more endothermal benzylium formation is favored. For  $IE + E_{\text{int}} \approx 12 \text{ eV}$ , the total rate is about  $10^5 \text{ s}^{-1}$ , and extrapolating their RRKM results, these authors predict the rate to rise to above  $10^8 \text{ s}^{-1}$  for  $IE + E_{\text{int}} \approx 13.7 \text{ eV}$ . The authors of Ref. [155] also used the PEPICO method, but come to the conclusion that the rate reaches a constant value of  $k = (1.5 \pm 0.4) \times 10^5 \text{ s}^{-1}$  for excitation energies of the toluene parent ion exceeding 3.7 eV (see Fig. 4.11). In the present experiment, no  $C_7H_7^+$  signal is observed for peak intensities below  $\sim 6 \times 10^{13} \text{ W cm}^{-2}$ , and beyond this threshold intensity the yield is about 3% of the parent ion yield, this ratio being almost independent of the peak intensity. For a correct interpretation of this fragmentation yield, the so-called kinetic shift must be taken into account; since one is dealing here with fragmentation times that are comparable to the time between the creation of an ion and its detection (the time of flight), fragmentation processes take place during the flight of the ions through the TOF spectrometer. The time of flight of the  $C_7H_7^+$  fragment will depend on (i) which sector of the TOF spectrometer the fragmentation takes place in and (ii) what amount of extra kinetic energy is gained by the  $C_7H_7^+$  fragment as a result of the fragmentation. In order to clarify the fragmentation data obtained here, the TOF spectra are simulated by making trajectory calculations for toluene ions that undergo a fragmentation process governed by a single exponential decay in time. As described in Ref. [154], the amount of translational energy that is deposited in the  $C_7H_7^+$  fragment as a result of the fragmentation reaction (4.11) is very small; at most 10% of the excess energy in the parent ion is converted into translational energy of the products, and the light hydrogen atom will carry away almost 99% of this energy. As a result, the translational energy deposited in the  $C_7H_7^+$  fragment is less than the thermal kinetic energy of the parent ion it is created from, and it is neglected in these simulations. Indeed, the experimental widths of the peaks at  $M = 91$  and  $M = 92$  are not significantly different, and they agree very well with the simulations, assuming an initial 298-K thermal velocity distribution of the neutral toluene molecules. Thus, for a fragmentation process taking place in the field-free drift sector of the spectrometer (where the ions spend most of their time), the difference in speed between the  $C_7H_7^+$  fragment and the parent ion is negligible, and the time of flight of this fragment will therefore be identical to that of a parent ion, i. e., as if the parent ion did not decay at all. The simulations show that the observed ratio of 3% between the heights of the peaks at  $M = 91$  and  $M = 92$

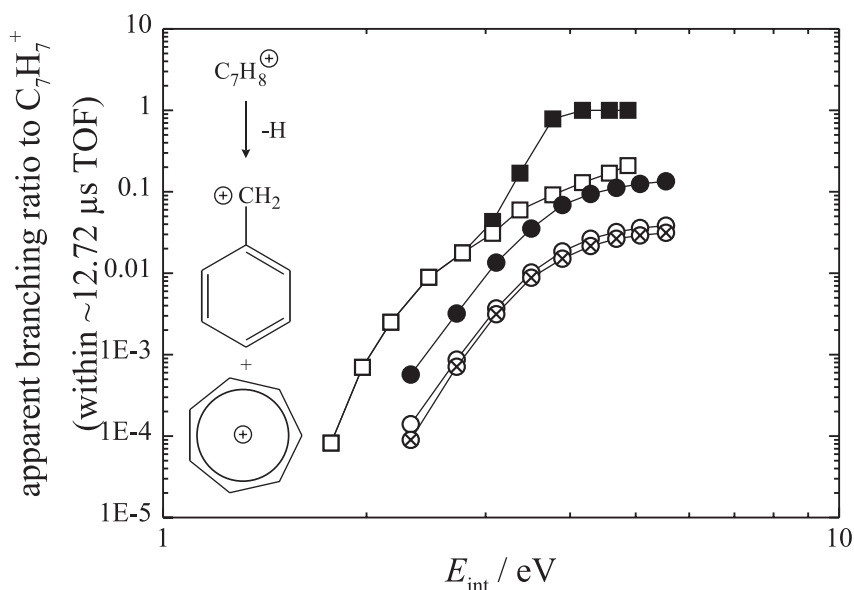


**Figure 4.11:** Calculated apparent branching ratios to  $C_7H_7^+$  as a function of internal energy of the ion, determined from TOF trajectory simulations. For increasing internal energies, the decay rate of the excited toluene parent ion increases from  $\sim 10^3 \text{ s}^{-1}$  at  $E_{\text{int}} \approx 2.3 \text{ eV}$  to  $\sim 10^5 \text{ s}^{-1}$  at  $E_{\text{int}} \approx 5.5 \text{ eV}$ . Because the corresponding decay times are long in comparison to the time of flight of the parent ion in this setup ( $\sim 12.72 \mu\text{s}$ ), fragmentation takes place during the whole trajectory inside the TOF machine. Because the ejected neutral fragment is the light H atom and the amount of kinetic energy deposited into the products is known to be small [154], recoil effects have a negligible influence on the velocity of the fragment ion  $C_7H_7^+$ . Therefore, the time of flight of all fragments created by fragmentation in the drift tube is indistinguishable from the time of flight of an unfragmented parent ion. The resulting apparent branching ratio is shown in this figure for the five different sets of decay rates (squares cf. Ref. [154]; filled squares, tropylium and benzylium; open squares, tropylium only; filled circles,  $C_7H_7^+$ , cf. Ref. [155]; open circles,  $k/3.75$ ; crossed circles,  $k/4.50$ ). The latter set has been found to be in good agreement with the present fragmentation data.

corresponds to a fragmentation rate  $k = 0.4 \times 10^5 \text{ s}^{-1}$ , but that in spite of this seemingly modest amount of fragmentation the real fragment ratio is much higher; in fact, during the total flight time of  $t_{92} = 12.86 \mu\text{s}$  for the parent ion as many as  $\sim 40\%$  ( $= 1 - e^{-k \cdot t_{92}}$ ) of the parent ions undergo dissociation.

In Fig. 4.10 an (apparent) fragment ion yield curve (dashed line) is shown that is numerically calculated using the rates given in Ref. [155] after dividing these by a factor of 4.5. The calculation is made as follows. To make use of known rate-energy curves, one needs to know the amount of internal energy deposited by the photoionization process into the toluene parent ion. An obvious way to deposit energy in the ion is by recollision of the electron just after it is freed from the ionic core and starts its quiver motion. Such a recollision model was developed by Corkum *et al.* [156] to explain higher-harmonic generation. For a monochromatic wave and an atomic ionic core (i. e., a core of negligible spatial extent), the maximum return energy of the electron is  $\sim 3.17$  times the ponderomotive energy, but already in the first few cycles the electron can return to the vicinity of the ion with a considerable amount of kinetic energy. In the case of molecules, the ionic core that the electron returns to is still in the nuclear configuration of the neutral molecule in its ground state. To explain the fragmentation of the toluene cations, it will now be assumed that recollision of the electron and the core

will bring a certain amount of excess energy into the system, and this amount is assumed to equal the ponderomotive energy  $U_p$  as given in Eq. 4.6, where an intensity is taken that prevailed at the moment of ionization to calculate  $U_p$ . Then, after the laser pulse is over, this excess energy is assumed to be rapidly converted into vibrational energy of the unperturbed toluene cation in its ground electronic state, so that finally the ponderomotive energy at the time of photoionization becomes available to the toluene cation as internal energy. For each peak intensity, the internal energy distribution for the created ensemble of toluene cations is numerically determined, taking the volume integral into account. Finally, using trajectory calculations, the fraction of cations could be ascertained that will end up in the peak corresponding to  $C_7H_7^+$  after their flight through the TOF spectrometer. Fig. 4.10 shows that the agreement between the fragmentation yield curve thus calculated and the experiment is very satisfactory, including the detection threshold at  $\sim 6 \times 10^{13} \text{ W cm}^{-2}$ . At this point the absence of the  $C_5H_5^+$  fragment should be considered again. For a detection time in the order of  $10 \mu\text{s}$ , the appearance energy of this fragment starting from the neutral toluene molecule is  $\sim 16 \text{ eV}$  [154]. This amount of internal energy could just be reached with an 11-photon absorption process. However, as a result of saturation, few molecules survive the rising edge of the pulse to be ionized with so many photons. The simulations presented here show that even for the highest peak intensity available, the fraction of molecules with an internal energy of  $15.75 \text{ eV}$  or higher is of the order of  $10^{-6}$ . Therefore, the absence of the  $C_5H_5^+$  fragment confirms the model derived here, in which saturation effectively suppresses the occurrence of MPI processes with orders beyond 11. If tunneling were very dominant, the tenth and lower order processes would be accompanied by non-negligible contributions from eleven-photon processes, but the absence of the  $C_5H_5^+$  fragment leaves no doubt that 11-photon MPI must be of negligible importance. Again, it is seen that the LOPT-MPI picture describes the obtained data adequately. Unfortunately, one can only roughly estimate the amount of excess energy that can be deposited into the ion as a result of recollisions, but the estimation of this excess energy by the ponderomotive energy gives a satisfactory reproduction of the measured fragmentation data, even though this estimation is rather on the low side in relation to the  $3.17 U_p$  maximum recollision energy found for the atomic case. The non-maximum amount of recollision kinetic energy can perhaps be explained by the fact that the toluene ionic core is greater in extent than an atomic ion, so that collisions between an accelerating quasi-free electron and the ionic core before the electron ever managed to reach its first turning point are conceivable, which could reduce the amount of kinetic energy the electron can acquire from the field. In any case, the absence of the  $C_5H_5^+$  fragment clearly proves that the amount of internal energy deposited into the ion must be limited. In particular, this fragment is also absent for the highest peak intensity of  $2.8 \times 10^{14} \text{ W cm}^{-2}$  available here, in which case a ponderomotive energy of more than  $16 \text{ eV}$  could be acquired by the electron. In this model, it is the intensity at the moment of ionization that is taken to calculate the ponderomotive energy, not the peak intensity. With the maximum peak intensity of  $2.8 \times 10^{14} \text{ W cm}^{-2}$  the saturation regime can be easily reached, where there is a large difference between the peak intensity and the highest intensity on the rising edge of the pulse that still leads to non-negligible amounts of ionization. The lack of  $C_5H_5^+$  even for the highest intensities supports the model in which the electron's kinetic energy is calculated with the intensity that prevailed at the moment of ionization, and also suggests that the interaction between the electron and the ionic core takes place within a few optical cycles after the ionization took place. Successive channel closing and LOPT-MPI processes of orders up to 11 inclusive are all taken into account in the calculations of the internal energy distribution presented here, and the resulting fragmentation is in good agreement (within a factor of the order of unity)

with the rate-energy curve of Ref. [155]. Therefore, it can be concluded that the photoionization of the toluene molecule using linearly polarized, 800-nm, 80-fs laser pulses is strongly dominated by LOPT-MPI processes, taking successive channel closing into account.

To shed more light on the ionization mechanism, polarization-dependent measurements are made in addition. In Fig. 4.12 the parent ion and  $C_7H_7^+$  yields are shown as a function of intensity for circularly polarized light normalized to the same (arbitrary) scale as the ion yields for linearly polarized light. The data in Fig. 4.12 are taken under the same conditions as the data of Fig. 4.10; all measurements involved one and the same quarter-wave plate in the beam. To change the polarization from linear to circular, the fast axis of this quarter-

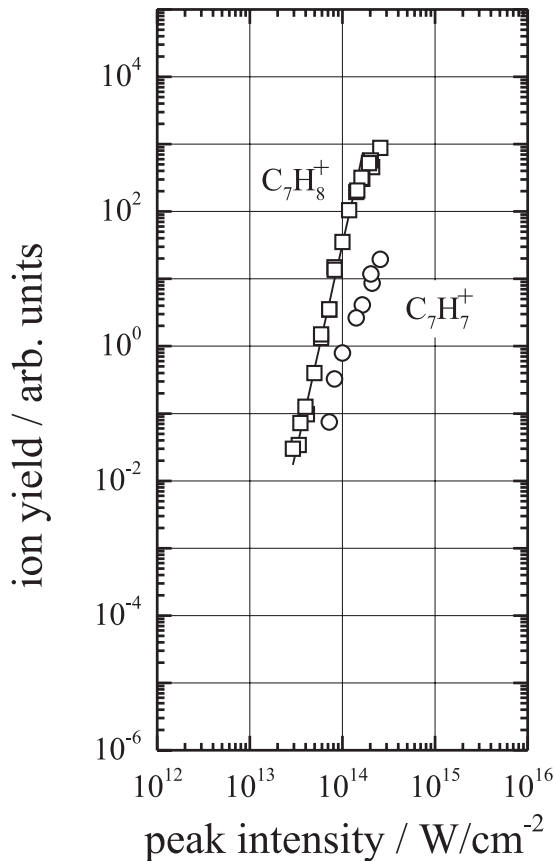


**Figure 4.12:** Ion yields as a function of peak intensity for 800-nm, 80-fs, circularly polarized laser pulses irradiating gaseous toluene. Squares, parent ion,  $C_7H_8^+$ ; circles, fragment ion,  $C_7H_7^+$ .

wave plate is moved from  $0^\circ$  (i. e., parallel to the linear polarization direction of the laser) to  $45^\circ$ . For circular polarization, the saturation intensity is somewhat higher than in the linear polarization case,  $\sim 1.4 \times 10^{14} \text{ W cm}^{-2}$ . This value is determined as the peak intensity for which the parent ion yield is as high as it is for the saturation intensity using linear polarization. Due to the higher saturation intensity, fewer data points can be recorded in the saturation regime, which impedes accurate determination of the saturation intensity by fitting a curve to the data points. In the circular polarization case, an effective  $I^6$  dependence is again found before saturation is reached; fitting a straight line through the non-saturated part of this curves gives a slope of  $6.14 \pm 0.17$ . On the basis of this similarity between the curves, one other measurement (see Fig. 4.13) is made in which the intensity is kept fixed at the value  $8.5 \times 10^{13} \text{ W cm}^{-2}$ , and parent ion yields are recorded as a function of the ellipticity



of the light by varying the angle  $\theta$  between the fast axis of the quarter-wave plate and the direction of the linear polarization of the laser. With  $Y_{\text{lin}}$  and  $Y_{\text{circ}}$  denoting the parent ion

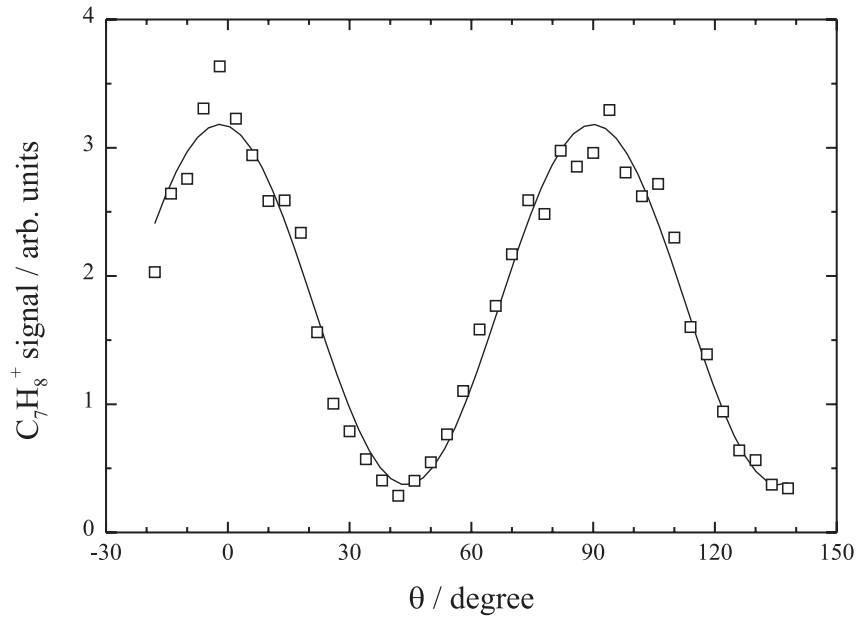


**Figure 4.13:** Parent ion yield as a function of the ellipticity for 800-nm, 80-fs, laser pulses irradiating gaseous toluene, for a fixed peak intensity of  $8.5 \times 10^{13} \text{ W cm}^{-2}$ , measured by varying the angle  $\theta$  between the fast axis of the quarter-wave plate and the polarization direction of incoming linearly polarized light (see text).

yields for, respectively, linear polarization ( $\theta = 0^\circ$ ) and circular polarization ( $\theta = 45^\circ$ ) these data are well described by

$$Y(\theta) = Y_{\text{circ}} + (Y_{\text{lin}} - Y_{\text{circ}}) \cos^2(2\theta), \quad (4.12)$$

and from a fit to the data the ratio  $(Y_{\text{lin}}/Y_{\text{circ}})^{1/6} = 1.4$  can be determined, which confirms the ratio between the saturation intensities for linear and circular polarization.

As a consequence of the higher saturation intensity for circular polarization, ionization processes can now take place at intensities for which there are no longer any neutral molecules left in the linear case. This implies that, although field-ionization mechanisms could be excluded for the case of linear polarization, the ionization mechanism will now have to be reconsidered in view of the higher intensities the molecules can be exposed to with circular polarization. The 11-photon channel closes at  $1.38 \times 10^{14} \text{ W cm}^{-2}$ , a value close to the saturation intensity. Within the framework of the multiple-order model described above, one could now include the twelfth, thirteenth, etc. orders and try to find values for the corresponding generalized cross sections in a consistent way as described before. Knowing that the eleventh order was already needed for the case of linear polarization, it is immediately clear that at least the twelfth order would now have to be included. This 12-photon channel would start to be active from the 11-photon channel-closing intensity of  $1.38 \times 10^{14} \text{ W cm}^{-2}$ , which is close to the experimental saturation intensity. Because a substantial fraction of the molecules is always ionized for intensities beyond the saturation intensity, a non-negligible number of toluene cations would then be formed with internal energies between  $8.2 \text{ eV}$  ( $11\hbar\omega - IE$ ) and  $9.8 \text{ eV}$  ( $12\hbar\omega - IE$ ). Such internal energies would be more than enough to see the secondary fragment  $\text{C}_5\text{H}_5^+$ , but this species is *not* observed in this experiment! Within the scenario of a recolliding electron bringing an excess energy of the order of the ponderomotive

energy into the cation, the lack of the secondary fragment,  $\text{C}_5\text{H}_5^+$ , for the circular polarization case in spite of the higher intensity can be made plausible by the fact that the semi-classical electron trajectories are now different. For circular polarization, the trajectory of a free electron is like an outgoing spiral, and it never really returns to the position it started at, as it could do in the linear polarization case. This may hinder the energy deposition mechanism.

As already mentioned, for a Keldysh adiabaticity parameter of the order of unity, as is the case in the present work, both MPI and field-ionization mechanisms could be anticipated. For (poly)aromatic molecules the simultaneous occurrence of the two mechanisms has been deduced from the structure of the photoelectron spectra [148]. The reduction in the ion yield observed here for circular polarization could be made plausible for both mechanisms. For the case of MPI using circular polarization, the selection rules for the magnetic quantum number  $M_J$  ( $J$  being the total angular momentum of the particle to be ionized) prescribe that  $\Delta M_J = +1$  or  $-1$  (the sign depending on the helicity of the polarization, i. e., left- or right-hand) for each intermediate absorption step. The reduction may then be ascribed to the reduced number of states that is addressable under this condition in comparison to the linear case, for which the less stringent selection rule  $\Delta M_J = 0, \pm 1$  applies. In a perturbative, non-resonant picture, the generalized cross section is proportional to a  $(K - 1)$ -fold summation of probability amplitudes squared ( $K$  being the lowest number of photons required for ionization), with each summation extending over all allowed states (Ref. [150] describes the atomic case). Clearly, this sum will be smaller as the selection rules become more stringent. Therefore, insofar as this atomic MPI picture holds for the molecular case, a reduction can be rationalized (see Ref. [157] for a similar effect in He). However, a reduction could also be compatible with a field-ionization mechanism. It must be noted that, for equal intensities, the peak electric field strength for  $\varepsilon = 0$  (linear polarization) is a factor of  $\sqrt{2}$  larger than the peak electric field strength for  $\varepsilon = 1$  (circular polarization). Experiments with Ne and Xe using 1053-nm, 1.9-ps pulses in the intensity range  $10^{13}$  to  $10^{15}$   $\text{W cm}^{-2}$  [158] have shown that singly charged ions of these noble gases are produced by a tunneling ionization mechanism, and that a change of the polarization from linear to circular for a fixed intensity leads to a significant decrease of the ion signal. For the whole intensity range studied in Ref. [158], however, the original ion signal is regained if the change in polarization from linear to circular is accompanied by an increase of the intensity by a factor of 1.5 (for Ne) or 1.7 (for Xe), and these factors are shown to be compatible with ADK tunneling theory [159]. For an over-the-barrier process for which the frequency of the light field is irrelevant (see Ref. [158]), the ionization probability depends only on the field strength, so that a factor of exactly two would be expected in such a case. (Note that in order to have equal electric field strengths for both polarizations, the intensity used in the circular polarization case needs to be *two* times higher than in the linear polarization case.) For molecules, the situation must be more complicated, due to orientational effects. For small molecules, for instance, it has been shown that the ionization probability for linear polarization may depend on the orientation of the molecule in the field [160–162]. Such orientational effects play a negligible role here as is evident from the following argumentation that is based on the assumption that the light field does not align the toluene molecules, so that their orientation in space can be taken random and frozen during the whole temporal evolution of the pulse. If a linearly polarized field is then applied, there will always be a limited fraction of the toluene molecules present within the detection volume for which the orientation with respect to the electric field happens to be optimal for ionization. If a circularly polarized field (with the same peak field strength) is applied, a larger fraction of the molecules can be addressed, due to the constantly changing orientation of the electric field vector in time, so that ion signal is

expected to increase. Apparently such orientational effects, if present at all, are completely counteracted by the reduced overall ionization efficiency of the circularly polarized light.

The results of the present experiment were obtained in an attempt to elucidate the ionization and fragmentation mechanism of a medium-sized organic molecule. In general, this mechanism can have both MPI and field aspects. It could be shown that the photoionization of the toluene molecule in the gas phase under the influence of 80-fs, 800-nm, linearly polarized laser pulses with peak intensities up to  $2.8 \times 10^{14} \text{ W cm}^{-2}$  is well described by a multiple-lowest-perturbation-order MPI model where orders up to 11 are included and channel closing is taken into account. Tunneling and/or over-the-barrier mechanisms are shown to be of minor importance. This ionization mechanism is in agreement with the observed effective sixth-order dependence of the parent ion yield on the intensity. An electron recollision model in which an excess energy of the order of the ponderomotive energy is brought into the toluene cation is shown to be in good agreement with existing literature data on the internal energy dependence of the fragmentation of the toluene cation into  $\text{C}_7\text{H}_7^+$  and H. The general reduction of the ion yield that is observed when circular polarization is applied and the lack of the secondary fragmentation product,  $\text{C}_5\text{H}_5^+$ , can be explained by the reduced recollision probability of the electron in this case. It has also been demonstrated that a low amount of non-linear distortion of the beam, as expressed by the  $B$ -integral, is of paramount importance for molecular photoionization and photofragmentation experiments: higher charge states and extensive fragmentation are easily observed if this  $B$ -integral grows above generally accepted upper limits [163–165].

## 4.2.2 Influence of continuum generation on the fragmentation of toluene

After the comprehensive discussion of the ionization mechanism of toluene in intense laser fields, a closer look will be now taken at the photofragmentation behavior of this molecule which is also a subject of much dispute in the literature. With Fourier-limited pulses in the NIR ( $\lambda \approx 800 \text{ nm}$ ), strong fragmentation takes place only at intensities beyond  $\sim 10^{15} \text{ W cm}^{-2}$  [146]. To shed light on the fragmentation behavior at lower intensities, the temporal shape of the laser pulses is varied by increasing the laser intensity to which the  $\text{CaF}_2$  entrance window of the vacuum system is exposed. This induces nonlinear effects that lead to a broadening of the power spectra of the pulses. In general, for an intense laser beam with wavelength  $\lambda$  passing through a material with nonlinear refractive index  $n_2$ , a critical power  $P_{cr}$  exists that is required for self-focusing to overcome the diffractive spreading of the beam in this material. The value of  $P_{cr}$  is, according to Ref. [166], given by

$$P_{cr} = \frac{c \varepsilon_0 \lambda^2}{8\pi n_2}. \quad (4.13)$$

As stated in Ref. [166] “it is the beam *power* that must exceed a certain threshold for self-focusing, not the beam intensity. Thus if a beam of a certain power  $P < P_{cr}$  is focused with a lens to create a very large intensity, self-focusing will not occur, simply because the reduction in beam diameter increases the diffractive spreading that must be overcome to realize a net focusing.” For an 800-nm laser beam in  $\text{CaF}_2$  ( $n_2 = 1.9 \times 10^{-16} \text{ cm}^2 \text{ W}^{-1}$ ), as is the case in the present work,  $P_{cr}$  amounts to 3.6 kW. The power levels used in the present experiment vary between 2 GW and 15 GW, i. e. about six orders of magnitude larger. Therefore, it is possible for self-focusing to take place in the  $\text{CaF}_2$  window. Because the length of the beam path inside the  $\text{CaF}_2$  window is only 2 mm, filamentation, i. e. the laser

beam breaks up into a filamentary structure as a result of the growth of small perturbations of the laser wave front [167], does not occur. According to investigations of A. Brodeur and S.L. Chin [124,168], ultrafast white-light continuum generation is triggered by self-focusing in transparent condensed media with a dependence on the bandgap of the media. As shown by A. Brodeur and S.L. Chin [124], the process of self-focusing, which is induced by a positive contribution to the index of refraction according to  $n = n_0 + \gamma \cdot I$ , and occurs simultaneously with continuum generation, is counteracted by the negative contribution to the index of refraction that arises from the electrons that are promoted by an intense laser pulse from the valence band into the conduction band. Clearly, the larger the bandgap, the more intensity is required to promote enough electrons into the conduction band to stop the self-focusing. All in all, therefore, one expects the generated continuum to be stronger for materials with a larger bandgap. Since  $\text{CaF}_2$  has a quite large bandgap of 10.2 eV [124], it is particularly suited for continuum generation. This effect is exploited here to study the fragmentation of toluene. For this purpose, several mass spectra of gaseous toluene and the corresponding wavelength spectra are taken as a function of the intensity to which the  $\text{CaF}_2$  entrance window is exposed; the applied laser radiation has a fundamental wavelength of 800 nm (see Fig. 4.14). The recorded wavelength spectra are expected to be somewhat broader than those at focus, because the radiation has to pass through the exit window of the vacuum chamber before it is analyzed by the fiber spectrometer. Since the focus is centered between the entrance and the exit window and both windows are essentially identical, it can be assumed that the amount of spectral broadening in the second  $\text{CaF}_2$  window is comparable to that in the entrance window. Therefore, the actual light pulse interacting with the toluene molecules exhibits a frequency spectrum, the broadening of which is increased only by half. The intensity to which the entrance window is exposed is varied by changing the pulse energy by means of an attenuator in the beam path and using a plano-convex lens with a focal length of  $f = 1000$  mm to provide a sufficiently high intensity in the  $\text{CaF}_2$  window (see Sec. 3.5.4.2). Consequently, the mass spectra are taken not only with differently distorted pulses, but also at different peak intensities so they are composed of ion yield peaks varying over many decades. For a better visualization of these data, the mass spectra depicted in Fig. 4.14 are normalized to the parent ion mass peak. Additionally, the parts where smaller fragments are expected ( $\leq 88$  amu/e) are expanded by a factor of 50, to stress the onset of fragmentation. Clearly, both the spectral broadening and the formation of smaller fragments increases significantly with increasing intensity in the  $\text{CaF}_2$  window. In addition to strong fragmentation of the toluene molecule, doubly charged ions and peaks originating from residual gas like  $\text{H}_2\text{O}$ ,  $\text{O}_2$  and  $\text{N}_2$  are also observed, the  $\text{H}_2\text{O}^+$  peak (marked with an asterisk in Fig. 4.14 (b)) becoming particularly strong.

In order to prove that the enhanced fragmentation observed here is caused by nonlinear beam distortions and not by increasing the pulse energy and intensity in the interaction volume, two mass spectra of ionized toluene are compared (see Fig. 4.15): one recorded at higher intensity at focus ( $1 \times 10^{14}$  W cm $^{-2}$ ) and lower peak intensity to which the  $\text{CaF}_2$  entrance window is exposed ( $I_w = 7 \times 10^{10}$  W cm $^{-2}$ ), the other recorded at lower intensity at focus ( $6 \times 10^{13}$  W cm $^{-2}$ ) but higher  $I_w$  ( $3 \times 10^{11}$  W cm $^{-2}$ ). Although the former spectrum is recorded at an even higher intensity at focus than the latter, extensive fragmentation is only observed in the latter. Obviously, this must be a result of the different intensities in the  $\text{CaF}_2$  window.

In the following, the reasons for the enhanced fragmentation under the presence of nonlinear beam distortions caused by increasing intensity in the  $\text{CaF}_2$  window  $I_w$  will be discussed. In this context, it is most instructive to consider the influence of spectral broadening on the

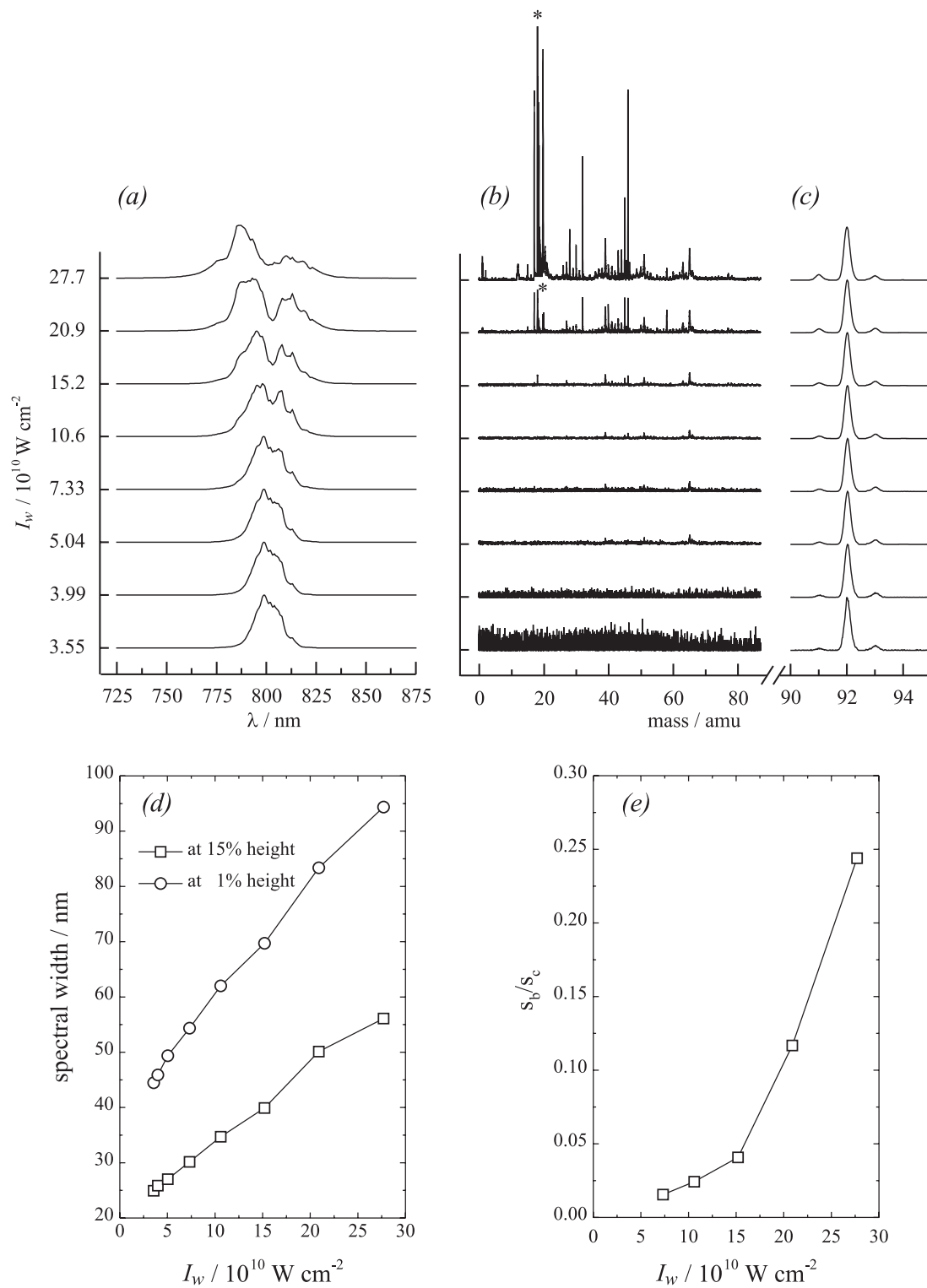


**Figure 4.14:** Mass spectra of gaseous toluene and corresponding wavelength spectra of the used laser light recorded at different intensities in the CaF<sub>2</sub> entrance window  $I_w$ . (a), recorded wavelength spectra dependent on  $I_w$ ; (b) and (c), mass spectra of toluene taken at the same  $I_w$  as the power spectra, the H<sub>2</sub>O<sup>+</sup> peak marked with an asterisk is cut. The part where smaller fragments are expected ( $\leq 88$  amu/e, panel (b)) is enlarged against the part in panel (c) by a factor of 50. (d), spectral broadening as a function of  $I_w$ ; (e), ratio of integrated fragment peaks (from panel (b)) to integrated peaks (from panel (c)) occurring also with Fourier-limited pulses as a function of  $I_w$ .

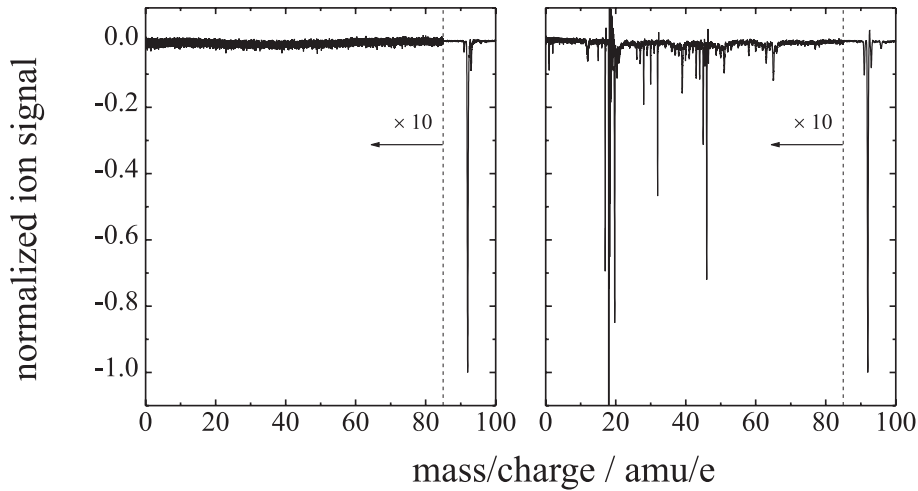


**Figure 4.15:** Comparison of two mass spectra of the toluene molecule. Although the left spectrum is recorded at an even higher intensity at focus ( $1 \times 10^{14} \text{ W cm}^{-2}$ ) than the right one ( $6 \times 10^{13} \text{ W cm}^{-2}$ ), strong fragmentation is only observed in the latter. Obviously, this is a result of the different peak intensities to which the  $\text{CaF}_2$  entrance window is exposed (left spectrum,  $I_w = 7 \times 10^{10} \text{ W cm}^{-2}$ ; right spectrum,  $I_w = 3 \times 10^{11} \text{ W cm}^{-2}$ ).

availability of difference frequencies. Having measured the spectral content  $S(\omega)$  of the nonlinearly distorted pulses (see Fig. 4.14 (a)), one can define the strength of a specific difference frequency  $\omega'$  as

$$D(\omega') = \int S(\omega) S(\omega + \omega') d\omega. \quad (4.14)$$

In Fig. 4.16, such difference-frequency spectra  $D(\omega')$  for various values of  $I_w$  are shown.

Clearly, the range of available difference frequencies is significantly broadened if  $I_w$  is increased. In particular, a strong increase can be observed in the range between  $200 \text{ cm}^{-1}$  and  $800 \text{ cm}^{-1}$ . In this range, nine vibrational modes of toluene are found, eight of which are known to be Raman-active. Seven of these Raman-active modes (see vertical lines in Fig. 4.16) are associated with vibrations of the carbon backbone, and it seems plausible that the strong increase of  $D(\omega')$  that is seen to occur in this range of frequencies could induce a strong fragmentation of the toluene molecule. In contrast, the spectral width of the pulse *without* continuum generation is *not* sufficient to induce such an enhancement of fragmentation, because the lowest energy mode involving three carbon atoms is at  $346 \text{ cm}^{-1}$  which is in the far wing of  $D(\omega')$  if  $I_w$  is small. The mode at  $217 \text{ cm}^{-1}$ , however, corresponds to a vibration between two carbon atoms and does not seem to play an important role in toluene fragmentation. In other words, the enhanced fragmentation occurring for substantially broadened power spectra can be explained by stimulated Raman scattering which may lead to significant amounts of coherent absorption of (difference) frequencies causing a vibrational excitation of the carbon backbone of the toluene molecule. This corresponds to a *coherent control* of fragmentation, since the net absorption of difference frequencies requires a coherent process, and the particular fragmentation patterns are controlled by changing the pulse properties. Obviously, the modification of the pulse shape that is the result of the nonlinear distortion taking place in the  $\text{CaF}_2$  entrance window is sufficient to induce qualitative changes in the fragmentation behavior of toluene. Using optimal control techniques, in which the pulse shape is deliberately tailored [170–175] (e. g. using evolutionary algorithms) with the

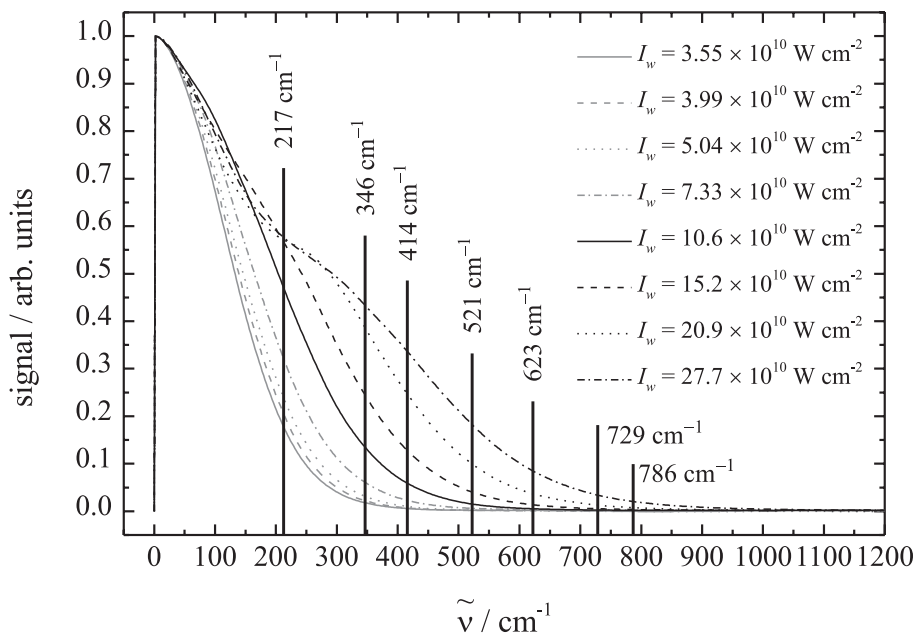


**Figure 4.16:** Difference frequencies derived according to Eq. 4.14 from the measured wavelength spectra recorded at different intensities in the  $\text{CaF}_2$  entrance window (see Fig. 4.14 (a)). The Raman-active modes of the carbon backbone of the toluene molecule between  $200 \text{ cm}^{-1}$  and  $800 \text{ cm}^{-1}$  taken from Ref. [169] are drawn in.

aim to optimize a specific reaction product, the fragment yield could probably be optimized further. However, as the results show, the fragmentation behavior can be controlled even without invoking optimal control techniques. Recently, it could be shown by T.C. Weinacht *et al.* that it is possible in principle to exploit a tailored ultrafast coherent continuum to excite selectively one or more Raman-active modes in a molecular liquid via stimulated Raman scattering using a genetic algorithm [176]. It should be noted parenthetically that resonance-enhanced fragmentation is also conceivable, because sub-detection-threshold amounts of VIS or UV light resulting from the continuum generation process in the  $\text{CaF}_2$  window could be sufficiently strong for such a mechanism. Even in a logarithmic representation of the wavelength spectra recorded down to  $200 \text{ nm}$ , essentially no other spectral components except those illustrated in Fig. 4.14 (a) are observable. A precise distinction which mechanism, i. e. stimulated Raman scattering or resonance enhancement, is crucial for the fragmentation behavior of toluene, deserves further investigations.

Independent of the underlying mechanism, it becomes obvious that the laser pulses are affected by the nonlinear distortions acquired in the  $\text{CaF}_2$  window. Although the absolute phase of the pulses is not measured, at least an idea of the temporal shape of the pulses as a function of the intensity  $I_w$  to which the entrance (and exit) window is exposed can be obtained from the recorded wavelength spectra. For this purpose, the frequency spectra are numerically Fourier-transformed into the time domain (see Fig. 4.17). Obviously, the temporal shape of the initially Gaussian laser pulses is changed fundamentally with increasing  $I_w$ . Furthermore, such pulses which are strongly distorted by nonlinearities exhibit temporal shapes that dramatically complicate the evaluation of time constants from pump-probe experiments which, in general, requires the knowledge of those signal features originating from the pulses contributing to the total signal. In addition to measuring wavelength spectra of the applied pulses, recording a toluene mass spectrum, which should consist of three peaks

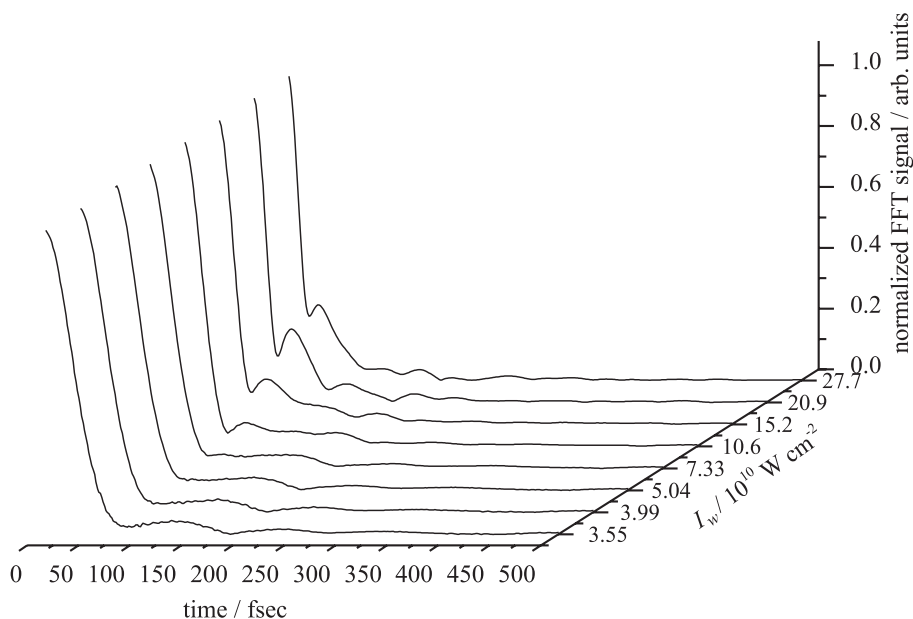


**Figure 4.17:** Fourier transformation of the wavelength spectra shown in Fig. 4.14 (a). Although the absolute phase is unknown, it is clear that the temporal shape of the laser pulses undergoes a significant change with increasing  $I_w$ .

(masses 91, 92 and 93), is exploited to check for proper experimental conditions using the final setup for pump-probe measurements, because nonlinear distortions of NIR pulses are accompanied by strong fragmentation at intensities  $< 10^{15} \text{ W cm}^{-2}$ .

### 4.3 Pump-probe measurements of 1,3,5-cyclooctatriene

As already mentioned in Sec. 2.2, the 1,3,5-cyclooctatriene system is believed to give great impetus to a deeper insight in molecular dynamics of electrocyclic ring openings of polyenes. From its molecular structure, it can be derived that it is flexible enough to undergo an ultrafast reaction after excitation with UV light. In an initial fs pump-probe experiment (see Fig. 4.18) where the sample molecules are excited using 267-nm photons and probed by 800-nm radiation, the expectation of very rapid relaxation is verified. From single-exponential fits (see Sec. 4.1.2), the results given in Tab. 4.3 can be derived. In order to make the

**Table 4.3:** Time constants  $\tau$  and vertical offsets at long pump-probe delays  $y_0$  extracted from the single-exponential fits to the data shown in Fig. 4.18.

mass	$\tau / \text{fs}$	$y_0 / \%$
106	46	—
105	75	3.1
91	75	3.5
78	75	1.8
39	75	5.2
1	210	13

fitting procedure converge properly, the rather noisy experimental raw data are subjected to a digital low-pass filter. Unfortunately, however, such a smoothing operation broadens peaked structures in the raw data. This implies that a fit of the filtered data automatically



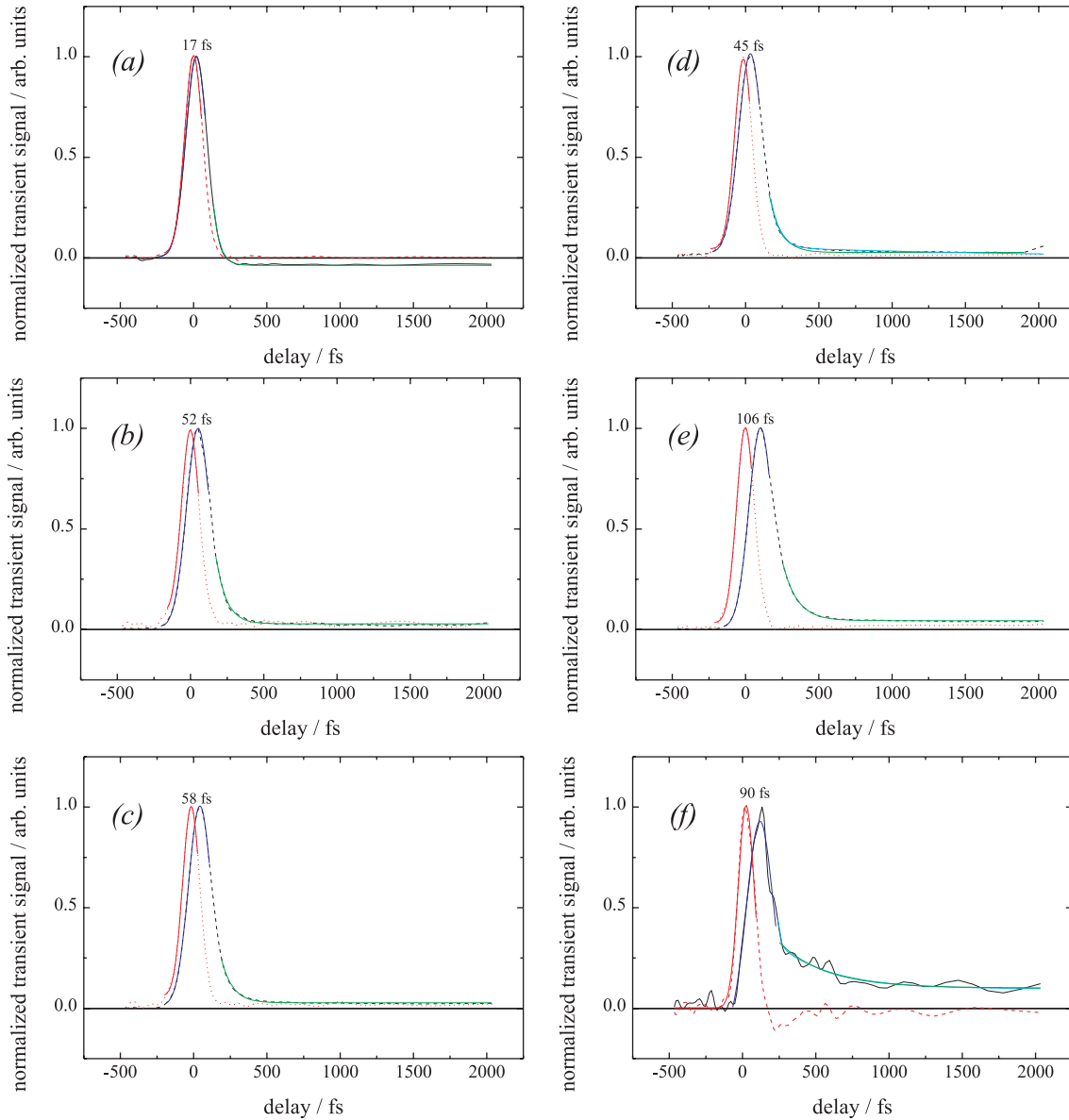


**Figure 4.18:** Normalized transient signals of different mass peaks of 1,3,5-cyclooctatriene ((a), mass 106; (b), mass 105; (c), mass 91; (d), mass 78; (e), mass 39; and (f), mass 1) versus Xe (dotted lines) recorded using the initial setup (see Sec. 3.4 and Sec. 3.6). In order to make the fitting procedure converge properly, the rather noisy experimental raw data are subjected to a digital low pass-filter which leads to a broadening of the response functions. The numbers given mark the temporal shift of the maxima of the particular 1,3,5-cyclooctatriene peaks versus the Xe signals. The detailed experimental conditions are given in the caption of Fig. 4.19 (a).

yields a broader response function than a fit of the raw data. The width of the response function has considerable influence on the time constant obtained from fitting, as will become obvious from Tab. 4.5. Due to this smoothing and because the experimental conditions in the interaction volume contain a number of uncertainties (see Sec. 3.4.2), the calculation of error tolerances of the extracted time constants is difficult. In contrast to the results of Ref. [19] obtained in solution by ps time-resolved UV resonance Raman spectroscopy ( $(12 \pm 2)$  ps for the photoproduct formation), the time constants derived here are much shorter. A reasonable explanation for this discrepancy is given in Sec. 4.3.3.

Useful as the measurements taken with the initial setup are as a starting point, a detailed comprehension of the evolution of a reacting molecule deserves, however, a pump-probe experiment in which additional measuring parameters are carefully determined. Especially when the  $\text{CaF}_2$  entrance window of the vacuum system is exposed to high intensities and concomitant to this the resulting pulse shapes seem to play a crucial role (see also Sec. 4.2.2). From Fig. 4.19, it becomes obvious that a too high intensity in the  $\text{CaF}_2$  window of the probe

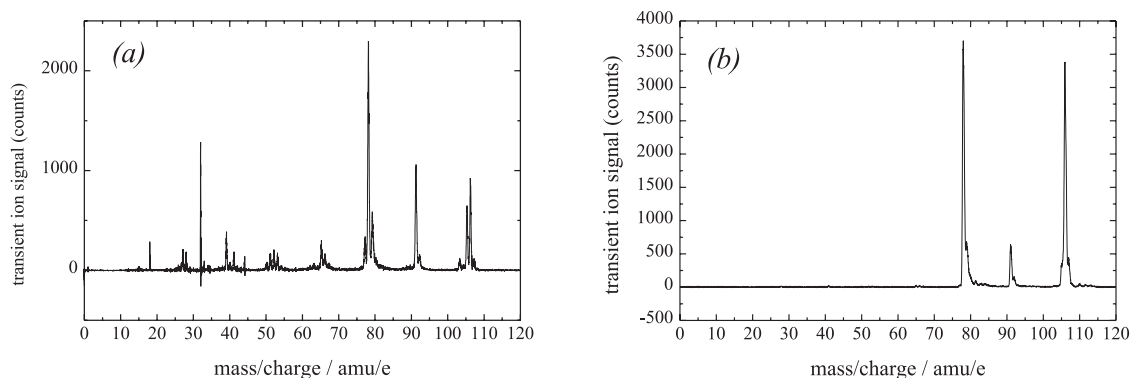


**Figure 4.19:** Transient mass spectra of 1,3,5-cyclooctatriene taken under different experimental conditions. (a), initial setup (see Sec. 3.4 and Sec. 3.6),  $\lambda_{\text{pu}} \approx 267$  nm,  $\lambda_{\text{pr}} \approx 800$  nm,  $\tau_{\text{pu}} \approx 130$  fs,  $\tau_{\text{pr}} \approx 112$  fs,  $I_{\text{pu}} \approx 4.1 \times 10^{11}$  W cm $^{-2}$ ,  $I_{\text{pr}} \approx 1.5 \times 10^{12}$  W cm $^{-2}$ ,  $p \approx 5 \times 10^{-6}$  mbar; (b), final setup (see Sec. 3.5 and Sec. 3.7),  $\lambda_{\text{pu}} = 265$  nm,  $\lambda_{\text{pr}} = 802$  nm,  $\tau_{\text{pu}} = 93$  fs,  $\tau_{\text{pr}} = 104$  fs,  $I_{\text{pu}} = 1.7 \times 10^8$  W cm $^{-2}$ ,  $I_{\text{pr}} = 2.9 \times 10^{12}$  W cm $^{-2}$ ,  $p = 7.2 \times 10^{-8}$  mbar. Obviously, the different fragmentation patterns are due to the different intensities to which the  $\text{CaF}_2$  entrance windows have been exposed, (a),  $I_{\text{w, pu}} \approx 6.5 \times 10^{10}$  W cm $^{-2}$ ,  $I_{\text{w, pr}} \approx 8.8 \times 10^{11}$  W cm $^{-2}$ ; (b),  $I_{\text{w, pu}} = 1.7 \times 10^8$  W cm $^{-2}$ ,  $I_{\text{w, pr}} = 1.9 \times 10^{11}$  W cm $^{-2}$ .

pulses ionizing the excited evolving molecules in particular has a noticeable influence on the results, because the two mass spectra are recorded under otherwise similar experimental conditions. In contrast to the mass spectrum shown in panel (b), the one in panel (a) exhibits, in addition to rather strong fragmentation, quite large numbers of doubly charged ions which are unexpected at this intensity at focus [143]. Although the pump intensities in the  $\text{CaF}_2$  window applied in the initial ((a)) and the final ((b)) experiments are very different, they both are too small for considerable distortions of the UV pulses.

In general, any (nonlinear) distortion of the pulses has to be carefully prevented in order to guarantee a *Gaussian* temporal shape at the interaction volume. This is required to allow Eq. 4.1 to be applied as fit function. However, the results thus derived become even more reliable, if all parameters not related to intrinsic molecular properties are measured independently. In this context, besides a precise determination of the pulse lengths, the

knowledge of the order of the ionization process is of great importance. For this purpose, the transient ion signals are measured at several different pump-probe delays and different probe intensities at every distinct delay.

### 4.3.1 Intensity-dependent measurements

In the framework of the present thesis, intensity-dependent measurements are carried out to elucidate ionization processes. Performing such measurements of the transient ion signals aims to determine the absolute width of the response function (see Eq. 4.3) valid for the 1,3,5-cyclooctatriene system investigated under the same experimental conditions as applied here. The order of the pump process ( $\lambda_{\text{pu}} = 266$  nm) is established to equal unity, because no signal can be detected by radiating the sample with pump light alone. The absorption of more than a single 266-nm-photon ( $\hat{=} 4.65$  eV) would lead to ionization of 1,3,5-cyclooctatriene, which has an ionization energy of 7.9 eV [177]. However, determining the order of the probe process ( $\lambda_{\text{pr}} = 801$  nm) demands more effort. Varying the intensity of the probe light at unchanged pump conditions yields the type and the order of the ionization process. Since the Keldysh adiabaticity parameter (see Sec. 2.3.1) here amounts to  $\gamma = 2.3$  at minimum, an MPI process is expected. The data evaluation procedure concerning the measurements described here can be found in Sec. 4.1.1. In Fig. 4.20, the solid lines are linear fits to the transient ion yields (originating from integrating discrete mass peaks of transient mass spectra), depicted here in a double-logarithmic representation. The fits are carried out without any weighting, but only five points lying in the probe intensity range from  $2.9 \times 10^{12}$  W cm $^{-2}$  to  $4.2 \times 10^{12}$  W cm $^{-2}$  are considered. This is reasonable because the data taken at these conditions exhibit quite low noise level even for low signal strengths, and the lower limit of this interval corresponds exactly to the probe intensity used for time-dependent measurements. Since all mass spectra are taken at the same sample pressure, at small pump-probe delays the ion yields of large peaks are reduced by saturation effects. To avoid this problem, instead of these masses their heavier isotopic variants are used to determine the particular slopes. From inspection of the eight panels of Fig. 4.20, it becomes evident that the transient ion yields are reduced dramatically with increasing time delay. However, in the first three panels ( $0 \text{ fs} \leq \Delta t \leq 33 \text{ fs}$ ) the slope remains unchanged. After this time-delay range, the slope increases and decreases again. It should be noted that this final decrease may not be significant as a result of the poor signal strength. These results are summarized in Fig. 4.21. Obviously, within the response function, the order of the ionization process is constant (within the error tolerance). Then the photon order increases which corresponds to a reduced ionization probability. Therefore, in this range a decay of the time-dependent signals is expected. From the photon orders thus determined, the widths of the response functions for each mass signal of 1,3,5-cyclooctatriene can be calculated by averaging the three data points between 0 fs and 33 fs. The total error of each averaged width is determined using the Gaussian law of error propagation. The widths of the response functions are needed to derive time constants from the time-dependent measurements.

### 4.3.2 Time-dependent measurements

The mass spectrum of 1,3,5-cyclooctatriene recorded with undistorted pulses (checked by taking a toluene mass spectrum which exhibits only three mass peaks (masses 91, 92 and 93)) consists of four mass peaks (106, 105, 91, and 78 and their heavier isotopic variants) which can be used to gain time-dependent information (see Fig. 4.19 (b)). As described in

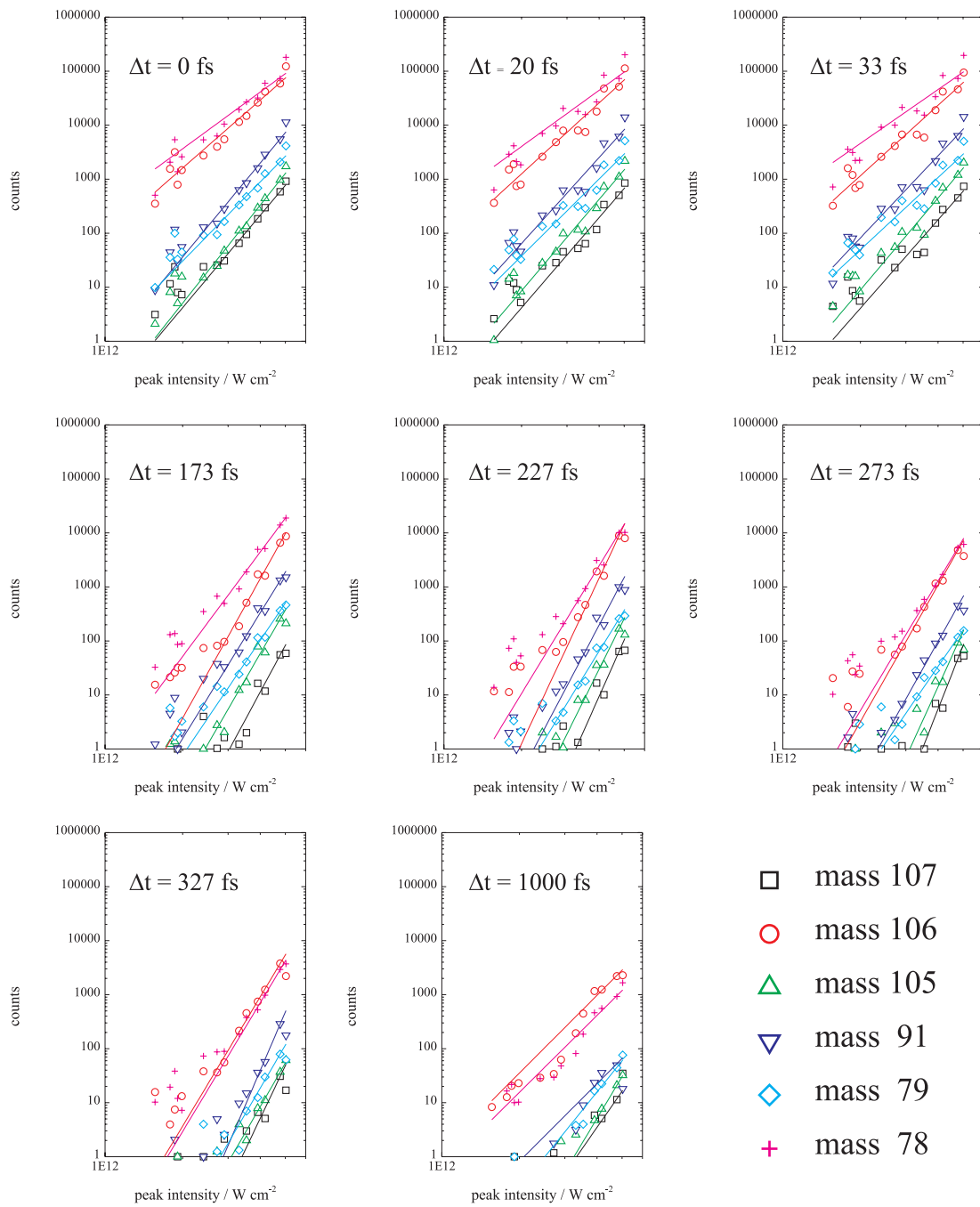


**Figure 4.20:** Determination of the order of the ionization process of excited 1,3,5-cyclooctatriene. The measured transient ion yields are plotted as a function of the peak intensity of the probe light at different pump-probe delays  $\Delta t$ . Each data point is the integral of a single mass peak of a transient mass spectrum taken under the following experimental conditions,  $\lambda_{\text{pu}} = 265$  nm,  $\lambda_{\text{pr}} = 801$  nm,  $\tau_{\text{pu}} = 115$  fs,  $\tau_{\text{pr}} = 105$  fs,  $I_{\text{pu}} = 3.8 \times 10^8$   $\text{W cm}^{-2}$ ,  $I_{\text{pr}} = 1.6 \times 10^{12} \dots 5.0 \times 10^{12}$   $\text{W cm}^{-2}$ ,  $p = 5.1 \times 10^{-8}$  mbar.

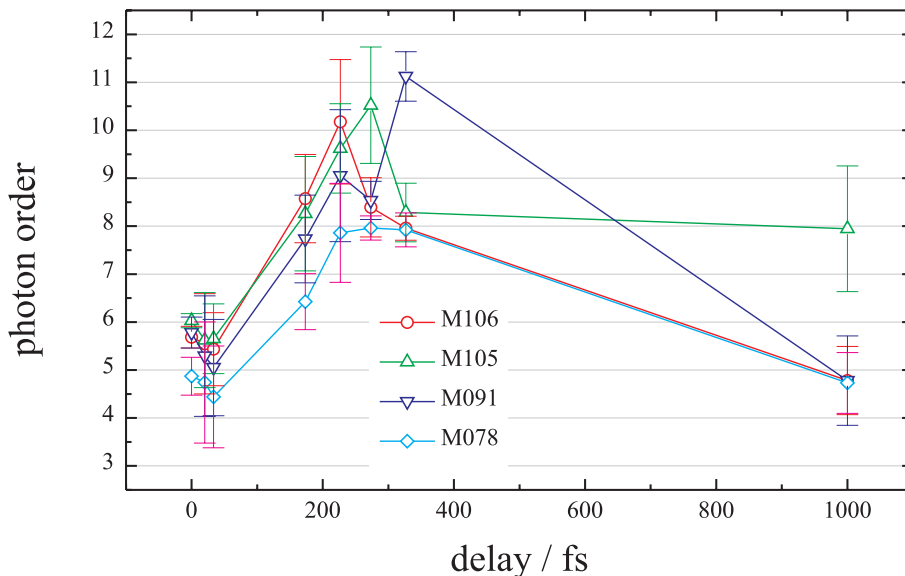


**Figure 4.21:** Orders of the ionization process of the single mass peaks of 1,3,5-cyclooctatriene as a function of the pump-probe delay.

Sec. 3.8.2, it is possible to record the time-dependent data of two mass peaks simultaneously. In order to allow for the application of moderate intensities, all fragments (masses 105, 91, and 78) are measured versus the parent ion as reference signal instead of Xe which exhibits a much higher ionization energy (12.1 eV [178]). Then the parent ion is measured versus Xe (gray data in Fig. 4.22) to obtain the relative time shift of the molecular signals. All signals are normalized because the determination of absolute ion yields would require, among other things, the knowledge of the transmission of the grids and the quantum efficiency of the MCP. Furthermore, knowing absolute signal heights is not important for investigating this kind of molecular dynamics.

The solid gray line in Fig. 4.22 represents a pure Gauss fit to the measured data (gray squares). Obviously, the data points and the fit are in good agreement which verifies the expectation that Xe atoms should not exhibit any time-dependent behavior at the timescales used here. In the function applied to fit the measured transient signals of 1,3,5-cyclooctatriene (given in Eq. 4.1), the calculated widths of the response functions are inserted. According to Eq. 4.3, this width depends on three parameters. Although the applied pump and probe pulse durations are essentially the same for all measured mass signals, the widths of the response functions are not the same, because the orders of the *probe* process are different for each mass peak (see Sec. 4.3.1).

From Fig. 4.22, it becomes clear that the parent ion (black circles) exhibits the shortest decay time. The signal of the fragment with mass 78 comes up next, but shows a slower decay than the signals of the other two fragments. The signals corresponding to the masses 105 and 91, however, exhibit substantially the same time behavior, apart from the fact that a second time-constant can be derived from the signal of mass 91. It should be noted that no signal shows a significant offset at long decay times. The fitting results are given in Tab. 4.4. On a trial basis, all data sets are fitted with one additional time constant, but in all cases two of the time-constants delivered by the fitting procedure are identical. This way, the existence of more time constants than the derived is definitely excluded.

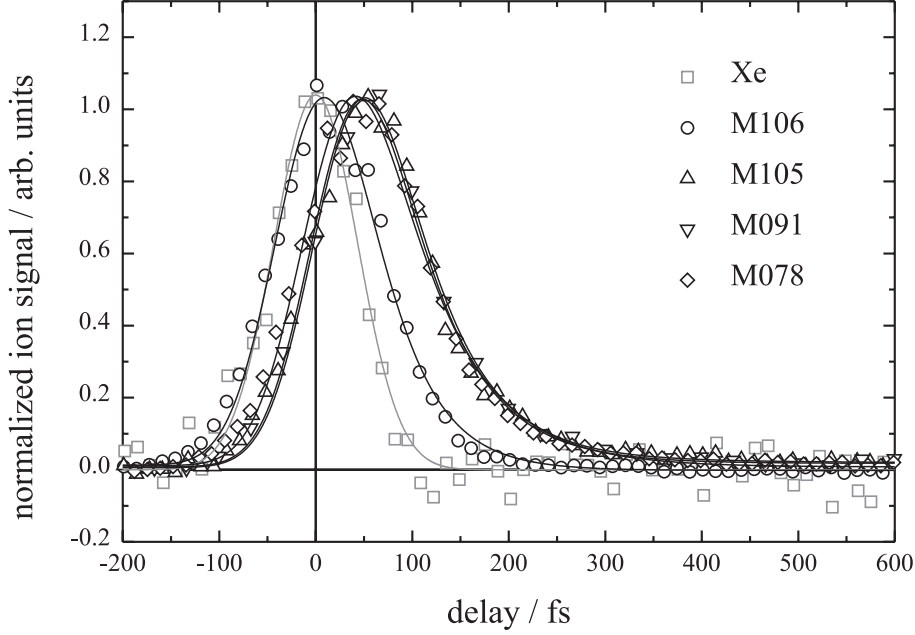


**Figure 4.22:** Normalized transient signals of the parent ion and all measurable fragment masses of 1,3,5-cyclooctatriene as a function of the pump-probe delay, taken at  $\lambda_{\text{pu}} = 265$  nm,  $\lambda_{\text{pr}} = 802$  nm,  $\tau_{\text{pu}} = 93$  fs,  $\tau_{\text{pr}} = 104$  fs,  $I_{\text{pu}} = 1.7 \times 10^8$  W cm $^{-2}$ ,  $I_{\text{pr}} = 2.9 \times 10^{12}$  W cm $^{-2}$ ,  $p = 7.2 \times 10^{-8}$  mbar. The Xe signal indicates  $\Delta t = 0$  fs. The solid lines are fits using Eq. 4.1.

**Table 4.4:** Results of the exponential fits (see Eq. 4.1) to the measured time-dependent transient data of 1,3,5-cyclooctatriene (see Fig. 4.22). The variable  $N$  denotes the order of the ionization process,  $w_{\text{FWHM}}$  is the FWHM-width of the response function,  $\Delta S$  is the relative shift of the particular 1,3,5-cyclooctatriene parent ion and fragment signals with respect to the Xe peak, and  $\tau_1$  and  $\tau_2$  are the exponential decay constants. For a detailed description of the given errors see text.

mass	$N$	$w_{\text{FWHM}} / \text{fs}$	$\Delta S / \text{fs}$	$\tau_1 / \text{fs}$	$\tau_2 / \text{fs}$
106	$5.6 \pm 0.7$	$102.9 \pm 1.3$	$14.7 \pm 1.4$	$48.1 \pm 1.2$	$746 \pm 64$
105	$5.8 \pm 0.6$	$102.6 \pm 1.1$	$42.9 \pm 1.5$	$61.3 \pm 0.8$	
91	$5.4 \pm 0.9$	$103.3 \pm 1.9$	$43.3 \pm 1.5$	$59.8 \pm 1.6$	
78	$4.7 \pm 0.9$	$104.7 \pm 2.6$	$27.8 \pm 1.5$	$68.3 \pm 1.8$	

The errors resulting from the fitting procedure carried out in the software ORIGIN (Microcal, version 5.0 professional) are smaller than those given in Tab. 4.4. Because the probe step contributes to the signal in a most nonlinear way, it is reasonable to derive the error of the extracted parameters from the determined error of the order of the ionization process. This is done by fitting the data curves once again, inserting the original width altered by the margin of error for the width of the response function.

In order to substantiate the enormous effort determining the actual width of the response function  $w$  independently from the time-dependent measurements, the results of fitting the same time-dependent data with and without inserting this width into the fit function are compared. As already mentioned above, the time-dependent parent ion signal is measured three times at the same experimental conditions. From Fig. 4.23 it becomes obvious that the measured data are well reproducible. First, the fit function (see Eq. 4.1) is applied

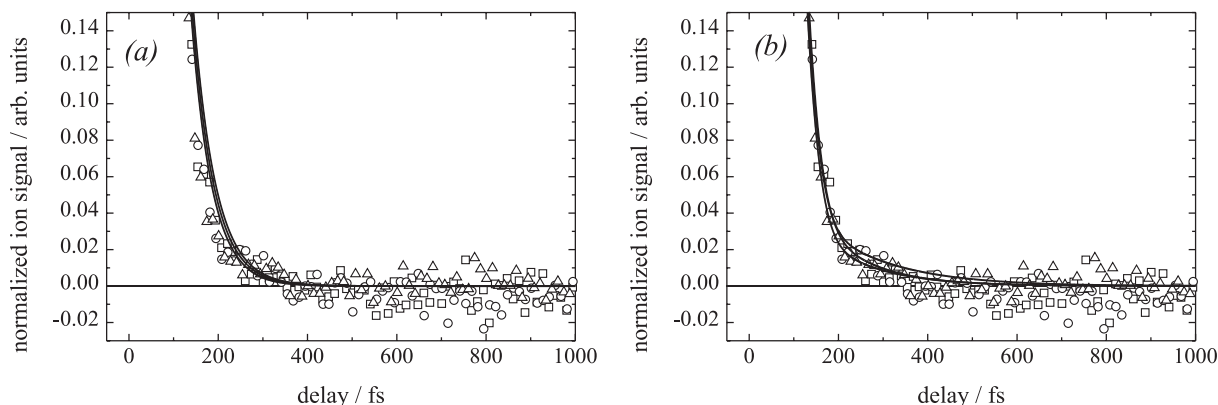


**Figure 4.23:** Expanded view of time-dependent signals of the 1,3,5-cyclooctatriene parent ion. The three data sets are identical in both panels. Each solid line represents a fit to one of these data sets (squares, circles and triangles) applying the same fit function given in Eq. 4.1 to all, but different numbers of free parameters. In (a) the width of the response function determined before is inserted as a fixed parameter. In (b), however, this width is treated as an additional free parameter in the fitting procedure.

to these three data sets inserting the value of  $w$  determined before as a fixed parameter. Then, the same three data sets are fitted by the same fit function, but treating  $w$  as an additional free parameter which is, however, not related to intrinsic molecular properties. This is depicted in Fig. 4.23. Clearly, the fits in (a) are almost identical, whereas the ones in (b) differ significantly from each other. Additionally, in the latter case, the exponential part has a low amplitude showing up essentially in the noise leading to huge error tolerances. The resulting values for the time-constants of the single-exponential decay are given in Tab. 4.5. Obviously, the time constants resulting from fitting with  $w$  as a fixed parameter are essentially

**Table 4.5:** Comparison of time constants obtained from fitting the same three data sets of the parent ion mass of 1,3,5-cyclooctatriene by inserting the width of the response function  $w$  as fixed or free parameter. The errors given for fitting with  $w$  as free parameter result from the ORIGIN fitting procedure (see above).

fit with $w$ as fixed parameter		fit with $w$ as free parameter	
$w_{\text{FWHM}} / \text{fs}$	$\tau_1 / \text{fs}$	$w_{\text{FWHM}} / \text{fs}$	$\tau_1 / \text{fs}$
$102.9 \pm 1.3$	$49.9 \pm 2.1$	$136.8 \pm 1.4$	$112 \pm 42$
$102.9 \pm 1.3$	$48.1 \pm 2.1$	$136.0 \pm 1.0$	$159 \pm 45$
$102.9 \pm 1.3$	$46.2 \pm 2.2$	$135.2 \pm 1.4$	$125 \pm 61$

identical, which is also confirmed by the small error tolerances (which are greater than the ones resulting from the ORIGIN fitting procedure and, therefore, based on the errors in the ionization yield data). In contrast to this, the time constants derived from fitting with  $w$  as a free parameter differ significantly from each other and exhibit much larger relative errors. For the mean values it amounts to 2.6% in case of  $w$  as a fixed parameter and to 24% in case of  $w$  as a free parameter. Additionally, fitting with  $w$  as a free parameter gives a value for  $w$  which can be used for calculating the order of the probe process according to Eq. 4.3. This order corresponds to the thick line in Fig. 4.24. It becomes obvious that the calculated order differs clearly from the measured data. Therefore, it is concluded that measuring the order

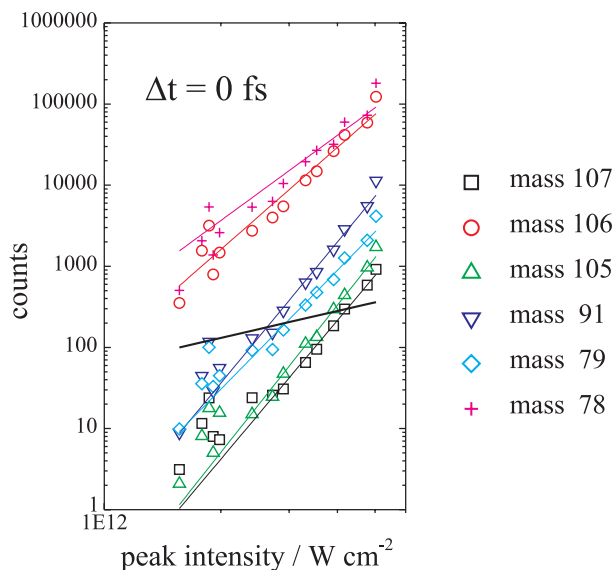


**Figure 4.24:** Comparison of slopes of ion yields as a function of probe intensity. The data points and the thin solid lines correspond to Fig. 4.20. The thick solid line results from calculating the order of the probe process according to Eq. 4.3 from the fitted width of the response function (see Fig. 4.23 and Tab. 4.5). Obviously, the slope thus calculated does not agree with the experimental data.

of the probe process and thus determining the width of the response function independently of molecular dynamics measurements is necessary to derive reliable time constants that are in the order of the applied pulse durations.

To shed more light on the reliability of the time-dependent data presented above which are measured under well-defined experimental conditions with 800 nm as probe wavelength, similar measurements are taken with 400 nm probe light. The comparison of these two data sets shows that the application of different probe wavelengths leaves the measured transient signals essentially unaltered. This is depicted in Fig. 4.25 for the 1,3,5-cyclooctatriene fragment with mass 78 as an example. Because the order of the ionization process changes with the probe wavelength, and this order has not been determined for the case of UV probe light, the fit to the UV data is carried out using the same time constant (68.3 fs) as derived from measurements with NIR probe light. This means that in this case the time constant is inserted into the fit function as a fixed parameter, whereas the width of the response function acts as a free parameter. From Fig. 4.25 it becomes obvious that the thus generated fitting curve fits very well to the measured UV data confirming that no dependence on the probe wavelength exists.

In order to check if the transient mass spectra taken at different probe wavelengths exhibit the same peaks which can be used for extracting time information, two mass spectra of 1,3,5-cyclooctatriene are recorded, one of them probed by NIR light, the other probed by UV light (see Fig. 4.26). Although the signal strength of the UV mass spectrum is two orders of magnitude smaller than that of the corresponding NIR mass spectrum, it is possible to record the spectrum with a signal-to-noise ratio sufficient to resolve the different mass peaks. Evidently, the two spectra look very similar, confirming that the fragmentation behavior of 1,3,5-cyclooctatriene is independent of the probe wavelength at these experimental conditions. From these results it can be concluded that the derived time constants are intrinsically related to molecular properties.



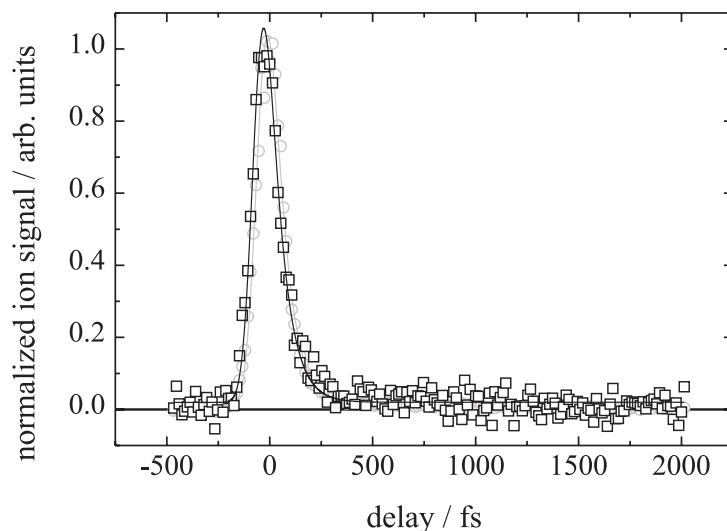


**Figure 4.25:** Comparison of transient signals of the 1,3,5-cyclooctatriene fragment with mass 78, exemplarily illustrated. Black squares,  $\lambda_{\text{pu}} = 265$  nm,  $\lambda_{\text{pr}} = 401$  nm,  $\tau_{\text{pu}} = 88$  fs,  $\tau_{\text{pr}} = 80$  fs,  $I_{\text{pu}} = 3.9 \times 10^8$  W cm $^{-2}$ ,  $I_{\text{pr}} = 2.2 \times 10^{11}$  W cm $^{-2}$ ,  $p = 1.0 \times 10^{-7}$  mbar; gray circles,  $\lambda_{\text{pu}} = 265$  nm,  $\lambda_{\text{pr}} = 802$  nm,  $\tau_{\text{pu}} = 93$  fs,  $\tau_{\text{pr}} = 104$  fs,  $I_{\text{pu}} = 1.7 \times 10^8$  W cm $^{-2}$ ,  $I_{\text{pr}} = 2.9 \times 10^{12}$  W cm $^{-2}$ ,  $p = 7.2 \times 10^{-8}$  mbar. The solid lines representing fits to the data are described in the text.

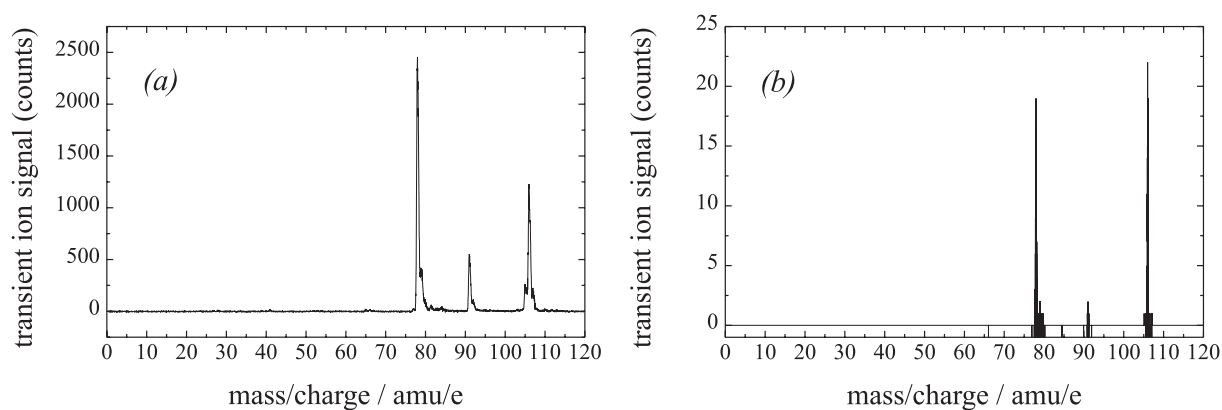


**Figure 4.26:** Comparison of transient mass spectra of 1,3,5-cyclooctatriene taken at different probe wavelengths ((a), NIR; (b), UV) under the experimental conditions described in the caption of Fig. 4.25.

Until now, only three data points of the determination of the photon order of the probe process (between 0 fs and 33 fs delay, see Fig. 4.21) have been exploited to ascertain the widths of the response functions. However, it seems to be reasonable to include also all other information about the ionization process into the evaluation of the pump-probe measurements of 1,3,5-cyclooctatriene. Since it is impossible to determine saturation intensities of transient signals and consequently the corresponding absolute values of ionization cross sections (see Sec. 4.1.2), the ionization dynamics, which requires inclusion of absolute ionization yields, cannot be incorporated into a straightforward fit function. Instead, the measured data are modeled using a simulation function very similar to the fit function used for extracting time constants,

$$M(\Delta t) = y_{\text{offs}} + \int_0^\infty \frac{1}{\sqrt{\pi}w} \cdot \underbrace{\exp\left[-\frac{(t' - (\Delta t - S))^2}{w^2}\right]}_{\text{response function}} \cdot \underbrace{\left[A_D \cdot \exp\left[-\frac{t'}{\tau}\right] + y_0\right]}_{\text{exponential decay of the evolving molecule}} \cdot \underbrace{a \cdot c^{N(t')}}_{\text{ionization dynamics}} dt' \quad (4.15)$$

which contains in addition to Eq. 4.1 a convolution term describing the time dependence of the ionization dynamics superimposed with the response function and the exponential decay of the evolving molecule. Because all terms and their variables aside from the ionization dynamics term are already described in Sec. 4.1.2 (see Eq. 4.1 and Fig. 4.3), only the latter needs discussion. As the true dependence of the ionization probability on the actual photon order is unknown, an assumption has to be made. It seems to be reasonable to use a power law to simulate the ionization dynamics. The function  $N(t')$  is obtained by applying a cubic spline interpolation to the measured data points of the photon order dependent on the pump-probe delay (see gray curve in Fig. 4.27). The variable  $c$  denotes the base of the power law and has to be smaller than unity, because the ionization probability is expected to decrease with increasing photon order  $N(t')$  if resonances are absent. The amplitude  $a$  is required to adjust the contribution of the ionization dynamics within the convolution. This is necessary, because all other parameters obtained as described above (see Fig. 4.22 and Tab. 4.4) are kept unchanged. The criterion for the best simulation is the minimization of the sum of the squared errors. This procedure is carried out only for the 1,3,5-cyclooctatriene parent ion, because for fragment masses an additional complication by fragmentation processes is expected. The result is depicted in Fig. 4.27. Clearly, the measured data can be simulated very well by additionally including the time-dependent ionization dynamics into the fit function.

### 4.3.3 Reaction dynamics of the photoinduced electrocyclic ring opening of 1,3,5-cyclooctatriene

The ultrashort time constants derived from the pump-probe measurements of the photoinduced electrocyclic ring opening of 1,3,5-cyclooctatriene (see Tab. 4.4) give evidence for the involvement of conical intersections in the reaction dynamics of this molecule. In contrast to that, P.J. Reid *et al.* established, in a ps time-resolved resonance Raman experiment, a ground-state appearance time of  $(12 \pm 2)$  ps for the 1,3,5-cyclooctatriene ring-opening reaction [19,20]. They used for their investigations pulses exhibiting an autocorrelation of 2.8 ps FWHM. However, the primary reaction takes place within a fraction of this long pulse length, as shown in the present work. This probably leads to the complication that a primary product formed during the pump pulse duration is excited by the same pulse, inducing a subsequent reaction which then may be probed.

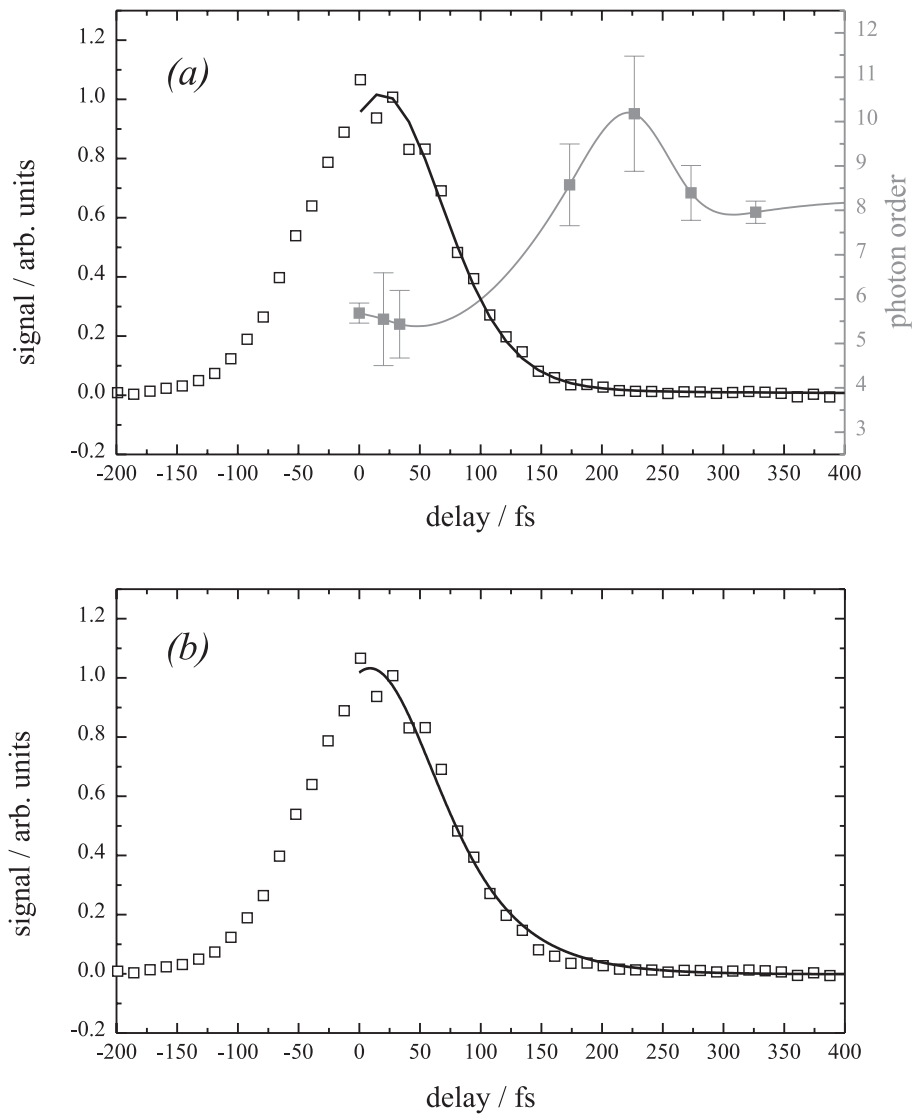


**Figure 4.27:** Simulation of the time-dependent behavior of the transient signal of the 1,3,5-cyclooctatriene parent ion (black squares) using Eq. 4.15 (black line, (a)) with  $a = 24.2$  and  $c = 0.57$ . The gray curve represents  $N(t')$  (see text). In panel (b), the same data as in (a) and the fit function used for extracting time constants are depicted for comparison.

As described in Sec. 2.2, the photochemical ring-opening reaction of 1,3,5-cyclooctatriene proceeds from the excited state ( $1B_2$ ) via the spectroscopically dark  $2A_1$  state to the ground state ( $1A_1$ ). The molecule exists in two different conformations (twist-boat and

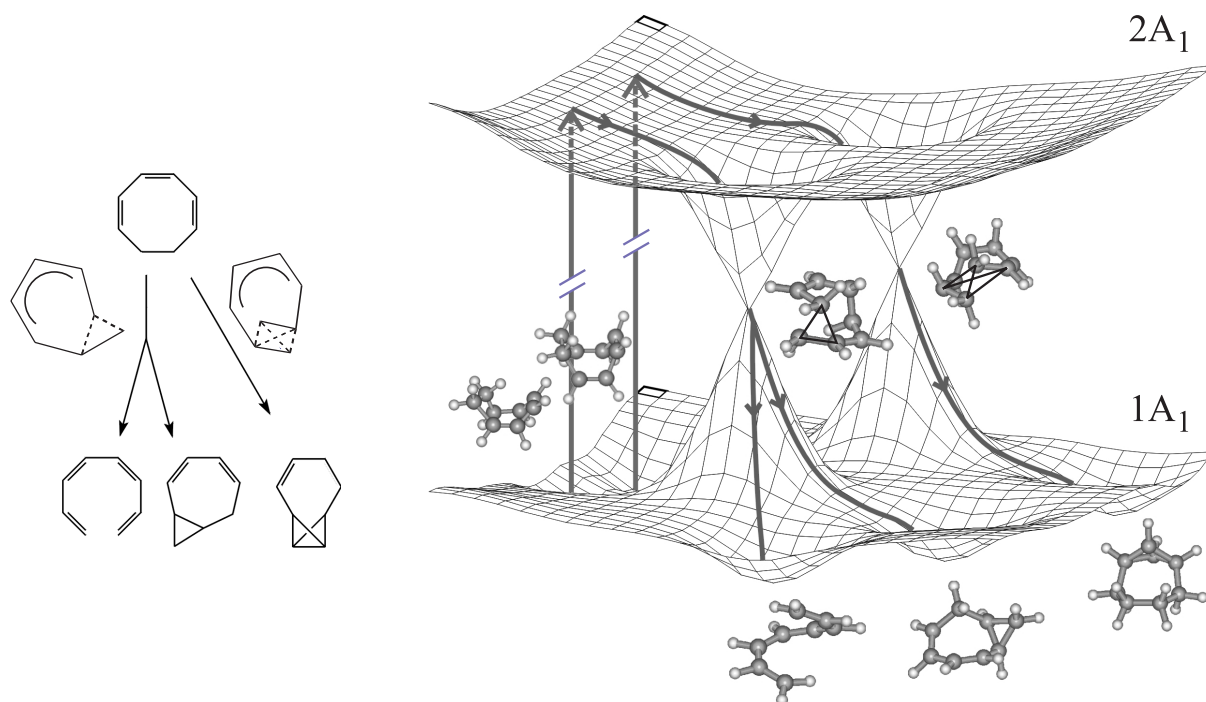


**Figure 4.28:** Model potential energy surfaces involved in the photoinduced electrocyclic ring opening of 1,3,5-cyclooctatriene with the two different reaction channels leading to three products. The  $1B_2$  surface has been omitted for clarity, as indicated by the break mark in the arrows representing the excitation. The molecular structures at ground state are geometry optimized, the ones at conical intersections are assumptions [48]. The 3-center and 4-center substructures at the  $2A_1-1A_1$  conical intersections are emphasized by black lines.

boat), which in comparison to the excitation energy (4.65 eV), have only slightly different energy contents ( $\Delta E = 20.1 \text{ kJ mol}^{-1} = 208 \text{ meV}$ ), the twist-boat conformer being the more stable [179]. Because of this, the molecule evolves on the excited state surfaces starting from two different points. From there, the two conformers are expected to follow two different paths (corresponding to different intermediate structures) to the ground state, forming the products or the reactant again. The evolution of the two 1,3,5-cyclooctatriene conformers is schematically depicted in Fig. 4.28. The  $1B_2$  surface has been omitted for clarity, as indicated by the break mark in the arrows representing the excitation.

From Fig. 4.28 it becomes obvious that the intermediate structure at the  $2A_1-1A_1$  conical intersection containing a 3-center substructure can only be reached from the twisted conformer of 1,3,5-cyclooctatriene. From there, the two products all-*cis*-1,3,5,7-octatetraene and bicyclo[5.1.0]octa-2,4-diene or the reactant 1,3,5-cyclooctatriene can be formed. From the boat conformer of the molecule which is less rigid and more reactive than the twisted one, however, a 4-center substructure at the  $2A_1-1A_1$  conical intersection is achieved. From this structure, the formation of the product tricyclo[4.1.0.0<sup>6,8</sup>]octa-2-ene or internal conversion can take place. Of course, the molecules reach the ground state highly vibrationally excited (“hot”) which enables them to undergo subsequent thermal reactions first requiring a redistribution of the vibrational energy located primarily in specific modes.

Although a straightforward assignment of decay times to molecular dynamics is generally impossible without a quantum-chemical investigation of the potential energy surface driving the particular reaction, on the basis of what is known on similar reactions such as the ring opening of 1,3-cyclohexadiene ([15–18,88–90] and references therein) at least a rational interpretation of the measured data can be obtained. The time constants derived from the parent ion and the fragments of 1,3,5-cyclooctatriene (masses 106, 105, 91 and 78) can be allocated to the reaction model (Fig. 4.28) as follows. The parent ion decays with a time constant of  $(48.1 \pm 1.2)$  fs and exhibits a shift of  $(14.7 \pm 1.4)$  fs versus the Xe signal indicating the absolute time zero. Both its decay time and its shift are the shortest times observable in the 1,3,5-cyclooctatriene system. Therefore, the time-dependent behavior of the parent ion can be allocated to the disappearance of the molecule from the spectroscopically bright  $1B_2$  to the dark  $2A_1$  state. This assignment seems to be reasonable, because this region of the potential energy surface lies energetically so high that the molecule remains unbroken due to the sufficiently small amount of vibrational energy received. Fragmentation of a reacting molecule occurs when the evolving molecule acquires enough vibrational energy during its downhill motion on potential energy surfaces. Since all fragments must evolve from the parent mass, they appear significantly later than the transient parent ion signal. Therefore, their temporal behavior has to be allocated to molecular dynamics occurring later in time than that to which the parent ion decay has been assigned. The fragments with masses 105 and 91 show an essentially identical behavior with respect to the short time constants ( $(61.3 \pm 0.8)$  fs and  $(59.8 \pm 1.6)$  fs) and the shifts to time zero ( $(42.9 \pm 1.5)$  fs and  $(43.3 \pm 1.5)$  fs). Consequently, the 60-fs decay time is assigned to one of the two conical intersections to the ground state. However, the mass 91 transient signal exhibits a second, much longer decay time ( $(746 \pm 64)$  fs). It may be related to a relaxation to the ground state at an alternative decay channel (there must be more than one conical intersection for each conformer in an opened ring polyene [180]) of the  $2A_1-1A_1$  conical intersections and after evolution on the  $2A_1$  potential energy surface. The assignment to a subsequent reaction of one of the initially hot products either all-*cis*-1,3,5,7-octatetraene or tricyclo[4.1.0.0<sup>6,8</sup>]octa-2-ene (see Sec. 2.2) does not seem to be reasonable, because a time constant which is on the order of hundreds of fs is believed to be too short for such a process. These ground state reactions would require a redistribution of the vibrational energy localized in those critical modes which have driven the reaction so far and are usually different from those which drive subsequent reactions. Such IVR processes require themselves times in the order of one ps at least [181]. In contrast to the other two fragments, the fragment with mass 78 exhibits a significantly longer (short) time constant of  $(68.3 \pm 1.8)$  fs, but it is only  $(27.8 \pm 1.5)$  fs shifted from time zero. Due to this early appearance in combination with the longer decay time compared with the behavior of the other two fragments, it is assigned to the second conical intersection leading to the third product tricyclo[4.1.0.0<sup>6,8</sup>]octa-2-ene or back to the reactant. Thus the hypothesis that the relaxation to the ground state takes place via two different reaction channels, probably involving a 3-center and a 4-center substructure corresponding to two different conical intersections, is proved.

Although it is in general impossible to distinguish between different compounds with identical mass using ionization techniques, the assignment of the time constants derived from pump-probe measurements to different reaction channels seems to be reasonable. However, the advantage of using ionization as the probe step emerges from the following. Probing molecules evolving on excited states is always accompanied by the intrinsic problem of the lack of information about the change in the optical properties (e. g. absorption or ionization cross sections) exploited for detection during their evolution. It could be shown above that

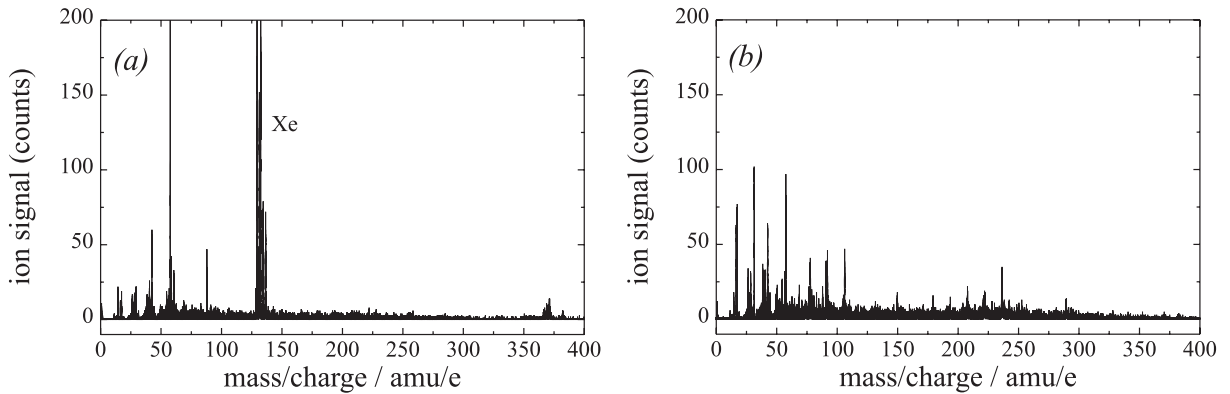
it is, in fact, possible at least to simulate the contribution of this additional (detection) dynamics (non-molecular dynamics) by using ionization instead of absorption. However, for this purpose measurements of the transient signals as a function of the probe intensity are inevitable. Additionally, the method applied provides a sufficiently high time resolution to detect the true primary events of a photoinduced reaction, because the pulse lengths used are on the order of single vibrational periods. This excludes subsequent reactions that may take place during the pump pulse duration.

## 4.4 Pump-probe measurements of 7-dehydrocholesterol

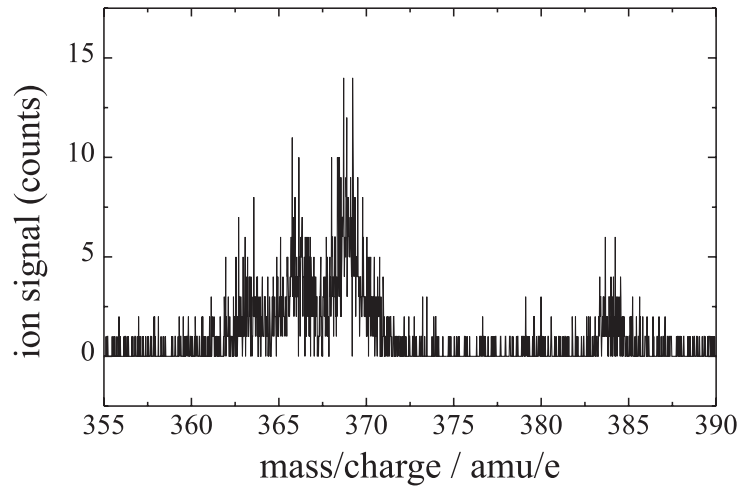
7-Dehydrocholesterol is a precursor in vitamin D<sub>3</sub> biosynthesis and technical synthesis and is of exceptional interest in photobiology (see Sec. 2.2). Although investigations carried out in the gas phase are not directly transferable to processes in natural environment, the knowledge of the behavior of undisturbed molecules is of paramount importance in understanding molecular dynamics. The primary event in 7-dehydrocholesterol photochemistry is the electrocyclic ring opening which leads to previtamin D<sub>3</sub> and is induced by UV light. It is expected to proceed on a timescale on the order of hundreds of fs, because the homologous photoreaction of 1,3-cyclohexadiene, which corresponds to the photochemically active part of 7-dehydrocholesterol to form *s-cis,Z,s-cis*-1,3,5-hexatriene, is known from investigations in the gas phase to be completed after 200 fs [88–90]. Recently, R.J. Sension *et al.* published their results on the photoinitiated ring opening of 7-dehydrocholesterol to previtamin D<sub>3</sub> studied in methanol solution with fs transient absorption spectroscopy [21]. The authors establish an S<sub>1</sub> lifetime of  $(0.95 \pm 0.1)$  ps, while the initially prepared S<sub>2</sub> state has a lifetime of  $\leq 0.1$  ps. In contrast to this publication, the present work aims to determine the temporal behavior of this reaction in the *gas phase*. A comparison of the relaxation speed of the 7-dehydrocholesterol system to that of an unsubstituted cyclic polyene is believed to provide information about the influence of bulky substituents on the reaction rate. To establish the role of such a steric factor, it is essential to measure the two different molecules under similar conditions.

### 4.4.1 Time-dependent measurements

The time behavior of the photoinduced electrocyclic ring opening of 7-dehydrocholesterol is investigated by fs pump-probe spectroscopy using 266-nm photons for excitation. The probe wavelength is chosen so that the parent ion yield is as large as possible. In Fig. 4.29 two mass spectra of 7-dehydrocholesterol taken with different probe wavelengths (800 nm and 400 nm) are shown. Obviously, fragmentation is much stronger using UV instead of NIR light for ionization. Therefore, time-dependent measurements are carried out with 800-nm radiation as probe light, because only fragments emerging directly from the parent ion exhibit time constants related to the molecular dynamics of the primary event of the ring-opening reaction. Figure 4.30 shows a magnification of the mass spectrum of Fig. 4.29 (a) in the region in which the parent ion is expected. From Fig. 4.30 it becomes obvious that the sample pressure of 7-dehydrocholesterol, which is only slightly volatile (see Sec. 2.2), is too low to obtain a strong signal, although the whole mass spectrometer is heated to  $\sim 373$  K. Nevertheless, it is possible to evaluate the time-dependent signal of the fragment with mass 369 which is the parent ion minus a methyl group, due to the excellent stability of the laser system and the experimental setup (see Sec. 3.5). However, the time-dependent signals of the parent ion (mass 384) and all other fragments are too noisy for a proper convergence of



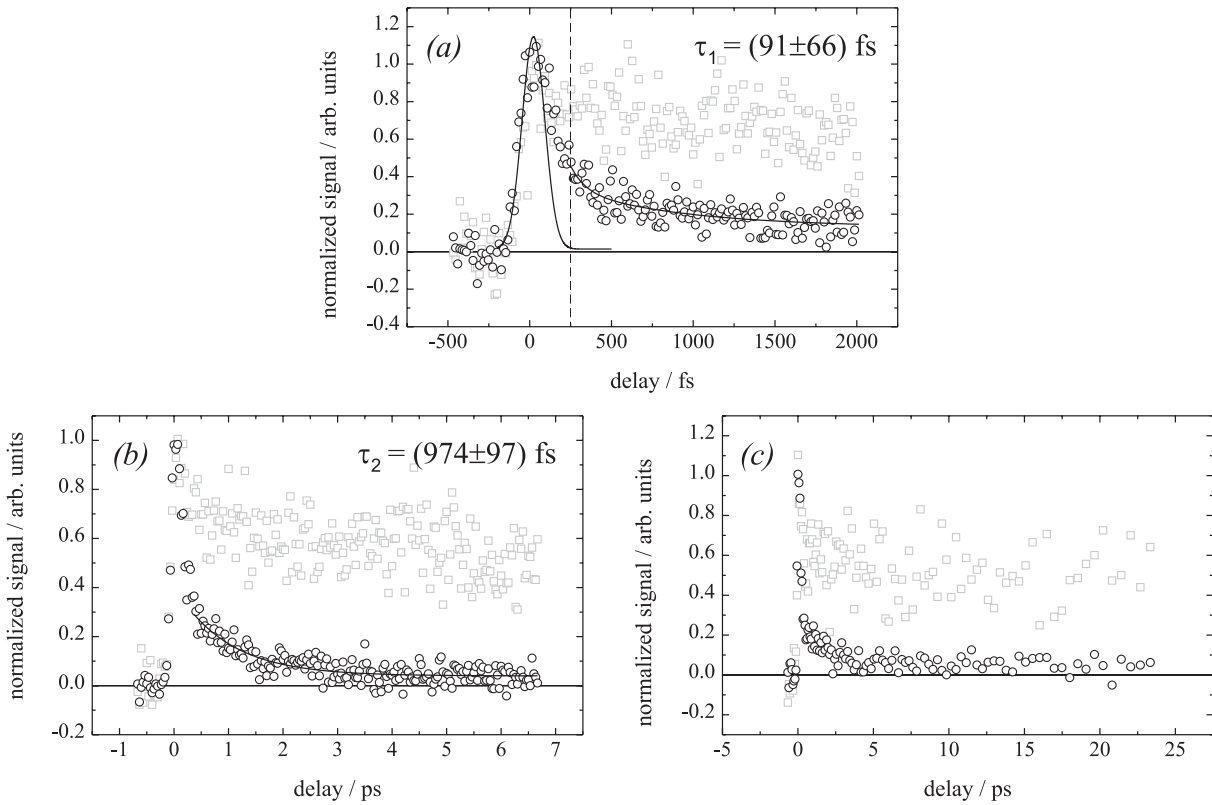
**Figure 4.29:** Mass spectra of 7-dehydrocholesterol taken under different experimental conditions, (a),  $\lambda_{\text{pu}} = 266$  nm,  $\lambda_{\text{pr}} = 800$  nm,  $\tau_{\text{pu}} = 99$  fs,  $\tau_{\text{pr}} = 93$  fs,  $I_{\text{pu}} = 8.5 \times 10^8$  W cm $^{-2}$ ,  $I_{\text{pr}} = 4.3 \times 10^{12}$  W cm $^{-2}$ ,  $p \approx 1 \times 10^{-7}$  mbar; (b),  $\lambda_{\text{pu}} = 266$  nm,  $\lambda_{\text{pr}} = 400$  nm,  $\tau_{\text{pu}} = 99$  fs,  $\tau_{\text{pr}} = 86$  fs,  $I_{\text{pu}} = 2.0 \times 10^9$  W cm $^{-2}$ ,  $I_{\text{pr}} = 6.6 \times 10^{11}$  W cm $^{-2}$ ,  $p \approx 1 \times 10^{-7}$  mbar. In case (a), Xe ( $p_{\text{Xe}} \approx 2 \times 10^{-7}$  mbar) is added for calibration. Both spectra are averaged over 150000 sweeps.



**Figure 4.30:** Enlarged view of the 7-dehydrocholesterol mass spectrum probed by NIR light (see Fig. 4.29 (a)).

the fitting procedure due to their small ion yield. The transient signals of the masses 384 and 369 as a function of pump-probe delay are depicted in Fig. 4.31.

The weakness of the ion signals does not allow transient measurements to be made as a function of probe intensity which would be necessary to determine the absolute width of the response function, as was undertaken for the 1,3,5-cyclooctatriene measurements (see Sec. 4.3.1). Therefore, the fit function (Eq. 4.1) cannot be applied to extract time constants from the measured data. Although the actual order of the probe process within the response function is unknown, the maximum width of the Gauss curve representing the response function can be estimated to be 116 fs using the pulse durations ascertained ( $\tau_{\text{pu}} = 99$  fs,  $\tau_{\text{pr}} = 93$  fs) and the fact that at least 2 probe photons of the energy 1.55 eV are required to ionize an excited 7-dehydrocholesterol molecule (the comparable unsubstituted 1,3-cyclohexadiene molecule has an ionization energy of  $IE = 8.25$  eV [182]). In Fig. 4.31 (a), a Gauss curve with this width is drawn in. The starting point (marked by the dashed line in



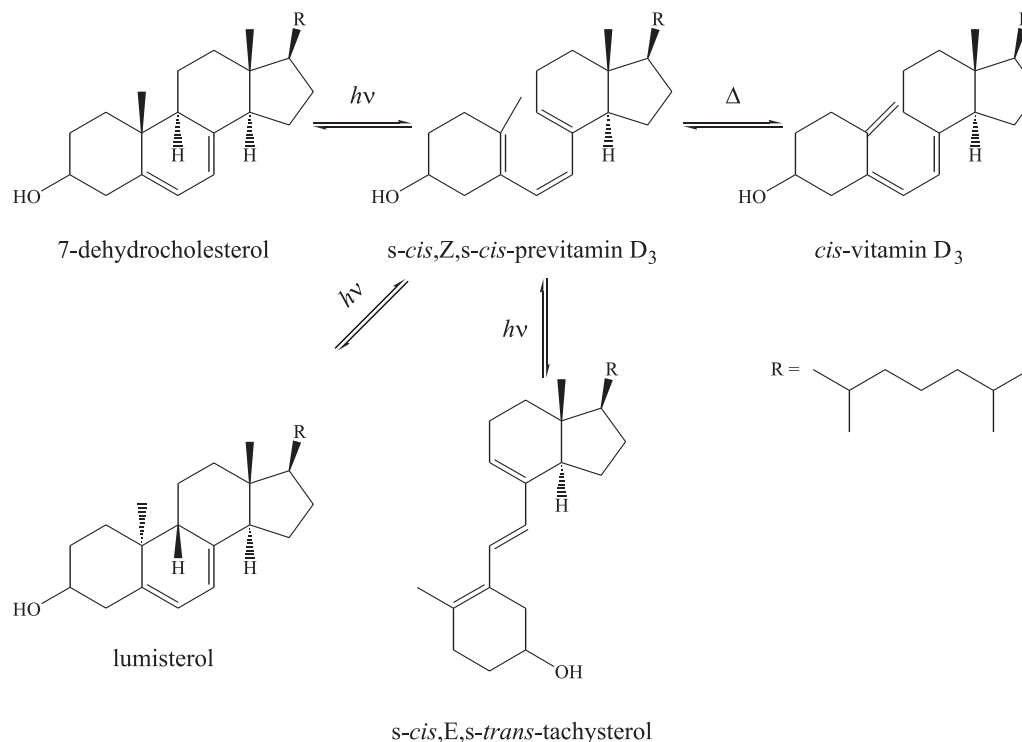
**Figure 4.31:** Transient ion signals of 7-dehydrocholesterol (gray squares, mass 384; black circles, mass 369) recorded under the same experimental conditions as given in the caption of Fig. 4.29 (*a*) with different time resolutions in different pump-probe delay ranges (*a*), resolution, 13 fs, delay from  $\sim -0.5$  ps to 2 ps; (*b*), resolution, 33 fs, delay from  $\sim -0.7$  ps to  $\sim 7$  ps; (*c*), resolution varying from 67 fs to 667 fs, delay from  $\sim -0.7$  ps to  $\sim 23$  ps). In (*a*) the solid lines represent a Gauss fit and a double-exponential fit, the starting point of which is marked by the dashed line. The solid line in (*b*) is a single-exponential fit to the data points. Every data point is averaged over 8000 laser pulses.

Fig. 4.31 (*a*) of the exponential decay is chosen to be 253 fs. Obviously, at this pump-probe delay, the Gauss curve has effectively vanished. The measured transient signal of mass 369 can only be fitted using a double-exponential decay resulting in a short time constant of  $(91 \pm 66)$  fs and a longer one which is in the order of 1 ps but is affected by a huge error due to the too small measurement range compared to the time constant. Nevertheless, it needs to be introduced for a proper running of the fitting procedure. It should be noted that the value of the short time constant is only a rough estimation, because a possible influence of the response function on the exponential decay even at these delay times cannot be excluded. From measuring the same fragment mass in a more extended measurement range, but with a temporal resolution of only 33 fs (*b* in Fig. 4.31), this longer time constant can be determined to be  $\tau = (970 \pm 100)$  fs. For this purpose, the data points are fitted using a single-exponential decay starting at a pump-probe delay of 367 fs. At this point, the amplitude of the shorter time constant is negligible compared to the noise. In addition, one curve is recorded with an even smaller resolution (which is actually varied, starting at 67 fs and gradually increased to 667 fs applying an exponential growth), but up to a more extended pump-probe delay, to prove that the signal remains at the same level at long delay times.



#### 4.4.2 Reaction dynamics of the photoinduced electrocyclic ring opening of 7-dehydrocholesterol

The primary process in 7-dehydrocholesterol photochemistry is the electrocyclic ring opening of the reactant to form the *s-cis,Z,s-cis* conformer of previtamin D<sub>3</sub>. This initially hot product can isomerize to form the more stable *s-cis,Z,s-trans* conformer by rotation around the sterically less hindered single bond. Previtamin D itself is unstable and can undergo several reactions induced by UV light or thermally initiated. In Fig. 4.32 its photoreactions and the (thermally activated) formation of *cis*-vitamin D<sub>3</sub> are depicted. With *s-cis,Z,s-cis*-



**Figure 4.32:** Reaction scheme of vitamin D<sub>3</sub> synthesis with side reactions induced by UV light.

previtamin D as the reactant, the following photoreactions can take place: ring closure leading to 7-dehydrocholesterol or lumisterol and double bond (Hula twist) *cis-trans* isomerization (see Sec. 2.1.2) to form *s-cis,E,s-trans*-tachysterol.

In analogy to the electrocyclic ring opening of 1,3-cyclohexadiene, the ring-opening reaction of 7-dehydrocholesterol is known to proceed through conical intersections from the initially prepared 1B<sub>2</sub> state via the 2A<sub>1</sub> state to the ground state (see Fig. 4.33). The assignment of the measured time constants to this reaction scheme is, therefore, based on the insights in the molecular dynamics of the 1,3-cyclohexadiene reaction which is known to undergo a very rapid decay from the 1B<sub>2</sub> to the 2A<sub>1</sub> state and a slower relaxation on a sub-ps timescale to the ground state [88–90]. The ultrafast potential energy surface transitions occur via conical intersections which have been characterized theoretically and established to be easily accessible without any considerable barrier on the excited state surface [16–18]. Similar conical intersections should be present on the potential energy surfaces involved in the 7-dehydrocholesterol ring-opening reaction. This has been confirmed theoretically for ergosterol, the precursor for vitamin D<sub>2</sub>, which differs from 7-dehydrocholesterol only in the side chain (R in Fig. 4.32) [183].

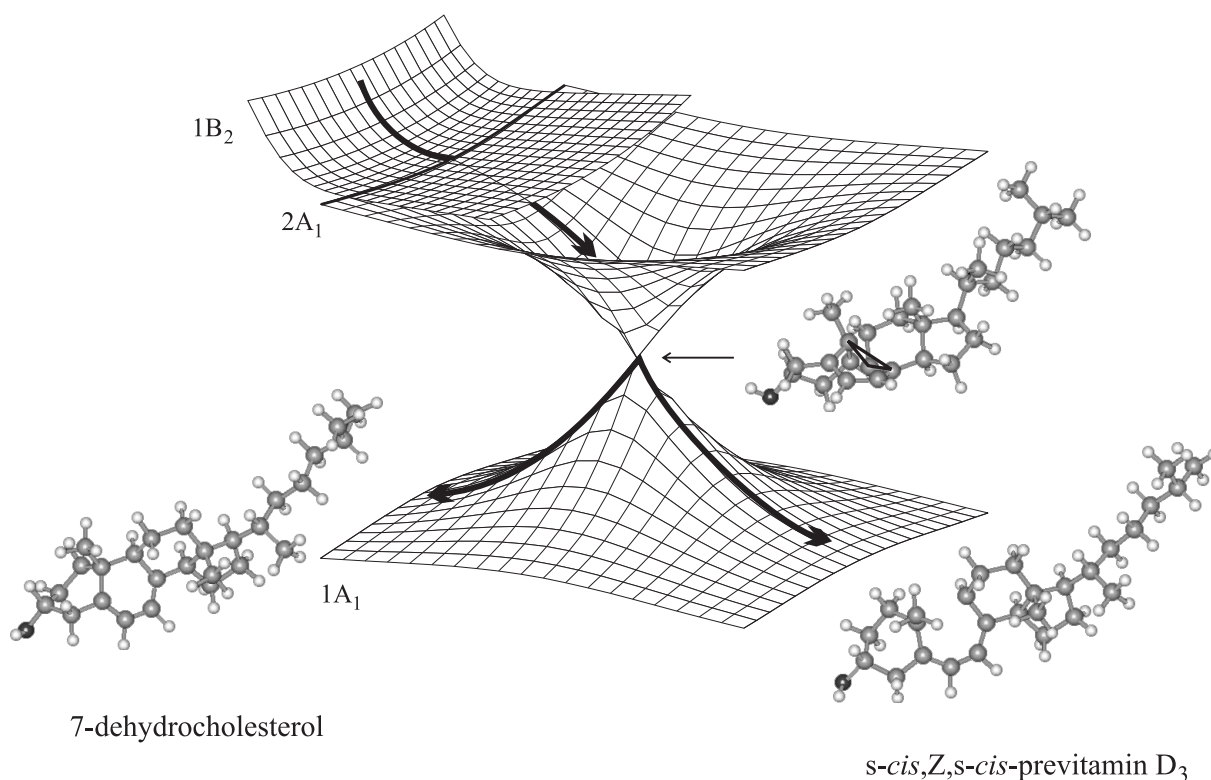


**Figure 4.33:** Model potential energy surfaces involved in the photoinduced electrocyclic ring opening of 7-dehydrocholesterol to form *s-cis,Z,s-cis*-previtamin D<sub>3</sub> via an intermediate structure exhibiting a triangular substructure (marked by the black triangle) at the 2A<sub>1</sub>–1A<sub>1</sub> conical intersection.

The time constants derived from the decay of the 7-dehydrocholesterol fragment with mass 369 can be allocated to the reaction scheme (see Fig. 4.33) as follows. The fact that two time constants are extracted from one signal proves that, in the case of a sequential process, the shorter decay time must occur earlier in time than the longer one. The short time constant which amounts approximately to 100 fs can be assigned to the 1B<sub>2</sub> lifetime reflecting the disappearing of the molecule from the spectroscopically bright 1B<sub>2</sub> state to the dark 2A<sub>1</sub> state. The long decay time of around 1 ps will consequently be allocated to the 2A<sub>1</sub> lifetime. This interpretation would be in agreement with the findings of R.J. Sension *et al.* [21]. However, the existence of a second conical intersection between the 2A<sub>1</sub> state and the ground state which is more difficult to reach and a concomitant splitting of the wavepacket has been proved theoretically for the 1,3-cyclohexadiene ring-opening reaction [16–18]. Accordingly, the 100 fs decay time could potentially be related to an easily accessible 2A<sub>1</sub>–1A<sub>1</sub> transition. In this case, the topology of the excited potential energy surface has to be such that the wavepacket splits into two fractions which evolve through two different conical intersections to the ground state. From the data obtained in the present work, a final statement about the assignment of the measured short time constant to the actual wavepacket dynamics cannot be made. However, it becomes obvious that the 1 ps time constant, in fact, corresponds to a relaxation to the ground state.

In contrast to the 1,3-cyclohexadiene system, the accessibility of the conical intersections involved in the 7-dehydrocholesterol ring-opening reaction will potentially be affected by the bulky substituents on the critical modes and the existence of barriers in the vicinity of these surface transitions. From the comparison of the 1 ps time constant with the corresponding

decay time established for the ring-opening reaction of the unsubstituted cyclic polyene 1,3,5-cyclooctatriene ( $\tau \approx 750$  fs), which has been investigated under almost identical experimental conditions, it can be concluded that steric hindrance plays only a minor role in this case. This means that the triangular substructure, which seems to be characteristic for ultrafast photochemical reactions of polyenes involving conical intersections, is easily accessible despite of the rather bulky substituents. Consequently, the vibrational energy is extremely localized in a few special modes which drive the reaction and the course of this reaction is not influenced by the other parts of the molecule.

## 5 Summary

In the present work, the ultrafast dynamics of the photoinitiated electrocyclic ring-opening reactions of 1,3,5-cyclooctatriene and 7-dehydrocholesterol are investigated in a fs pump-probe experiment using ionization as the probe step. Concerning the 1,3,5-cyclooctatriene photoreaction, there are strong arguments for the participation of two different reaction channels (involving a 3-center and a 4-center substructure) which lead to three products. Studying the ring-opening reaction of 7-dehydrocholesterol, which is a substituted cyclic polyene, answers the crucial question to what extent an ultrafast reaction can be slowed down by the influence of a steric factor.

To elucidate reaction dynamics of molecules without disturbing influences of solvents, matrices or surfaces, the investigations are carried out in the gas phase. Since the gas particle density is too small for reliable transient absorption experiments, detection is performed by photoionization in combination with time-of-flight mass spectrometry. Particular care is taken in the experiment to establish well-defined conditions and, especially, to shed light on the probe step with the help of the similar-sized molecule toluene by exploring several fundamental aspects of its ionization and fragmentation behavior.

The ionization mechanism and the fragmentation behavior of toluene are discussed controversially in the literature. The photoionization of toluene is investigated using 80-fs, 800-nm pulses, with intensities in the focused laser beam of up to  $2.8 \times 10^{14} \text{ W cm}^{-2}$ . Measurements of the spatial beam profile, the temporal autocorrelation function, and the frequency spectrum of the pulse after its passage through the entrance window of the vacuum system show the laser pulse to remain essentially unaltered, proving that nonlinear effects such as self-focusing or self-phase modulation do not have any influence. Both for linear and circular polarization of the laser light, all recorded mass spectra exhibit only three peaks, the parent ion and its heavier isotopic variant as well as one fragment generated by hydrogen abstraction. The ionization mechanism is established to be a multiple-order MPI process [163–165].

In contrast to this experiment, which deals with the nonlinear photoionization mechanism of toluene, the focusing for the investigation of its fragmentation is such that the intensity in the entrance window of the vacuum system is sufficiently high to induce nonlinear effects. With Fourier-limited pulses in the near-IR, a strong fragmentation takes place only at intensities beyond  $\sim 10^{15} \text{ W cm}^{-2}$  [146]. To shed light on the fragmentation behavior at lower intensities, the shape of the laser pulses is varied by increasing the intensity in the CaF<sub>2</sub> entrance window of the vacuum system which leads to a broadening of the power spectra. The particular influence of such nonlinear beam distortions becomes evident if one compares two mass spectra of ionized toluene: one recorded at higher intensity ( $1 \times 10^{14} \text{ W cm}^{-2}$ ) at focus but lower peak intensity in the CaF<sub>2</sub> window ( $7 \times 10^{10} \text{ W cm}^{-2}$ ), the other taken at lower intensity at focus ( $6 \times 10^{13} \text{ W cm}^{-2}$ ) but higher peak intensity in the CaF<sub>2</sub> window ( $3 \times 10^{11} \text{ W cm}^{-2}$ ). Although the former spectrum is recorded at an even higher intensity at focus than the latter, extensive fragmentation is only observed in the latter. Obviously, this must be a result of the different intensities to which the CaF<sub>2</sub> window is exposed. For a sufficiently broad spectrum, stimulated Raman scattering may lead to significant amounts of coherent absorption of (difference) frequencies that are in the order of  $350 \text{ cm}^{-1}$  and higher, causing a vibrational excitation of the carbon backbone of the toluene molecule. In this way, the increased fragmentation for increasing intensity in the entrance window can be rationalized from the broadening of the frequency spectra. In other words, this is a clear example of coherent control of fragmentation. It should be noted that resonance-enhanced fragmen-

tation induced by non-detectable amounts of radiation generated in the visible or UV by nonlinear processes in the CaF<sub>2</sub> window cannot be excluded. Independent of the underlying mechanism, however, it could be shown that the temporal shapes of the initially Gaussian laser pulses are affected fundamentally by nonlinear distortions acquired in the CaF<sub>2</sub> window. In pump-probe experiments (with ionization as probe step), these temporal shapes play a crucial role in the evaluation of time constants which, in general, requires the knowledge of those signal features originating from the pulses contributing to the total signal.

The photoinduced ring opening of 1,3,5-cyclooctatriene is investigated using two different experimental setups. On the basis of these measurements, it could be proved that any nonlinearity present in the laser beam must be avoided to allow for a proper interpretation of the measured data. Additionally, it was demonstrated that, especially for time constants in the order of the pulse duration, it is of paramount importance to know the order of the MPI process and the pulse lengths, to obtain all parameters not related to intrinsic molecular properties. This yields the conditions for a reasonable determination of the decay constants. Besides previous investigations of P.J. Reid *et al.* who established in a ps time-resolved resonance Raman experiment a ground-state appearance time of  $(12 \pm 2)$  ps for the 1,3,5-cyclooctatriene ring-opening reaction [19,20], this study represents the first true sub-ps measurement of this reaction. The transient mass spectrum of 1,3,5-cyclooctatriene consists of four peaks (plus their heavier isotopic variants): the parent ion (mass 106), and the fragments with masses 105, 91, and 78. Three short time constants and one longer are derived from the raw data. The parent ion decays with a time constant of  $(48 \pm 1)$  fs and exhibits a shift of  $(15 \pm 1)$  fs versus the absolute time zero that is determined in experiments with Xe. Both its decay time and its shift are the shortest times observable in the 1,3,5-cyclooctatriene system. Therefore, the time-dependent behavior of the parent ion can be assigned to the  $1B_2-2A_1$  transition. The fragments with masses 105 and 91 show an essentially identical behavior with respect to their short time constants ( $(61 \pm 1)$  fs and  $(60 \pm 2)$  fs) and their shifts to time zero ( $(43 \pm 2)$  fs in both cases). Consequently, the 60-fs decay time is assigned to one of the two conical intersections to the ground state. However, the mass 91 transient signal exhibits a second, much longer decay time ( $(750 \pm 60)$  fs). It is probably related to a relaxation to the ground state via an alternative decay channel (there must be more than one conical intersection for each conformer in an opened ring polyene [180]) of the  $2A_1-1A_1$  conical intersections and after evolution on the  $2A_1$  potential energy surface. In contrast to the other two fragments, the fragment with mass 78 exhibits a significantly longer (short) time constant of  $(68 \pm 2)$  fs than the other two fragments, but it appears earlier ( $(28 \pm 2)$  fs shift to time zero). Consequently, it is attributed to the second conical intersection leading to another product. Thus, the existence of two different reaction channels, probably involving a 3-center and a 4-center substructure corresponding to two different conical intersections, is proved. The results remain essentially unaltered by changing the probe wavelength from 800 nm to 400 nm. On the basis of measuring transient signals as a function of the probe intensity, in addition to deriving reliable time constants, the total signal including the time dependence of the ionization dynamics, which superimposes the response function and the exponential decay of the evolving molecule, could be simulated.

In contrast to 1,3,5-cyclooctatriene, the 7-dehydrocholesterol molecule is a substituted cyclic polyene which leads to a weak signal as a result of its limited volatility. Therefore, the order of the probe process cannot be determined. From the time-dependent measurements, however, two time constants can be derived, the shorter amounting to approximately 100 fs and the longer amounting to  $(970 \pm 100)$  fs. The short time constant can be assigned to the  $1B_2$  lifetime, whereas the long decay time of around 1 ps will be allocated to the  $2A_1$

lifetime. This interpretation could be seen in agreement with recent results of an experiment in solution of the group of R. Sension [21]. However, alternatively, the 100 fs decay time could also be related to an easily accessible  $2A_1-1A_1$  transition. This would imply a topology of the excited potential energy surface with properties which lead to a splitting of the wavepacket into two fractions that evolve through two different conical intersections to the ground state, as predicted theoretically for the 1,3-cyclohexadiene system [16–18]. From the comparison of this 1 ps time constant with the corresponding decay time established for the ring-opening reaction of the unsubstituted cyclic polyene 1,3,5-cyclooctatriene ( $\tau \approx 750$  fs), which has been investigated under almost identical experimental conditions, it can be concluded that steric hindrance plays only a minor role in this case. This means that the intermediate structure is easily accessible despite of the rather bulky substituents. Consequently, the vibrational energy is extremely localized in a few special modes which drive the reaction and the course of this reaction is not influenced by the other parts of the molecule.

From those pump-probe measurements, elucidating not only dynamical aspects but also detection mechanisms, decay times are derived which, in combination with quantum-chemical investigations of the involved potential energy surfaces, can provide detailed insights into the microscopic nature of ultrafast chemical reaction dynamics and will stimulate further theoretical work.

## A Derivation of the fit function of Eq. 4.1

In this appendix, the fit function of Eq. 4.1 that is used to extract time constants from the measured transient signals depending on the pump-probe delay is derived. For measurements of molecular dynamics, pump and probe pulses that are short compared to the time constants ( $\delta$ -pulses) would be desirable. Then, the measurable signal reflecting the time-dependent dynamics of the evolving molecule is given by the function  $D(t')$  which is considered to be non-existent before excitation (corresponding to  $t' < 0$ ) and to be described by an exponential decay for  $t' \geq 0$ ,

$$D(t') = \begin{cases} A_D \exp\left[-\frac{t'}{\tau}\right] + y_0 & \text{for } t' \geq 0 \\ 0 & \text{for } t' < 0 \end{cases} \quad (\text{A.1})$$

where  $t'$  is the temporal delay between pump and probe pulse,  $A_D$  the amplitude and  $\tau$  the time constant of the exponential decay. For  $t' \geq 0$ , an offset  $y_0$  is introduced which is related to molecular properties and is nonzero if the ionization efficiency of the product generated by the photoreaction is different from that of the reactant.

In reality, such  $\delta$ -pulses do not exist. Therefore, some mathematics must be applied to extract the information reflecting the molecular dynamics from the total signal which consists of a contribution related to intramolecular processes smeared out by the contributions of the laser pulses. Instructively, both pump and probe pulses can be considered to consist of an infinite number of  $\delta$ -pulses (see Fig. A.1). This means that, in the case of pump pulses,

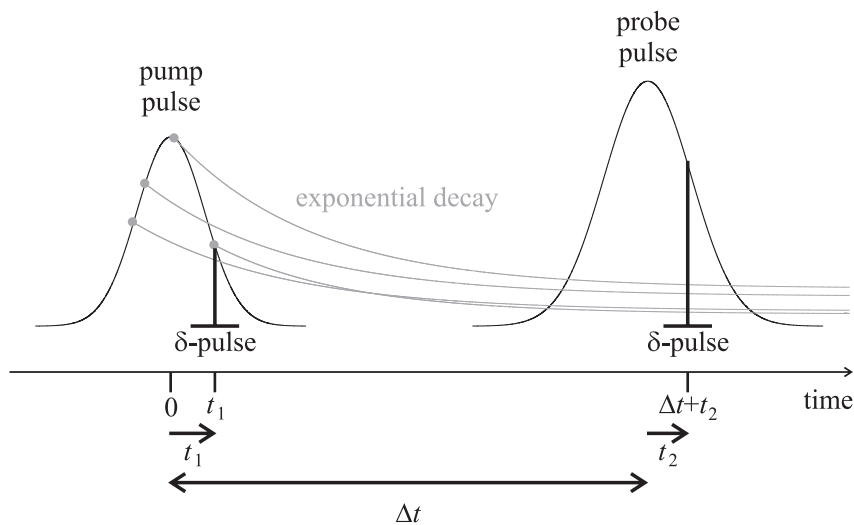


**Figure A.1:** Illustration of the time variables used for the derivation of the fit function of Eq. 4.1. each  $\delta$ -pulse contributes to the excitation probability  $P_{\text{pu}}$  (to the order of 1) and induces the photochemical reaction and the concomitant (exponential) decay of the signal at every point in time within the pump pulse. This leads to a smearing out of the begin of the reaction in the measurable signal. The time-dependent excitation function  $f(t)$  can be expressed as:

$$f(t) = \int_{-\infty}^{\infty} dt_1 P_{\text{pu}}^1(t_1) \cdot D(t - t_1) \quad (\text{A.2})$$

Also the probe pulse, which appears at a time delay  $\Delta t$  after the pump pulse, can be treated as an accumulation of infinitesimal short pulses. In order to model the measurable signal,

all contributions of these  $\delta$ -pulses to the ionization probability  $P_{\text{pr}}$  (to the order of  $N$ ) of the decaying signal have to be summed. This results in the total signal, given by

$$F(\Delta t) = \int_{-\infty}^{\infty} dt_2 \int_{-\infty}^{\infty} dt_1 P_{\text{pu}}^1(t_1) \cdot D(\Delta t + t_2 - t_1) \cdot P_{\text{pr}}^N(t_2). \quad (\text{A.3})$$

Substituting the integration variable  $t_1$  by  $\Delta t + t_2 - t'$ , the function  $F(\Delta t)$  of Eq. A.3 can also be expressed as

$$F(\Delta t) = - \int_{-\infty}^{\infty} dt_2 \int_{-\infty}^{\infty} dt' P_{\text{pu}}^1(\Delta t + t_2 - t') \cdot D(t') \cdot P_{\text{pr}}^N(t_2). \quad (\text{A.4})$$

This fit function  $F(\Delta t)$  is a function of the pump-probe delay  $\Delta t$  and consists of the time-dependent dynamics of the evolving molecules  $D(t')$  convoluted with the response function  $R(t' - \Delta t)$  which is also a function of time. Then, the total fit function can be expressed as

$$F(\Delta t) = \int_{-\infty}^{\infty} R(t' - \Delta t) D(t') dt'. \quad (\text{A.5})$$

Assuming the pump and probe pulses to have a Gaussian temporal shape, the response function  $R(t' - \Delta t)$  has the form

$$\begin{aligned} R(t' - \Delta t) &= \int_{-\infty}^{\infty} \underbrace{\exp \left[ - \left( \frac{t - (t' - \Delta t)}{\tau_{\text{pu}}} \right)^2 \right]^1}_{\text{pump pulse}} \cdot \underbrace{\exp \left[ - \left( \frac{t}{\tau_{\text{pr}}} \right)^2 \right]^N}_{\text{probe pulse}} dt \\ &= \int_{-\infty}^{\infty} \sqrt{\pi} w \cdot \exp \left[ - \left( \frac{t - (t' - \Delta t)}{w} \right)^2 \right] dt \end{aligned} \quad (\text{A.6})$$

with the width of the response function

$$w = \sqrt{\tau_{\text{pu}}^2 + \frac{1}{N} \tau_{\text{pr}}^2}. \quad (\text{A.7})$$

For practical use, the two signal contributions given in Eq. A.6 and Eq. A.1 are inserted into Eq. A.5. Normalization to the area of the response function leads to the fit function of Eq. 4.1,

$$F(\Delta t) = y_{\text{offs}} + \int_0^{\infty} \underbrace{\frac{1}{\sqrt{\pi} w} \cdot \exp \left[ - \left( \frac{t' - (\Delta t - S)}{w} \right)^2 \right]}_{\text{response function}} \cdot \underbrace{\left[ A_D \cdot \exp \left[ - \frac{t'}{\tau} \right] + y_0 \right]}_{\text{exponential decay of the evolving molecule}} dt'. \quad (\text{A.8})$$

Because the origin of the measured signal is unknown, it is adjusted by introducing the parameter  $S$ , which allows the temporal shift of the measured signal versus a simultaneously measured reference ion signal (e.g. the parent ion or Xe) to be determined, as well as the offset  $y_{\text{offs}}$ , which compensates for any vertical shift in the measured signal. Such shifts are usually small and caused by noise.



The integral in Eq. A.8 is numerically solved using the error function defined as

$$\frac{1}{2} - \frac{1}{2} \operatorname{erf}(x) = \frac{1}{\sqrt{\pi}} \int_x^\infty \exp[-z^2] dz, \quad (\text{A.9})$$

leading to

$$F(\Delta t) = y_{\text{offs}} + y_0 \left[ \operatorname{erf} \left( \frac{\Delta t - S}{w} \right) + 1 \right] + \frac{1}{2} A_D \exp \left[ \frac{w^2}{4\tau^2} - \frac{\Delta t - S}{\tau} \right] \left[ \operatorname{erf} \left( \frac{\Delta t - S}{w} - \frac{w}{2\tau} \right) + 1 \right]. \quad (\text{A.10})$$

Using this fit function  $F(\Delta t)$ , the offsets  $y_{\text{offs}}$  and  $y_0$  which are not strongly dependent on other fit parameters, the amplitude of the exponential decay  $A_D$ , the shift versus time zero  $\Delta S$ , and the time constant  $\tau$  can be extracted from the measured transient data.

It should be noted that, in general, the measured signal can contain, in addition to the response function and molecular decay, a contribution called coherence peak  $C(\Delta t)$ , which is caused by non-resonant coherent combinations of pump and probe photons and only becomes evident if pump pulse and probe pulse overlap. The coherence peak with amplitude  $A_C$  can

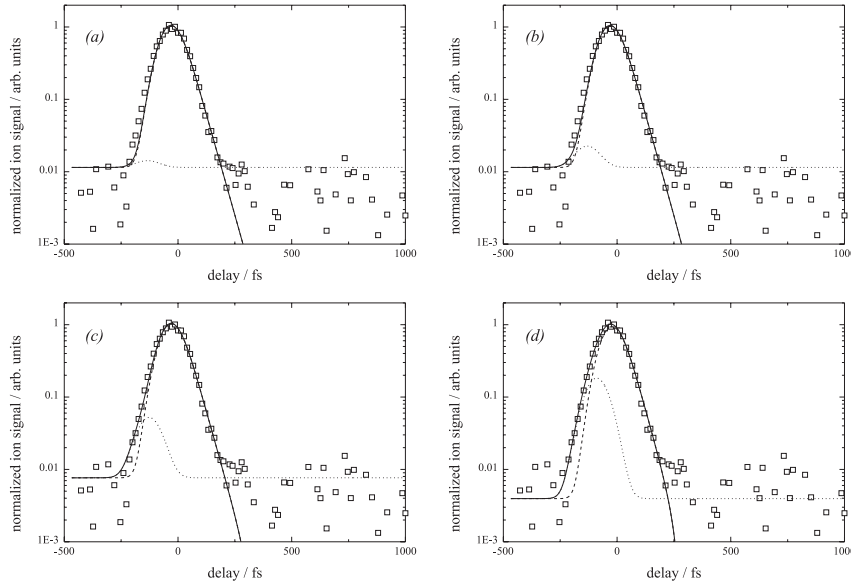


**Figure A.2:** Logarithmic representation of the measured time-dependent signal of the parent ion of 1,3,5-cyclooctatriene (squares) and the corresponding fits (solid lines, total function (Eq. A.10+Eq. A.11); dashed lines, convolution term (Eq. A.10); dotted lines, coherence peak (Eq. A.11)). From panel (a) to (d), the portion of the coherence peak with respect to the area of the total signal is increased ((a), 0.4%; (b), 1.3%; (c), 4.0%; (d), 15.3%). Independent of the contribution of the coherence peak, the parameters related to molecular dynamics remain unchanged.

be expressed analogously to the response function

$$C(\Delta t) = A_C \cdot \underbrace{\int_{-\infty}^{\infty} \exp \left[ - \left( \frac{t' - t_0 - \Delta t}{\tau_{\text{pu}}} \right)^2 \right]^1}_{\text{pump pulse}} \cdot \underbrace{\exp \left[ - \left( \frac{t' - t_0}{\tau_{\text{pr}}} \right)^2 \right]^{N'}}_{\text{probe pulse}} dt' \quad (\text{A.11})$$

where the order of the probe process  $N'$  may differ from that inserted in the response function. Although the actual order  $N'$  is unknown, the maximum width of the Gauss curve

representing the coherence peak can be estimated using the same measured pulse durations used to determine the width of the response function and the fact that at least 2 probe photons of the energy 1.55 eV are required to ionize an excited 1,3,5-cyclooctatriene molecule ( $IE = 7.9$  eV [177]). Additionally, the coherence peak is shifted in time by the amount  $t_0$  versus the signal contribution originating from the convolution term (Eq. A.8). In order to reveal the effect of the coherence peak on the molecular information extracted from the measured data, the measured data of the parent ion of 1,3,5-cyclooctatriene are simulated exemplarily by a function where  $C(\Delta t)$  is included with different proportions of  $C(\Delta t)$  to the total signal (see Fig. A.2).

It is clear that the parameters related to molecular dynamics, such as time constant  $\tau$  and temporal shift versus a reference signal  $S$ , are not affected by the contribution of the coherence peak. Therefore, it is neglected and the fit function  $F(\Delta t)$  of Eq. A.8 is applied to fit the measured data.

# Abbreviations

$\alpha$	coefficient
$\beta$	coefficient
$\gamma$	coefficient, Keldysh adiabicity parameter, nonlinear refractive index in units of $\text{cm}^2 \text{W}^{-1}$
$\Delta\varphi$	phase shift
$\Delta E$	energy gap
$\Delta k$	difference between the propagation constants of incident and generated wave
$\Delta S$	relative temporal shift of the measured signal versus a time zero
$\Delta t$	time delay
$\theta$	angle, ellipticity, phase-matching angle
$\lambda$	wavelength
$\lambda_0$	fundamental wavelength
$\nu$	light frequency
$\varphi$	phase-matching angle
$\phi_{(nuc)}$	nuclear wavefunction
$\chi$	atomic orbital, material susceptibility
$\psi_{(el)}$	electron wavefunction
$\Psi$	total wavefunction
$\sigma$	MPI cross section
$\sigma_h$	horizontal mirror plane
$\sigma_v$	vertical mirror plane
$\sigma_x$	semiaxis of an ellipse in the $x$ -direction
$\sigma_y$	semiaxis of an ellipse in the $y$ -direction
$\tau$	pulse duration, time constant
$\omega$	angular frequency
$a$	voltage ratio $U_1/U_2$
A	attenuator
A	area
$A(\omega)$	frequency distribution
$A_C$	amplitude of the coherence peak
$A_D$	amplitude of the exponential function reflecting the molecular dynamics
ADK	Ammosov-Delone-Krainov
ATI	above-threshold ionization

---

BBO	$\beta$ -barium borate
BK7	boron-kron glass 7
$c$	coefficient, speed of light
$C(\Delta t)$	coherence peak
$C_2$	two-fold rotary axis
CI	conical intersection
CCD	charged coupled device
circ	circular
CPA	chirped pulse amplification
$d$	beam diameter, thickness
$D$	diameter
$D(t')$	time-dependent dynamics of the evolving molecule
$D_x$	measured diameter of the spatial laser beam profile in the $x$ -direction
$D_y$	measured diameter of the spatial laser beam profile in the $y$ -direction
DFG	difference-frequency generation
DFM	difference-frequency measurement
$E$	electric field, energy
$E_{\text{int}}$	internal energy
eff	effective
el	electronic
exc	excitation
$f$	final, focal length
F	filter
$F(\Delta t)$	fit function
FW	full width
FWHM	full width at half maximum
G	grid
GC-MS	gas chromatography mass spectrometry
GVD	group velocity dispersion
$\hat{H}$	Hamiltonian
HOMO	highest occupied molecular orbital
HPLC	high performance liquid chromatography
$i$	initial, number
$I$	intensity
$I_0$	peak intensity
$I_{\text{sat}}$	saturation intensity

---

$I_w$	intensity to which the CaF <sub>2</sub> window is exposed
IC	internal conversion
$IE$	ionization energy
ISC	intersystem crossing
IVR	intramolecular vibrational relaxation
$J$	angular momentum
$k$	exchange interaction, proportionality factor, rate
$K$	lowest number of photons required for ionization
KLM	Kerr lens mode-locking
$l$	interaction length
L	lens
$L$	distance
LBO	lithium barium borate
LCAO	linear combination of atomic orbitals
lin	linear
LOPT	lowest-order-perturbation theory
LUMO	lowest unoccupied molecular orbital
$m$	mass
M	mirror
$M$	ion mass, molecular mass
<b>M</b>	reactant molecule in the ground state
<b>M*</b>	reactant molecule in the excited state
$M(\Delta t)$	model function used to simulate the ionization dynamics
$M_J$	magnetic quantum number
max	maximum
MCP	multichannel-plate
MPI	multiphoton ionization
MS	mass spectrometer
$n$	number of H atoms in a hydrocarbon, refractive index, variable
$n_0$	refractive index
$n_2$	nonlinear refractive index
$N$	number of modes, order of an ionization process, order of the probe process
$N'$	order of the probe process within the coherence peak
NIR	near-infrared
nuc	nuclear
OD	optical density

OTBI	over-the-barrier-ionization
$p$	sample pressure as indicated by the pressure gauge
$P$	ionization probability, power
<b>P</b>	product(s)
$P_{cr}$	critical power
$P_{pr}$	ionization probability by the probe light
$P_{pu}$	excitation probability by the pump light
PEPICO	photoelectron-photoion coincidence
pr	probe
pu	pump
$q$	charge number, vibrational coordinate
<b>q</b>	internal coordinates
$r$	distance, spatial coordinate
<b>r</b>	spatial coordinates of the electrons
R	repeller
$R$	diameter, internuclear distance
<b>R</b>	spatial coordinates of the nuclei
$R(\Delta t)$	response function
RRKM	Rice-Ramsperger-Kassel-Marcus
$s$	number of internal coordinates
$S$	temporal shift of the measured signal (versus a simultaneously measured reference ion signal)
$S_0$	singlet ground state
$S_1$	singlet first excited state
SFG	sum-frequency generation
SHG	second-harmonic generation
SI	international unit system (système international d'unités)
SPM	self-phase modulation
$t$	time
$t_0$	shift in time
$T$	temperature
$\hat{T}$	kinetic energy operator
TDL	times diffraction limited
TEM	transverse electromagnetic mode
TH	top hat
TOF	time-of-flight

---

$u$	atomic mass unit
$U_p$	ponderomotive energy
UVFS	ultraviolet fused silica
UV	ultraviolet
$V$	adiabatic coupling, potential
$\hat{V}$	potential energy operator
VIS	visible
$w$	beam radius, half 1/e-width of the response function
W	window
$x$	spatial coordinate in transverse direction
$y$	spatial coordinate in transverse direction
$y_0$	offset for positive time delays
$y_{\text{offs}}$	offset
$Y$	yield
$z$	Rayleigh length, spatial coordinate in propagation direction

## References

- [1] V. Bonačić-Koutecký and J. Michl, *Theor. Chim. Acta* **68**, 45 (1985).
- [2] F. Bernardi, S. De, M. Olivucci, and M.A. Robb, *J. Am. Chem. Soc.* **122**, 1737 (1990).
- [3] S. Xantheas, S.T. Elbert, and K. Ruedenberg, *Theor. Chim. Acta* **78**, 365 (1991).
- [4] A.L. Sobolewski, C. Woywood, and W. Domcke, *J. Chem. Phys.* **98**, 5627 (1993).
- [5] D.R. Yarkony, *J. Chem. Phys.* **100**, 3639 (1994).
- [6] P. Celani, F. Bernardi, M. Olivucci, and M.A. Robb, *J. Chem. Phys.* **102**, 5733 (1995).
- [7] M. Klessinger, *Angew. Chem.* **107**, 597 (1995), (in German).
- [8] Y. Haas, M. Klessinger, and S. Zilberg, (Eds.), *Special Issue*, vol. **259** of *Chemical Physics*, 2000.
- [9] The Nobel Foundation, <http://mirror.nobel.ki.se/laureates/chemistry-1999.html> (1999).
- [10] V. Sundström, (Ed.), *Femtochemistry & Femtobiology: Ultrafast Reaction Dynamics at Atomic-Scale Resolution*, Nobel Symposium, World Scientific, Singapore, 1996.
- [11] M.A. El-Sayed, I. Tanaka, and Y. Molin, *Ultrafast Processes in Chemistry and Photobiology*, Blackwell Science, 1995.
- [12] S. Pedersen, J.L. Herek, and A.H. Zewail, *Science* **266**, 1359 (1994).
- [13] A.H. Zewail, *Sci. Am.* **263**, 40 (1990).
- [14] P. Celani, F. Bernardi, M.A. Robb, and M. Olivucci, *J. Phys. Chem.* **100**, 19364 (1996).
- [15] M. Garavelli, P. Celani, M. Fato, M.J. Bearpark, B.R. Smith, M. Olivucci, and M.A. Robb, *J. Phys. Chem. A* **101**, 2023 (1997).
- [16] M. Garavelli, F. Bernardi, M. Olivucci, T. Vreven, S. Klein, P. Celani, and M.A. Robb, *Faraday Discuss. Chem. Soc.* **110**, 51 (1998).
- [17] A. Hofmann and R. de Vivie-Riedle, *J. Chem. Phys.* **112**, 5054 (2000).
- [18] A. Hofmann, L. Kurtz, and R. de Vivie-Riedle, *Appl. Phys. B* **71**, 391 (2000).
- [19] P.J. Reid, S.J. Doig, and R.A. Mathies, *J. Phys. Chem.* **94**, 8396 (1990).
- [20] P.J. Reid, M.K. Lawless, S.D. Wickham, and R.A. Mathies, *J. Phys. Chem.* **98**, 5597 (1994).
- [21] N.A. Anderson, J.J. Shiang, and R.J. Sension, *J. Phys. Chem.* **103**, 10730 (1999).
- [22] The Nobel Foundation, <http://mirror.nobel.ki.se/laureates/chemistry-1998.html> (1999).



- [23] M.J. Frisch *et al.*, GAUSSIAN 94, 1995.
- [24] W. Domcke and G. Stock, *Adv. Chem. Phys.* **100**, 9 (1997).
- [25] R.B. Woodward and R. Hoffmann, *J. Am. Chem. Soc.* **87**, 395 (1965).
- [26] P. Celani, S. Ottani, M. Olivucci, F. Bernardi, and M.A. Robb, *J. Am. Chem. Soc.* **116**, 10141 (1994).
- [27] P.W. Atkins, *Physikalische Chemie*, VCH, Weinheim, 1990, (in German).
- [28] K. Fukui, *Tetrahedron Letters* **1965**, 2009, 2427 (1965).
- [29] K. Fukui and H. Fujimoto, *Tetrahedron Letters* **1966**, 251 (1966).
- [30] W.T.A.M. van der Lugt and L.J. Oosterhoff, *J. Am. Chem. Soc.* **91**, 6042 (1969).
- [31] H.C. Longuet-Higgins and E.W. Abrahamson, *J. Am. Chem. Soc.* **87**, 2045 (1965).
- [32] L.D. Landau, *Z. Phys. Sov.* **2**, 46 (1932).
- [33] C. Zener, *Proc. R. Soc. London, Ser. A, Math. Phys. Sci.* **137**, 696 (1932).
- [34] J. von Neumann and E. Wigner, *Phys. Z.* **30**, 467 (1929).
- [35] E. Teller, *J. Chem. Phys.* **41**, 109 (1937).
- [36] G.J. Atchity, S.S. Xantheas, and K. Ruedenberg, *J. Chem. Phys.* **95**, 1862 (1991).
- [37] M. Klessinger and J. Michl, *Excited States and Photochemistry of Organic Molecules*, VCH, New York, 1995.
- [38] R. Engelman, *The Jahn-Teller Effect in Molecules and Crystals*, Wiley-Interscience, 1972.
- [39] I.B. Bersuker, *Coord. Chem. Rev.* **14**, 357 (1975).
- [40] C.A. Mead and D.G. Truhlar, *J. Chem. Phys.* **70**, 2284 (1979).
- [41] R. Bruckmeier, Ch. Wunderlich, and H. Figger, *Phys. Rev. Lett.* **72**, 2550 (1994).
- [42] D. Azinovic, R. Bruckmeier, Ch. Wunderlich, H. Figger, G. Theodorakopoulos, and I.D. Petsalakis, *Phys. Rev. A* **58**, 1115 (1998).
- [43] G. Herzberg, *Einführung in die Molekülspektroskopie*, Steinkopf, Darmstadt, 1973, (in German).
- [44] I.N. Ragazos, M.A. Robb, F. Bernardi, and M. Olivucci, *Chem. Phys. Lett.* **197**, 217 (1992).
- [45] P. Celani, M.A. Robb, M. Garavelli, F. Bernardi, and M. Olivucci, *Chem. Phys. Lett.* **243**, 1 (1995).
- [46] F. Bernardi, M. Olivucci, and M.A. Robb, *Chem. Soc. Rev.*, 321 (1996).
- [47] F. Bernardi, M. Olivucci, and M.A. Robb, *Pure Appl. Chem.* **67**, 17 (1995).

- [48] M. Olivucci, priv. comm., 1999.
- [49] F. Bernardi, M. Olivucci, and M. Robb, *Isr. J. Chem.* **33**, 265 (1993).
- [50] M. Garavelli, B. Frabboni, M. Fato, P. Celani, F. Bernardi, M.A. Robb, and M. Olivucci, *J. Am. Chem. Soc.* **121**, 1537 (1999).
- [51] A.M. Müller, S. Lochbrunner, W.E. Schmid, and W. Fuß, *Angew. Chem. Int. Ed. Engl.* **37**, 505 (1998).
- [52] A.M. Müller, S. Lochbrunner, W. Fuß, W.E. Schmid, and K.-L. Kompa, Low-temperature photochemistry of previtamin D: First confirmation of the predicted geometry of a conical intersection, in *17th IUPAC Symposium on Photochemistry*, Sitges, Barcelona, Spain, 1998, Book of Abstracts, PA-29, p. 80.
- [53] A.M. Müller, S. Lochbrunner, W. Fuß, and W.E. Schmid, Low-temperature photochemistry of previtamin D: First confirmation of the predicted geometry of a conical intersection, in *1st GAIPHOS*, Bad Gastein, Austria, 1998, Book of Abstracts, P-13.
- [54] W. Fuß, S. Lochbrunner, A.M. Müller, T. Schikarski, W.E. Schmid, and S.A. Trushin, *Chem. Phys.* **232**, 161 (1998).
- [55] D. Heidrich, W. Kliesch, and W. Quapp, *Properties of Chemically Interesting Potential Energy Surfaces*, vol. **56** of *Lecture Notes in Chemistry*, Springer-Verlag, Berlin, 1991.
- [56] W. Domcke and G. Stock, *Adv. Chem. Phys.* **100**, 1 (1997).
- [57] H. Köppel, W. Domcke, and L.S. Cederbaum, *Adv. Chem. Phys.* **57**, 59 (1984).
- [58] R. Schneider, W. Domcke, and H. Köppel, *J. Chem. Phys.* **92**, 1045 (1990).
- [59] U. Manthe and H. Köppel, *J. Chem. Phys.* **93**, 345 (1990).
- [60] U. Manthe and H. Köppel, *J. Chem. Phys.* **93**, 1658 (1990).
- [61] L. Seidner and W. Domcke, *Chem. Phys.* **186**, 27 (1994).
- [62] L. Seidner, Dissertation, TU München, 1996, (in German).
- [63] F. Hund, *Z. Phys.* **40**, 742 (1927).
- [64] G. Calzaferri, H. Gugger, and S. Leutwyler, *Helv. Chim. Acta* **59**, 1969 (1976).
- [65] M. Kasha, *Discuss. Faraday Soc.* **9**, 14 (1950).
- [66] P.A. Geldorf, R.P.H. Rettschnick, and G.J. Hoytink, *Chem. Phys. Lett.* **4**, 59 (1969).
- [67] G. Wald, *Science* **162**, 230 (1968).
- [68] Q. Wang, R.W. Schoenlein, L.A. Peteanu, R.A. Mathies, and C.V. Shank, *Science* **266**, 422 (1994).
- [69] L.A. Peteanu, R.W. Schoenlein, Q. Wang, R.A. Mathies, and C.V. Shank, *Proc. Natl. Acad. Sci. USA* **90**, 11762 (1993).

- [70] P. Hamm, M. Zurek, T. Röschinger, H. Patzelt, D. Oesterheld, and W. Zinth, *Chem. Phys. Lett.* **263**, 613 (1996).
- [71] J. Dobler, W. Zinth, and W. Kaiser, *Chem. Phys. Lett.* **144**, 215 (1988).
- [72] R.A. Mathies, C.H. Brito Cruz, W.T. Pollard, and C.V. Shank, *Science* **240**, 777 (1988).
- [73] D. Kirmaier and D. Holten, *Photosynth. Res.* **13**, 225 (1987).
- [74] G. Feher, J.P. Allen, M.Y. Okamura, and D.C. Rees, *Nature* **339**, 111 (1989).
- [75] S.G. Boxer, *Annu. Rev. Biophys. Chem.* **19**, 267 (1990).
- [76] M. Bixon, M.E. Michel-Beyerle, and J. Jortner, *Isr. J. Chem.* **28**, 155 (1988).
- [77] M. Bixon and J. Jortner, *Chem. Phys. Lett.* **159**, 17 (1989).
- [78] R.A. Marcus, *Isr. J. Chem.* **28**, 205 (1988).
- [79] S. Gliesing, M. Reichenbacher, H.-D. Ilge, and D.Z. Fassler, *Z. Chem.* **29**, 21 (1989).
- [80] G.G. Kochendoerfer and R.A. Mathies, *Isr. J. Chem.* **35**, 211 (1995).
- [81] D. Oesterheld, *Isr. J. Chem.* **35**, 475 (1995).
- [82] J.K. Lanyi and G. Yaro, *Isr. J. Chem.* **35**, 365 (1995).
- [83] R.R. Birge, *Biochim. Biophys. Acta* **1016**, 293 (1990).
- [84] F.A. Carey and R.J. Sundberg, *Organische Chemie*, VCH, Weinheim, 1995.
- [85] T. Goldfarb and L. Lindquist, *J. Am. Chem. Soc.* **89**, 4588 (1967).
- [86] W.R. Roth and B. Peltzer, *Liebigs Ann. Chem.* **685**, 56 (1965).
- [87] W.G. Dauben, E.L. McInnis, and D.L. Michno, *Rearrangements in Ground and Excited States*, vol. **3**, Academic Press, New York, 1980.
- [88] W. Fuß, T. Schikarski, W.E. Schmid, S. Trushin, and K.L. Kompa, *Chem. Phys. Lett.* **262**, 675 (1996).
- [89] S.A. Trushin, W. Fuß, T. Schikarski, W.E. Schmid, and K.L. Kompa, *J. Chem. Phys.* **106**, 9386 (1997).
- [90] W. Fuß, W.E. Schmid, and S.A. Trushin, *J. Chem. Phys.* **112**, 8347 (2000).
- [91] A.M. Müller, unpublished results, 1995.
- [92] M. Protopapas, C.H. Keitel, and P.L. Knight, *Rep. Prog. Phys.* **60**, 389 (1997).
- [93] C.J.G.J. Uiterwaal, priv. comm., 2000.
- [94] S. Speiser and J. Jortner, *Chem. Phys. Lett.* **44**, 399 (1976).
- [95] L.V. Keldysh, *Zh. Eksp. Teor. Fiz.* **47**, 1945 (1964), *Sov. Phys. JETP* **20**, 1307 (1965).

- [96] T.D.G. Walsh, F.A. Ilkov, J.E. Decker, and S.L. Chin, *J. Phys. B: At. Mol. Opt. Phys.* **27**, 3767 (1994).
- [97] F.A. Ilkov, J.E. Decker, and S.L. Chin, *J. Phys. B: At. Mol. Opt. Phys.* **25**, 4005 (1992).
- [98] M.J. DeWitt, D.W. Peters, and R.J. Levis, *Chem. Phys.* **218**, 211 (1997).
- [99] M.J. DeWitt and R.J. Levis, *J. Chem. Phys.* **108**, 7045 (1998).
- [100] M.J. DeWitt and R.J. Levis, *J. Chem. Phys.* **108**, 7739 (1998).
- [101] M.J. DeWitt and R.J. Levis, *J. Chem. Phys.* **110**, 11368 (1999).
- [102] M.J. DeWitt and R.J. Levis, *J. Phys. Chem. A* **103**, 6493 (1999).
- [103] A.H. Zewail, *Femtochemistry: Ultrafast Dynamics of the Chemical Bond*, vol. **I and II**, World Scientific, Singapore, 1994, and references therein.
- [104] W.C. Wiley and I.H. McLaren, *Rev. Sci. Instrum.* **26**, 1150 (1955).
- [105] D.E. Spence, P.N. Kean, and W. Sibbett, *Opt. Lett.* **16**, 42 (1991).
- [106] I. Spinelli, B. Couillaud, N. Goldblatt, and D.K. Negus, in *Tech. Digest Conf. on Lasers and Electro-Optics*, vol. **paperCPD97**, p. 583, 1991.
- [107] O. Svelto, *Principles of Lasers*, Plenum Press, New York, 4th ed., 1998.
- [108] E.P. Ippen, H.A. Haus, and L.Y. Liu, *J. Opt. Soc. Am. B* **6**, 1736 (1989).
- [109] P. Moulton, *Opt. News* **8**, 9 (1982).
- [110] K.L. Sala, G.A. Kenney-Wallace, and G.E. Hall, *IEEE J. Quantum Electron.* **16**, 990 (1980).
- [111] D. Strickland and G. Mourou, *Opt. Commun.* **56**, 219 (1985).
- [112] F. Gan, *Laser Materials*, World Scientific, Singapore, 1994.
- [113] N. Bloembergen, (Ed.), *Encounters in Nonlinear Optics*, vol. **16** of *Series on the 20th Century Physics*, World Scientific, Singapore, 1996.
- [114] R.W. Boyd, *Nonlinear Optics*, Academic Press, New York, 1992.
- [115] D.L. Mills, *Nonlinear Optics: Basic Concepts*, Springer, Berlin, 1991.
- [116] Y.R. Shen, *The Principles of Nonlinear Optics*, Wiley, New York, 1984.
- [117] V.G. Dmitriev, G.G. Gurzadyan, and D.N. Nikogosyan, *Handbook of Nonlinear Optical Crystals*, vol. **64** of *Springer Series in Optical Sciences*, Springer-Verlag, Heidelberg, 2nd ed., 1997.
- [118] Gsänger Optoelektronik GmbH, *Frequency Conversion for Ti:Sapphire Lasers*, D-82152 Planegg, 1995.
- [119] G.D. Boyd and D.A. Kleinman, *J. Appl. Phys.* **39**, 3597 (1968).

- [120] K. Sändig, priv. comm., 1999.
- [121] W.T. Berthold, priv. comm., 1999.
- [122] J.-C. Diels and W. Rudolph, Measurement Techniques of Femtosecond Spectroscopy, in *Ultrashort Laser Pulse Phenomena: Fundamentals, Techniques, and Applications on a Femtosecond Time Scale*, p. 401, Academic Press, London, 1996.
- [123] H.E. Lessing and A.V. Jena, Continuous Picosecond Spectroscopy of Dyes, in *Laser Handbook*, edited by M.L. Stitch, p. 793, North-Holland Publ., Amsterdam, 1979.
- [124] A. Brodeur and S.L. Chin, Phys. Rev. Lett. **80**, 4406 (1998).
- [125] A.E. Siegman, *Lasers*, University Science Books, Mill Valley, California, 1986.
- [126] A.E. Siegman, M.W. Sasnett, and T.F. Johnston, Jr., IEEE J. Quantum Electron. **27**, 1098 (1991).
- [127] J.D. Jackson, *Classical Electrodynamics*, Wiley, New York, 2nd ed., 1975.
- [128] E.R. Cohen and P. Giacomo, Physica **146A**, 1 (1987).
- [129] W. Koechner, *Solid-State Laser Engineering*, vol. **1** of *Springer Series in Optical Sciences*, Springer, Berlin, 2nd ed., 1988.
- [130] A.A. Kaminskii, *Laser Crystals*, vol. **14** of *Springer Series in Optical Sciences*, Springer, Berlin, 2nd ed., 1990.
- [131] A. Yariv, *Optical Electronics*, Saunders College Publishers, Fort Worth, 4th ed., 1991.
- [132] Th. Schikarski, Dissertation, Ludwigs-Maximilians-Universität München, 1999, (in German).
- [133] J.L. Wiza, Nucl. Instr. Methods **162**, 587 (1979).
- [134] H. Schröder, priv. comm., 1999.
- [135] Design proposed by C.R. Gebhardt, 1999.
- [136] Leybold, *Vacuum Technology - its Foundations Formulae and Tables*, vol. **09/87**, 1987.
- [137] G. Beck, Rev. Sci. Instrum. **47**, 537 and 849 (1976).
- [138] DMS, *UV Atlas of Organic Compounds*, vol. **II**, Verlag Chemie, Butterworths, 1966.
- [139] K. Breuer, Fraunhofer-Institut für Bauphysik, GC-MS analysis of the toluene sample, 2000.
- [140] A.C. Cope, A.C. Haven, Jr., F.L. Ramp, and E.R. Trumbull, J. Am. Chem. Soc. **74**, 4867 (1952).
- [141] J.M. Greathead and S.W. Orchard, Int. J. Chem. Kinet. **15**, 1069 (1983).
- [142] A.M. Müller, Diplomarbeit, TU München, 1997, (in German).

- [143] K.W.D. Ledingham, D.J. Smith, R.P. Singhal, T. McCanny, P. Graham, H.S. Kilic, W.X. Peng, S.L. Wang, A.J. Langley, P.F. Taday, and C. Kosmidis, *J. Phys. Chem. A* **103**, 2952 (1999).
- [144] D.R. Lide and H.P.R. Frederikse, (Eds.), *CRC Handbook of Chemistry and Physics*, CRC Press, Boca Raton, 1993.
- [145] D.J. Smith, K.W.D. Ledingham, R.P. Singhal, H.S. Kilic, T. McCanny, A.J. Langley, P.F. Taday, and C. Kosmidis, *Rapid Commun. Mass Spectrom.* **12**, 813 (1998).
- [146] K.W.D. Ledingham, R.P. Singhal, D.J. Smith, T. McCanny, P. Graham, H.S. Kilic, W.X. Peng, S.L. Wang, A.J. Langley, P.F. Taday, and C. Kosmidis, *J. Phys. Chem. A* **102**, 3002 (1998).
- [147] M. Castillejo, S. Couris, E. Koudoumas, and M. Martn, *Chem. Phys. Lett.* **308**, 373 (1999).
- [148] M.J. DeWitt and R.J. Levis, *Phys. Rev. Lett.* **81**, 5101 (1998).
- [149] S.G. Lias, Ionization Energy Evaluation, in *NIST Chemistry WebBook, NIST Standard Reference Database Number 69*, edited by W.G. Mallard and P.J. Linstrom, p. 20899 (<http://webbook.nist.gov>), National Institute of Standards and Technology, Gaithersburg, MD, 1998.
- [150] P. Lambropoulos, *Comments At. Mol. Phys.* **20**, 199 (1987).
- [151] P. Lambropoulos, *Phys. Rev. Lett.* **55**, 2141 (1985).
- [152] V. Schyja, T. Lang, and H. Helm, *Phys. Rev. A* **57**, 3692 (1998).
- [153] J.G. Story, D.I. Duncan, and T.F. Gallagher, *Phys. Rev. A* **49**, 3875 (1993).
- [154] R. Bombach, J. Dannacher, and J.-P. Stadelmann, *J. Am. Chem. Soc.* **105**, 4205 (1983).
- [155] A.V. Golovin, M.E. Akopyan, and Yu.L. Sergeev, *Khim. Fiz.* **1983**, 379 (1983), *Sov. J. Chem. Phys.* **2**, 632 (1985).
- [156] C.B. Corkum, *Phys. Rev. Lett.* **71**, 1994 (1993).
- [157] C.J.G.J. Uiterwaal, D. Xenakis, and D. Charalambidis, *Z. Phys., D* **38**, 309 (1996).
- [158] D. Augst and D.D. Meyerhofer, *Laser Phys.* **4**, 1155 (1994).
- [159] M. Ammosov, N. Delone, and V. Krainov, *Sov. Phys. JETP* **64**, 1191 (1986).
- [160] A.D. Bandrauk and J. Ruel, *Phys. Rev. A* **59**, 2153 (1999).
- [161] M. Schmidt, S. Dobosz, P. Meynadier, P. D'Oliveira, and D. Normand, *Phys. Rev. A* **60**, 4706 (1999).
- [162] J.H. Posthumus, J. Plumridge, L.J. Frasinski, K. Codling, A.J. Langley, and P.F. Taday, *J. Phys. B* **31**, L985 (1998).

- [163] A.M. Müller, C.J.G.J. Uiterwaal, B. Witzel, J. Wanner, and K.-L. Kompa, *J. Chem. Phys.* **112**, 9289 (2000).
- [164] A.M. Müller, C.J.G.J. Uiterwaal, B. Witzel, J. Wanner, and K.-L. Kompa, Photoionization and photofragmentation of gaseous toluene using 80-fs, 800-nm laser pulses, in *99. Bunsentagung*, Würzburg, Germany, 2000, Vortragszusammenfassung, Programmheft B 66.
- [165] A.M. Müller, C.J.G.J. Uiterwaal, J. Wanner, B. Witzel, and K.-L. Kompa, Photoionization and Coherent Control of the Photofragmentation of Toluene, in *13th European Conference on Dynamics of Molecular Collisions, MOLEC 2000*, Jerusalem, Israel, 2000, Book of Abstracts, J-4, p. 192.
- [166] P.W. Milonni and J.H. Eberly, *Lasers*, Wiley, New York, 1988.
- [167] R.W. Boyd and G.S. Agarwal, *Phys. Rev. A* **59**, R2587 (1999).
- [168] A. Brodeur and S.L. Chin, *J. Opt. Soc. Am. B* **16**, 637 (1999).
- [169] L.M. Sverdlov, M.A. Kovnor, and E.P. Krainov, *Vibrational spectra of polyatomic molecules*, Wiley, New York, 1974.
- [170] P. Brumer and M. Shapiro, *Chem. Phys. Lett.* **126**, 541 (1986).
- [171] D.J. Tannor and S.A. Rice, *J. Chem. Phys.* **83**, 5013 (1985).
- [172] D.J. Tannor, R. Kosloff, and S.A. Rice, *J. Chem. Phys.* **85**, 5805 (1986).
- [173] R.S. Judson and H. Rabitz, *Phys. Rev. Lett.* **68**, 1500 (1992).
- [174] H. Rabitz, R. de Vivie-Riedle, M. Motzkus, and K. Kompa, *Science* **288**, 824 (2000).
- [175] H. Rabitz and W. Zhu, *Acc. Chem. Res.* **33**, 572 (2000).
- [176] T.C. Weinacht, J.L. White, and P.H. Bucksbaum, *J. Phys. Chem. A* **103**, 10166 (1999).
- [177] C. Batich, P. Bischof, and E. Heilbronner, *J. Electron Spectrosc. Relat. Phenom.* **1**, 333 (1973).
- [178] D.R. Lide, (Ed.), *Ionization Potentials of Atoms and Atomic Ions*, CRC Handbook of Chemistry and Physics, CRC Press, Boca Raton, 1992.
- [179] F.A.L. Anet and I. Yavari, *Tetrahedron Letters* **48**, 4221 (1975).
- [180] M. Olivucci, priv. comm., 2000.
- [181] D. Boyall and K.L. Reid, *Chem. Soc. Rev.* **26**, 223 (1997).
- [182] K. Kimura, S. Katsumata, Y. Achiba, T. Yamazaki, and S. Iwata, Ionization energies, Ab initio assignments, and valence electronic structure for 200 molecules, in *Handbook of HeI Photoelectron Spectra of Fundamental Organic Compounds*, Japan Scientific Soc. Press, Tokyo, 1981.
- [183] F. Bernardi, M. Olivucci, I.N. Ragazos, and M.A. Robb, *J. Am. Chem. Soc.* **114**, 8211 (1992).





## Acknowledgements

First and foremost I want to express my gratitude to *Prof. Dr. Dr. h.c. Karl-Ludwig Kompa* for having given me the opportunity to carry out my thesis in his group, and for being always open for the discussion of new ideas. I am deeply indebted to him for generously providing the funds both for materials and for numerous opportunities to present the obtained results at meetings and conferences at home and abroad. Moreover, he confidently encouraged me to pursue my own ideas (which gave me the chance to learn from my mistakes).

I would especially like to thank

*Dr. habil. Jochen Wanner* for openly having offered me the possibility to continue my experiments in his laboratory, and for his dedicated effort to support this work. The final experiment could not have been performed without his well organized coordination during the build-up phase of the laboratory. Although things were sometimes difficult, he never lost his belief in me successfully finishing this thesis. I am also committed to him for a wealth of advice, for proofreading this thesis, and for encouraging me to carry on with science in the future;

*Dr. Thomas Schikarski* for the excellent cooperation and understanding that he showed during all stages of this thesis. In particular, he competently introduced me to work in a fs laser laboratory. I would also like to thank him for many intensive and fruitful scientific discussions and cheerful conversations touching also non-physical issues, and for his technical expertise in all questions concerning computers and measurement electronics. Although his patience was taxed on many weekends, he supported the writing, especially with respect to the  $\text{\LaTeX}$  text processing program, in a very pleasant working atmosphere. Without his competent contributions, this work could not have been completed in its present form at this time;

*Dr. Kees Uiterwaal* for his infectious enthusiasm and his professional and personal interest in the success of the present work. I am obliged to him for many inspiring discussions, for his great support in putting into operation and testing the TOF mass spectrometer used for the final experiments, and for the collaboration in the toluene experiments presented in this thesis in a pleasant and considerate working atmosphere. He also supported me greatly by proofreading the present work;

*Walter Ritt* for daily switching on the laser system used for the initial experiments, for skillfully constructing the TOF mass spectrometer used for the final experiments, and for designing, assembling and maintaining the vacuum equipment with great care and competence. I also acknowledge his tireless commitment in supporting the laboratory work during all stages of this thesis and the pleasant and considerate working atmosphere;

*Arnold Steyer*, who greatly aided the experimental work presented here, for all his wonderful technical and human support. He was always cheerful, never failed to smile and brightened my day;

*Dr. Werner Fuß*, *Dr. Wolfram E. Schmid*, and *Dr. Sergei A. Trushin* for their introduction into the field of ultrafast chemistry, sharing their experimental setup for the initial experiments of this work, and lending me the TOF mass spectrometer under construction and other essential components for the final pump-probe experiments;

*Dr. Stefan Lochbrunner* for stimulating discussions concerning ultrafast reaction dynamics and short-pulse laser technology in the initial phase of this work;

*Dr. Hartmut Schröder* and *Christoph R. Gebhardt* for fruitful discussions concerning mass spectrometry;

*Dr. Bernd Witzel* for many rewarding discussions dealing with diverse issues in the initial phase of this work, and for drawing the  $H_3$  potential energy surfaces appearing in Fig. 2.7. I also want to acknowledge the good collaboration in the toluene experiments presented in this thesis;

*Priv.-Doz. Dr. Regina de Vivie-Riedle*, *Angelika Hofmann*, and *Dr. Karsten Sundermann* for stimulating discussions concerning the theoretical treatment of the photoreaction of 1,3-cyclohexadiene;

*Dr. Georg A. Schmitt* for many fruitful tips concerning the alignment of the Quantronix laser system and computer problems in the initial phase of this thesis;

*Wolfram Berthold* for sharing his expertise and vast knowledge about frequency conversion and laser pulse diagnostics, for his continuous helpfulness and willingness to lend me components, especially in the end-phase of the experimental work, and also for his true interest in the progress and success of this work;

*Dr. Detlev Proch* for his kind support, especially in the initial phase of this work;

*Dr. Christine Bucher* for linguistic proofreading the experimental part of this thesis, and for many cheerful conversations and good laughs together in the end-phase of this work;

*Margot Nagl*, who always had a warm-hearted and kind word for me, for organizational affairs;

*Dr. Hartmut Figger* for kindly permitting me to take part in the introduction course for the Spectra-Physics laser system in his laboratory, and for stimulating discussions on the  $H_3$  molecule;

*Dr. Karsten Sändig* for the excellent cooperation concerning the Spectra-Physics laser system, for many fruitful discussions and useful tips for designing the homebuilt frequency tripler, for generously lending me optical components for the final experiments, and for many amusing conversations;

*Dr. Gerhard G. Paulus* for kindly lending me his fast multiscaler;

*Prof. Dr. Massimo Olivucci*, Siena, Italy, and *Dr. Marco Garavelli*, Bologna, Italy, for sharing their vast knowledge about the concept of conical intersections in organic photochemistry;

*Dr. Thomas Feurer*, Jena, Germany, and the Jena group for many useful tips concerning short-pulse laser technology, frequency conversion, and pulse diagnostics;

*Ludwig Ertl*, *Thomas Strobl*, and their team of the machine shop for responding very quickly, precisely, and always of exceptional quality;

*Georg Brandl* for the manufacturing of excellent dielectric mirrors in the coating laboratory of the MPQ, for rapidly carrying out the orders, and for his kind willingness to make his absorption spectrometer available to me for testing of optics;

*Wolfgang Frisch* for manufacturing electronic circuits and repairing computers;

*Jürgen Borchers*, *Werner Kaiser*, and the whole purchasing department for their invaluable support in negotiating with companies, and for their great commitment to the fast handling of orders;

*Franz Demeter* for his kind willingness to open the stockroom also outside normal office hours;

*Jürgen Perchermeier* for skillfully carrying out the purification of 1,3,5-cyclooctatriene via cryodistillation and recording the absorption spectra of 1,3,5-cyclooctatriene and toluene;

*Dr. Boris Ruffing, Hans-Peter Hechler, Fritz Staudt* and the Spectra-Physics team for the competent introduction to the Spectra-Physics laser system used for the final experiments, skillful technical support, providing spare parts very quickly and without a great deal of red tape, and for the always excellent cooperation and pleasant atmosphere;

*Stefan Schwedt* (Excel Quantronix) for technical support of the Quantronix laser system used for the initial experiments;

*Dr. Stefan Kaesdorf* for his competent support and useful tips concerning the maintenance of MCP's and the TOF mass spectrometer used for the final experiments;

*Laura Thurston* for her competent linguistic reviews of this thesis;

*Jens Leyendecker* for his help and technical expertise in printing;

and my fellow students and friends *Dr. Claudia Breindl, Markus Eigner, Dr. Dieter Gleich, Dirk Goldbeck, Dr. Wolfgang Hieringer, Wolfgang Kling, Dieter Kraus, Roman Messerschmid, Martina Prinz,* and *Frank Sagmeister* for the wonderful shared experience.

Also many thanks to the people, not mentioned by name, who contributed to the successful completion of this thesis.

Moreover, I wish to express my deepest gratitude to my family – my parents and my brother Lutz. I could always count on their love, affectionate support and encouragement.



## Curriculum vitae

Name	Astrid M. Müller
Date of birth	January 29, 1972
Place of birth	Weingarten, Germany
Citizenship	German
1978 – 1982	Elementary school, Ravensburg, Germany
1982 – 1991	Humanistisches Spohn-Gymnasium, Ravensburg, Germany
June 17, 1991	Abitur, Prize of the Spohn-Gymnasium for the achievement of exceptional results, Prize of the foundation “Humanismus Heute” of the state Baden-Württemberg for the achievement of outstanding results in Latin, Book Prize of the “Fonds der Chemischen Industrie” for the achievement of exceptional results in Chemistry
1991 – 1997	Diplom Chemie (Honours in Chemistry) at the Technische Universität München, Munich, Germany
November 1996 – May 1997	Diploma thesis <i>“Tieftemperatur-Photochemie von 7-Dehydrocholesterol und Previtamin D” (Low Temperature Photochemistry of 7-dehydrocholesterol and previtamin D)</i> in the group of K.-L. Kompa, Laser Chemistry Division, Max-Planck-Institut für Quantenoptik, Garching, and V.E. Bondybey, Technische Universität München, Munich, Germany
June 1997 – December 2000	Doctoral thesis <i>“Ultrafast Reaction Dynamics of Polyatomic Molecules Probed by Ionization”</i> in the group of K.-L. Kompa, Laser Chemistry Division, Max-Planck-Institut für Quantenoptik, Garching, Germany

# Lebenslauf

Name	Astrid M. Müller
Geburtstag	29. Januar 1972
Geburtsort	Weingarten
Staatsangehörigkeit	deutsch
1978 – 1982	Grundschule, Ravensburg
1982 – 1991	Humanistisches Spohn-Gymnasium, Ravensburg
17. Juni 1991	Abitur, Preis des Spohn-Gymnasiums für besondere Leistungen, Preis der Stiftung “Humanismus Heute” des Landes Baden-Württemberg für hervorragende Leistungen im Fach Latein, Buchpreis des “Fonds der Chemischen Industrie” für besondere Leistungen in Chemie
1991 – 1997	Chemiestudium an der Technischen Universität München
November 1996 – Mai 1997	Diplomarbeit “ <i>Tieftemperatur-Photochemie von 7-Dehydrocholesterol und Previtamin D</i> ” bei K.-L. Kompa, Abteilung Laserchemie, Max-Planck-Institut für Quantenoptik, unter der formalen Betreuung von V.E. Bondybey, Technische Universität München
Juni 1997 – Dezember 2000	Doktorarbeit “ <i>Ultrafast Reaction Dynamics of Polyatomic Molecules Probed by Ionization</i> ” bei K.-L. Kompa, Abteilung Laserchemie, Max-Planck-Institut für Quantenoptik



